Computational analysis of fluid dynamics at the asceding thoracic aorta in Marfan syndrome patients

Ramon Maria Pons Cots

DOCTORAL THESIS

Title	Computational analysis of fluid dynamics at the ascending thoracic aorta in Marfan syndrome patients.
Presented by	Ramon Maria Pons Cots
Centre	IQS School of Engineering
Department	Chemical Engineering and Material Sciences
Directed by	Dr. Jordi Martorell López

Acknowledgments

A la família, per l'esforç realitzat en que pugues rebre la millor formació possible, tant en l'àmbit personal com en l'acadèmic. Sense vosaltres aquest camí hauria estat impossible. Moltes gràcies.

Al Dr. Jordi Martorell, per les seves idees i sempre veure una llum al final del camí, tot i haver-nos entrebancat moltes vegades.

Al Dr. José Javier Molins, por sus ayudas en todo lo referente a calculo incluso cuando no era de su ámbito.

Al Dr. Andrea Guala y la Dr. Lydia Dux-Santoy, gracias por siempre atenderme cuando lo he necesitado y ayudarme para que esto saliera adelante.

Al Dr. Arturo Evangelista y al Dr. José F Rodríguez con todo el equipo médico de Vall d'Hebron, gracias por contar conmigo en este proyecto y aconsejarme siempre lo mejor posible en el camino a seguir.

Al Dr. Juan Carlos Cajas, las simulaciones iniciales fueron un gran problema y sin ti este proyecto no tendría el color que tiene hoy. Muchas gracias.

Al Dr. Mariano Vázquez y todo el equipo del BSC, gracias por vuestras grandes aportaciones y por ayudarme a tirar adelante este proyecto.

Als companys de pis, vosaltres heu fet que aquesta dècada a Barcelona s'hagi passat rapidíssima i sense el vostre suport

Als amics dels Alamús, perquè tot i que ens hem separat al llarg dels anys sempre heu estat allí quan ho necessitava i espero que hi sigueu sent.

Als companys de GEVAB, per les seves idees esperançadores i per fer els dies de treball més amens.

A la Marina, per ser el pilar més important en aquests darrers 3 anys. El suport incondicional, les ganes de riure, els petits detalls i moltes virtuts més que espero que mai perdis, et fan la persona més especial de la meva vida.

Abstract

Aortic aneurysms are a progressive and irreversible dilation of the aortic wall, which can lead to vessel rupture or dissection, resulting in catastrophic blood loss leading to death. Initial pharmacological treatment is focused on growth arrest to prevent rupture, but invasive open repair or endovascular repair are required in patients at risk. Patient management and risk stratification after diagnosis are critical, especially in the ascending aorta since no endovascular treatments are currently available. According to current guidelines, maximum aortic diameter is the only patient-specific geometrical or fluidodynamic criterion accepted as clinical rupture risk predictor. However, abnormal fluid dynamics at the ascending aorta have been widely reported as potential origin of aortic aneurysms and their understanding could improve the risk assessment of patients.

In this study, the fluid dynamics of aortae from healthy controls and patients with Marfan syndrome have been evaluated. To do so, we have compared the performance of computational fluid dynamics and fluid-structure interaction simulations using clinical imaging as patient-specific inputs. We have also designed an *in vitro* system that could expose human aortic endothelial cells to a fluidodynamic environment that mimics that of aortic simulations.

The study has revealed, in Marfan patients, that considering the wall elasticity in simulations is critical to derive precisely fluid dynamic values that hold the potential to stratify such patients. In this sense, fluid-structure interaction simulations have outperformed classic computational fluid dynamics at a moderate computational cost. As a result of this study, a dimensionless parameter, the shear stress ratio, has shown its potential as marker of aneurysm progression in Marfan patients.

Resumen

Los aneurismas aórticos son una dilatación progresiva e irreversible de la pared aórtica, que puede causar la ruptura o disección de los vasos, lo que resulta en una pérdida catastrófica de sangre que conduce a la muerte. El tratamiento farmacológico inicial se centra en detener el crecimiento para prevenir la ruptura, pero se requiere una reparación invasiva abierta o una reparación endovascular en pacientes en riesgo. El manejo del paciente y la estratificación del riesgo después del diagnóstico son críticos, especialmente en la aorta ascendente, ya que actualmente no hay tratamientos endovasculares disponibles. Según las directrices actuales, el diámetro aórtico máximo es el único criterio geométrico o fluidodinámico específico del paciente aceptado como predictor clínico del riesgo de ruptura. Sin embargo, la anormal fluidodinámica en la aorta ascendente se ha reportado ampliamente como una posible fuente de aneurismas aórticos y su comprensión podría mejorar la evaluación del riesgo del paciente.

En este estudio, se evaluó la fluidodinámica en aortas de controles sanos y pacientes con síndrome de Marfan. Para hacer esto, hemos comparado el rendimiento de las simulaciones de dinámica de fluidos computacional y de interacción fluido-estructura utilizando imágenes clínicas como condiciones específicas del paciente. También hemos diseñado un sistema *in vitro* que podría exponer las células endoteliales aórticas humanas a un entorno fluidodinámico que imita el de las simulaciones aórticas.

El estudio ha revelado, en pacientes Marfan, que considerar la elasticidad de la pared en las simulaciones es esencial para obtener con precisión los valores dinámicos de los fluidos que tienen el potencial de estratificar a estos pacientes. En este sentido, las simulaciones de interacción fluido-estructura han superado la fluidodinámica computacional clásica a un costo computacional moderado. Como resultado de este estudio, un parámetro adimensional, la relación de esfuerzo cortante, ha demostrado su potencial como marcador de progresión de aneurisma en pacientes con Marfan.

Resum

Els aneurismes aòrtics són una dilatació progressiva i irreversible de la paret aòrtica, que pot causar la ruptura o dissecció dels vasos, el que resulta en una pèrdua catastròfica de sang que condueix a la mort. El tractament farmacològic inicial se centra en aturar el creixement per prevenir la ruptura, però requereix una reparació invasiva oberta o una reparació endovascular en pacients en risc. El maneig del pacient i l'estratificació de risc després del diagnòstic són crítics, especialment en l'aorta ascendent, ja que actualment no hi ha tractaments endovasculars disponibles. Segons les directrius actuals, el diàmetre aòrtic màxim és l'únic criteri geomètric o fluidodinàmic específic del pacient acceptat com a predictor clínic del risc de ruptura. No obstant això, l'anormal fluidodinàmica en l'aorta ascendent s'ha reportat àmpliament com una possible font d'aneurismes aòrtics i la seva comprensió podria millorar l'avaluació del risc del pacient.

En aquest estudi, es va avaluar la fluidodinàmica en aortes de controls sans i pacients amb síndrome de Marfan. Per fer això, hem comparat el rendiment de les simulacions de dinàmica de fluids computacional i d'interacció fluid-estructura utilitzant imatges clíniques com a condicions específiques del pacient. També hem dissenyat un sistema *in vitro* que podria exposar les cèl·lules endotelials aòrtiques humanes a un entorn fluidodinàmic que imita el de les simulacions aòrtiques.

L'estudi ha revelat, en pacients Marfan, que considerà l'elasticitat de la paret en les simulacions és essencial per obtenir amb precisió els valors fluidodinàmics que tenen el potencial d'estratificar aquests pacients. En aquest sentit, les simulacions d'interacció fluid-estructura han superat la fluidodinàmica computacional clàssica a un cost computacional moderat. Com a resultat d'aquest estudi, un paràmetre adimensional, la relació d'esforç tallant, ha determinat el seu potencial com a marcador de progressió d'aneurisma en pacients amb Marfan.

Index

Contenido

1.1. The essence of the Aorta 2
1.1.1. Anatomy of the aorta 2
1.1.2. Pulsatile blood flow 4
1.1.3. Blood vessel structure 5
1.2. Aortic aneurysms 7
1.2.1. Classification 7
1.2.2. Etiology and molecular mechanisms involved in aneurysm formation 9
1.2.3. Diagnosis and Treatment 12
1.3. Computational models 16
1.3.1 Continuum mechanics 18
1.3.2 Finite Elements Method 20
1.3.3 Unmet needs in fluidodynamic assessment of aortic diseases 22
1.4 Hypothesis and Objectives 23
2.1. Pre-analysis 26
2.1.1. Data from Medical Images 26
2.1.2 Raw data extraction 26
2.1.3. Geometry segmentation 29
2.1.4 Inlet boundary condition 33
2.1.4.1 B-spline 34
2.1.5. Patient-specific boundary conditions 38
2.1.6 GiD 40
2.2. Calculus 42
2.2.1. Alya 42
2.2.2. Minotauro 46
2.2.3. Mare Nostrum 47
2.3. Post-analysis 48
2.3.1. Visualization 48
2.3.2. Fluid dynamic parameters calculus 48
2.3.3 Statistical analysis 57
3.1. Simulation model 60
3.2. Boundary conditions modelling 68
3.2.1. Inlet 4D-MRI 68

3.2.2. Windkessel method 70
3.2.3. Pulse wave velocity 74
3.2.4. Clinical data 75
3.3. Simulation analysis 77
3.4. Windkessel Effect 149
3.5. Pulse Wave Velocity 151
3.6. Primary fluidodynamic parameters 152
3.7. Secondary fluidodynamic parameters 155
3.7.1 Methodology of shear stress calculation 155
3.7.2 Axial and Circumferential Shear Stresses and Vorticity analysis 158
3.7.3 Shear Stress Ratio Analysis 164
3.8 Replicating rotating flow in vitro 169
3.8.1 Straight tube of 10 mm diameter 170
Conclusions 174
References 176
Annex 182

List of Figures and Tables

Figure 1. Aorta main parts; thoracic and abdominal (A), valve and sinotubular junction (B). 3
Figure 2. Aortic pulsatile blood flow[9] 4
Figure 3. Artery vessel structure 6
Figure 4. Types of aneurysm; fusiform (A), saccular (B), and dissection (C). 8
Figure 5. TGF-β1 pathway diagram 10
Figure 6. Open and close valve morphology; tricuspid (A), bicuspid (B) and with stenosis (C). . 12
Figure 7. Clinical imaging techniques to diagnose aneurysm; echocardiography (A), CT (B), MRI (C). 13
Figure 8. Path to follow after detection of ascending aortic aneurysm by European Society of Cardiology[44]. 14
Figure 9. Aneurysm treatments; open surgery (A) and endovascular repair (B). 15
Figure 10. (A) Segmentation of an aorta from MRI imaging. (B) Flow though aorta analyzed with 4D-MRI. 17
Figure 11. CFD simulation results; (A) pressure , (B) velocity in streamlines[62] and (C) WSS at systolic peak. 18
Figure 12. FEM method scheme. 21
Figure 13. Mesh element types distributed by dimensions; 1D, 2D and 3D..... 21
Figure 14. (A) Generalized geometry to mimic aneurysm and (B) velocity profile from literature. 22
Figure 15. Patient-specific (A) geometry and (B) flow profile. 22
Figure 16. Segmentation of the geometry of a healthy control. 27
Figure 17. The contours of ascending and descending aorta in Mass. 27
Figure 18. Ascending and descending flows of a healthy control in Mass..... 28
Figure 19. Velocity extraction of 4D-MRI images with Mass. 28
Figure 20. Interface for geometry creation at SolidWorks; (A) main interface tab, (B) fluid ascending tab, (C) solid brachiocephalic tab. 29
Figure 21. Fluid domain construction; (A) circumferences and splines creation of the aorta, (B) loft operation, (C) creation of the three upper arteries, (D) loft and extrusion of the upper arteries. 31
Figure 22. Solid domain construction; (A) circumferences and splines creation of the wall vessel, (B) loft and unloft operations, (C) creation of the three upper arteries, (D) loft, unloft and extrusion of the upper arteries. 32
Figure 23. Final geometries; (A) fluid domain, (B) solid domain. 33
Figure 24. Aorta impressed in 3D with the STL file. 33
Figure 25. Velocity vectors from 4D-MRI at Paraview. 34
Figure 26. Bicubic B-spline method at Patch 1..... 35
Figure 27. Appliance of bicubic B-spline method; (A) 4D-MRI points with inlet nodes of the mesh, (B) zoom of B-spline point with inlet nodes of the mesh. 37
Figure 28. Velocity profile at (A) 10 milliseconds, (B) 70 milliseconds, (C) 110 milliseconds and (D) 300 milliseconds of a pulse. 37
Figure 29. Electrical circuit analogous to a Windkessel model of 2-elements..... 38
Figure 30. Codes applied to (A) fluid domain and (B) solid domain..... 40
Figure 31. The meshes of (A) fluid domain and (B) solid domain. 41
Figure 32. Mare Nostrum servers at Barcelona Supercomputing Center. 46

Figure 33. (A) Ascending and descending planes in the aorta where fluid dynamic parameters as (B) jet angle, (C) maximum velocity and flow displacement are analyzed. 49
Figure 34. Axial shear stress of thoracic aorta calculated with the first method. 51
Figure 35. Velocity field (A, B) of the mesh and (C, D) after applying patches at systole and diastole steps. 52
Figure 36. Shear stress in a straight tube calculated from (A) Method 1 and (B) Tdyn. 53
Figure 37. Conceptual representation of a section grid division, patches and velocities. 53
Figure 38. Grid points and nodes coordinates of a slice. 54
Figure 39 Shear stress calculation for the mesh nodes; a node inside the grid (A) and a node outside the grid (B). 55
Figure 40. MRI image where ascending aorta is divided in four quadrants. 55
Figure 41. Streamlines of an aorta showing velocity and vorticity parameters. 56
Figure 42. Meshed geometry of (A) healthy control and (B) BAV patient. 60
Figure 43. Inlet boundary condition after Matlab treatment (A) in healthy control (B) and BAV patient. 60
Figure 44. CFD convergence with constant inlet velocity of (A, B) the healthy control and (C, D) the BAV patient. 62
Figure 45. CFD convergence with 4D-MRI inlet velocity of (A, B) the healthy control and (C, D) the BAV patient. 63
Figure 46. BAV patient FSI convergence (A, B) of the fluid and (C) the coupling in the first iteration of the method. 64
Figure 47. BAV patient FSI convergence (A, B) of the fluid and (C, D) the coupling in the second iteration of the method. 65
Figure 48. BAV patient FSI convergence (A, B) of the fluid and (C, D) the coupling in the third iteration of the method. 66
Figure 49. Healthy control FSI convergence (A, B) of the fluid and (C, D) the coupling. 67
Figure 50. Flow of sinotubular junction (A) with 4D-MRI technique and (B) after the spatial-temporal interpolation in Matlab. 69
Figure 51. Mesh of the Y geometry (A) and velocity field of the simulation with no Windkessel. 70
Figure 52. Velocity field in Y geometry with a Windkessel of (A) R=100, (B) R=500, (C) R=1000, (D) R=2000. 71
Figure 53. Velocity field in Y geometry with a Windkessel of R=4000. 71
Figure 54. Convergence of Y simulation with Windkessel (A, B) and divergence of R=4000 (C, D). 72
Figure 55. Outlets flow versus the Windkessel resistance. 72
Figure 56. Flow at descending aorta using multiple Windkessel resistance values. 73
Figure 57. Delay between sinotubular junction and descending aorta with (A) CFD and (B) FSI simulations. 74
Figure 58. Visualization of C1 aorta with MRI using Mass. 77
Figure 59. (A) Reconstruction of the aorta vessel and the wall, (B) meshing of the fluid and (C) meshing of the wall. 78
Figure 60. Flows at sinotubular junction and descending aorta of C1 from MRI images. 79
Figure 61. Sinotubular junction blood flow profile after interpolation of C1. 79
Figure 62. Fluid dynamic results of healthy control 1; (A) velocity, (B) vorticity, (C) displacement, (D) axial shear stress, (E) circumferential shear stress and (F) shear stress ratio. 81
Figure 63. Visualization of C2 aorta with MRI using Mass. 83

Figure 64. Reconstruction of the aorta vessel and the wall (A), meshing of the fluid (B) and the wall (C). 84
Figure 65. Flows at sinotubular junction and descending aorta of C2 with MRI technique. 84
Figure 66. Flow curve of C2 at sinotubular junction after B-spline interpolation. 85
Figure 67. C2 FSI convergence of (A, B) the fluid, (C, D) the coupling. 85
Figure 68. Fluid dynamic results of healthy control 2; (A) velocity, (B) vorticity, (C) displacement, (D) axial shear stress, (E) circumferential shear stress and (F) shear stress ratio. 88
Figure 69. Visualization of C3 aorta with MRI using Mass. 89
Figure 70. (A) Reconstruction of the aorta vessel and the wall, (B) meshing of the fluid and (C) meshing of the wall. 90
Figure 71. Flows at sinotubular junction and descending aorta of C3 with MRI technique. 90
Figure 72. Flow curve of C3 at sinotubular junction after B-spline interpolation. 91
Figure 73. C3 FSI convergence of (A, B) the fluid, (C, D) the coupling. 91
Figure 74. Fluid dynamic results of healthy control 3; (A) velocity, (B) vorticity, (C) displacement, (D) axial shear stress, (E) circumferential shear stress and (F) shear stress ratio. 94
Figure 75. Visualization of C4 aorta with MRI using Mass. 95
Figure 76. (A) Reconstruction of the aorta vessel and the wall, (B) meshing of the fluid and (C) meshing of the wall. 96
Figure 77. Flows at sinotubular junction and descending aorta with MRI technique of C4. 96
Figure 78. Flow curve of C4 at sinotubular junction after B-spline interpolation. 97
Figure 79. C4 FSI convergence of (A, B) the fluid, (C, D) the coupling. 97
Figure 80. Fluid dynamic results of healthy control 4; (A) velocity, (B) vorticity, (C) displacement, (D) axial shear stress, (E) circumferential shear stress and (F) shear stress ratio. 100
Figure 81. Visualization of S1 aorta with MRI using Mass. 101
Figure 82. (A) Reconstruction of the aorta vessel and the wall, (B) meshing of the fluid and (C) meshing of the wall. 102
Figure 83. Flows at sinotubular junction and descending aorta of S1 with MRI technique. 102
Figure 84. Flow curve of S1 at sinotubular junction after B-spline interpolation. 103
Figure 85. S1 FSI convergence of (A, B) the fluid, (C, D) the coupling. 103
Figure 86. Fluid dynamic results of stable patient 1; (A) velocity, (B) vorticity, (C) displacement, (D) axial shear stress, (E) circumferential shear stress and (F) shear stress ratio. 106
Figure 87. Visualization of S2 aorta with MRI using Mass. 107
Figure 88. (A) Reconstruction of the aorta vessel and the wall, (B) meshing of the fluid and (C) meshing of the wall. 108
Figure 89. Flows at sinotubular junction and descending aorta with MRI technique of S2. 108
Figure 90. Flow curve of S2 at sinotubular junction after B-spline interpolation. 109
Figure 91. S2 FSI convergence of (A, B) the fluid, (C, D) the coupling. 109
Figure 92. Fluid dynamic results of stable patient 2; (A) velocity, (B) vorticity, (C) displacement, (D) axial shear stress, (E) circumferential shear stress and (F) shear stress ratio. 112
Figure 93. Visualization of S3 aorta with MRI using Mass. 113
Figure 94. (A) Reconstruction of the aorta vessel and the wall, (B) meshing of the fluid and (C) meshing of the wall. 114
Figure 95. Flows at sinotubular junction and descending aorta with MRI technique of S3. 114
Figure 96. Flow curve of S3 at sinotubular junction after B-spline interpolation. 115
Figure 97. S3 FSI convergence of (A, B) the fluid, (C, D) the coupling. 115

Figure 98. Fluid dynamic results of stable patient 3; (A) velocity, (B) vorticity, (C) displacement, (D) axial shear stress, (E) circumferential shear stress and (F) shear stress ratio..... 118
Figure 99. Visualization of S4 aorta with MRI using Mass. 119
Figure 100. (A) Reconstruction of the aorta vessel and the wall, (B) meshing of the fluid and (C) meshing of the wall. 120
Figure 101. Flows at sinotubular junction and descending aorta of S4 with MRI technique. .. 120
Figure 102. Flow curve of S4 at sinotubular junction after B-spline interpolation. 121
Figure 103. S4 FSI convergence of (A, B) the fluid, (C, D) the coupling. 121
Figure 104. Fluid dynamic results of stable patient 4; (A) velocity, (B) vorticity, (C) displacement, (D) axial shear stress, (E) circumferential shear stress and (F) shear stress ratio. 124
Figure 105. Visualization of patient D1 aorta with MRI using Mass. 125
Figure 106. (A) Reconstruction of the D1 aorta vessel and the wall, meshing (B) of the fluid and (C) of the wall. 126
Figure 107. Flows at sinotubular junction and descending aorta of D1 with MRI technique... 126
Figure 108. Flow curve of D1 at sinotubular junction after B-spline interpolation. 127
Figure 109. D1 FSI convergence of (A, B) the fluid, (C, D) the coupling. 127
Figure 110. Fluid dynamic results of dilating patient 1; (A) velocity, (B) vorticity, (C) displacement, (D) axial shear stress, (E) circumferential shear stress and (F) shear stress ratio. 130
Figure 111. Visualization of D2 aorta with MRI using Mass. 131
Figure 112. (A) Reconstruction of the aorta vessel and the wall, (B) meshing of the fluid and (C) meshing of the wall. 132
Figure 113. Flows at sinotubular junction and descending aorta with MRI technique of D2... 132
Figure 114. Flow curve of D2 at sinotubular junction after B-spline interpolation. 133
Figure 115. D2 FSI convergence of (A, B) the fluid, (C, D) the coupling. 133
Figure 116. Fluid dynamic results of healthy control 4; (A) velocity, (B) vorticity, (C) displacement, (D) axial shear stress, (E) circumferential shear stress and (F) shear stress ratio. 136
Figure 117. Visualization of D3 aorta with MRI using Mass. 137
Figure 118. (A) Reconstruction of the aorta vessel and the wall, (B) meshing of the fluid and (C) meshing of the wall. 138
Figure 119. Flows at sinotubular junction and descending aorta with MRI technique of D3... 138
Figure 120. Flow curve of D3 at sinotubular junction after B-spline interpolation. 139
Figure 121. D3 FSI convergence of (A, B) the fluid, (C, D) the coupling. 139
Figure 122. Fluid dynamic results of dilating patient 3; (A) velocity, (B) vorticity, (C) displacement, (D) axial shear stress, (E) circumferential shear stress and (F) shear stress ratio. 142
Figure 123. Visualization of D4 aorta with MRI using Mass. 143
Figure 124. (A) Reconstruction of the aorta vessel and the wall, (B) meshing of the fluid and (C) meshing of the wall. 144
Figure 125. Flows at sinotubular junction and descending aorta with MRI technique of D4... 144
Figure 126. Flow curve of D4 at sinotubular junction after B-spline interpolation. 145
Figure 127. D4 FSI convergence of (A, B) the fluid, (C, D) the coupling. 145
Figure 128. Fluid dynamic results of dilating patient 4; (A) velocity, (B) vorticity, (C) displacement, (D) axial shear stress, (E) circumferential shear stress and (F) shear stress ratio. 148

Figure 129. Comparison of flow extracted from MRI images versus 4D-MRI images at systolic peak. 149
Figure 130. Flow ratio of CFD and FSI simulations versus MRI. 150
Figure 131. PWV calculated from 4D-MRI versus FSI simulation. 151
Figure 132. Comparison between 4D-MRI and both simulation of (A) normalized displacement, (B) jet angle and (C) maximum velocity in ascending and descending planes. 154
Figure 133. Visualization of axial shear stress with the old and the new method. 156
Figure 134. Visualization of circumferential shear stress with the old and the new method. . 156
Figure 135. Axial shear stress in healthy controls and stable and dilating patients at the ascending aorta, aortic arch and descending aorta. 158
Figure 136. Circumferential shear stress in healthy controls and stable and dilating patients at the ascending aorta, aortic arch and descending aorta. 160
Figure 137. Circumferential shear stress in healthy controls and stable and dilating patients at the ascending aorta, aortic arch and descending aorta. 162
Figure 138. (A) Ascending aorta division into proximal (red) and distal (yellow) and SSR versus the distance to the aortic root at (B) proximal and (C) distal aorta in healthy controls. 165
Figure 139. (A) Ascending aorta division into proximal (red) and distal (yellow) and SSR versus the distance to the aortic root at (B) proximal and (C) distal aorta in stable patients. 166
Figure 140. (A) Ascending aorta division into proximal (red) and distal (yellow) and SSR versus the distance to the aortic root at (B) proximal and (C) distal aorta in dilating patients. 166
Figure 141. Cumulative frequency of shear stress ratio from all the cases. 168
Figure 142. Ascending aorta shear stress ratio from one control, one stable patient and one dilating patient with their respective graphs versus the distance to aortic root. 168
Figure 143. *In vitro* system designed to test endothelial cells. 169
Figure 144. Helixes designed to replicate the rotational flow from simulations (A) 0,75 revolutions and (B) 1,5 revolutions and (B, D) printed in 3D. 169
Figure 145. Axial and circumferential shear stress after the helix in the first simulation. 170
Figure 146. Axial shear stress after the helix in the second simulation. 171
Figure 147. Circumferential shear stress after the helix in the second simulation. 172
Figure 148. Axial shear stress after the helix in the third simulation. 172
Figure 149. Circumferential shear stress after the helix in the third simulation. 173

Table 1. Number of points extracted from 4D-MRI images, after interpolation and from inlet mesh surface. 68
Table 2. Values to test the influence of thickness in PWV. 74
Table 3. Demographic and clinical data of four healthy controls, four stable patients and four dilating patients. 75
Table 4. Average demographic and clinical history of healthy controls, stable and dilating Marfan patients. 76
Table 5. Geometry data extracted from MRI images to reconstruct C1 aorta in SolidWorks. ... 78
Table 6. Final flows at descending aorta and flow ratio of C1. 80
Table 7. Geometry data extracted from MRI images to reconstruct C2 aorta in SolidWorks. ... 83
Table 8. Final flows at descending aorta and flow ratio of C2. 86
Table 9. Young's modulus iterations to match clinical PWV of C2. 86
Table 10. Geometry data extracted from MRI images to reconstruct C3 aorta in SolidWorks. . 89
Table 11. Final flows at descending aorta and flow ratio of C3. 92
Table 12. Young's modulus iterations to match clinical PWV of C3. 92
Table 13. Geometry data extracted from MRI images to reconstruct C4 aorta in SolidWorks. . 95
Table 14. Final flows at descending aorta and flow ratio of C4. 98
Table 15. Young's modulus iterations to match clinical PWV of C4. 98
Table 16. Geometry data extracted from MRI images to reconstruct S1 aorta in SolidWorks. 101
Table 17. Final flows at descending aorta and flow ratio of S1. 104
Table 18. Young's modulus iterations to match clinical PWV of S1. 104
Table 19. Geometry data extracted from MRI images to reconstruct S2 aorta in SolidWorks. 107
Table 20. Final flows at descending aorta and flow ratio of S2. 110
Table 21. Young's modulus iterations to match clinical PWV of S2. 110
Table 22. Geometry data extracted from MRI images to reconstruct S3 aorta in SolidWorks. 113
Table 23. Final flows at descending aorta and flow ratio of S3. 116
Table 24. Young's modulus iterations to match clinical PWV of S3. 116
Table 25. Geometry data extracted from MRI images to reconstruct S4 aorta in SolidWorks. 119
Table 26. Final flows at descending aorta and flow ratio of S4. 122
Table 27. Young's modulus iterations to match clinical PWV of S4. 122
Table 28. Geometry data extracted from MRI images to reconstruct D1 aorta in SolidWorks.125
Table 29. Final flows at descending aorta and flow ratio of D1. 128
Table 30. Young's modulus iterations to match clinical PWV of D1. 128
Table 31. Geometry data extracted from MRI images to reconstruct D2 aorta in SolidWorks.131
Table 32. Final flows at descending aorta and flow ratio of D2. 134
Table 33. Young's modulus iterations to match clinical PWV of D2. 134
Table 34. Geometry data extracted from MRI images to reconstruct D3 aorta in SolidWorks.137
Table 35. Final flows at descending aorta and flow ratio of D3. 140
Table 36. Young's modulus iterations to match clinical PWV of C4. 140
Table 37. Geometry data extracted from MRI images to reconstruct D4 aorta in SolidWorks.143
Table 38. Final flows at descending aorta and flow ratios of D4. 146
Table 39. Young's modulus iterations to match clinical PWV of D4. 146
Table 40. Normalized displacement calculated from 4D-MRI, CFD and FSI simulations in both planes. 152
Table 41. Jet angle calculated from 4D-MRI, CFD and FSI simulations in both planes. 152
Table 42. Maximum velocity calculated from 4D-MRI, CFD and FSI simulations in both planes. 153
Table 43. Error reduction of FSI versus CFD at the ascending aortic plane. 153

Table 44. Error reduction of FSI versus CFD at the descending aortic plane. 154
Table 45. Volumetric analysis of OSI, TAWSS and SSR at distal and proximal aorta from healthy controls and stable and dilating patients. 164
Table 46. Shear stress ratio at interior, exterior, anterior and posterior wall surfaces..... 167

ABBREVIATIONS

ATAA	Ascending thoracic aortic aneurysm
TAA	Thoracic aortic aneurysm
AAA	Abdominal aortic aneurysm
ECM	Extracellular matrix
SMC	Smooth muscle cells
TGF-B1	Transforming growth factor beta one
BAV	Bicuspid aortic valve
MFN	Marfan
CT	Computed tomography
MRI	Magnetic resonance imaging
4D-MRI	Four-dimensional magnetic resonance imaging
WSS	Wall shear stress
FEM	Finite element method
CFD	Computational fluid dynamic
FSI	Fluid-structure interaction
VTK	Visualization Tool Kit
CAD	Computer aided design
PWV	Pulse wave velocity
ALE	Arbitrary Lagrangian Eulerian
NAN	Not a number
AWSS	Average wall shear stress
OSI	Oscillatory shear index
ATWSS	Average-time wall shear stress
SSR	Shear stress ratio

1.Introduction

1.1. The essence of the Aorta

1.1.1. Anatomy of the aorta

The aorta (Figure 1A) is the largest artery in the human body, measuring more than one meter in length and reaching up to three centimeters in diameter in a healthy adult[1,2]. It is an elastic, flexible and extensible artery and the initial part of the cardiovascular system. Its main function is to distribute blood to all the vital organs of the body though the cardiovascular system. The primary role of the cardiovascular system consists on distributing essential chemicals to tissues and removing metabolic byproducts from them[3]. The heart is the pump of this system, and the vasculature is the closed network of tubes that propels blood from the heart to the tissues and back. The aorta receives oxygenated blood expelled by the left ventricle via the aortic root and branches out into arteries that gradually diminish in diameter up to billions of capillaries. These are microvessels that exchange the aforementioned chemicals with the cells and that regroup into veins that discharge the blood back to the heart and the lungs[4].

The aorta is divided in two main sections; thoracic and abdominal[3,5]. The thoracic aorta starts at the aortic root of the left ventricle and extends to the diaphragm. It can be divided in three segments: the ascending aorta, the aortic arch and the descending aorta. The abdominal aorta starts at the diaphragm and extends until the bifurcation of the common iliac arteries[6].

The aortic root is a very complex system consisting of the tricuspid aortic valve, and the openings for the coronary arteries[6,7]. The three flaps of the valve are biological controllers of pressure, remaining open while the pressure inside the ventricle is higher (systole) and closing when the pressure of the aorta is higher (diastole), impeding retrograde flux to the heart[7]. The aortic root finishes at the sinotubular junction, which is the union to the aorta. Figure 1B shows the aortic root with a cut at the sinotubular junction, where the three flaps of the valve can be observed.

As the aorta is the largest artery of the body, it has many bifurcations and derivations along its length. The most important divisions along the thoracic aorta are the left and right coronary arteries at the aortic root and the three divisions at the aortic arch, the brachiocephalic, the left common carotid and the left subclavian arteries[3,6]. At the abdominal aorta, the main divisions are the superior and inferior mesenteric arteries, the left and right renal arteries, and at the left and right iliac arteries[6,7].

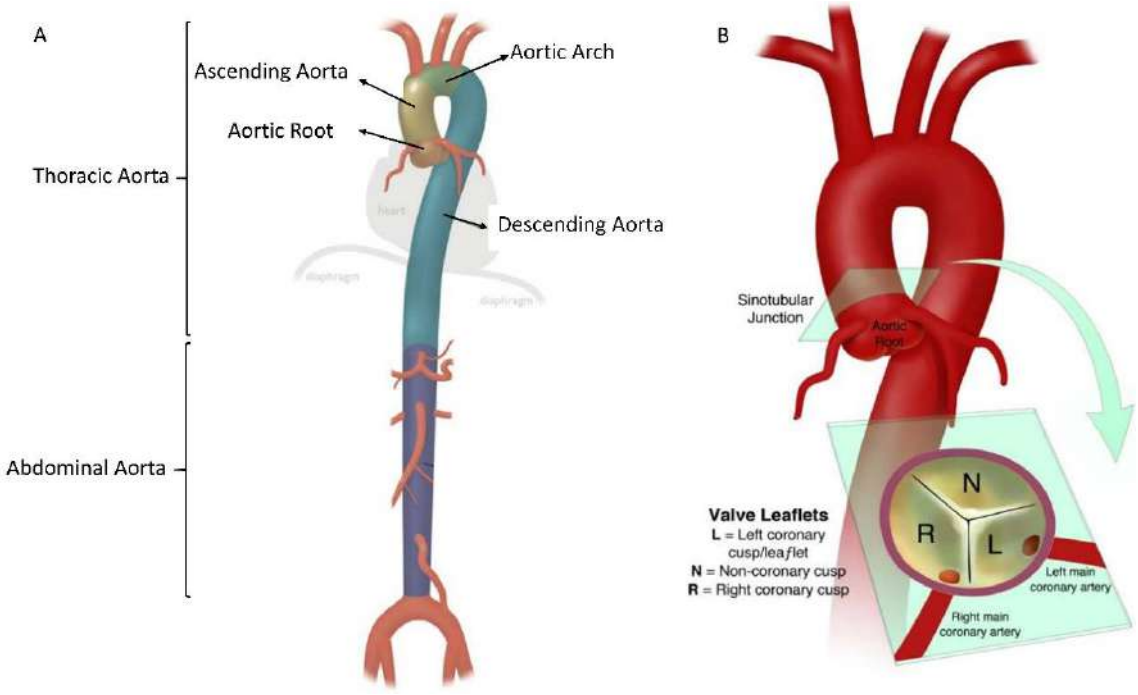

Figure 1. Aorta main parts; thoracic and abdominal (A), valve and sinotubular junction (B).

Coronary arteries supply blood to the heart muscle. They are divided many times along their path but, fundamentally, the right coronary artery irrigates the right part of the heart and left coronary artery irrigates the left part. Coronary arteries are irrigated in the transition from systolic to diastolic flow due to its bulb-shape. When blood flows backwards at the end of systole, it helps the aortic valve recovering blood that would otherwise try to flow backwards into the heart. Counterintuitively, the ratio of blood used to feed the coronaries is nearly negligible when compared to the total amount of blood ejected by the heart at every pulse.

The aortic arch divisions are those that supply blood to the upper body. The brachiocephalic artery, the first division, splits into the right carotid artery and the right subclavian artery. Both carotid arteries, right and left, irrigate the head; brain and face organs. Both subclavian arteries, right and left, irrigate the upper extremities of the body; arms and hands. The aortic arch divisions are extremely important in terms of flow distribution, as around 30% of the blood expelled at every pulse is captured by these ramifications[8].

1.1.2. Pulsatile blood flow

The cardiac cycle generates pulsatile flow in two steps, systole and diastole. The cycle has a mean period of around 1 second; systole normally takes one third of the pulse while diastole takes the other two thirds. In systole, the left ventricle contracts, acting as a pump, to eject blood through the aortic valve. The average flow expelled is about 5 liters per minute. In diastole, the heart relaxes and refills the left ventricle with blood[9]. During the transition from systole to diastole, blood flows backwards to irrigate coronary arteries. This is commonly magnified in patients with valvular or aortic diseases. A typical aortic flow pulse is shown in Figure 2.

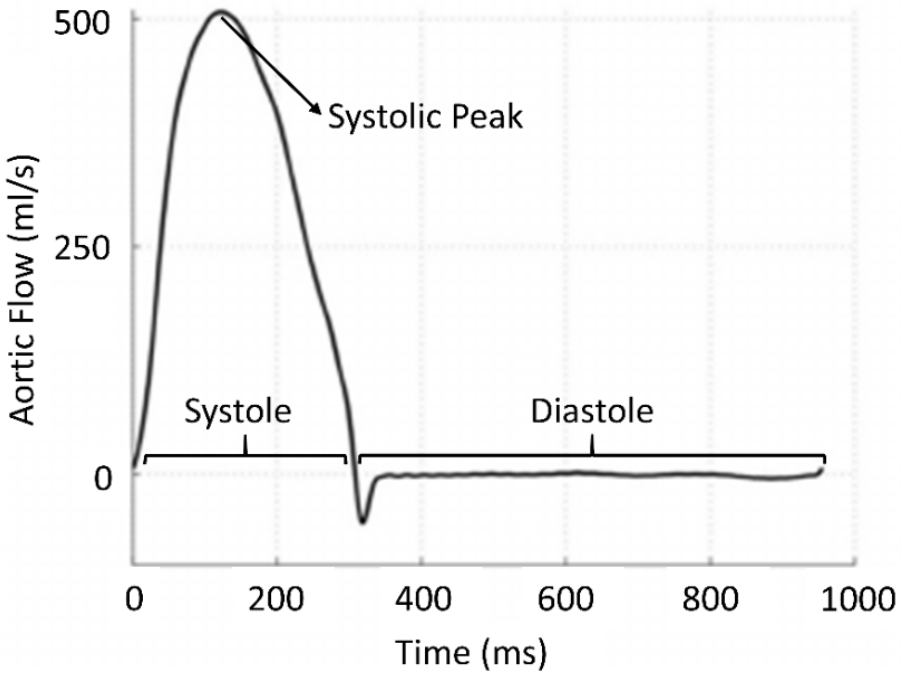

Figure 2. Aortic pulsatile blood flow[9]

Aortopathies can disrupt flow profile in two ways. First, losing the smoothness of the characteristic systolic peak, and second, displacing the maximum velocity vector frequently located at the center of the tricuspid valve and forming a zone of reverse flow during systole.

The effect of contracting and relaxing during the pulse affects the blood vessel structure due to pressure variations along the cardiac cycle. These pressure alterations have a direct impact on wall vessel, especially in aorta, where pressure is at its highest point.

1.1.3. Blood vessel structure

Blood vessels have a structure of three concentric layers; the inner layer or intima, a middle layer or media, and an outer layer or adventitia, that are known as tunicas[5]. Every layer has its own functionality and can differ in thickness and composition depending on the vessel's role [10,11]. Figure 3 represents an artery vessel structure. In detail, the three layers are:

- Intima: the thinnest layer of the vessel structure. Its main function is to exchange substances between blood and the vessel wall. It is formed by a monolayer of endothelial cells, a layer of connective tissue and a layer of elastin fibers. Endothelial cells are a semipermeable barrier that regulates the transference of molecules from blood to the interstitial compartments[11,12]. Elastin fibers provide an increase of the elasticity allowing the wall to expand and contract.
- Media: the thicker layer is composed of smooth muscle cells and multiple layers of elastic laminae that provide not only tensile strength but also distensibility and elasticity, properties vital to the aorta's circulatory role[12]. Its main function is to regulate blood pressure.
- Adventitia: the external layer that envelopes the blood vessel. It is formed by a network of collagen fibers with vessels, the *vasa vasorum*, which nourish the external part and a major part of the media[11,12]. These vessels are more abundant in veins than in arteries.

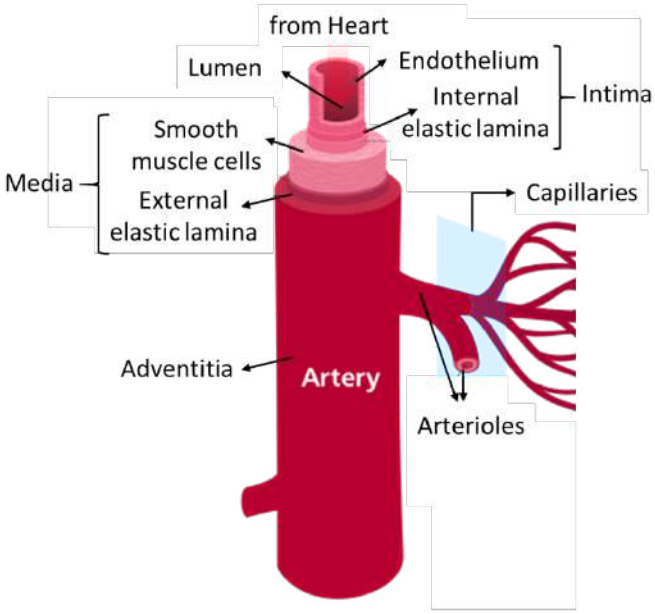

Figure 3. Artery vessel structure

The elastic properties of the aorta are important to its normal function. The elasticity of the wall allows the aorta to accept the pulsatile output of the left ventricle in systole and to modulate continued forward flow during diastole. With aging, medial elastic fibers undergo thinning and fragmentation[4]. The ordinary concentric arrangement of the laminae is disturbed. These degenerative changes are accompanied by increases in collagen and ground substance. The loss of elasticity and compliance of the aortic wall contributes to the increase in pulse pressure commonly seen in the elder and diseased aortae.

1.2. Aortic aneurysms

An aneurysm is a permanent, progressive and irreversible dilation of the vessel wall producing a cross sectional diameter more than 1.5 times its normal value. Of note, values between 1.1 and 1.5 are considered dilated or ectatic[13–15]. Aneurysms are generally asymptomatic, and the continuous dilation without medical treatment can lead to a vessel rupture or dissection[16]. A vessel rupture can result in catastrophic blood loss leading to death, especially if the vessel is the aorta due to the amount of blood carried. A dissection occurs when the vessel wall is teared but not totally and bleeding occurs between two layers of the wall[17]. Aortic dissections can be classified, according to the Stanford classification, in type A or B, depending on whether the ascending aorta is involved[18]. Type A involves the ascending aorta and/or aortic arch, while. Type B involves the descending aorta or the arch, without the involvement of the ascending aorta[16]. Both types are dangerous and can be fatal.

1.2.1. Classification

Aneurysms may be classified by morphology, type and location[15]. By morphology, macroscopic shape and size, aneurysm can be saccular or fusiform. Saccular aneurysms are spherical in shape and involve only a portion of the vessel wall; and fusiform aneurysms are spindle-shaped, more elongated, and often involve large portion of the vessel. The shape of an aneurysm is not specific for a location or disease. Fusiform and saccular shapes can be observed in Figure 4A and Figure 4B respectively.

By type, aneurysms can be grouped in true or false aneurysms. A true aneurysm is a dilation that includes the three layers of the artery vessel. In the other hand, a false aneurysm is a collection of blood that leaks out of the artery and is held by the connective tissue forming a false lumen, Figure 4C.

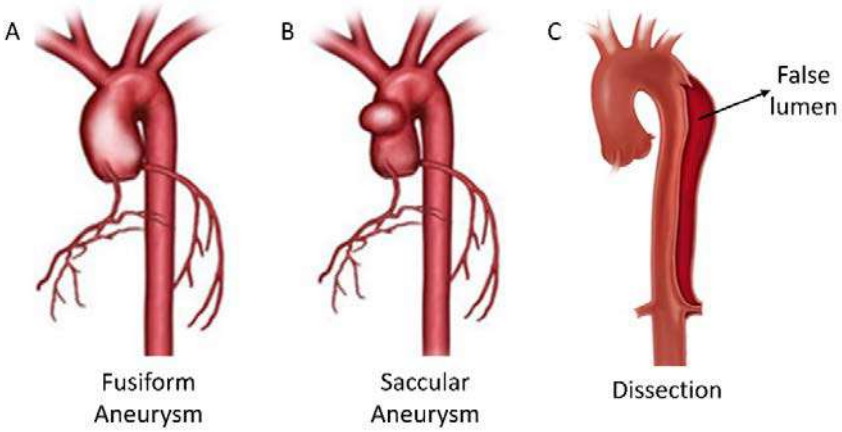

Figure 4. Types of aneurysm; fusiform (A), saccular (B), and dissection (C).

By location, aneurysms can appear in nearly all arteries. However, they are more frequently found in the aorta, the brain and the legs. Aortic aneurysms are classified, according to the affected area, in two types: thoracic or abdominal. Abdominal aneurysms are more frequent, and both can grow large without causing symptoms. Thoracic aorta aneurysms can be subclassified depending on the affected zone, ascending, arch or descending.

Ascending thoracic aortic aneurysms (ATAA) can enlarge the aortic valve making closure virtually impossible. This can lead to regurgitation and blood flowing back into the heart[15]. These aneurysms are the most common in thoracic aorta with an incidence estimated as 10.4 cases per 100 000/year. Age at onset is 65 years and is more predominant in men, with a 1.7:1 male to female ratio[19]. Most ascending aortic aneurysms have unknown etiology and are classified as idiopathic[20].

Aortic arch aneurysms are the less common type of TAA, accounting for 10% of the cases[15]. Descending aorta aneurysms are easier to treat as endovascular treatment is more available and open surgery presents less risks. Differences in anatomical and cellular composition between the ascending and descending aorta may be at the origin of differences in TAAs etiology. In particular, the compliance of the ascending aorta is significantly higher than the descending's, as it contains a greater concentration of elastic fibers[21].

1.2.2. Etiology and molecular mechanisms involved in aneurysm formation

In arteries or veins, the extracellular matrix (ECM) constitutes more than half of the wall mass and contains mainly collagens and elastin. Other relevant vascular wall components are fibronectin, microbifrils (mostly fibrillins), abundant amorphous or soluble proteoglycans, and leucine-rich glycoproteins. The majority of collagen and elastin is produced by smooth muscle cells (SMC). Transforming growth factor beta one (TGF-β1) controls wall remodeling by stimulating SMC proliferation and ECM production. This is a strictly controlled mechanism of adaptation to flow alterations and to mechanical or biochemical (i.e. atherosclerosis) agressions[22].

For example, when blood pressure is chronically elevated, the arterial wall thickens in response to the increased load, and persistently altered rates of blood flow may cause artery diameter changes. This remodeling usually seeks to maintain the artery and the cellular lining in an optimal homeostatic state. However, pathological remodeling can occur, as in the development of an aneurysm[23].

The TGF-β1 signaling pathway is implicated in several important cellular processes, and defects in regulation of this pathway have been correlated to several human disorders including cancer, autoimmune and cardiovascular diseases[24]. It is known that it plays a pivotal role in the formation of aortic aneurysms. Genetic alterations affecting components of this network are known to be a direct cause of increased risk of aortic aneurysm and dissection[25]. Two of the most relevant syndromes causing aneurysms through this pathway are Marfan and Loeys-Dietz syndromes.

In the TGF-β1 pathway, signal transduction is mediated by a phosphorylation cascade. Binding of the growth factor TGF-β1 to the receptor TGFBR2 leads to phosphorylation of receptor TGFBR1, which switches to its active form. Then, TGFBR1 phosphorylates SMAD2 and SMAD3 transcription factors, which in turn also activate and form a complex together with 10 transcription factor SMAD4. This SMAD2/3/4 complex translocates to the nucleus of the cell and increases transcription of several target genes. This series of steps are what is called the canonical TGF-β1 pathway (Figure 5[26]).

Apart from the canonical pathway, alternative mechanisms for transcriptional regulation of SMAD2/3/4 target genes exist through TGF-β1 binding to TGFBR2. This interaction also initiates a phosphorylation cascade of other cytoplasmic transcription factors, such as PP2A, RhoA and mitogen-activated protein kinases (MAPK). This pathway is called the non-canonical pathway.

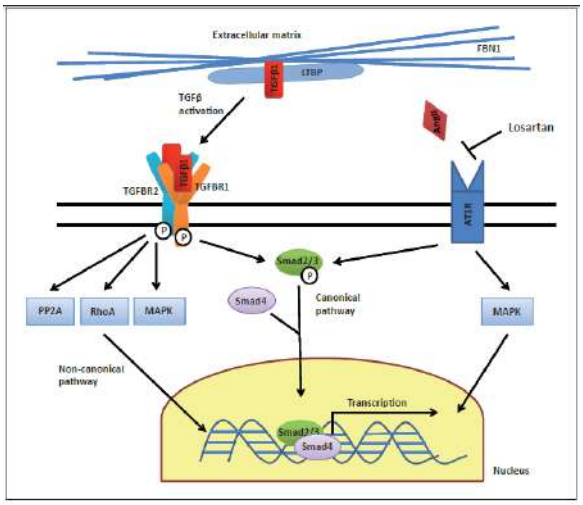

Figure 5. TGF-β1 pathway diagram

In order to better understand the causes of ATAAs, one of the relevant anatomical features to consider is the higher elasticity of the ascending aorta as compared to the descending aorta. Along the aorta, the elastin-to-collagen ratio decreases progressively, which may explain why the etiology of ascending and descending aortic aneurysms is essentially different[27]. Elastin degradation is one of the most consistently observed signatures of human ATAAs[21,22] and aneurysmal tissue presents fragmentation of elastic fibers. It has been identified that the increased relative abundance and activity of ECM proteolytic systems such as matrix metalloproteinases (MMPs)[28] may be behind this phenomenon. MMPs are a large family of proteinases, which are regulated by endogenous tissue inhibitors (TIMPs) in a complex but controlled manner. Aneurysm formation may be related to relative changes in the balance between MMP/TIMP abundance favoring proteolysis. The induction of proteolytic MMPs causes the release of inflammatory molecules, which trigger an inflammatory reaction in the adjacent environment. This creates a vicious cycle, where inflammation further exacerbates endothelial and smooth muscle cell dysfunction, activates MMPs, and ultimately contributes to the progressive weakening of the arterial wall that gives rise to aneurysms.

An additional factor to consider is that the ascending and descending aorta originate from differentiated tissues in the embryo. The ascending aorta is formed from a primitive region called the aortic sac, whereas the descending aorta derives from a region called the dorsal aorta[29]. Interestingly, while aneurysms are usually a result of connective tissue degeneration in the ascending aorta, it is mainly caused by arteriosclerosis in the descending aorta.

The causes for tissue degeneration are usually considered idiopathic, as little is known about the specifics of its pathogenesis[30]. However, risk factors include hypertension, smoking, aging and certain genetic defects like Marfan, Loeys-Dietz and Ether-Danlos syndromes. ATAA's are normally associated to arterial and valvular dysfunctions like atherosclerosis or bicuspid aortic valve (BAV), calcification or stenosis[31]. These conditions alter vessel wall hemodynamics[32].

Stenosis is an abnormal narrowing of a vessel or structure that according to severity can affect the blood flow[33,34]. This narrowing, in particular to the aorta and its valve, may occur due to calcification. Calcification is the formation of calcium deposits on the aortic valve that can narrow its opening[35].

Bicuspid aortic valve is a relatively common congenital cardiac anomaly in which two of the leaflets of the aortic valve fuse during development in the womb resulting in a two-leaflet valve (bicuspid valve) instead of the normal three-leaflet valve (tricuspid)[36,37]. BAV has an incidence in the general population of 0.9 to 2.0% and a frequency of 54% of all patients aged >15 years with valvular aortic stenosis. In most cases, it remains undetected until infective endocarditis or calcification occurs[38]. The bicuspid aortic valve may function normally throughout life or may develop progressive calcification, stenosis or regurgitation. The association of bicuspid aortic valve with aortic dissection is also common[37]. Figure 6 shows opening and closure of a tricuspid aortic valve, a BAV and a valve with stenosis.

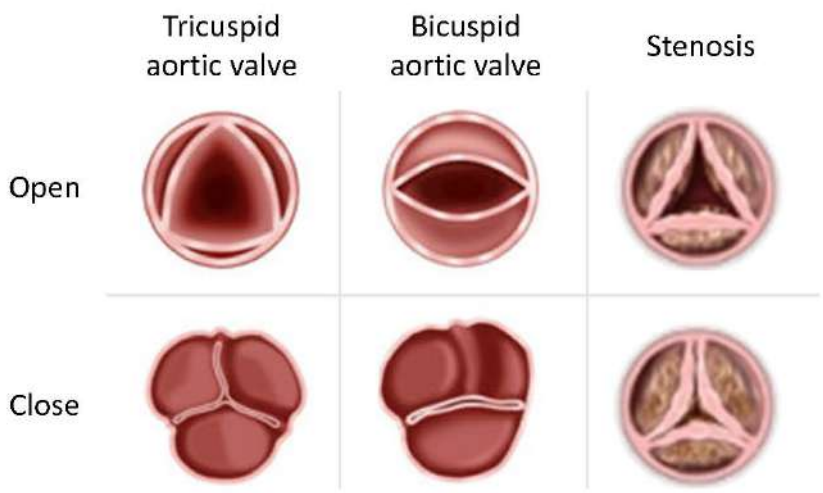

Figure 6. Open and close valve morphology; tricuspid (A), bicuspid (B) and with stenosis (C).

Marfan syndrome is a relatively common autosomal dominant genetic disorder of the connective tissue that affects the ocular, skeletal and cardiovascular systems caused by mutations in fibrillin-1 gene affecting his synthesis[24,39]. Specifically, patients may present susceptibility to ascending aorta aneurysms, long-bone overgrowth and eye lens dislocation. It has an impact on 1.5 to 17.2 out of 100.000 inhabitants in the general population[40].

1.2.3. Diagnosis and Treatment

Aneurysms are mainly detected by incidental finding on abdominal or chest radiography during the investigation of other medical conditions[13]. Until final phases, aneurysms remain asymptomatic and their mortality can reach 90% when the aneurysm leads to rupture of the aorta[41].

Once an aneurysm is identified, ultrasound echography (e.g. echocardiography) is the principal imaging method for aortic aneurysm monitoring in clinical practice[42]. Echocardiography is able to measure the aortic size and detect wall lesions, additionally, is widely available, painlessness, without risk and with low cost[13,14]. However, ultrasound-derived measurements of vessel diameter are not especially accurate, and many experts recommend its use just for follow-up of small aneurysms. Computed tomography (CT) or magnetic resonance imaging (MRI) are required for larger aneurysms and surgery planning[7,14]. These relatively non-invasive imaging modalities permit visualizing the entire aorta in 3D to identify the affected parts adequately[43].

Compared to MRI, CT requires a shorter time for image acquisition and processing, and is a widely available technique[13]. MRI does not require dangerous ionizing radiation as CT; thus, it is highly suitable for serial follow-up studies in patients with known aortic disease. MRI also allows to visualize and measure blood flow, thus important fluid dynamic parameters can be determined[13].

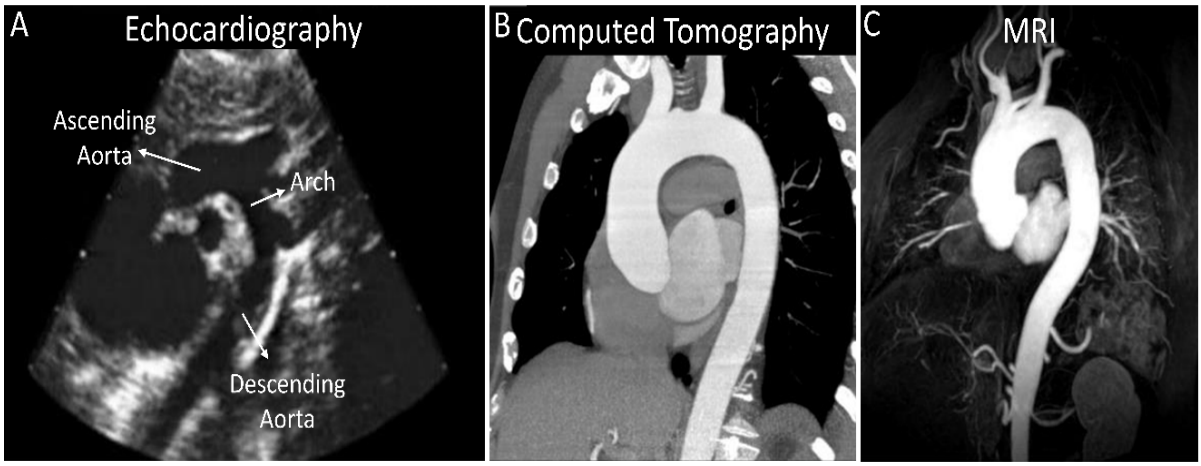

Figure 7. Clinical imaging techniques to diagnose aneurysm; echocardiography (A), CT (B), MRI (C).

The protocol to follow once an aneurysm is detected is detailed by the European Society of Cardiology in Figure 8[44]. Detection of an ATAA can be diagnosed as too small and will be only monitored over time until higher risk of rupture is achieved, and a surgical intervention may be needed. The maximum diameter of an aneurysm has long been the preferred clinical method for assessing rupture risk. Aneurysms with diameter inferior to 4,5 cm are monitored biannually. Aneurysms with diameter between 4,5 and 4,9 cm are monitored annually. When the aneurysm reaches 5,0 cm, it is monitored every six months and if other conditions like coarctation or hypertension are involved, surgical treatment may be necessary. Surgical intervention is indicated for aneurysms with diameter larger than 5,5 cm, 5,0 cm in MFS patients, and for fast growing aneurysms (>5 mm/ year)[44,45].

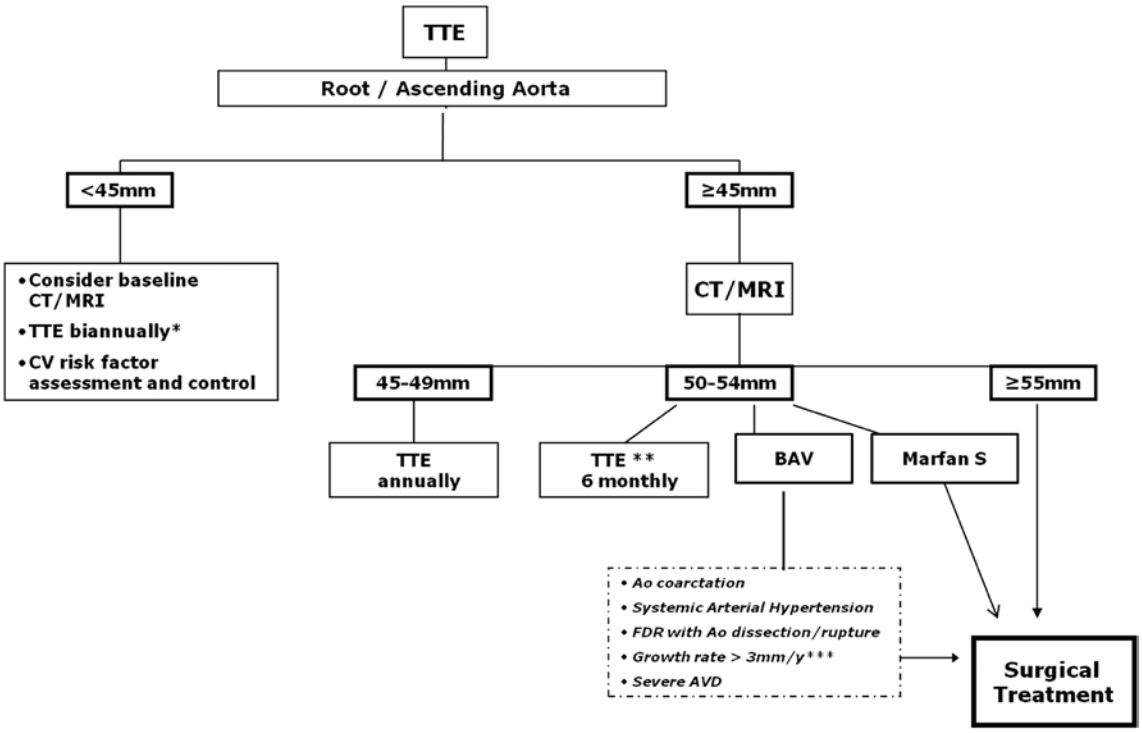

Figure 8. Path to follow after detection of ascending aortic aneurysm by European Society of Cardiology[44].

Once the ATAA detected is diagnosed with high risk of rupture, vascular or thoracic surgeons, in agreement with echocardiographs, define patient management individually. The two main options are watchful surveillance with hypotensive treatment or surgical intervention, whether via open surgery or endovascular repair[13]. Open surgery is an invasive procedure in which the weakened section of the artery is replaced by a synthetic tubular graft. This procedure requires hypo-thermic circulatory arrest[14,43] and implies a high risk of mortality, so the risk of rupture should compensate it[13]. Endovascular repair consists on placing a grafted stent inserted via femoral access. The stent is made of self-expandable Nitinol stent and a tubular synthetic graft[7]. The catheter is guided using X-Ray through the aorta and is expanded against the wall. This treatment is safe but needs regular follow-up[46,47] and can only be performed when the geometry is suitable. Parallel surgeries may be required if concomitant conditions contribute or are affected by the aneurysm, such as problems in aortic root when aneurysm is at ascending aorta may need a replacement of the valve. The two main treatments are represented in Figure 9.

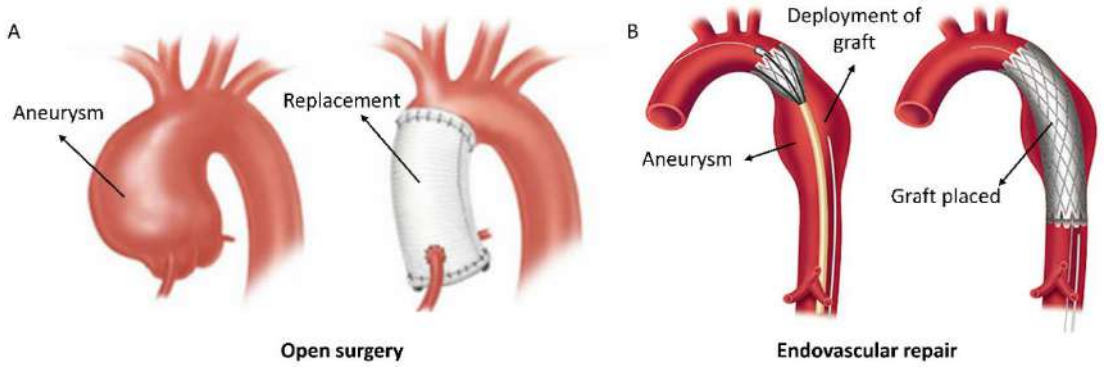

Figure 9. Aneurysm treatments; open surgery (A) and endovascular repair (B).

Patient management guidelines are published and reviewed continuously. Unfortunately, current management criteria can lead to inconsistences in surgical practice as they cannot address the unique vascular architecture of each individual and remain far from personalized medicine[14,48]. Retrospective data on abdominal aorta aneurysms (AAA) show that stratification based simply on diameter may lead to unnecessary surgical intervention of large but stable aneurysms, while smaller aneurysms with higher risk of rupture may be left untreated. Two long-term follow-up studies have reported a 60% excess of surgeries; in other words, 60% of the patients may not have needed an intervention at the time the surgery was performed[49]. This confirms that diameter alone can be improved as risk of rupture biomarker.

The use of biomechanical factors in the prediction of aneurysms rupture risks is a promising alternative to the rather simplistic criterion of diameter. Factors such as peak wall stress or vorticity may estimate the risk of rupture more reliably than only the diameter[32,50,51]. Pressure acting on the inner wall is the major determinant of wall stress. Aortic flow is pulsatile and pressure inside an aneurysm is non-uniform[52]. Moreover, asymmetry and tortuosity of ATAAs affect pressure and wall shear stress (WSS) distributions along the aneurysm. For example, a finite-element (FE) analysis demonstrated that the sensitivity and specificity of peak wall stress at aneurysm are superior to aneurysm diameter when determining the risk for rupture[49]. A patient-specific study demonstrated that maximum wall stress was 12% more accurate and 13% more sensitive in predicting abdominal aorta aneurysm rupture than maximum diameter[53]. In another patient-specific study, peak stress was found significantly higher in ruptured abdominal aorta aneurysm than non-ruptured[52,54].

1.3. Computational models

Mathematical and computational models are used to estimate biomechanical factors such as shear stress and vorticity and try to predict growth of aortic aneurysms. Accuracy of the computed ATAA fluid dynamic parameters, which derive into rupture risk estimation, require performing patient-specific finite element (FE) analysis[55,56]. The accuracy of the model, which relies on patient-specific conditions, is crucial to achieve the most realistic possible results. Fluid dynamic analysis of aortic flow and structural analysis of the aorta need the following patient-specific inputs: vessel 3D geometry, wall thickness, wall mechanical properties, velocity profile at the inlet and outlet pressure. Obtaining these inputs non-invasively for each patient represents important challenges.

Computational prediction of wall stress in patient-specific aortic models has become possible as techniques to create computational 3D models from clinical imaging modalities such as computed tomography (CT) and magnetic resonance imaging (MRI) have emerged[43]. Figure 10A shows the segmentation of an aorta using MRI technique. CT scans, systematically available before any surgical repair of an ATAA, and MRI scans, widely available, are commonly used for the reconstruction of patient-specific geometries[7,14]. Obtaining accurately the local thickness of the wall vessel and its properties is still challenging, despite the importance of these parameters to replicate wall displacement. Pulse wave velocity estimation is the gold standard nowadays to derive the stiffness despite the technique's limitations.

The estimation of boundary conditions remains the major issue to obtain accurate fluid flow predictions. Regarding patient-specific blood velocity profiles, 4D-MRI can provide information on the regional hemodynamics of the aorta (Figure 10B). However, 4D-MRI sequences have a low temporal and spatial resolution compared to the requirements of CFD and the equipment is only available in selected centers. Outlet state is depicted by the Windkessel model, which describes the whole arterial system, in terms of a pressure-flow relation, by two parameters that have a physiological meaning[57,58].

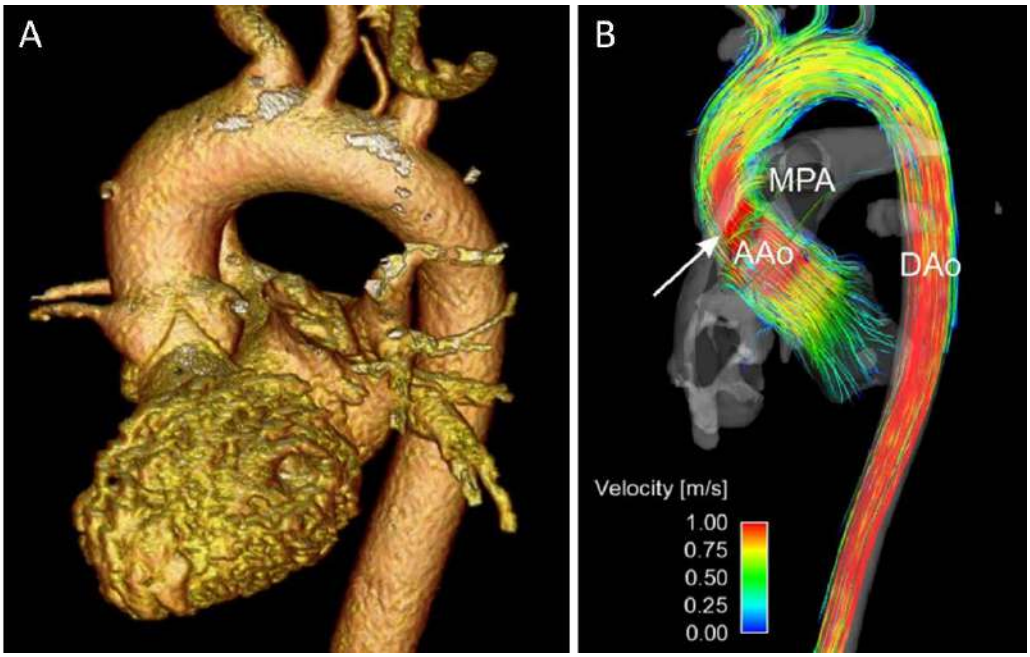

Figure 10. (A) Segmentation of an aorta from MRI imaging. (B) Flow though aorta analyzed with 4D-MRI.

The reliability of CFD for estimation of flow through aneurysms was validated using particle image velocimetry measurements on idealized and on realistic models[59]. These simulations can show time-varying spatially non-uniform pressure load at the wall. However, CFD disregard wall motion, e.g. the interaction between pulsatile blood flow and the compliant arterial wall. This affects the estimation of wall shear stress distribution along the wall, as it neglects blood flow accumulation during systole and blood release during diastole. The computation of fluid-structure interaction (FSI) problems has gained relevance in the past decade as supercomputers have become more available to general scientists and parallel computing has tremendously evolved. FSI is the interaction of a movable or deformable structure with a fluid, which in this study are the vessel walls coupled with blood flow. Few FSI studies have been performed on anatomically realistic aneurysms models[60]. For example, Torii[61] investigated the FSI in two cerebral aneurysms under normotensive and hypertensive blood pressures. Wall deformation effect on aneurysm geometry has shown to be relevant on distribution of WSS. Investigation with CFD and FSI techniques with idealized abdominal aortic aneurysm geometry and linear and nonlinear material models revealed that, compared to FSI, CFD simulations underestimate the WSS on average by 20%-30% for variable wall thickness and 10% for uniform wall thickness.

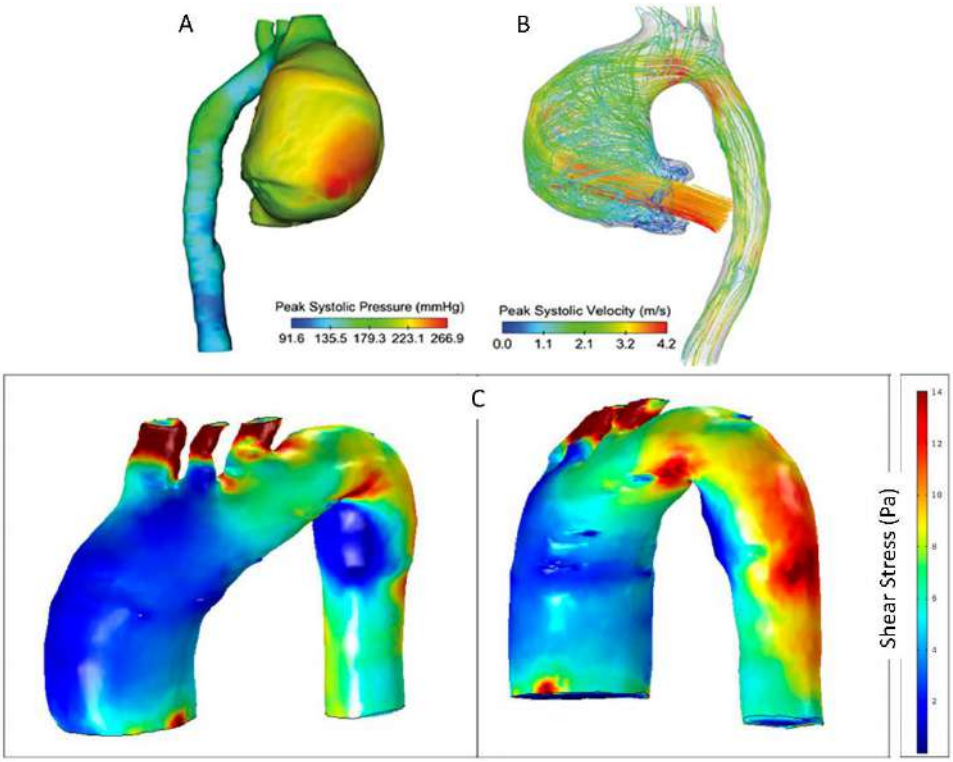

Figure 11. CFD simulation results; (A) pressure , (B) velocity in streamlines[62] and (C) WSS at systolic peak.

1.3.1 Continuum mechanics

Continuum mechanics is the branch of physics that studies the mechanical behavior of materials modeled as a continuous mass. It is divided into fluid mechanics which involves the study of fluids; liquids and gases, and solid mechanics[63,64]. Fluid mechanics can be divided into fluid statics, study of fluids at rest, and fluid dynamics, study of fluids in motion. To study the fluids, it is necessary to know the physical equations that describe their movement. The three equations in which fluid mechanics is based are the conservation of momentum, conservation of mass and conservation of energy[65].

Equation of continuity, related to the conservation of mass, states that in steady state the rate at which mass enters a system is equal to the rate at which mass leaves it, Eq.1[66].

$$\frac{\partial \rho}{\partial t} = -\left[\frac{\partial(\rho u)}{\partial x} + \frac{\partial(\rho v)}{\partial y} + \frac{\partial(\rho w)}{\partial z}\right] = -(\nabla \cdot \rho \vec{v}) \qquad \text{Equation 1}$$

where *u*, *v* and *w* are the velocity components at X, Y and Z axis respectively, ρ is the fluid density and *t* is the time.

In most cases, liquids are used as incompressible fluids because density is constant in time. This assumption simplifies Eq.1 to Euler equation, Eq.2.

$$\boldsymbol{\nabla \vec{v} = \left[\frac{\partial u}{\partial x} + \frac{\partial v}{\partial y} + \frac{\partial w}{\partial z}\right] = 0} \qquad \text{Equation 2}$$

When conservation of momentum is performed in an infinitesimal volume, the equations of motion are obtained[66]. Once resolved, rearranged with Eq.2 and simplified with the assumptions of constant density and viscosity in time, the Navier-Stokes vector form is obtained, Eq.3.

$$\boldsymbol{\rho\left[\frac{\partial \vec{v}}{\partial t} + \vec{v}\nabla\vec{v}\right] = -\nabla p + \mu\nabla^2\vec{v} + \rho\vec{g}} \qquad \text{Equation 3}$$

where ρ is the fluid density, v is the vector velocity, μ is the fluid viscosity, p is the pressure and g the gravity acceleration.

To solve a fluid mechanics problem, Eq.2 and the three equations derived from the vector form of Eq.3 must be resolved simultaneously. Four equations to determine at a point the pressure and three velocity components.

Reynolds (Re) number quantifies the balance between inertial and viscous forces of a fluid. Real fluid flow through a pipe can present three regimes, laminar (Re<2100), transitional (2100<Re<4000) or turbulent (Re>4000). Equation 4 is used to calculate the Reynolds number.

$$\boldsymbol{\mathrm{Re} = \frac{\rho v d}{\mu}} \qquad \text{Equation 4}$$

where ρ is the density, v is the velocity, d is the pipe diameter and μ is the fluid viscosity.

Solid mechanics study the motion and deformation under forces of solid materials[64]. To study the solid, the deformable equation must be solved, Eq.5.

$$\rho_s \frac{\partial d_s}{\partial t} = \nabla \cdot P + b \qquad \text{Equation 5}$$

where ρ_s is the solid density, d_s is the displacement field of the solid, P is the first Piola-Kirchhoff stress tensor, t is the time and b represent the body forces.

Computational fluid dynamics (CFD) is the branch of fluid mechanics that uses numerical analysis to analyze and solve problems that involve fluid flows. CFD can be coupled with structural analysis, fluid-structure interaction (FSI), to solve simultaneously the fluid flow and the motion of a solid. Equations of both domains must be resolved with appropriate initial and boundary conditions. At the interface, the coupling conditions to be imposed are the continuity of the forces and displacements. Displacements must be equal in both domains and forces of traction must be the same value but opposite sign.

Multiple discretizing methods exist for obtaining numerical solutions to these equations, finite volume method, finite element method or finite difference method. Finite element method (FEM) is one of the most widely used on computational field because of its generality and ease of introducing complex calculations domains (2D and 3D).

1.3.2 Finite Elements Method

The finite elements method (FEM) is a general numerical method to find approximate solutions to partial differential equations, mostly used to solve engineering problems. MEF allows to obtain an approximate numerical solution on a continuous medium (body) on which are defined certain differential equations which characterize the physical behavior of the problem. To obtain the solution, the continuum is discretized into subdomains called elements. Each element will be defined by a series of points called nodes. The connection between the set of nodes along the body form the mesh problem, therefore, the operation of dividing the body into subdomains is called meshing. The calculation of each partial differential equation is performed on each element finding a solution that is combined integrating the entire domain.

Throughout this project, FEM has been used for obtaining numerical solutions to CFD and FSI equations for its good features. The analysis of a problem with MEF method consists of three steps: pre-process, calculation and post-process. The pre-process involves the creation of the geometry, applying boundary conditions and meshing. The calculus consists on running the simulation to obtain results. The post-process consists of analyze and treat the results. Figure 12 shows the steps to resolve a problem with FEM method.

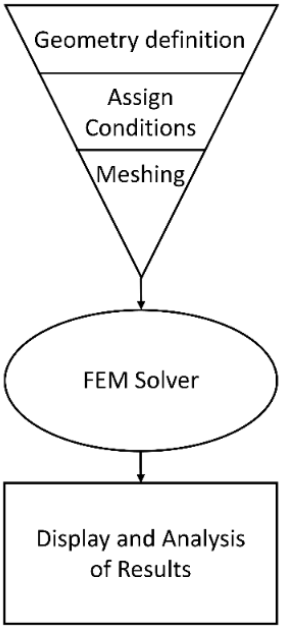

Figure 12. FEM method scheme.

Generating the mesh is an important part that will set the simulation time and the quality of the results. Increasing the nodes of the mesh normally means more time to perform the simulation and better-quality results. However, there is a point that results do not improve, and the performing time continues increasing, so, optimizing the mesh is crucial. Meshing elements can be set in three ways throughout the domain; structured, semi-structured or unstructured. The structured is characterized by a regular connection between the elements, whereby the elements available for this mesh are reduced. Otherwise, unstructured is characterized by an irregularity between elements allowing a greater combination. Typical elements divided according to the dimensions for the meshing are shown at Figure 13.

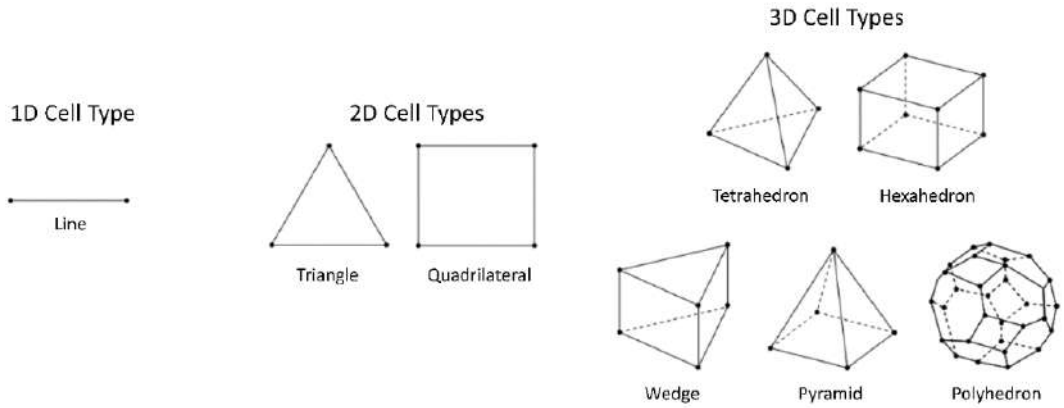

Figure 13. Mesh element types distributed by dimensions; 1D, 2D and 3D.

1.3.3 Unmet needs in fluidodynamic assessment of aortic diseases

Many studies have taken a computational focus when studying hemodynamics of the aorta[52,56,67–71]. However, most of them only present data from a single geometry (simplified or patient-specific), and/or use literature values (not patient-specific) for most boundary conditions (flow profile, flow ratio, stiffness…). Moreover, most simulations are just performed in CFD. For example, Figure 14 shows an FSI study of the effect of modelling techniques[71]. A generalized geometry is used for the fluid and solid domains and inlet velocity profile is adopted from literature. Another example is Figure 15, in which the study consisted on the impact of patient-specific inflow conditions and fluid-structure interaction on coupling. Geometry and inflow profiles are extracted from medical images, but stiffness is adopted from literature and just one case is studied. A clear unmet need arises for patient-specific computational platforms that can work as descriptive tools for fluidodynamic characterization of aortic flow in health and disease and that can produce predictive outputs to better manage aortic disease patients.

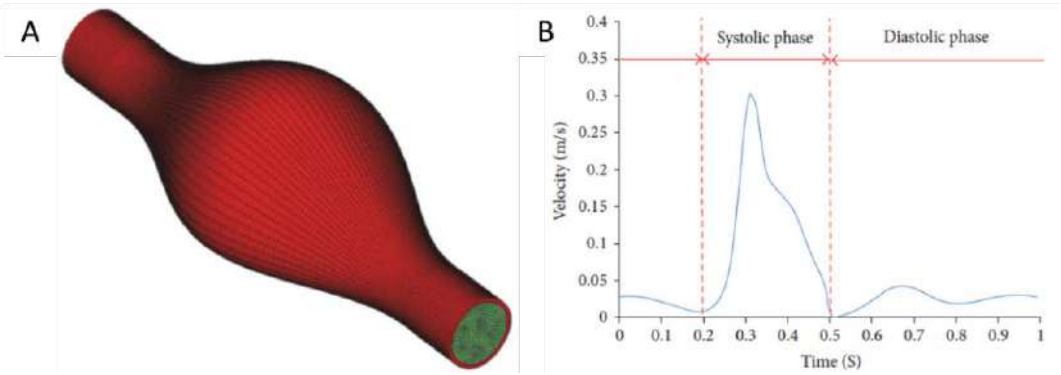

Figure 14. (A) Generalized geometry to mimic aneurysm and (B) velocity profile from literature.

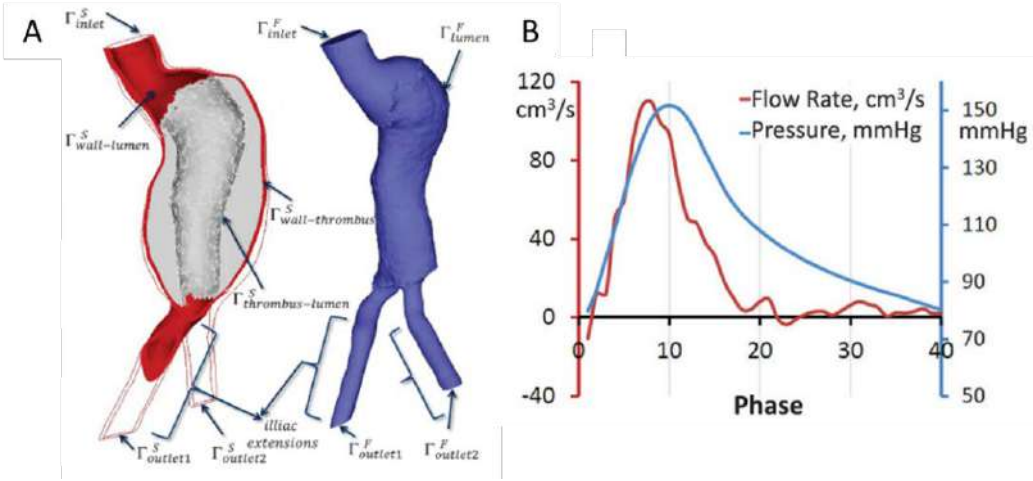

Figure 15. Patient-specific (A) geometry and (B) flow profile.

1.4 Hypothesis and Objectives

This project focuses on performing computational fluid dynamics and fluid-structure interaction simulations using MRI and 4D-MRI data from healthy controls and patients to compare their fluid dynamic parameters and correlate them with aneurysm progression in the ascending aorta.

We hypothesized that patient-specific boundary conditions with wall motion must be incorporated into classic fluid dynamics simulations to accurately describe the biomechanical behavior of the thoracic aorta. Such simulations could deliver at least one fluidodynamic parameter that could better predict the progression of ascending aorta aneurysms.

Therefore, five main objectives are defined to accomplish our hypothesis:

1. To develop a computational platform to reconstruct aortic geometries and to perform computational fluid dynamic and fluid-structure interaction simulations using patient-specific boundary conditions derived from medical imaging.
2. To establish a robust simulation strategy able to calculate fluid dynamics coupled to wall motion in healthy and diseased thoracic aortae.
3. To study the efficiency and accuracy of CFD and FSI simulations relative to real 4D-MRI data.
4. To map the fluid dynamics at the aneurysm and determine which parameters best characterize aneurysm progression.
5. To design a system that replicates *in vitro* in a cylindrical pipe the shear stress profiles observed in simulations.

2. Methods

Multiple methods have been used during this project, although FEM method, explained in 1.3.2, includes all of them in its various steps during the pre-analysis, calculus and post analysis. So, FEM method will be the line to follow during this section explaining all the processes step by step.

The pre-analysis consists of 4 parts. First part is the data extraction from MRI and 4D-MRI images of geometry and velocities data respectively using Mass. Second part is the segmentation of the aorta with the data extracted using a personalized code in SolidWorks. Third part is the numerical treatment of the 4D-MRI velocities with bicubic B-spline method for the inlet boundary condition. Last part is the appliance of codes and meshing of the geometry.

The calculus consists on running big data problems in two supercomputers; Mare Nostrum and Minotauro. The program used to run the simulations and to analyze the convergence of them is Alya.

The post-analysis consists of visualizing the simulation results in Paraview and calculate multiple parameters based on simulations to compare the results between CFD and FSI versus 4D-MRI and to correlate the aneurysm progression with the fluid dynamic. All the calculations have been done by in-house programmed functions in Matlab.

2.1. Pre-analysis

2.1.1. Data from Medical Images

Eight Marfan syndrome patients with no history of aortic dissection or surgery and four healthy control were selected at Vall d'Hebron Hospital. A radially-undersampled acquisition (PC-VIPR) with 5-point balanced velocity encoding[72] was used for 4D flow imaging of the entire thoracic aorta. Data were acquired using the following parameters: velocity encoding 250 cm/s, field of view 400x400x400 mm, acquisition matrix 160x160x160, voxel size 2.5x2.5x2.5 mm, flip angle 8º, repetition time 4.2-6.4 ms and echo time 1.9-3.7 ms. This data set was reconstructed according to the nominal temporal resolution of each patient and was (5xTR) 21 ms-32 ms. Reconstructions were performed offline with corrections for background phase from concomitant gradients, eddy currents and trajectory errors of the 3D radial acquired k-space[72]. A set of 2D cine MRI images on double-oblique sagittal plane were performed. Intravenous contrast was not given to minimize patient risk. Brachial systolic (SBP) and diastolic (DBP) pressures were taken immediately after the CMR study.

This study was approved by the internal review boards of both University Ramon Llull and Vall d'Hebron Hospital.

2.1.2 Raw data extraction

Mass is used to extract the geometry and flows data from MRI images and the 3D-velocities from 4D-MRI. The extension of the medical images provided is DICOM (Digital Imaging and Communications in Medicine) a standard for handling, storing, printing, and transmitting information in medical imaging. The tools mostly applied are location of coordinates of points in 3D, measurement of distances between points and creation of contours of surfaces to measure MRI flows and 4D-MRI velocities.

The geometry information extracted in all cases was the location of the central coordinates and radius of multiples circumferences in ascending aorta, aortic arch, descending aorta and the three branches at the arch; brachiocephalic, left carotid and left subclavian. Moreover, the coordinates of an extra point in each branch are needed to join them with the correct direction to the aorta. Figure 16 shows the circumferences where information is extracted and the diameter of each one at a healthy control.

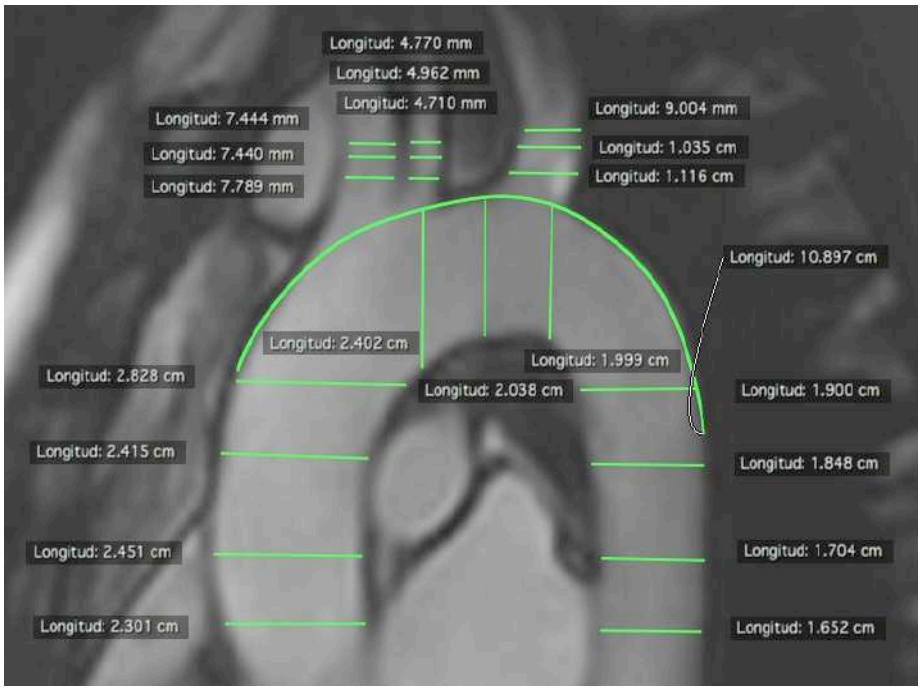

Figure 16. Segmentation of the geometry of a healthy control.

MRI images were also used to extract the pulsatile flow at sinotubular junction and at descending aorta at the same height. First, flow analysis must be selected in analysis options of Mass. Then, a contour is created with multiple points tool in each time step of the dataset tracking the inlet and outlet sections. Once contours are drawn, a graph can be observed in Mass and the data of flow over time can be exported. The flow ratio between descending and ascending aorta at systolic peak was calculated in each case. Figure 17 shows Mass with contours created in a healthy control and Figure 18 the flow graph obtained.

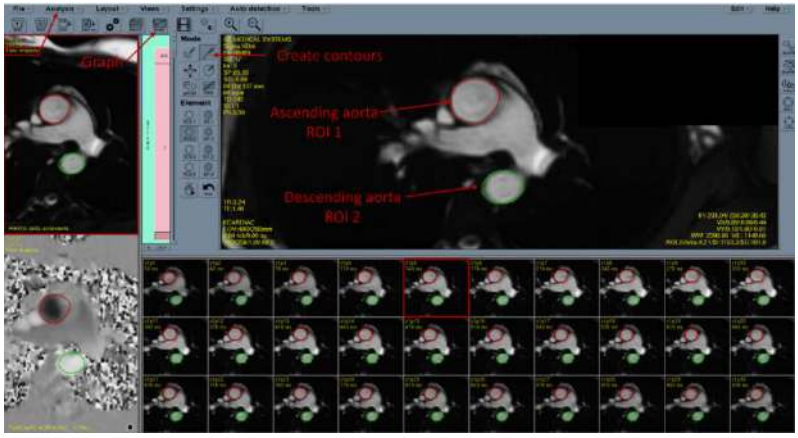

Figure 17. The contours of ascending and descending aorta in Mass.

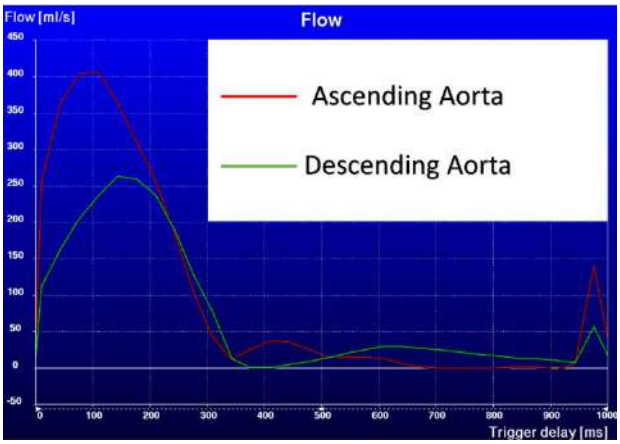

Figure 18. Ascending and descending flows of a healthy control in Mass.

Mass was also used to process 4D-MRI images to extract 3D-velocites at sinotubular junction. The protocol followed for extraction can be observed in Figure 19. First, locate a sagittal plane that cuts ascending and descending aorta as Plane 1 in Figure 19A. Once sagittal plane is obtained, make a second plane to cut sinotubular junction in perpendicular direction of jet flow as Plane 2 at Figure 19B. Finally, draw the contours of ascending aorta in each time step and export the velocities as VTK (Visualization Tool Kit) files. Figure 19C shows the contours; ascending aorta in systole can be observed as a white/grey area because flow is high, but in diastole, as flows is decreased, it is very difficult to apply contours perfectly.

Referring to 4D-MRI, the three components of the position and the velocity at voxels size of 2.5x2.5x2.5 mm with variable interval time of 21-32 ms are obtained. The number of points where data is acquired vary depending on sinotubular diameter. 4D-MRI data of sinotubular junction is extracted using Mass with VTK extension.

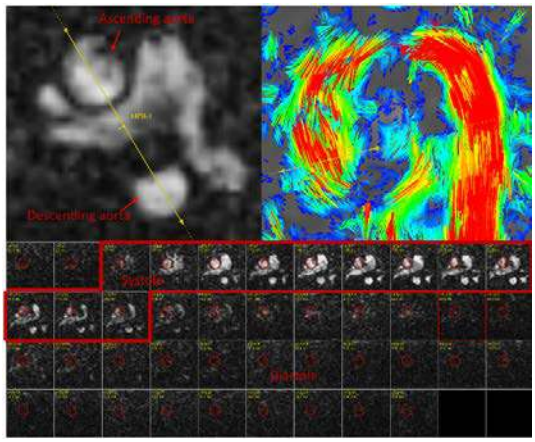

Figure 19. Velocity extraction of 4D-MRI images with Mass.

2.1.3. Geometry segmentation

The thoracic aorta, between the sinotubular junction and the distal end of the arch, limited by the three supraaortic vessels were segmented from cine MRI image datasets, using a computational assisted design (CAD) software for solid modelling, SolidWorks (Dassault Systèmes, France). As the model to reconstruct is patient-specific a proprietary and personalized semiautomatic macro has been created. This code allows the user to reconstruct the lumen and the arterial wall with variable thickness along the aorta using MRI or CT scan data. Position, diameters and wall thickness of multiple 2D sagittal slices along the vessels were used for the reconstruction. The descending aorta and the three supraaortic arteries were artificially extended by 3 cm in the longitudinal direction along the lumen centerline to ensure flow stabilization at the outlet surface and numerical convergence.

The macro consists of two parts; the interface, where the user must introduce the data extracted from DICOM images of the aorta, and the code, which will reconstruct the aorta with the values inserted.

- Interface

The interface is the part that allows the communication between the user and the code. When the macro is executed, the interface pops up with only the main tab. The main tab contains nine text boxes, two options button and two command buttons. The main tab of the interface can be observed at Figure 20:

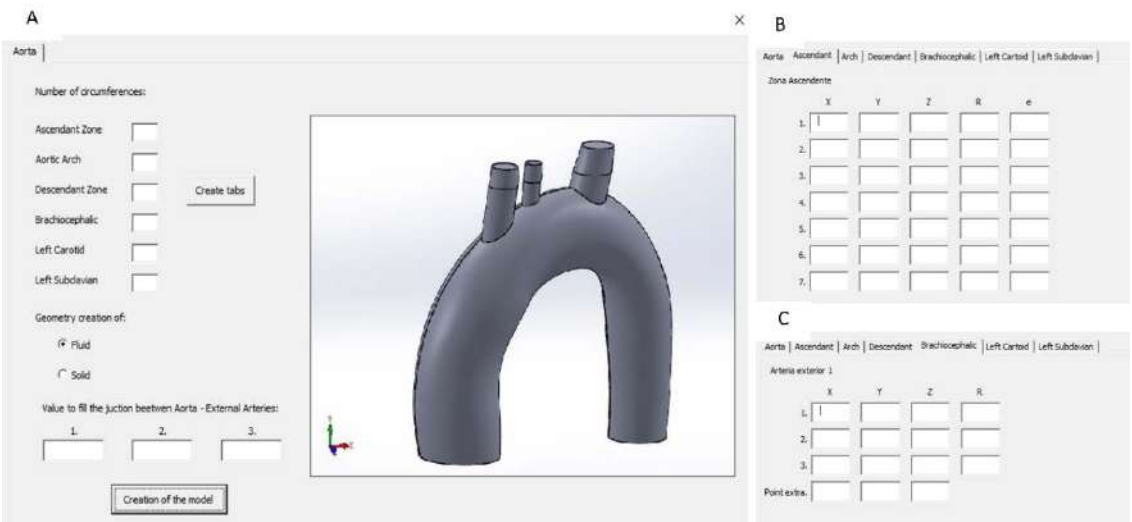

Figure 20. Interface for geometry creation at SolidWorks; (A) main interface tab, (B) fluid ascending tab, (C) solid brachiocephalic tab.

The first six text boxes allow the user to create six more tabs with the command button 'Create tabs'. Every tab created corresponds to a region of the aortic artery; ascending aorta, aortic arch, descending aorta, and the three arteries in which is divided at the aortic arch. Integer values inserted in the text boxes are the number of circumferences taken from DICOM images in each part. The option button allows the user to select if the geometry that is going to be created will be the fluid or the solid, the difference lies in adding thickness in every tab if solid is selected. Finally, when all the text boxes are filled, there is the final command button, 'Creation of the model', which will begin to run the code to reconstruct the aorta.

Two images are used to better understand the interface. Figure 16B shows an example of a tab, ascending tab, with 7 circumferences and solid option selected. Figure 16C shows one upper artery, brachiocephalic, with 3 circumferences and the extra point with fluid option selected.

- Code

The code is a set of instructions as text in Visual Basic for Applications (VBA), a computer language, which allows SolidWorks with the inputs of the interface to reconstruct an aorta model. The code has two manly parts, the interface code and the program code.

The interface code is the instructions to make the interface work properly; create tabs using the first command button with all their text boxes and labels depending on whether fluid or solid is selected and begin the execution of the program code when the second command button is used.

The program code constructs the model in three steps; creation of the aorta, creation of the three external arteries and finally joining them. Selecting the fluid option, the creation of the aorta consists on drawing the circumferences of the three parts in multiple sketches using the central point and the radius and trace four spline lines used as guidelines with Eq. 6 and Eq.7. Each equation generates 2 spline lines.

$$\mathbf{Points_x} = (\mathbf{x_{center}} \pm \mathbf{radius}, \mathbf{y_{center}}, \mathbf{z_{center}}) \quad \text{Equation 6}$$

$$\mathbf{Points_y} = (\mathbf{x_{center}}, \mathbf{y_{center}} \pm \mathbf{radius}, \mathbf{z_{center}}) \quad \text{Equation 7}$$

Finally, apply a program operation called loft which joins all the sketches smoothly into a feature. Same instructions are programmed to construct the external arteries, draw

the circumferences with four spline lines and join them with loft operation. Finally, the operation used to join the aorta with the external arteries is an extrusion. To extrude is required a surface, plane or base, which will be the lower circumferences of the arteries, and a direction, which will be a line drawn with the extra point added at the interface in every external artery and the centrum of the lower circumference, the one used as the base. With fluid option, extrusion has the final condition of ending at aorta surface. Figure 21 shows step by step the construction of the aorta fluid.

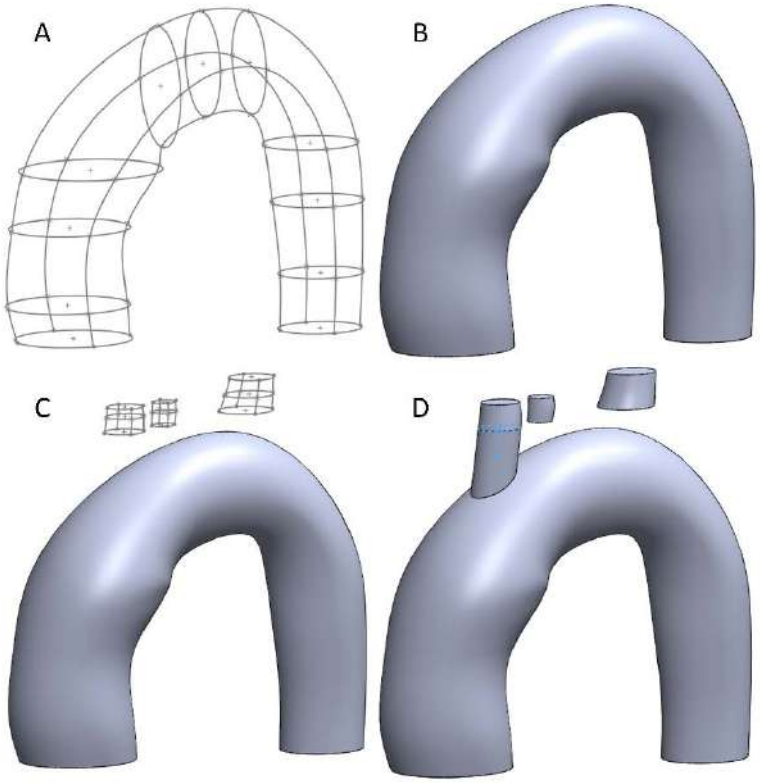

Figure 21. Fluid domain construction; (A) circumferences and splines creation of the aorta, (B) loft operation, (C) creation of the three upper arteries, (D) loft and extrusion of the upper arteries.

When solid option is selected, the instructions followed to create the model are slightly different. First step, aorta creation, it is done using two operations. The first one is the same changing the radius value by the sum of the radius with the thickness, draw circumferences with four splines lines and create the feature with loft. The second operation is also drawing the circumferences with the spline lines without the thickness, like in fluid option, but the operation done at the final is the reverse of the previous, cut loft. Cut loft will generate a hole at first feature leaving just the wall that wraps the fluid. Second step, external arteries creation, will be the same as the first step. First external

arteries are constructed including the thickness and then are emptied with the cut loft. Third step, the junction, is also done by an extrusion, but in this case, the base of the extrusion is the surface between the two concentric circumferences and the direction is the same as in the fluid option. The condition to end the extrusion is achieving the inner surface of the aorta wall. Figure 22 shows the reconstruction of the solid part.

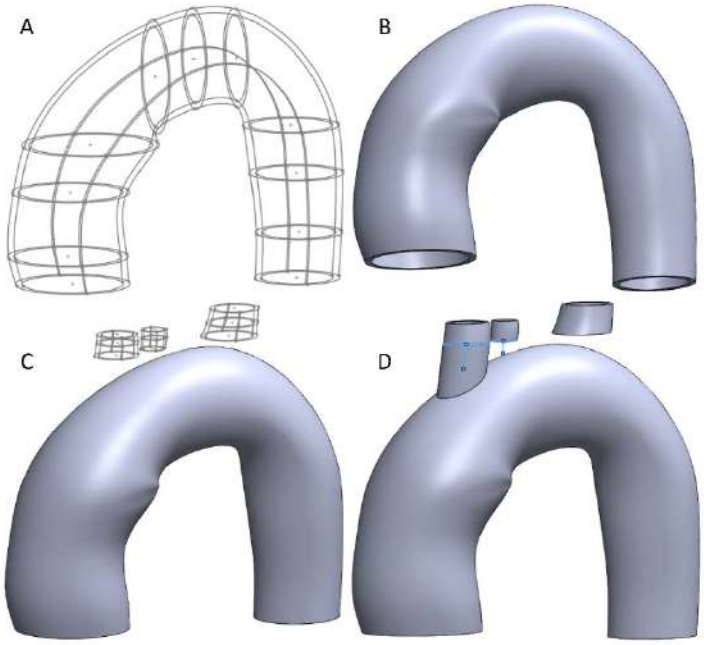

Figure 22. Solid domain construction; (A) circumferences and splines creation of the wall vessel, (B) loft and unloft operations, (C) creation of the three upper arteries, (D) loft, unloft and extrusion of the upper arteries.

Last instruction that code executes is save the geometry in a STEP file. STEP, Standard for the Exchange of Product Data, is a 3D model file that contains three-dimensional data in a format that can be recognized by multiple CAD programs. Final geometries saved can be observed at Figure 23. SolidWorks also allows to save the geometry in a format used for stereolithography (STL), a rapid prototyping technology used for producing three-dimensional parts. Figure 24 shows a 3D impression of a healthy aorta.

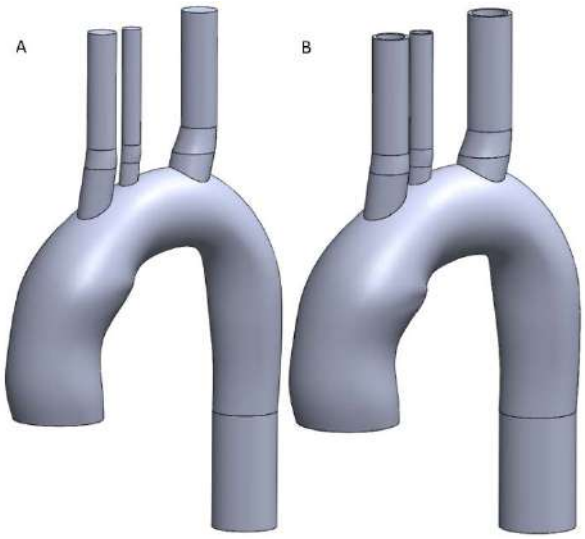

Figure 23. Final geometries; (A) fluid domain, (B) solid domain.

Figure 24. Aorta impressed in 3D with the STL file.

2.1.4 Inlet boundary condition

Once VTK files are generated as explained in Raw data extraction, these files need to be treated to improve spatial and temporal resolution of 4D-MRI technique and to interpolate the velocities at the nodes of the simulation model. Before the treatment, VTK extension needs to be changed to a readable format for Matlab.

Paraview (Sandia National Laboratories, USA), explained in 2.3.1, is used to change the extension of these files. First, VTK files were imported and a glyph command was performed to visualize the velocities as vectors. Every time step must be observed to detect all the velocities with non-sense values and delete them. Finally, all the vectors

are exported as CSV (Comma Separated Values) and imported to Matlab. Figure 25 shows the velocity vectors at one time step.

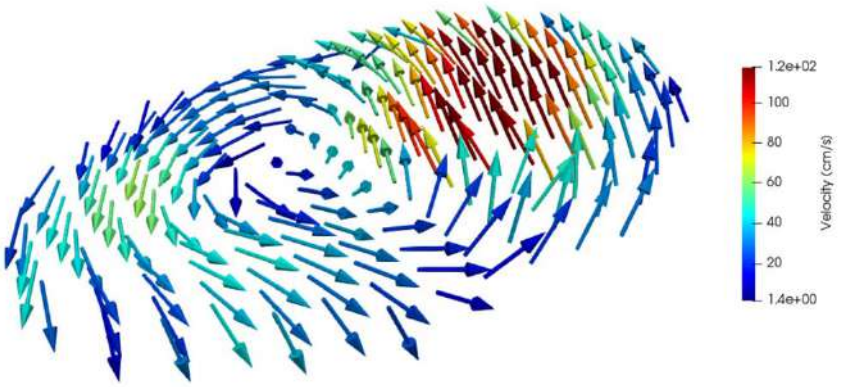

Figure 25. Velocity vectors from 4D-MRI at Paraview.

A code in Matlab has been programmed for the treatment and interpolation. Matlab function begins reading the data from CSV files and changing the positions of the points from an inclined plane to a plane with a constant high, removing the vertical axis (z) of the coordinate system. When all points are located at a XY plane, a B-spline, basis spline, is used to adjust a surface to increase the spatial resolution.

2.1.4.1 B-spline

B-spline adjust surfaces to four point that form a square, patch, with the twelve point that surround them[73]. The square where the surface will be adjusted has to be divided in both axis forming new points where the adjustment will give the value of the variable studied. The twelve surrounding points are necessary to give continuity at closest patches. As it is showed in the Figure 26, the sixteen DeBoor points are needed to adjust the surface to patch 1.

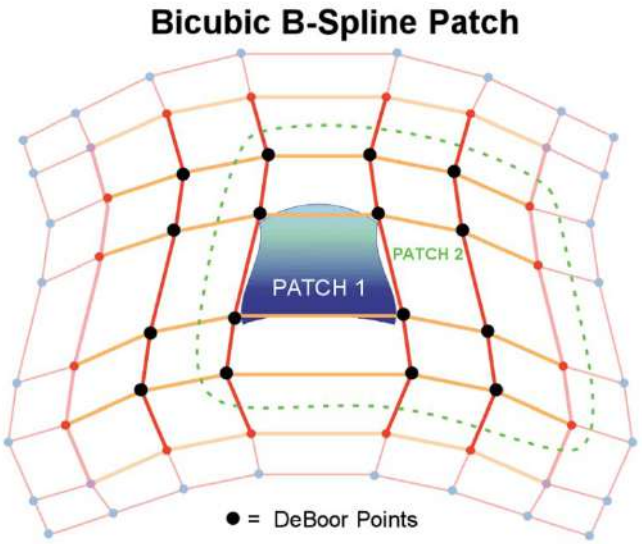

Figure 26. Bicubic B-spline method at Patch 1.

The function programmed in Matlab for the B-spline divides the patch ten times in both directions using two parameters, u and v, as Eq. 8. The values of both vectors must be between 0 and 1, so u= 0:0.1:1 and v= 0:0.1:1.

$$\mathbf{p_{i,j}(u,v)} \qquad \text{Equation 8}$$

To find the value of the variable an equation for each component is used; Eq. 9, Eq. 10 and Eq. 11.

$$\mathbf{x_{ij}(u,v)} = \frac{\mathbf{1}}{\mathbf{36}} * \left[\mathbf{u^3, u^2, u, 1}\right] * \mathbf{M_b} * \mathbf{X_{i,j}} * \mathbf{M_b}^{\mathbf{T}} * \left[\mathbf{v^3, v^2, v, 1}\right] \qquad \text{Equation 9}$$

$$\mathbf{y_{ij}(u,v)} = \frac{\mathbf{1}}{\mathbf{36}} * \left[\mathbf{u^3, u^2, u, 1}\right] * \mathbf{M_b} * \mathbf{Y_{i,j}} * \mathbf{M_b}^{\mathbf{T}} * \left[\mathbf{v^3, v^2, v, 1}\right] \qquad \text{Equation 10}$$

$$\mathbf{z_{ij}(u,v)} = \frac{\mathbf{1}}{\mathbf{36}} * \left[\mathbf{u^3, u^2, u, 1}\right] * \mathbf{M_b} * \mathbf{Z_{i,j}} * \mathbf{M_b}^{\mathbf{T}} * \left[\mathbf{v^3, v^2, v, 1}\right] \qquad \text{Equation 11}$$

Where $X_{i,j}$, $Y_{i,j}$ and $Z_{i,j}$ are the matrixes which contain the coordinates of the sixteen points used. Eq. 12 is an example of the component x:

$$\mathbf{X_{i,j}} = \begin{bmatrix} \mathbf{x_{i-1,j-1}} & \mathbf{x_{i-1,j}} & \mathbf{x_{i-1,j+1}} & \mathbf{x_{i-1,j+2}} \\ \mathbf{x_{i,j-1}} & \mathbf{x_{i,j}} & \mathbf{x_{i,j+1}} & \mathbf{x_{i,j+2}} \\ \mathbf{x_{i+1,j-1}} & \mathbf{x_{i+1,j}} & \mathbf{x_{i+1,j+1}} & \mathbf{x_{i+1,j+2}} \\ \mathbf{x_{i+2,j-1}} & \mathbf{x_{i+2,j}} & \mathbf{x_{i+2,j+1}} & \mathbf{x_{i+2,j+2}} \end{bmatrix} \qquad \text{Equation 12}$$

M_b is a 4x4 matrix that contain the values showed at Eq. 13:

$$\mathrm{M_b} = \begin{bmatrix} -1 & 3 & -3 & 1 \\ 3 & -6 & 3 & 0 \\ -3 & 0 & 3 & 0 \\ 1 & 4 & 1 & 0 \end{bmatrix} \qquad \text{Equation 13}$$

The weight applied to each of the sixteen points vary as u and v vary between 0 and 1. Eq. 14 and Eq. 15 contain the weights applied when u and v have the values of 0 and 1.

$$\mathbf{Weight}\ (\mathbf{u}=\mathbf{0},\mathbf{v}=\mathbf{0}) = \begin{bmatrix} \mathbf{1} & \mathbf{4} & \mathbf{1} & \mathbf{0} \\ \mathbf{4} & \mathbf{16} & \mathbf{4} & \mathbf{0} \\ \mathbf{1} & \mathbf{4} & \mathbf{1} & \mathbf{0} \\ \mathbf{0} & \mathbf{0} & \mathbf{0} & \mathbf{0} \end{bmatrix} \quad \text{Equation 14}$$

$$\mathbf{Weight}\ (\mathbf{u}=\mathbf{1},\mathbf{v}=\mathbf{1}) = \begin{bmatrix} \mathbf{0} & \mathbf{0} & \mathbf{0} & \mathbf{0} \\ \mathbf{0} & \mathbf{1} & \mathbf{4} & \mathbf{1} \\ \mathbf{0} & \mathbf{4} & \mathbf{16} & \mathbf{4} \\ \mathbf{0} & \mathbf{1} & \mathbf{4} & \mathbf{1} \end{bmatrix} \quad \text{Equation 15}$$

The 2.5 millimeters squares from 4D-MRI are divided ten times forming squares of 0.25 millimeters, new hundred points in each old square. To apply the B-spline at the outer points their DeBoor points are needed, as the 4D-flow technique doesn't give them it is assumed that any external point has a value of velocity equal to zero. Crossing all the patches a continuative surface is obtained at each time step.

Once every time step has a surface adjusted, a spline is used to increase the temporal resolution. Spline is a numeric function defined piecewise by polynomial functions, and which possesses a sufficiently high degree of smoothness at the places where the polynomial pieces connect, known as knots. Before applying the spline, the first three steps are copied at the final part of the matrix and the last three steps are copied at the beginning to give continuity at the cardiac cycle. The knots where the spline is applied are all the points at the different time steps with same coordinates x and y of the matrix. Matlab has its own function to do splines so it is not necessary to program it. Temporal resolution was interpolated from a variable interval time of 19-32 ms to 10 ms, same time step used at the simulation program. The spatial and temporal resolution can be modified easily by changing the divisors vectors of axis X and Y or the interval interpolation of the spline. When the spline is performed, the final velocity matrix is obtained.

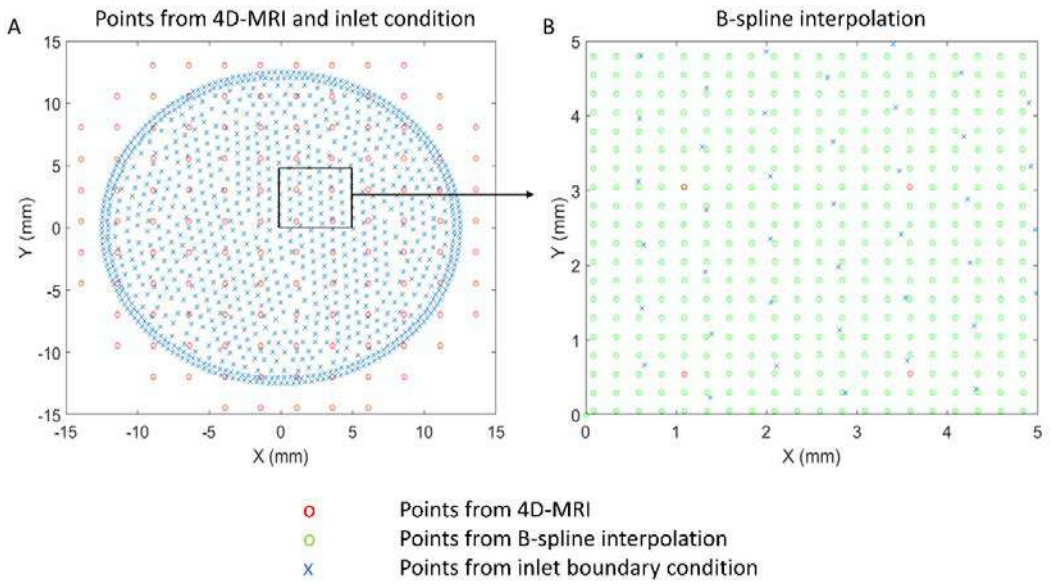

Figure 27. Appliance of bicubic B-spline method; (A) 4D-MRI points with inlet nodes of the mesh, (B) zoom of B-spline point with inlet nodes of the mesh.

The position of inlet boundary nodes is imported using Matlab. With its location, the four vertices of the square in which a node is located are searched and their velocities are used to perform a weight distance interpolation to assign a velocity to each node. Figure 27 shows the B-spline interpolation process to 4D-MRI data and the location of the inlet nodes of the mesh. Figure 28 shows the velocity profile at four steps of the cardiac cycle. Finally, all the velocity vectors of boundary nodes are saved in a script for Aya, one file for each time step.

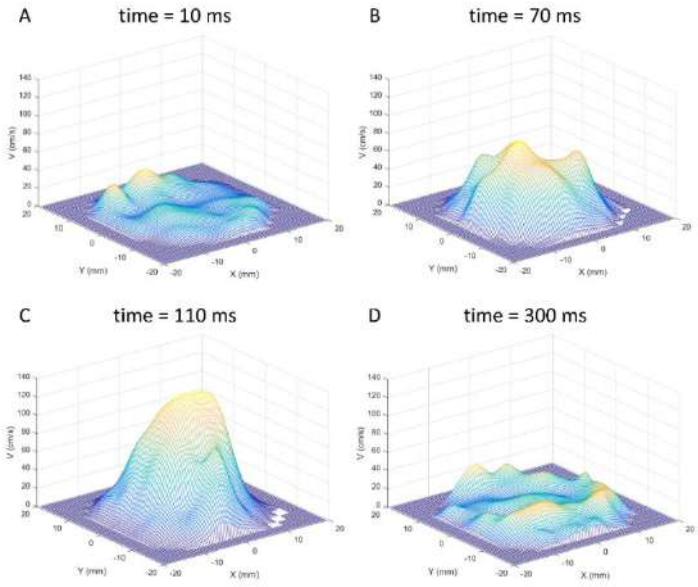

Figure 28. Velocity profile at (A) 10 milliseconds, (B) 70 milliseconds, (C) 110 milliseconds and (D) 300 milliseconds of a pulse.

2.1.5. Patient-specific boundary conditions

Outlet boundary condition and stiffness were patient-specific conditions for a better approach and were modelled with iterative processes.

Windkessel effect is a term used in medicine to account for the compliance of the aorta and large elastic arteries and the resistance of the smaller arteries and arterioles. There are multiple models' types of Windkessels effect, all of them are analogous to an electrical circuit and their equation is based on it. The simplest of the Windkessel models useful for replicating hemodynamics is the 2-Element Model[58,74]. It is assumed that the ratio of pressure to volume is constant and that outflow from the Windkessel is proportional to the fluid pressure. Volumetric inflow must equal the sum of the volume stored in the capacitive element and volumetric outflow through the resistive element. Eq. 16 describes the relationship between flow and pressure, where Q(t) is analogous to intensity, I(t), and P(t) to voltage, V(t). Figure 29 represents the analogous circuit of a 2-element model.

$$Q(t) = \frac{P(t)}{R} + C \cdot \frac{dP(t)}{dt} \qquad \text{Equation 16}$$

where *Q* is the flow, *P* is the pressure, *C* the arterial compliance and *R* the peripheral resistance.

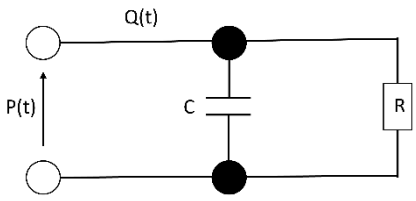

Figure 29. Electrical circuit analogous to a Windkessel model of 2-elements.

During a cardiac cycle, the two-element Windkessel model considers the effect of arterial compliance, that refers to the elasticity and extensibility of the major artery, and peripheral resistance, flow resistance encountered by the blood as it flows through the systemic arterial system. The arterial compliance (C in $cm^3/mmHg$) is represented as a capacitor with electric charge storage properties; the peripheral resistance of the systemic arterial system (R in $mmHg \cdot s/cm^3$) is represented as an energy dissipating resistor. A Windkessel model of two elements was implemented in Alya to modify the outlet boundary flow.

To test the influence of resistance parameter, a simple design of a bifurcation was created with SolidWorks. Multiple values of R were imposed to one outlet and flow distribution was analyzed. The process of creating geometry, applying conditions and meshing was the same as if an aorta was treated. Capacitor parameter was not included in this study and a value of 0 was applied in all the cases.

From MRI data, outlet flow at the descending aorta is known, so peripheral resistance (R) for the Windkessel model was adjusted in each simulation to match the rate of flow ratio between sinotubular junction and descending aorta measured in MRI images. Flow at sinotubular junction differs from MRI to 4D-MRI so flows could not be compared directly because if inflow differs, matching the outflows would suppose an erroneous distribution. The flow ratio parameter, which measures flow at the descending aorta divided by flow at sinotubular junction, was the parameter chosen to compare and match simulation with clinical data.

Young's modulus, the parameter used to model stiffness of the aortic wall in FSI simulations, was calculated iteratively for each patient. The PWV estimated using 4D flow MRI[75] was introduced in the Moens–Korteweg equation[76] (Eq.16) to obtain an initial Young's modulus E_0 which was introduced in the first FSI simulation. The radius and thickness used to calculate the elastic modulus were the mean value along multiple sections of the solid domain. Density was the same than the one used in the FSI simulations, 1200 kg/m^3. Young's modulus was applied on all the solid domain. After FSI calculations were performed, a new pulse wave velocity (PWV_i) was calculated dividing the distance (Δx) between the sinotubular junction and descending outlet by the wave travel time (Δt) between systolic peaks at both planes (Eq.17). This process was repeated until the relative error ε between PWV from 4D-flow MRI and PWVi was inferior to ±5% (Eq.19).

$$E_0 = \frac{2 \cdot PWV_{MR}{}^2 \cdot r * \rho}{h} \quad \text{Equation 16}$$

$$PWV_i = \frac{\Delta x}{\Delta t_i} \quad \text{Equation 17}$$

$$E_{i+1} = \frac{2 \cdot PWV_i^2 \cdot r * \rho}{h} \quad \text{Equation 18}$$

$$\varepsilon = \frac{\mathrm{PWV_i} - \mathrm{PWV_{MR}}}{\mathrm{PWV_{MR}}}$$ Equation 19

2.1.6 GiD

STEP files from SolidWorks were imported in GiD (Compass Ingeniería y Sistemas, Spain). GiD is an adaptive and user-friendly pre and post processor for numerical simulations in engineering. It covers all the common needs in the numerical simulations field like geometrical modeling, effective definition of analysis data, meshing and visualization of numerical results. In this project, GiD was used to apply boundary codes to both domains; lumen and wall vessel, and to create the finite element mesh. To apply codes at the geometry, GiD is linked to Alya program as a module.

Boundary codes are applied to surfaces as boundary 3D. The codes applied at lumen were six; inlet (1), wall (2), aorta outlet (3), brachiocephalic outlet (4), coronary left outlet (5) and subclavian left outlet (6). The codes applied at wall vessel were seven; inlet (1), exterior wall (2), interior wall (3), aorta outlet (4), brachiocephalic outlet (5), coronary left outlet (6) and subclavian left outlet (7). Figure 30 shows a lumen and a wall vessel with the codes marked with colors.

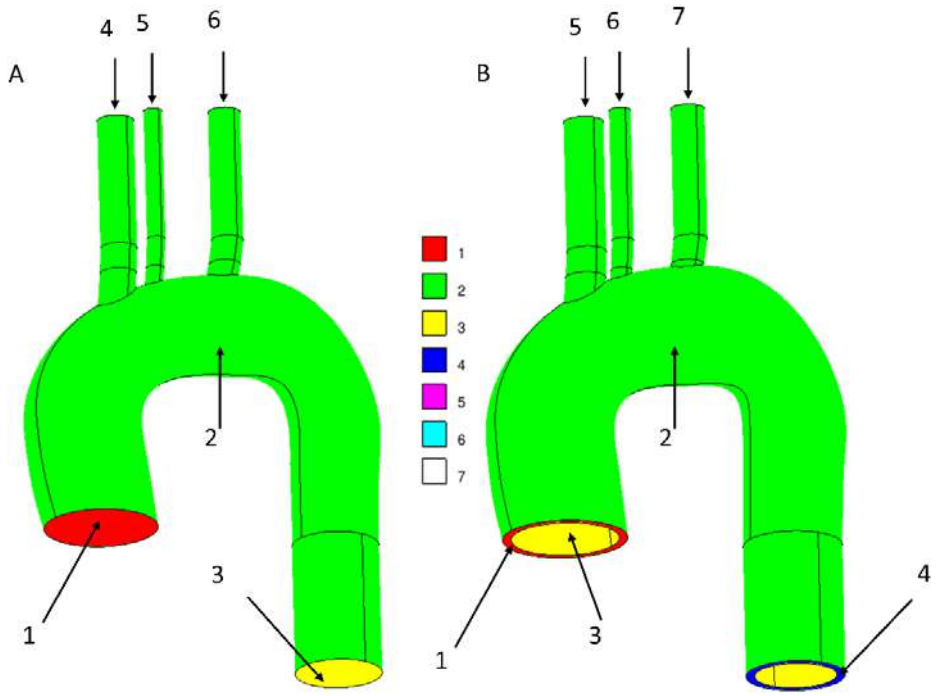

Figure 30. Codes applied to (A) fluid domain and (B) solid domain.

When codes are applied, both domains were meshed using unstructured elements, triangles at surfaces and tetrahedrons at the volume. The transition used in all geometries was 0,7. This is one of the most important parts of the process, it will stablish the computational time and the resolution of the results obtained. An example of both geometries meshed are shown in Figure 31.

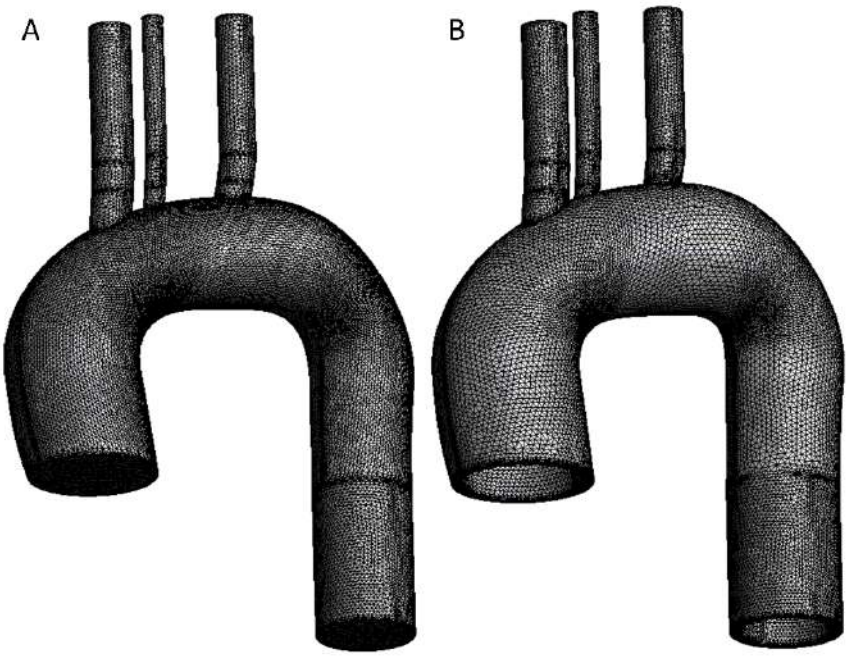

Figure 31. The meshes of (A) fluid domain and (B) solid domain.

GiD offers several quality criteria to validate that the mesh obtained has good quality. Minimum Jacobian criteria is used for this project because is considered the best approach to apply FEM. This term is based on create a Jacobian matrix for each element representing the difference between the formed mesh and the regular shape the elements of it should have. The minimum Jacobian is the minimum value of the determinants of the Jacobian matrices formed for each element. The higher the value, the better the quality of the mesh. Values below zero indicate a bad quality mesh and problems may be encountered in the simulation.

2.2. Calculus

2.2.1. Alya

CFD and FSI simulations in the ascending thoracic aorta are performed using Alya. Alya is a high-performance computational mechanics code based on a finite element formulation able to solve complex multi-physics problems. Alya is an open under collaboration agreement software developed at the Barcelona Supercomputing Center written in FORTRAN language. Alya relies on a modular architecture organized in kernel, modules and services. The kernel contains the facilities required to solve any set of discretized partial differential equations, while the modules provide the physical description of a given problem. There are modules to handle several different physical problems like NASTIN for incompressible flow equations, TEMPER for heat transfer problems in fluid and solid domains and SOLIDZ for structural mechanics and simulate problems where occur mesh deformation. Alya can also couple different modules like NASTIN and SOLIDZ for the fluid-structure interaction (FSI). In the present work, Alya was used to solve incompressible flow and multi-code coupled feature. In the multi-code coupled, the first code solves the fluid mechanics problem while the second one solves the solids mechanics case. The codes are coupled using parallel techniques[77]. All simulations were performed using supercomputer Mare Nostrum IV or Minotauro with 72 processor cores, 48 for the fluid and 24 for the solid.

For fluid dynamics calculations, the Navier-Stokes equations, Eq. 17, were discretized using the stabilized finite element method with variational multiscale stabilization. The momentum equation is separated from the continuity equation using the Schur complement for the pressure, Eq. 18. Each equation is solved independently, and the solution of the coupled system is obtained iteratively. The displacement of the fluid domain is achieved using the Arbitrary Lagrangian Eulerian (ALE) formulation. The time integration scheme used was a Backward Differentiation Formula of second order.

$$\rho_f \frac{\partial u_f}{\partial t} + \rho_f (f u_f \cdot \nabla) u_f - \nabla \cdot \left[2\mu_f \in (u_f) \right] + \nabla p = pf \qquad \text{Equation 17}$$

$$\nabla \cdot u_f = 0 \qquad \text{Equation 18}$$

where u_f is the fluid velocity field, ρ_f is the fluid density, μ_f is the fluid viscosity, p is the pressure, and ε is the velocity strain rate.

For the solid mechanics problem, the Euler equations, Eq. 19, were discretized using a standard Galerkin method for large deformations with a Newmark time integration scheme. For the deformable solid:

$$\rho_s \frac{\partial d_s}{\partial t} = \nabla \cdot P + b \qquad \text{Equation 19}$$

where ρ_s is the solid density, d_s is the displacement field of the solid, P is the first Piola-Kirchhoff stress tensor and b represent the body forces.

The coupling algorithm is a strongly coupled iterative method with Aitken's dynamical relaxation[78]. In each time step, the fluid mechanics problem is solved, the forces on the coupling surface are calculated and the Aitken's factor is applied. The forces are passed to the solid mechanics code, the body displaces, and the new domain location is passed to the fluid mechanics code. This process is repeated until convergence is achieved and then the time step is advanced.

To better understand what is needed for simulating using Alya, every file required is explained below. The 'SimName' is referred to the simulation name of the files, which has been along the project C1-4 for the healthy controls, S1-4 for the stable patients and D1-4 to the dilating patients. The files dom.dat, geo.dat, set.dat and fix.dat are the ones generated by GiD and contain the geometry and mesh information; these files are generated for the fluid and the solid domains and will only be explained once due to information contained is the same. The other files are divided into fluid or solid domain. To differ fluid domain files from solid domain files an S is inserted at the name; 'SimNameS'.

- SimName.dom.dat: This script contains mainly 5 parts. The dimensions, where there are the number of nodes, elements and boundaries and the space dimensions, 3D. The strategy, where a scale for the geometry can be used; all cases used a 0,1 scale to convert geometry into centimeters (CGS scale). The other three parts include the name of the scripts that contain the necessary information; geo, set and fix.
- SimName.geo.dat: This script contains all the data about the geometry in three parts. Nodes per element; that contains the number of nodes in each element, all elements have 4 nodes as all are tetrahedrons. Elements; that include the

number of the 4 nodes associated with every element. Coordinates, that contains the three coordinates of every node in the mesh.

- SimName.fix.dat: This script contains the boundary conditions information and is divided into two parts. First one encloses the elements where a code was applied at GiD. Second one contains which nodes of the elements are affected by that code.
- SimName.dat: Main script for the simulation. There are one for fluid and one for the solid and both are divided into two parts; run data and problem data. Run data is the initial information to Alya when simulation starts; the number applied to fluid, the file for the output information and the run type, which can be no-continuative, if simulation starts from zero, or continuative, if the simulation starts from a restart; which gives to all the domain an initial value. Problem data is the information to use during all the simulation; time coupling, which is global because all the modules are going to use the same time step and can be prescribed if is defined by user or from critical if the program calculates it. If prescribed is selected, time step size and number of steps must be defined. There are also the modules this simulation is going to use; NASTIN and ALEFOR for the fluid domain and SOLIDZ for the solid domain.
- SimName.nsi.dat: Script for nastin module which is divided in four parts. Physical problem; includes the problem definition and the properties of the fluid, density and viscosity. Numerical treatment; includes the method and all the parameters to solve the partial equations of the fluid. Output and post-process; allows the user to select the variables that will be saved for visualize and analyze at the post-process. Boundary conditions; which gives values to the codes applied.
- SimName.ale.dat: Script for alefor module which is divided in three parts. Numerical treatment; include the method and the parameters to solve the fluid force at outer surfaces. Output and post-process; allows the user to select the variables that will be saved for visualize and analyze. Boundary conditions; which gives values to the codes applied.
- SimName.ker.dat: Script for the kernel module that allows the connection between all the others. Physical problem; include the modules to couple, nastin and alefor. Numerical treatment; include mesh division, each axis is divided 2^n;

if n is 1 the number of mesh nodes are multiplied by 8, time functions, if a function is needed to a boundary condition and file input if external information is needed for the function. Output and post-process; allows the user to visualize CODNO variable at Paraview, contains codes applied, and select after how many steps variables will be stored.

- SimName.post.alyadat: Script to make possible the post-process of variables chosen. It must be duplicated; one for the fluid domain and one for solid domain.
- SimNameS.sld.dat: Script for solidz module which is divided in four parts. Physical problem; includes the values of solid properties; density, Young's modulus and Poisson's coefficient. Numerical treatment; includes the method and all the parameters to solve the partial equations of the solid. Output and post-process; allows the user to select the variables that will be saved for analyze at the post- process. Boundary conditions; which gives values to codes applied.

With all the scripts defined, the job could be run at a personal computer or at big data clusters. Personal computer was used at the beginning for simulating low density meshes to understand and vary parameters and see how they affect the results. Clusters performed all the final simulations due to big data meshes and time reduction.

Mare Nostrum IV and Minotauro are the two clusters located at UPC that performed all the simulations. The access has been brought by our collaboration with Barcelona Supercomputing Center (BSC). Their mission is to research, develop and manage information technology to facilitate scientific progress. For this purpose, special effort has been dedicated in research areas such as Computer Sciences, Life Sciences, Earth Sciences and Computational Applications in Science and Engineering[79]. An account is needed with a username and password for both supercomputers. Once connected to the machines, you will be presented with a UNIX shell prompt and you will normally be in your home directory. Basis of UNIX should be known before doing anything useful. Figure 32 shows an image of Mare Nostrum IV.

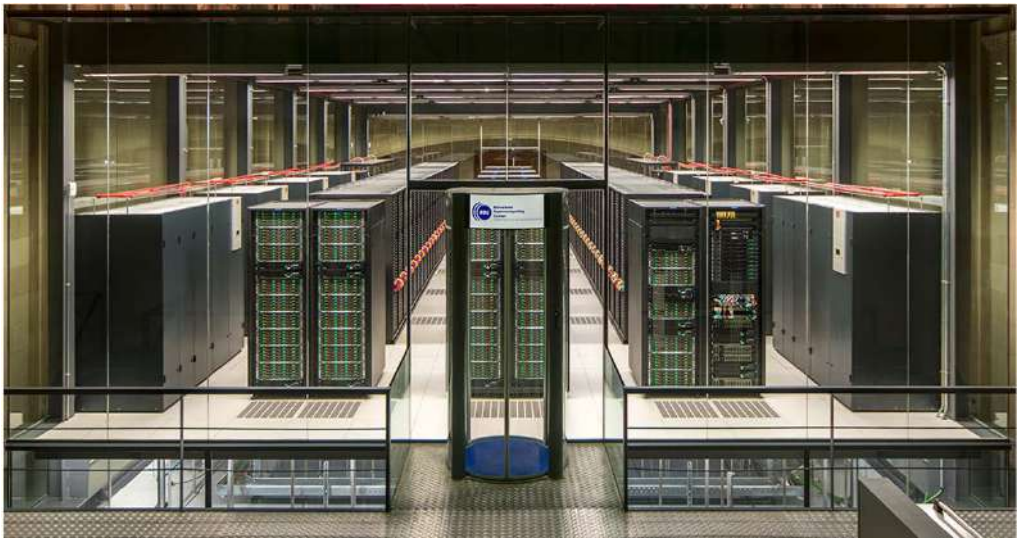

Figure 32. Mare Nostrum servers at Barcelona Supercomputing Center.

2.2.2. Minotauro

Minotauro is the second supercomputer more powerful in Barcelona Supercomputing Center (BSC) and one of the most energetic efficiency in Europe by Green500. It has a maximum performance of 190 teraflops with a cluster comprised of 128 computes nodes. Each node has two Intel Xeon 6-Core at 2.53 GHz with 24 GB of RAM memory, 12MB of cache memory, 250 GB local disk storage (SSD), two NVIDIA M2090 and a parallel file system disk storage of about 2 PB. This supercomputer is programmed in Red Hat Linux operative system[79].

There are two nodes to login in Minotauro; mt1 and mt2. Slurm is the utility used for batch processing support, so all jobs must be run through it. A job is defined by a text file containing a set of directives describing the job and the commands to execute it. The basic commands for jobs are submission, mnsubmit <job-script>, show the jobs submitted, mnq, and remove a job from the queue system or cancel the execution, mncancel <job-id>.

There are basic directives to inform the batch system about job characteristics as job name, directory where the job will run, output file, error file, cpus needed and wall-clock limit. Additionally, the job script may contain a set of commands to execute. If not, an external script may be provided with the executable directive.

2.2.3. Mare Nostrum

Mare Nostrum is the most powerful supercomputer in Spain and third in Europe. So far, four versions have been installed and two of them; Mare Nostrum III and IV, have been used in this project. At the end of June 2017 begun operating MareNostrum IV, which is the one explained below.

It has a peak performance of 13.7 Petaflops with a block of 48 racks housing 3456 nodes with a grand total of 165,888 processor cores and 390 Terabytes of main memory. Each node two sockets Intel Xeon Platinum 8160 CPU with 24 cores each at 2.10GHz with a file system storage of 14 PB.

There are four nodes to login in Mare Nostrum, mn1 to mn4. A job is defined by a text file containing a set of directives describing the job and the commands to execute it. The basic commands for jobs are submission, sbatch <job-script>, show the jobs submitted, squeue, and remove a job from the queue system or cancel the execution, scancel <job-id>.

2.3. Post-analysis

2.3.1. Visualization

The visualization of the simulation results and all the parameters post-calculus have been done in Paraview. Paraview is a multi-platform data analysis and visualization application. Users can quickly build visualizations in 3D to analyze their data using qualitative and quantitative techniques. Paraview offers different tools to observe parameters. The tools used during this project are four; slide, glyph, streamlines and warp.

Slide is used to cut the domain creating planes or boxes to eliminate some parts and see values of variables inside the domain. Glyph places a vector field at different nodes randomly and shows the magnitude and the direction of the variable selected, commonly used in velocity. Streamlines are a family of curves, tangent to velocity vectors of the flow, that represent the trajectories massless particles would travel. The curves initiate at a spherical seed placed at aortic inlet. Finally, warp multiplies the variable values solution by a number to clarify and understand. This tool is only used to visualize displacement of aorta vessel, due to its low values compared to aortic size.

2.3.2. Fluid dynamic parameters calculus

The final steps before trying to correlate the aneurysm with fluid dynamics parameters were to validate the simulation results comparing CFD and FSI parameters versus in vivo MRI data and calculate and analyze three potential parameters related to aneurysm progression in all cases; axial shear stress, circumferential shear stress and vorticity. The three parameters have been calculated in Matlab and visualized in Paraview.

To validate the simulations, we have measured three basic flow parameters; flow displacement, jet angle and maximum velocity. The three parameters were calculated at two planes, one at ascending aorta close to aortic arch and the other at the beginning of descending aorta, and were compared to real data obtained with 4D-MRI in Vall d'Hebron hospital. Figure 33A shows the localization of both planes at the thoracic aorta.

Flow displacement was calculated by defining the anatomical center of the aorta and measuring the distance in millimeters between this anatomical center and the location

of the maximum velocity of the forward flow at peak systole. The distance is normalized through dividing it by the aortic diameter at each analysis plane for the comparison between patients.

Flow angle was calculated by defining the normal vector through the plane studied and measuring the angle (º) between this vector and the maximum velocity vector of the forward flow at peak systole.

Maximum velocity was calculated by vectorization all the velocities of the nodes at the plane and rearrange them from maximum to minimum. The vector value was the maximum velocity.

A representation of the jet angle parameter is shown in Figure 33B and maximum velocity and flow displacement in Figure 33C.

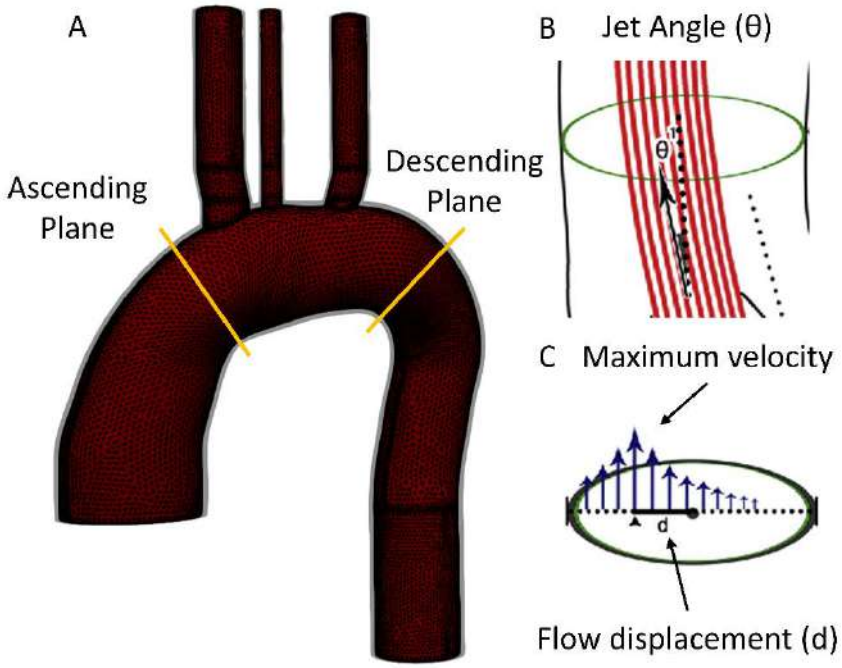

Figure 33. (A) Ascending and descending planes in the aorta where fluid dynamic parameters as (B) jet angle, (C) maximum velocity and flow displacement are analyzed.

Once validation is completed, potential fluid dynamics markers are studied. In this project, three main potential markers have been studied; axial shear stress, circumferential shear stress and vorticity. Moreover, our group created a new parameter, shear stress ratio (SSR), as a potential marker for stratification of Marfan

patients. SSR analysis is performed together with oscillatory shear index (OSI) and time-averaged wall shear stress (TAWSS).

Shear Stress (SS) is the component of stress coplanar with a material cross section and is calculated as the viscosity of the fluid μ multiplied by a velocity gradient as indicated in Eq. 20. During the thesis, two methods have been developed to calculate shear stress in our simulations. Both methods have been developed to calculate shear stress from a randomly discrete data, the mesh. The necessity of points being aligned and perpendicular to the wall makes very difficult to calculate the shear stress directly from a discrete distribution.

$$\tau = \mu * \frac{du}{dx} \qquad \text{Equation 20}$$

where τ is the shear stress, μ is the viscosity and u the velocity component.

The numerical method used in both cases to calculate the derivative term of Eq.19 have been central derivatives at Matlab program. The difference between both methods has been the treatment of the mesh discrete data. Even though both methods consisted in creating patches from the discrete data, first method consisted in creating the patches from the original discrete data of the mesh and the second methods consisted in creating the patches from a grid data previously created from the original mesh.

The necessity of a second method was due to results of the first methods were not enough good. The visualization of the first methods results presented clear patches in the wall due to the impossibility of reducing the patch size for the appearance of NaN values along the vessel. Figure 34 shows the problems of first methods that did rethink how to handle discrete data.

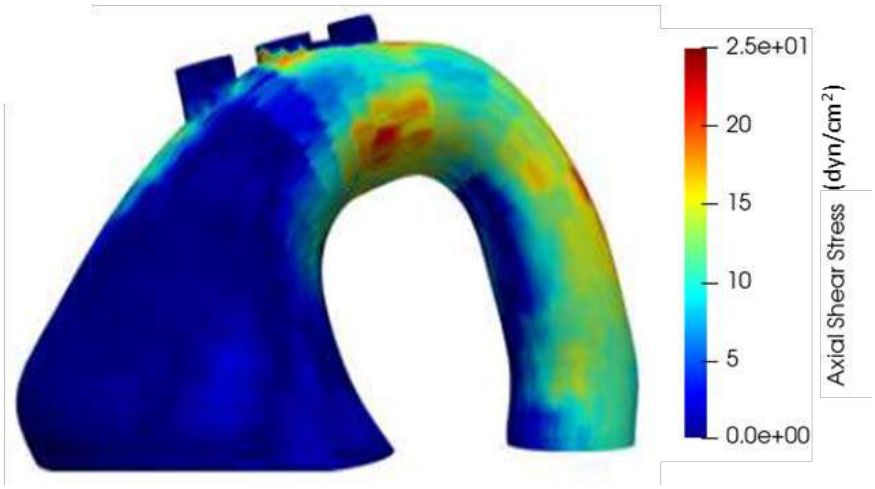

Figure 34. Axial shear stress of thoracic aorta calculated with the first method.

Another problem associated with the method, central derivatives, is the points at the extremes of the geometry. They are not situated between two points and it is impossible to use central derivates. At these extreme points, the value of the shear stress is calculated by finite difference forward and backwards derivates.

The discrete data in both methods has been divided in multiple 200 transversal slices, sections, along the vessel. All the points of a section are considered as the same plane. Each section has been divided in a circular grid of 12 radial divisions and 100 circular divisions, creating a total of 1200 patches per section.

In the first methods, the grid division has been performed in function of the mesh size due to the dependency that every patch needs at least 1 mesh point inside to make possible the calculation of the patch velocity. If the patch doesn't have a mesh point inside, it will receive at value of NaN. Figure 35 shows the velocity of a systole step (left images) and a diastole step (right images) before (top) and after (low) applying the patches.

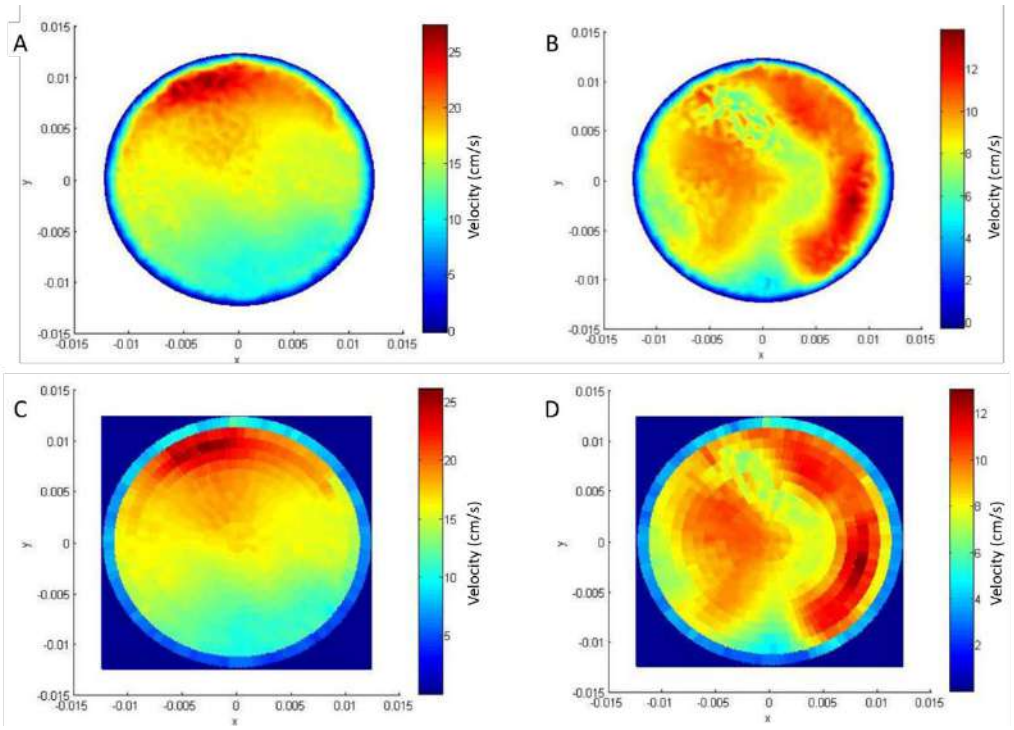

Figure 35. Velocity field (A, B) of the mesh and (C, D) after applying patches at systole and diastole steps.

A validation procedure was performed to verify the method's accuracy. Shear stress was calculated using Tdyn in flow across a straight pipe and compared with the shear stress values calculated with the method herein defined.

Figure 36 shows the shear stress calculated with Tdyn in the left image and the shear stress calculated with method 1 in the right. The wall shear stress calculated with Tdyn oscillated in a range between 0.245 and 0.276 Pa and the shear stress was estimated 0.270 Pa if calculated with our method. This test validates the derivatives calculation and the success in defining the selection of points by creation of patches.

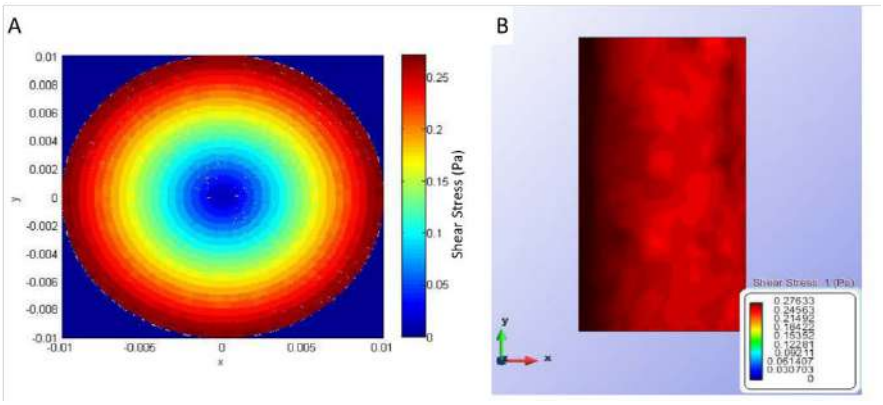

Figure 36. Shear stress in a straight tube calculated from (A) Method 1 and (B) Tdyn.

Even though the method worked for most of the patches and values were coherently matched with Tdyn, our group thought that results were not enough good finding patches too much perceptible for the eyes and NaN values, even being less than 1%, stood up so much.

In the second method, the grid division has been performed with a function of Matlab, griddata. Griddata fits a surface of the form z=f(x,y) to the data and interpolates this surface to the points, forming the specified grid. Griddata does not extrapolate, so if grid points are outside the original mesh, they will receive a NaN. Figure 37 represents a conceptual concept of a grid section.

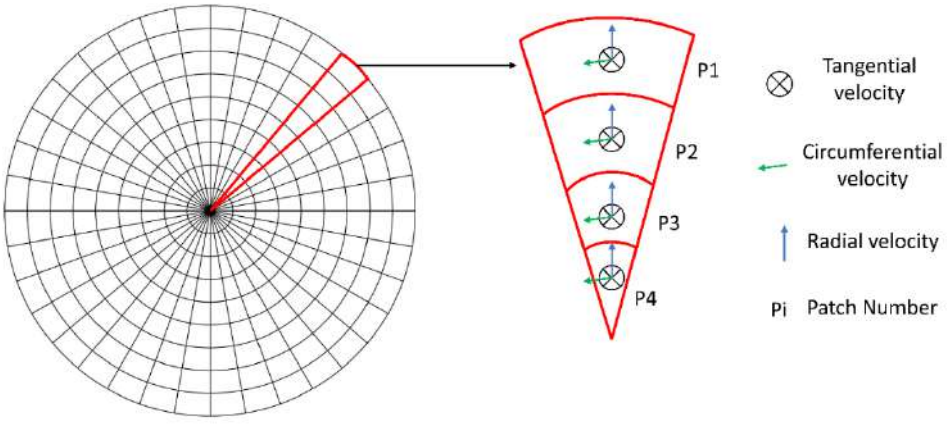

Figure 37. Conceptual representation of a section grid division, patches and velocities.

The points are initially generated in polar coordinates and are transformed to Cartesians coordinates. Velocity interpolation at all patches is performed with the nodes. With a velocity for all patches, central derivatives are applied. The axial and the circumferential

velocities have been used to calculate the axial and the circumferential shear stress respectively to all the grid points. Figure 38 shows the grid points and the mesh nodes.

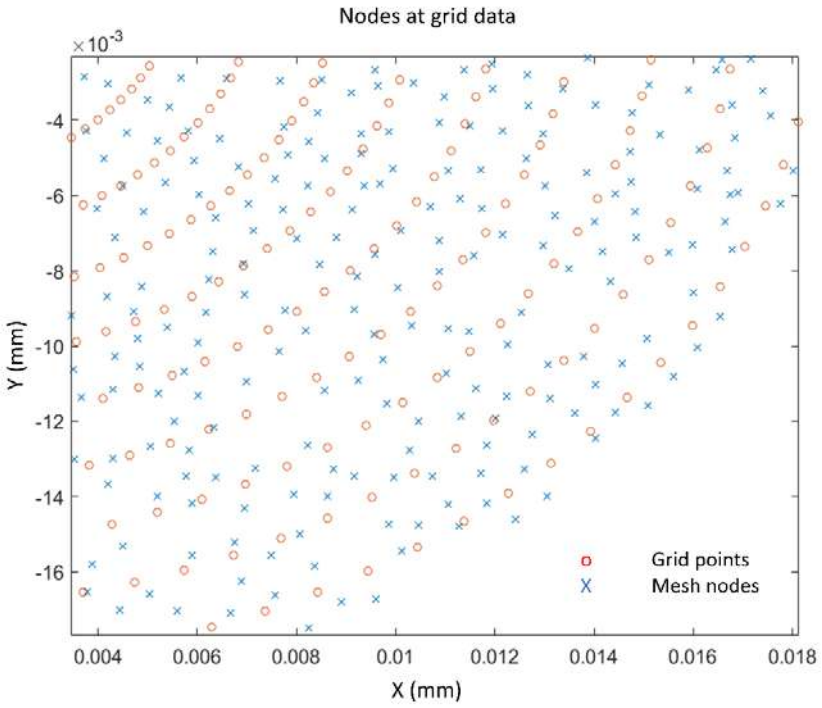

Figure 38. Grid points and nodes coordinates of a slice.

Finally, in both methods, it is necessary to assign the shear stress values from the grid to each node of the mesh. The shear stress of most nodes is calculated with a weight interpolation of the four closest grid points as shows Figure 39A. However, there are nodes located between the first and the last angle or at the limit of the geometry, so they are not located inside a square and are treated as exceptions.

For the nodes situated between an angle of 0 and the first grid angle division or between the last grid angle and 0, the second pair of points to form the square should be assigned by increasing or decreasing the grid angle position by 1. For the nodes situated at the limit of the geometry, the shear stress should be calculated using only two grid points. This problem appears when the radius is below the first point or above the last point of the grid. Figure 39B shows the grid points selected to calculate the shear stress of a node situated outside of the grid zone (radius above the last point of the grid).

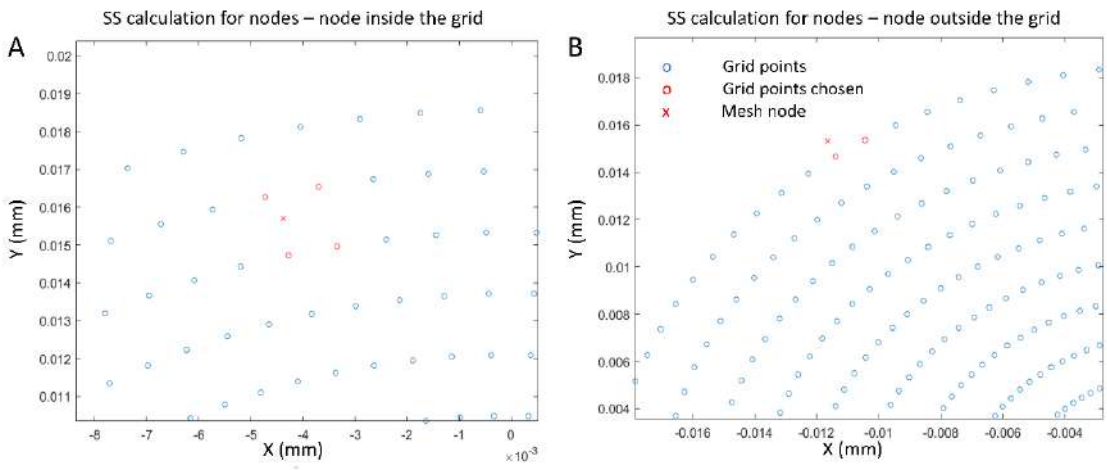

Figure 39 Shear stress calculation for the mesh nodes; a node inside the grid (A) and a node outside the grid (B).

This procedure is repeated for all the longitudinal sections of the tube. When all nodes of the mesh have a shear stress value, the final step is to generate an ENSI file readable for Paraview where all the values are exported.

Axial and circumferential shear stress and all other parameters have been studied diving the aorta in three segments; ascending, arch and descending, Moreover, each segment has been divided in four parts; anterior, posterior, interior and exterior to have a better approach of where parameters are significant. Figure 40 shows the division of the aorta in four quadrants in an MRI image.

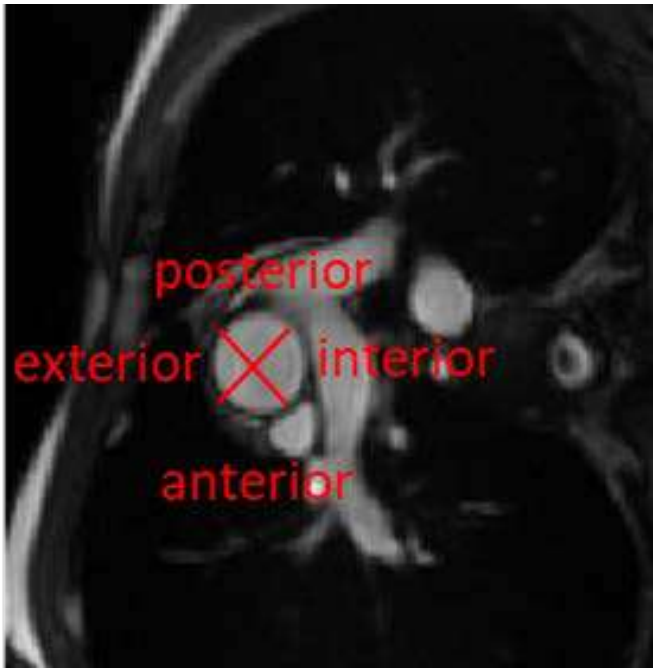

Figure 40. MRI image where ascending aorta is divided in four quadrants.

Vorticity is the pseudovector field that describes the local spinning motion of a continuum, the tendency of a fluid to rotate. Vorticity has been calculated with Paraview as Eq. 21.

$$\vec{\omega} = \nabla \cdot \vec{u} \qquad \text{Equation 21}$$

where ω is the vorticity and u the velocity.

First, streamline function of Paraview is applied to observe the fluid as streamlines. The seed was located at the inlet and the fluid domain is described with 3000 streamlines. When streamlines are adjusted, vorticity is calculated in each point of each streamline and values are saved in a file for each time step. Figure 41 shows an aorta as streamlines with velocity and vorticity fields. This data is imported at Matlab and is interpolated at all nodes. The interpolation consists on searching the four nearest points of the streamlines to each node of the mesh and perform a weight interpolation.

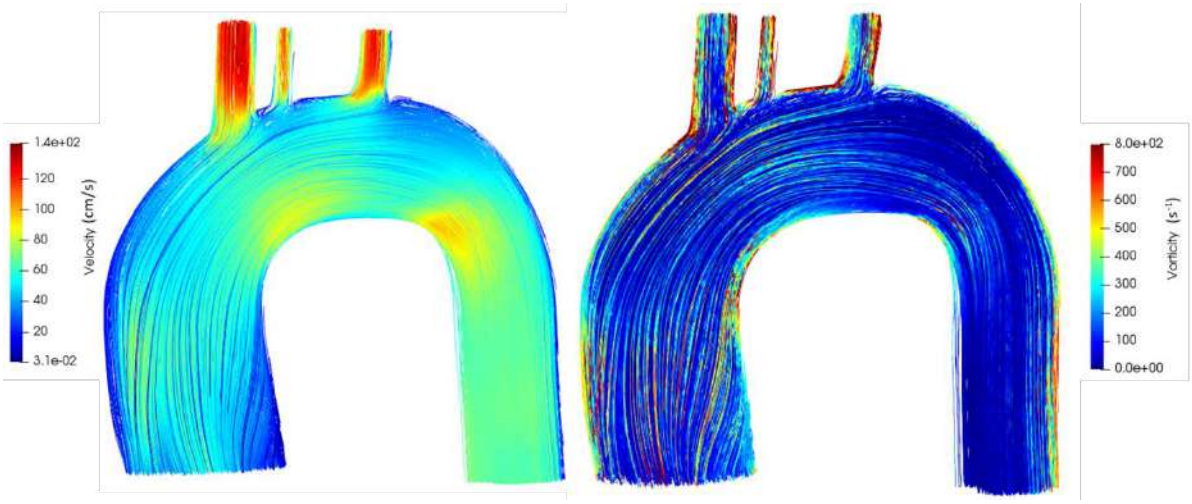

Figure 41. Streamlines of an aorta showing velocity and vorticity parameters.

Average wall shear stress (AWSS) is the average value of wall shear stress during the cardiac cycle (T)[80]. It is calculated as Eq. 22.

$$AWSS = \frac{1}{T} * \int_0^T \left|\overrightarrow{WSS}\right| \cdot dt \qquad \text{Equation 22}$$

where AWSS is the average wall shear stress, T is the time of the cardiac cycle and WSS is the wall shear stress.

Oscillatory shear stress index (OSI) is a temporal parameter that evaluates shear stress oscillation during a pulse of period T[80]. It depends of two magnitudes, the average wall

shear stress (AWSS) and the average wall shear stress vector (AWSSV), Eq. 23. OSI is calculated as Eq. 24.

$$AWSSV = \frac{1}{T} * \left| \int_0^T \overrightarrow{WSS} \cdot dt \right| \quad \text{Equation 23}$$

where AWSSV is the vector of the average wall shear stress, T is the time of the cardiac cycle and WSS is the wall shear stress.

$$OSI = 0.5 * (1 - \frac{AWSS}{AWSSV}) \quad \text{Equation 24}$$

where OSI is the oscillatory shear stress index.

OSI values vary between 0 for no-cyclic variation of wall shear stress vector and 0.5 for 180-degree deflection of WSS direction[81]. It is a very useful parameter that gives an approximation of which vessel regions present inconstant wall shear stress direction. Unfortunately, OSI has to be considered with caution as it only evaluates wall shear stress direction through time, without considering its magnitude[81].

Shear Stress Ratio (SSR) is a non-dimensional parameter which can be calculated by dividing the circumferential shear stress by the axial shear stress, as Eq. 25. This new parameter correlates the in-plane rotation of the fluid versus the through-plane advance of the fluid.

$$SSR = \frac{SS_{Circumferential}}{SS_{axial}} \quad \text{Equation 25}$$

where SSR is the shear stress ratio, $SS_{circumferential}$ is the circumferential shear stress and SS_{axial} is the axial shear stress.

2.3.3 Statistical analysis

Data are expressed as mean ± standard error of mean. Non-parametric Kruskal–Wallis test, followed by a Scheffé's post hoc analysis of the original measured values was conducted to determine statistical differences between values. Values of $p<0.05$ were considered statistically significant.

3. Results and Discussion

The results and discussion section are divided in three parts. The first one is the creation of a stable and robust simulation model for a bicuspid aortic valve (BAV) patient. Initially, the project was aimed to study aortic fluid dynamics in BAV patients. Part of this work was published by our group[82]. However, the complexity of boundary conditions in this type of patients rendered hard to standardize simulations strategies in fluid-structure interaction. In consequence, the project pivoted to Marfan patients, but the effort done to achieve the convergence in BAV patients was useful to build a robust model that performed consistently with Marfan patients.

In a second part, once the simulation model was stablished, eight Marfan syndrome patients and four healthy controls were simulated with CFD and FSI using MRI-derived patient-specific boundary conditions like geometry, inflow and wall stiffness. The main results from this part have been published recently[83]. The analysis of the results is divided in five parts. First, the boundary condition modeling and the clinical data analysis of all cases is studied. Second, the analysis of the whole simulation process is presented for each case from medical images to the analysis of derived fluid dynamics parameters such as shear stress. Third, the analysis of the Windkessel effect and the iterative process with the pulse wave velocity. Fourth, a comparative analysis for primary fluid dynamic parameters such as flow displacement, maximum velocity and jet angle calculated from CFD and FSI simulations versus clinical data. Finally, the derived fluid dynamic parameters as axial and circumferential shear stress, vorticity and shear stress ratio are studied and compared to find a correlation for the stratification of aneurysm risk.

In the third part, the axial and circumferential shear stress generated by a helix inside a tube have been analyzed and matched to real values observed in aortae simulations. Moreover, the helix designed has been printed in 3D and a fluid circuit has been set to test *in vivo* data.

3.1. Simulation model

All patients treated and analyzed along the results are MFS patients, but, at the beginning of the project, our aim was to treat patients with BAV dysfunction. The first BAV patient presented high dilation at the aortic root and complex flow profiles with high backward flow at the closure of the aortic valve. These factors prevented FSI simulations from converging. Although the project finally pivoted to MFS patients, the analysis of the BAV patient contributed to build a robust simulation model that converged easily in all MFS patients and healthy control cases.

The initial data came from a healthy control and a BAV patient. Both geometries were segmented and meshes are showed in Figure 42. 4D-MRI data was treated and flow profile of both was used as inlet conditions. Figure 43 shows the blood profiles after the interpolation in Matlab.

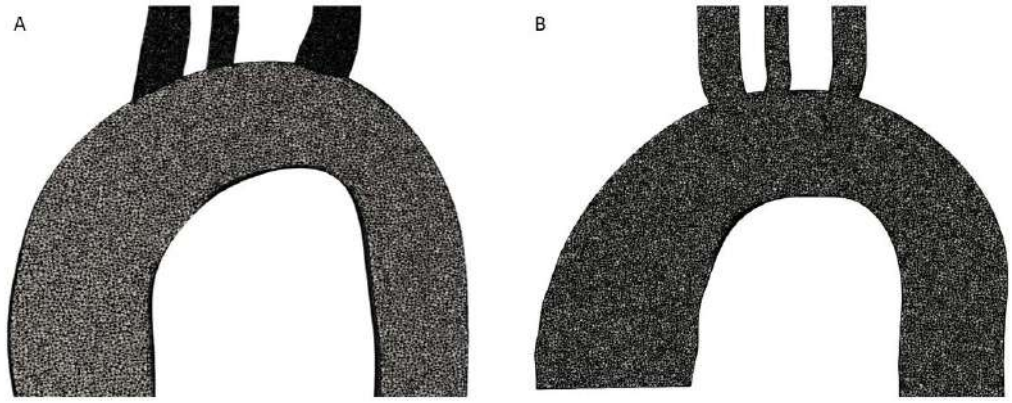

Figure 42. Meshed geometry of (A) healthy control and (B) BAV patient.

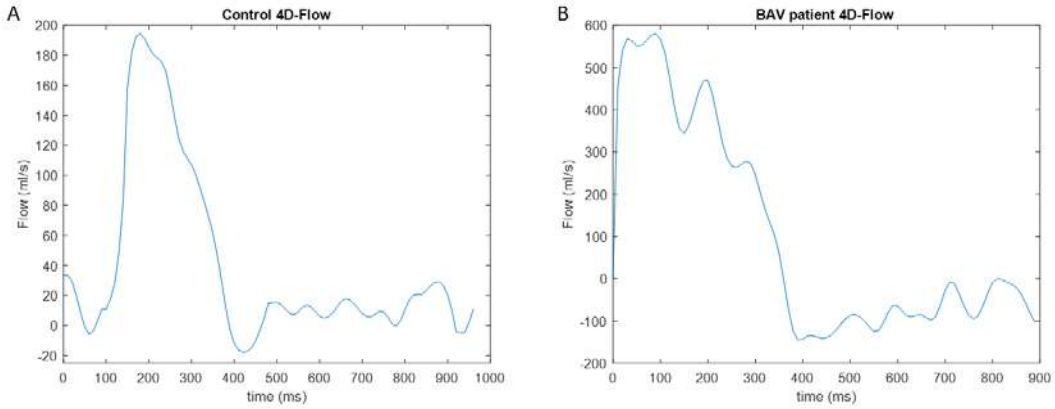

Figure 43. Inlet boundary condition after Matlab treatment (A) in healthy control (B) and BAV patient.

BAV patient diameter in the ascending aorta (40 mm) nearly doubles the diameter of the healthy control (24 mm), while the descending aorta diameter is closely the same in

both geometries (24 mm and 20 mm). In Figure 43, both flow inlet conditions are presented, and it can be observed that flow is tripled in the BAV patient compared to the healthy control. The cardiac cycle times are 930 ms and 900 ms in healthy control and BAV patient respectively. The systolic phase is 300 ms in the healthy control and 400 ms in the BAV patient, 100 ms more in the dysfunctional aorta. At 400 ms, after valve closure, both cases present their diastolic peak; while the healthy control presents negative flow of 20 ml/s, the BAV patient reaches a negative value of 160 ml/s, eight times higher. Moreover, the BAV patient maintains the negative flow during 400 ms while the healthy control's negative flow remains for less than 50 ms. The BAV patient flow profile is much more complex than the healthy control and the simulation convergence could be affected by the enormous flow during systole and backward flow during diastole.

First, CFD simulations of both cases were performed with constant inlet velocity. The first simulation model used, consisting of basic parameters destined to calculate in a fast and effective way to get an initial sense of performance and convergence. The simulation parameters are exposed below:

- A restart is used to give an initial solution to the fluid domain, so the initialization did not begin from null velocity.
- Inlet velocity is set to a constant value of 35 cm/s for the healthy control and 18 cm/s for the patient.
- Numerical treatment consisted of 200 iterations with a tolerance of $1 \cdot 10^{-7}$ and a ratio of 0.01 for momentum and continuity equations.
- Outlet conditions were set as zero pressure.
- 24 CPUs were used in both simulations.

Simulation time was 25 minutes in the healthy control and 40 minutes in the BAV patient. The inlet velocity difference between cases is due to the difference in size of the inlet surface; the inlet flow was approximately the same in these initial simulations. The restart is used because the first steps in a simulation normally take more iterations to converge, so time can be reduced.

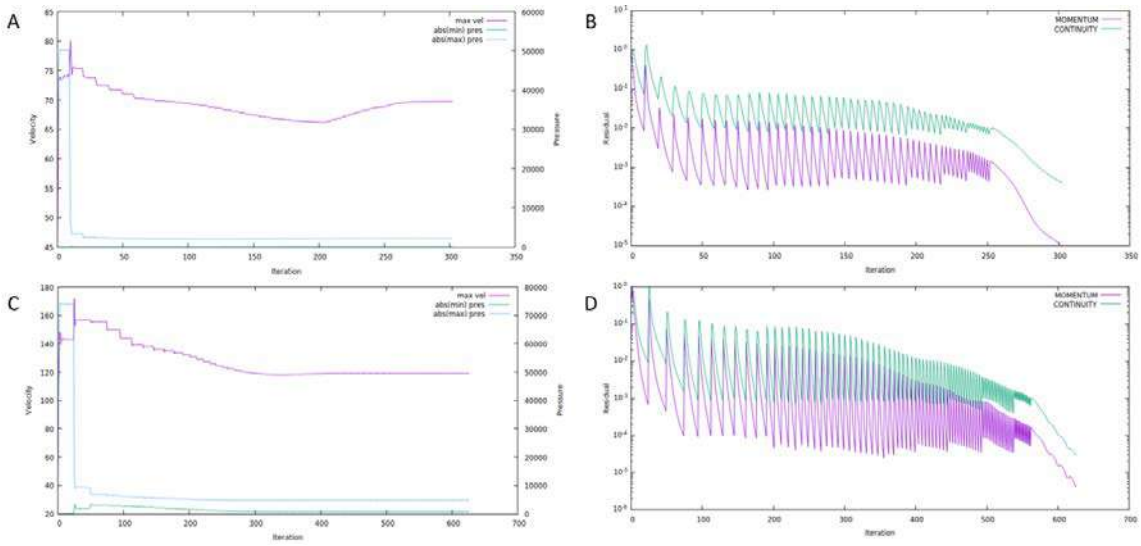

Figure 44. CFD convergence with constant inlet velocity of (A, B) the healthy control and (C, D) the BAV patient.

With the parameters presented above, as it can be observed in Figure 44, both simulations converged and results were coherent for the initial conditions. It can be observed in the maximum velocity graphs, Figure 44A and Figure 44C, that both simulations reached the steady state, as maximum velocity changes are nearly negligible in time and residuals progressively achieve the set point always in the first iteration. To reach steady state, the healthy control performed 89-time steps after a total of 300 iterations and the BAV patient performed 148-time steps after a total of 620 iterations. The maximum velocity in the healthy volunteer's descending aorta is 80 cm/s, while the patient's is the double. Although the inflow is nearly the same in both cases, the patient has higher velocities because of the geometry. Even using restart data, it can be observed in Figure 44B and Figure 44D that convergence is harder to obtain during the first steps of the simulation. The first 100 iterations are dedicated to progress 11 steps in the healthy control while only 4 steps are advanced in the BAV patient simulation. However, after stabilization, the number of iterations required to converge decreases to 1 iteration per step.

Once seen that convergence is achieved with constant velocity inlet, 4D-MRI velocities were tested in both cases keeping all other parameters as mentioned. Figure 45 shows the simulation convergence in the healthy control and in the BAV patient.

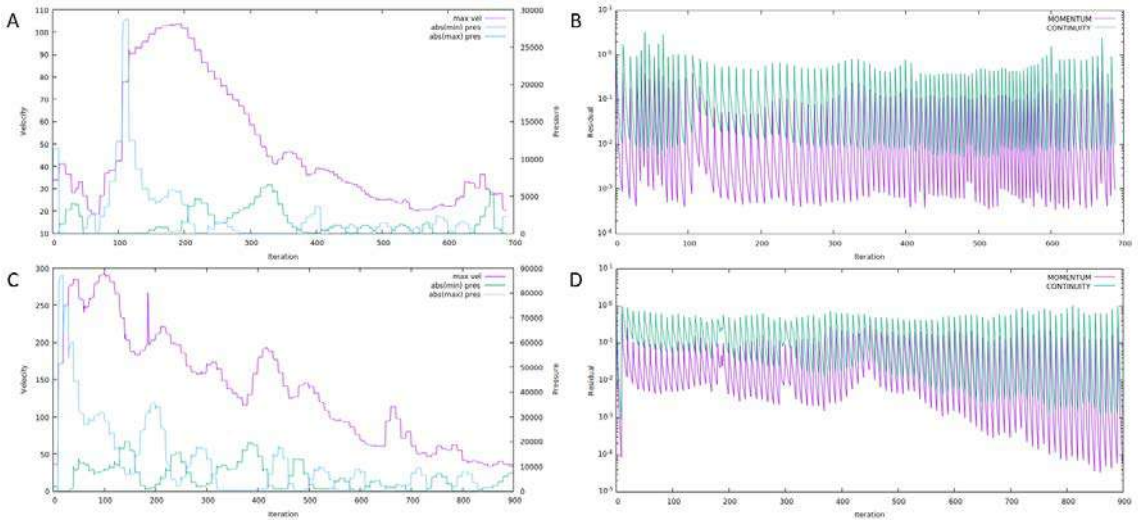

Figure 45. CFD convergence with 4D-MRI inlet velocity of (A, B) the healthy control and (C, D) the BAV patient.

Simulation time was 45 minutes for the healthy control and 55 minutes for the BAV patient. It can be observed that the maximum velocity curve follows the trend imposed (Figure 43). Both simulations are 90 steps long, which require 700 iterations for the healthy control and 900 iterations for the BAV patient. Overall, the healthy control was hence simpler to converge. The first systolic steps in both cases (iterations 120 to 300 in control and 0 to 200 in BAV patient) and the first diastolic steps in patient (iterations 400 to 500) require a higher number of iterations to converge because inlet velocity changes fast and the system needs to adapt. Steady state is obviously not achieved due to the unsteadiness of the inlet boundary condition. Regarding maximum velocity, one can observe that the systole of the healthy volunteer and the patient's are displaced in time. Healthy volunteer systole begins after 10 steps of the simulation while the patient's systole begins with the simulation. The maximum velocity achieved at systole in the healthy volunteer is 100 cm/s and 300 cm/s in the patient, both in the descending aorta. This 3-fold increase is consistent with the 3x increase in flow inlet between both cases. At diastole, the average maximum velocity is 35 cm/s in healthy control and 100 cm/s in BAV patient. Moreover, healthy volunteer has a diastole without relevant irregularities, while the patient shows more instability due to the geometry and the inflow. On iteration 450 of the BAV patient, a peak of 200 cm/s can be observed, matching with the beginning of the diastole.

FSI simulations were performed after CFD simulations converged with real inlet velocities. The first problems appeared when solid mechanics were introduced and coupled with CFD. The first model used to FSI simulation kept the CFD parameters mentioned before and added the parameters exposed below for the solid mechanics and the coupling parts:

- Arterial wall density of 1200 kg/m^3, Young modulus of 1 MPa and Poiseuille coefficient of 0.45 (taken from literature[84]).
- The numerical treatment for the algebraic solver of solid mechanics was set at 200 iterations with a tolerance of $1 \cdot 10^{-7}$ and a ratio of 0.01.
- The coupling is performed without using Aitken algorithm. The numerical treatment for the algebraic solver of the coupling was 20 iterations with a tolerance of $5 \cdot 10^{-3}$.

The performance of FSI with these parameters was poor and simulations did not converge to realistic results. Figure 46 shows that the BAV simulation could only perform two steps before diverging into negative Jacobian, which caused the maximum velocity to shoot upwards $2{,}5 \cdot 10^{33}$ m/s, Figure 46A. Figure 46B shows that the fluid began converging multiple iterations in the first step but the coupling disrupts it and hampers the path to achieve the residual values. During step 2, it can be observed that all the iterations needed the maximum number of solver iterations and yet the residual cannot be reduced to the desired value. The FSI simulation took 1 hour and 20 minutes.

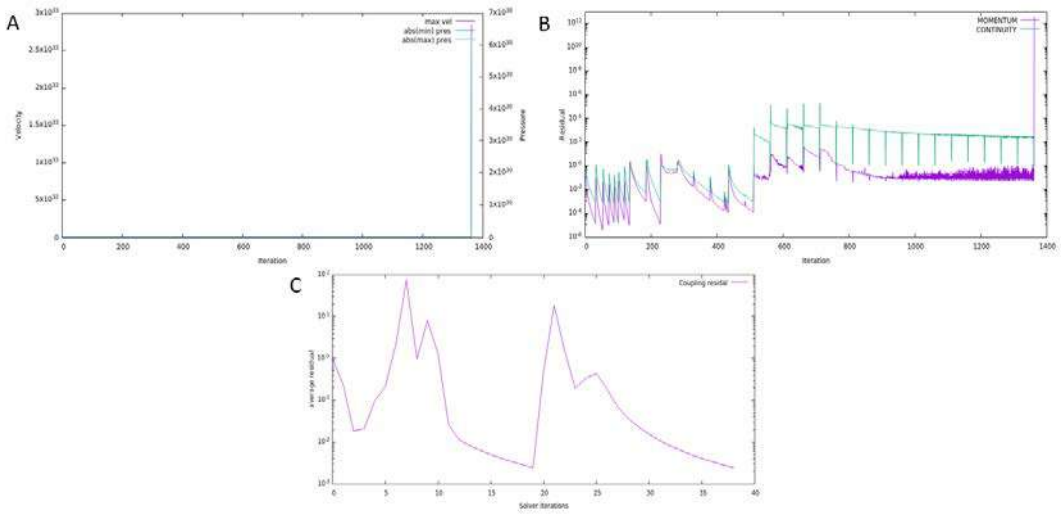

Figure 46. BAV patient FSI convergence (A, B) of the fluid and (C) the coupling in the first iteration of the method.

Observing that BAV patient would be very problematic to converge, the work was focused on trying to improve the convergence and changing multiple parameters until the entire cardiac cycle of the BAV patient could be performed. The next two FSI simulations only show the convergence of the BAV patient.

Even though CFD simulations were converging well and results were coherent with the initial conditions, some of the initial parameters exposed were changed to help the convergence of the coupling. The tolerance was reduced, and the number of iterations increased. These changes made results more accurate and could potentially improve the coupling part. The changes in the fluid mechanics are exposed below:

- Numerical treatment increased the number of iterations from 200 to 2000, tolerance was reduced from $1{\cdot}10^{-7}$ to $1{\cdot}10^{-10}$ and ratio was reduced from 0.01 to 0.001.

Apart from the fluid mechanics, the parameters of the solid mechanics were also adjusted to perform similarly to fluid. However, coupling parameters were maintained constant. The changes in the solid mechanics are exposed below:

- Numerical treatment increased the number of iterations from 200 to 2000 and tolerance was reduced from $1{\cdot}10^{-7}$ to $1{\cdot}10^{-10}$ and ratio was reduced from 0.01 to 0.001.

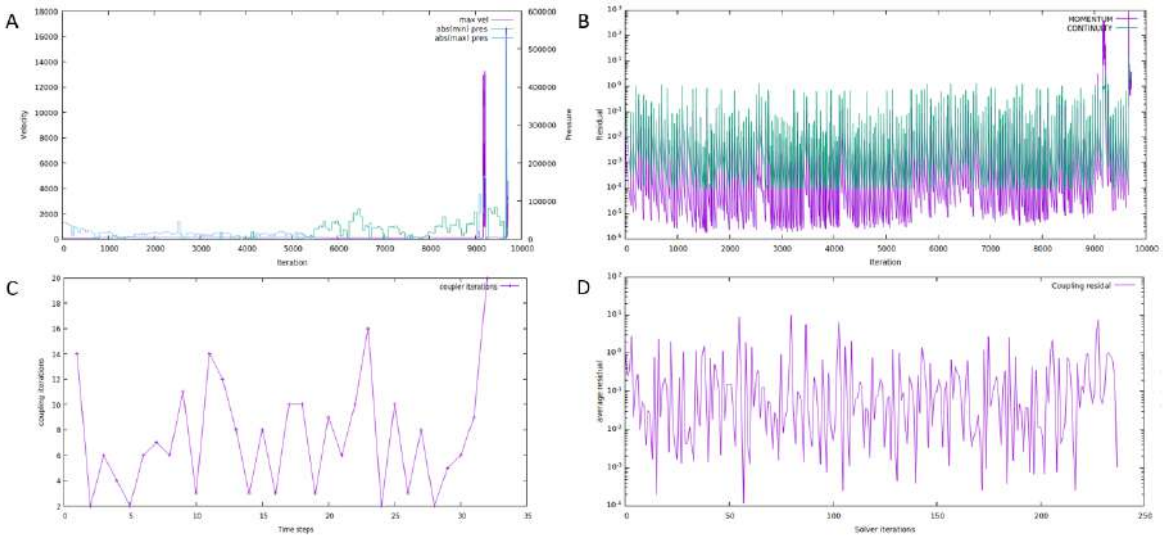

Figure 47. BAV patient FSI convergence (A, B) of the fluid and (C, D) the coupling in the second iteration of the method.

The simulation took 4 hours and 15 minutes. Figure 47 shows that simulation convergence improved with the parameters changed but ended up diverging in the transition from systole to diastole, at step 33. Figure 47A and Figure 47B show that the converge of the fluid was slower but more accurate and FSI simulation benefited from it, converging all systolic steps. Even though it is impossible to see the maximum velocity graphic due to the value achieved when the simulation did diverge, residual graphic shows that all the systole converged well with no abnormal values. Moreover, before divergence, Figure 47C and Figure 47D shows that the coupling between the fluid and the solid is converging good during solver iterations using from 2 to 16 coupling iterations.

Knowing that now the problem is focused in the beginning of the diastole, some parameters needed to be added to maintain the convergence during these hard steps due to the large negative velocities in the inlet boundary condition. For the fluid, five layers of 10 times the blood's density (1035 kg/m^3) were used at the outlet surfaces to help the transition between systole and diastole. For the coupling, Aitken scheme was added to try to couple the problem with less iterations and solve the problem in less time. Figure 48 shows the convergence of the BAV patient with these new two features.

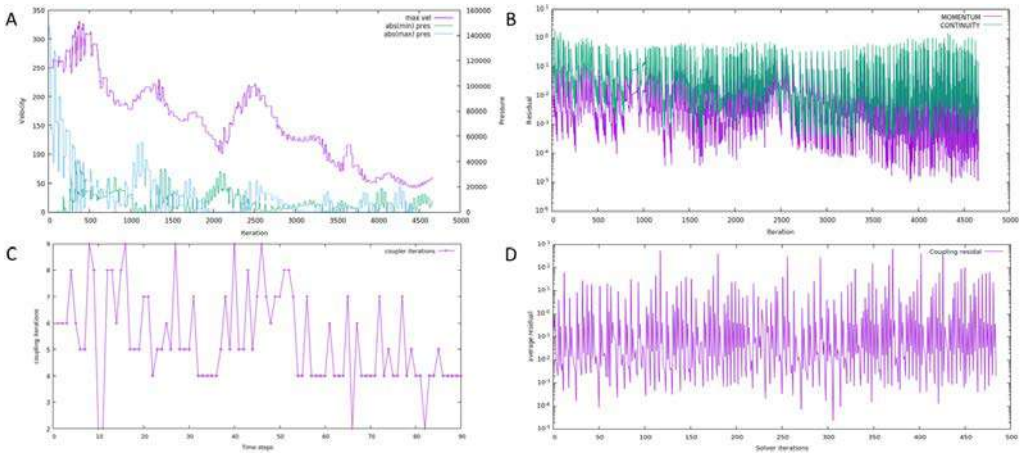

Figure 48. BAV patient FSI convergence (A, B) of the fluid and (C, D) the coupling in the third iteration of the method.

The simulation took 5 hours and 40 minutes. With the last changes, the simulation could perform the transition of the systole to the diastole in BAV patient. Finally, Figure 48A and Figure 48B show that maximum velocity does not present divergence and residuals are achieved in all time steps. Moreover, Aitken reduced significantly the coupling iterations needed from 5-16 (Figure 47C) to 4-8 (Figure 48C).

Once FSI simulation of the BAV patient cardiac cycle was finally converged, same parameters were used on FSI simulation of healthy control. Figure 49 presents the convergence of the healthy control FSI simulation. The simulation took 2 hours and 40 minutes to perform the entire cardiac cycle.

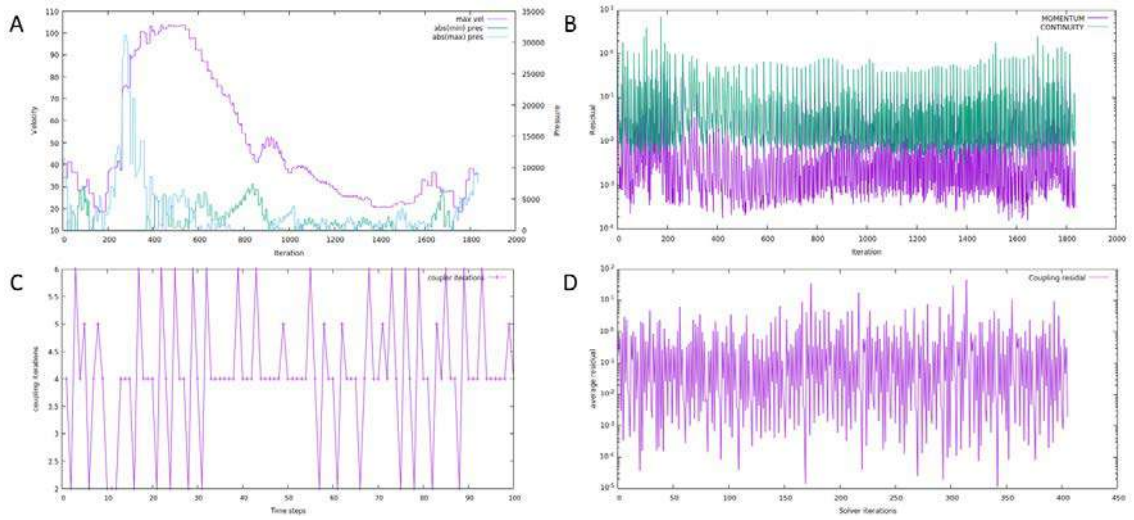

Figure 49. Healthy control FSI convergence (A, B) of the fluid and (C, D) the coupling.

Healthy control convergence is acquired in all time steps with no abnormal values in the maximum velocity graph (Figure 49A) and residuals are achieved in each time step (Figure 49B). The coupling also performed well and a mean value of 4 coupling iterations are needed per time step (Figure 49C).

Comparing the convergence of CFD to FSI, the maximum velocity remained equal in the healthy control and increased from 300 to 325 cm/s in the BAV patient. The iterations required increased from 700 and 1080 in CFD to 1800 and 4700 in FSI. For the coupling, the mean and maximum iterations needed were 4 and 6 in healthy control and 6 and 9 in BAV patient, showing that the BAV patient is harder to couple.

After thoroughly analyzing the number of parameters required to evaluate before achieving reliable simulations, our research group decided to look for patients with less backward flow at the diastole, which was the main driver of divergence issues and variability in BAV patients. Given that Marfan patients do not generally present significant backward inflow at the beginning of the diastole, the rest of this Thesis is focused on analyzing this type of patients.

3.2. Boundary conditions modelling

3.2.1. Inlet 4D-MRI

4D-MRI provides the velocity vectors in multiple points of a plane located at the sinotubular junction. The number of points extracted using 4D-MRI is proportionally related to the aortic diameter.; systolic phases present more points due to dilation of the aorta and diastolic phases present less due to contraction of the vessel. 4D-MRI data are treated and interpolated in Matlab to achieve a higher resolution than the mesh. The original number of points at the systolic peak and the number of points after the interpolation are described in Table 1. For example, the maximum ascending diameter (51 mm, Table 1) is presented in dilating patient 1, which presents the highest number of points extracted from 4D-MRI (310 points in systolic phase) and the highest number of nodes in the inlet surface of the mesh (2533 points).

		Number of Points			
		4D-MRI		Interpolation	Inlet nodes
		Systole	Diastole		
Cases	C1	116	98	3969	982
	C2	122	106	5041	1182
	C3	130	105	6241	1234
	C4	96	70	3721	937
	S1	172	159	6561	1622
	S2	102	79	3721	1006
	S3	131	109	6400	1170
	S4	135	112	6400	1140
	D1	310	282	9801	2533
	D2	183	140	7225	2011
	D3	157	121	6561	1377
	D4	280	254	8649	2262

Table 1. Number of points extracted from 4D-MRI images, after interpolation and from inlet mesh surface.

As explained in section 2.4.1, each inlet node of the mesh should be in a different square of the grid to have a unique velocity value. Coherently, the interpolated number of points must always be higher than the inlet nodes of the mesh. All cases present 3 to 5 times more interpolated points than the number of inlet nodes from the mesh.

Figure 50 provides an illustrative view of blood flow profile and its surface at systolic peak from the original 4D-MRI data and after the interpolation. The 4D-MRI data presents a sharpened flow curve. The visualized surface has a relatively low resolution, and especially a disconnection with the perimeter of the vessel, in a way that the no-slip condition of zero velocity at the edges is not accomplished. This is due to the manual creation of the vessel contour, that, in areas of low velocity such as the arterial wall, is very observer dependent. To overcome this issue, as seen in Figure 50B, 4D-MRI data are smoothened in time and space using the B-spline method. Furthermore, boundary conditions of null velocity are imposed at the wall surface, to comply with the no-slip condition.

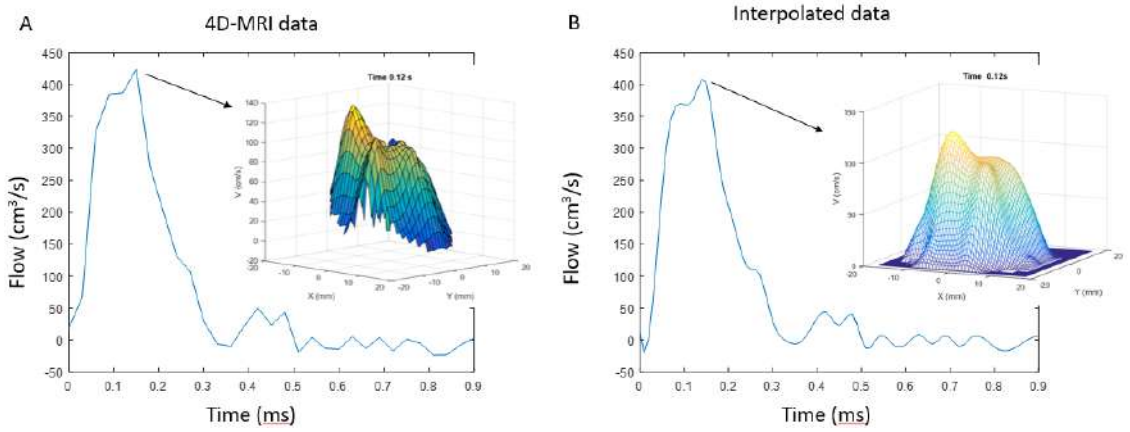

Figure 50. Flow of sinotubular junction (A) with 4D-MRI technique and (B) after the spatial-temporal interpolation in Matlab.

3.2.2. Windkessel method

The Windkessel method was tested in a simple bifurcated geometry before introducing it in aortic simulations. This geometry has an inlet and two outlets, which is perfect to apply a Windkessel in one outlet and observe changes in the flow distribution. Figure 51A shows the mesh of the geometry with the inlet and the two outlets. Outlet 1 is the surface where Windkessel was applied during the test and the mesh was formed by $5{,}7 \cdot 10^5$ elements.

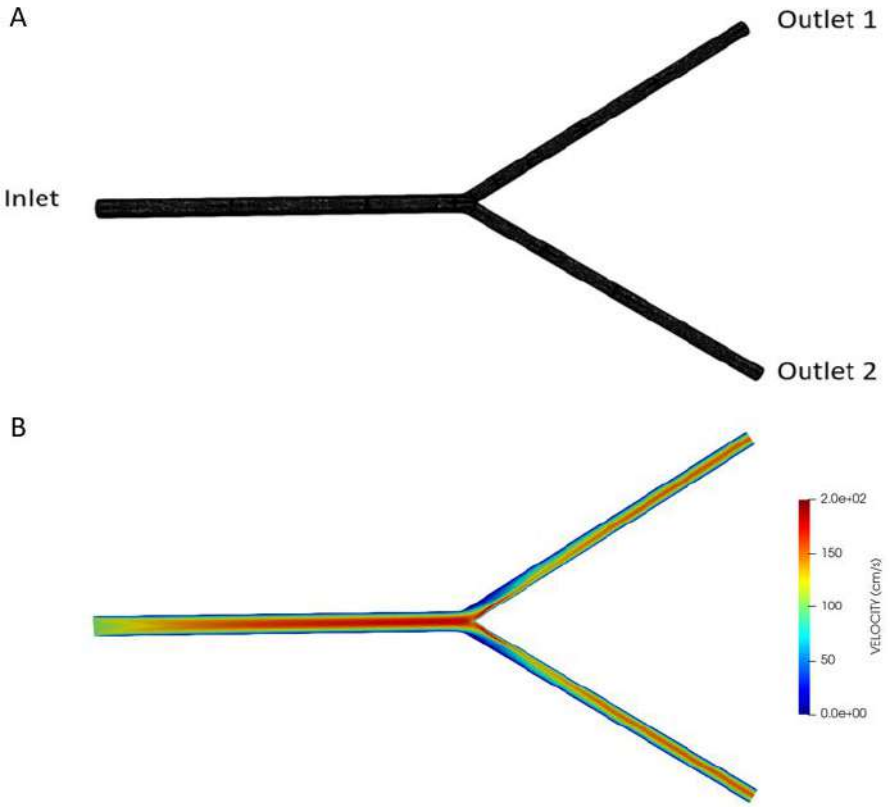

Figure 51. Mesh of the Y geometry (A) and velocity field of the simulation with no Windkessel.

First, the simulation was performed with a Windkessel resistance value of 0 mmHg·s/cm^3 (Figure 51B). As expected, the flow distribution was 50% for each branch and the flow profile symmetrical. When the value of the Windkessel was increased in Outlet 1, the flow distribution was affected by increasing the outlet flow in Outlet 2. The values of R tested were 100, 500, 1000, 2000 (Figure 52) and 4000 mmHg·s/cm^3 (Figure 53). At resistance of 2000 mmHg·s/cm^3, a flow ratio of 60%-40% was obtained. When the resistance value was increased to 4000 mmHg·s/cm^3, the simulation diverged due to excessive pressure, converting Outlet 1 into an inlet. Figure 52 shows the velocity

profile with four resistance values. The higher R, the more velocity is reached in Branch 2. Figure 53 shows that Branch 1 flipped and became an inlet.

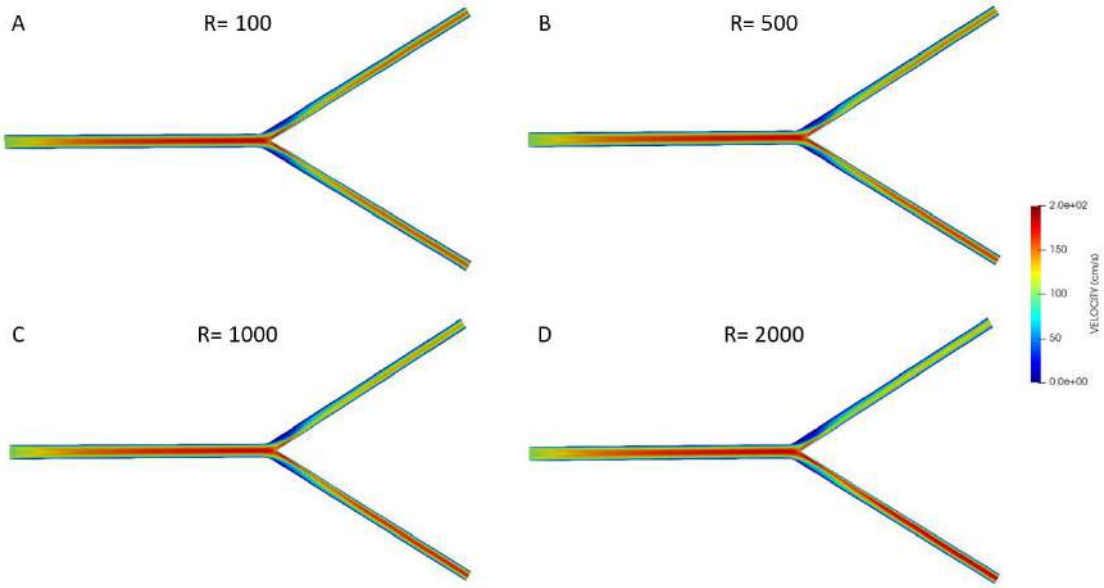

Figure 52. Velocity field in Y geometry with a Windkessel of (A) R=100, (B) R=500, (C) R=1000, (D) R=2000.

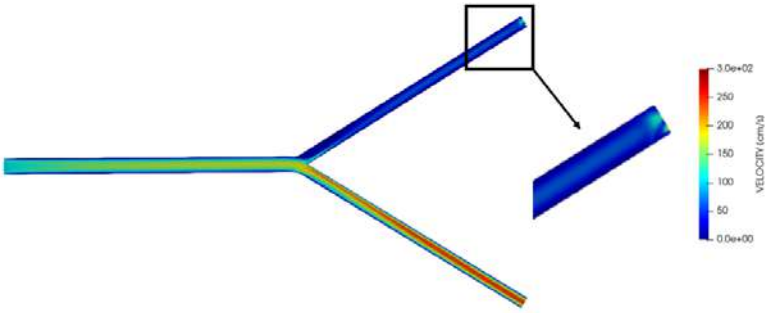

Figure 53. Velocity field in Y geometry with a Windkessel of R=4000.

The convergence of the simulation shows that all simulations, except for of the one of R=4000 mmHg·s/cm^3, achieve the steady state (Figure 54A and Figure 54B). Convergence of R=4000 mmHg·s/cm^3 seen in Figure 54C and Figure 54D, shows that velocity cannot reach the steady state.

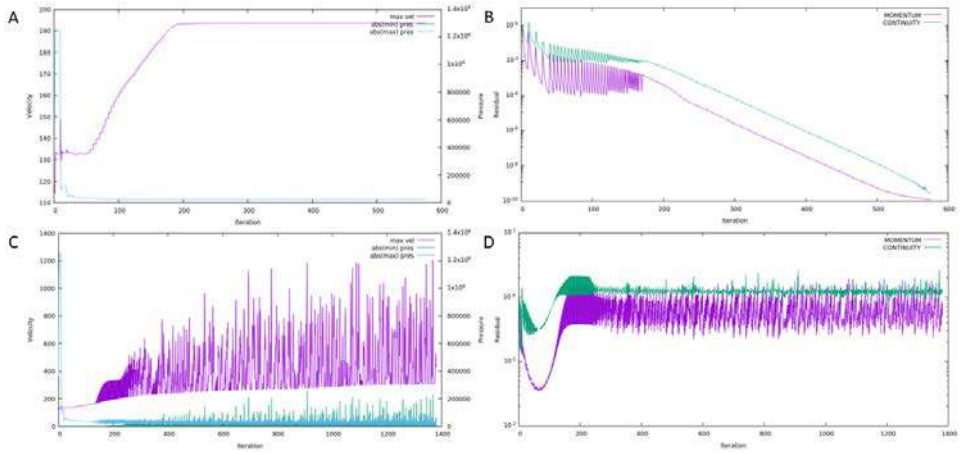

Figure 54. Convergence of Y simulation with Windkessel (A, B) and divergence of R=4000 (C, D).

Flow distribution was analyzed in Figure 55, the graph shows flows of outlet 1 and outlet 2 and the percentual difference (error) between inlets and outlets of the control volume versus Windkessel resistance.

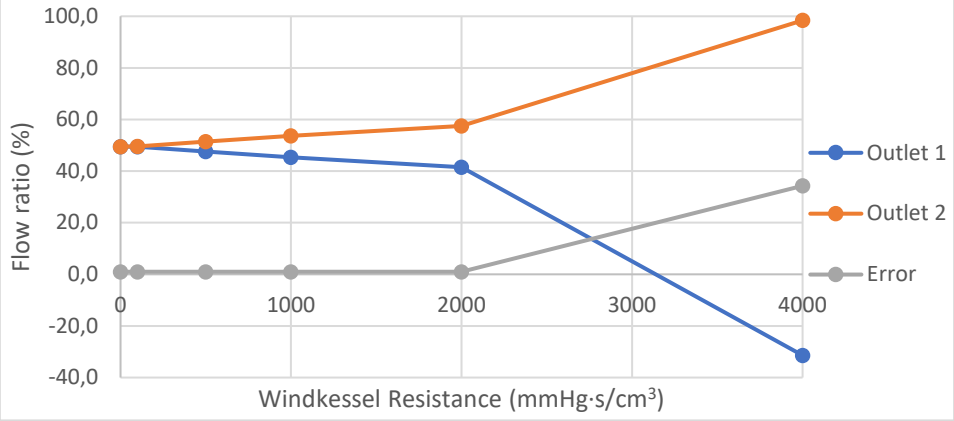

Figure 55. Outlets flow versus the Windkessel resistance.

As expected, when the resistance value was increased, flow at outlet 1 was reduced and flow at outlet 2 was increases. As discussed, the simulation diverged when the resistance was increased to 4000 mmHg·s/cm^3, with a continuity error of 31%.

Once observed that the Windkessel boundary condition could be imposed on a single geometry, it was tested on a healthy control simulation to observe changes in flow at the descending aorta. The healthy control flow ratio calculated from MRI was 70,3% and the inlet flow for the simulation was 407 ml/s. Knowing these values, the expected descending aorta flow would be 286 ml/s to match the flow ratio. Figure 56 shows the value of descending aorta flow with multiple resistance values at the descending aorta.

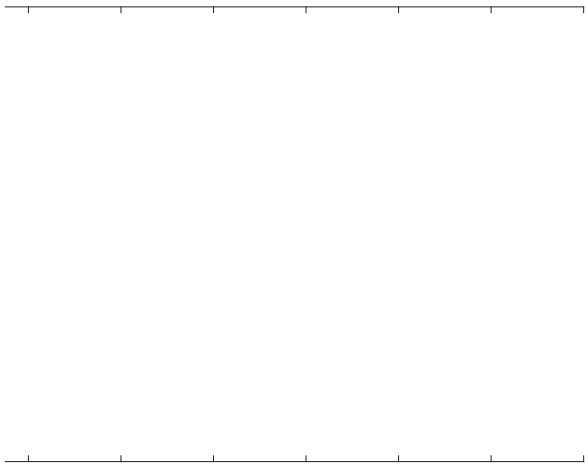

Figure 56. Flow at descending aorta using multiple Windkessel resistance values.

It can be observed in Figure 56 that the first simulation (R=0 mmHg·s/cm^3) resulted in a descending aorta flow of 309 ml/s, 23 ml/s above the expected value (error=5,6%). After trying different resistance values, a resistance of 4000 mmHg·s/cm^3 resulting in descending aorta flow of 288 ml/s, 0,5% above the expected value. Coherently, a Windkessel resistance of 4000 mmHg·s/cm^3 was imposed in further simulations for this case. This strategy was repeated for every case to match flow distribution from clinical images.

3.2.3. Pulse wave velocity

The PWV in FSI simulations was matched to that calculated from 4D-MRI images iteratively. Before the iterative process, a test was performed to observe the influence of the Young's modulus (E) times the thickness (h) on the pulse wave velocity of the simulation. Three simulations were performed with the same value of E·h calculated with Moens-Korteweg equation, Eq. 16. Values of thickness, Young's modulus and PWV are presented in Table 2.

	h [m]	E [kg/s2·m]	PWV (m/s)
1	1,00E-03	7,61E+05	6,7
2	1,50E-03	5,07E+05	6,6
3	2,00E-03	3,80E+05	6,6

Table 2. Values to test the influence of thickness in PWV.

We observed that the value of PWV was not affected by thickness if E·h remained constant. This result shows that, even if thickness is not quantified accurately from MRI images, the PWV calculated from 4D-MRI can be achieved through Young's modulus iterations.

Figure 57 shows the increment time between systolic peaks at sinotubular junction and descending aorta of a case simulated in CFD and FSI. It can be observed that in CFD simulation, the peaks are close in terms of time, while in FSI simulation the increment is tripled. If the distance between the two planes is 10 cm, PWV of CFD simulation is 16,6 m/s and in FSI simulation is 5,3 m/s. Just one case of the twelve analyzed has a PWV above 15 m/s, so seems reasonable to characterize the delay observed in medical data with FSI simulations due to flow accumulation after wall expansion and contraction.

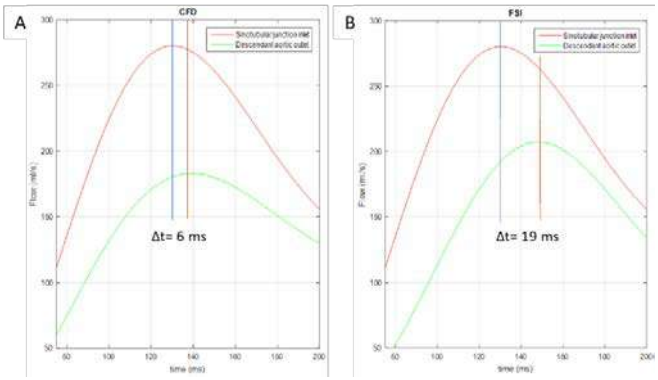

Figure 57. Delay between sinotubular junction and descending aorta with (A) CFD and (B) FSI simulations.

3.2.4. Clinical data

All clinical inputs received from Hospital Vall d'Hebron are presented in this section. They come from four healthy controls and eight Marfan patients: four of them stable over time and four of them dilating. An aneurysm is considered stable if the maximum diameter has grown less than 0.6 mm/year and is considered dilating if the maximum diameter has grown more than 0.6 mm/year.

Demographic and clinical history for each case analyzed are presented in Table 3 and Table 4 shows the averages of each group and the comparison between groups with their p-values. C1-C4 are healthy controls, S1-S4 are Marfan syndrome patients with stable aneurysms and D1-D4 are Marfan syndrome patients with dilating aneurysms.

Demographic and clinical data										
		Sex	Age [years]	Weight [kg]	Height [cm]	BSA [m2]	SBP [mmHg]	DBP [mmHg]	Diameter root [mm]	Diameter AAo [mm]
Controls	C1	Female	38	70	172	1.75	120	70	32	24
	C2	Male	30	68	175	1.83	110	63	32	28
	C3	Female	32	64	180	1.82	122	80	29	28
	C4	Female	30	58	175	1.71	123	51	26	22
Stable	S1	Male	25	98	210	2.43	150	76	43.5	31
	S2	Female	19	70	168	1.79	139	60	33	23
	S3	Male	23	90	180	2.1	121	64	37	29
	S4	Male	19	86	183	2.08	135	78	40	29
Dilating	D1	Female	22	56	180	1.72	109	60	38	51
	D2	Male	36	83	180	2.03	151	81	43	32
	D3	Female	42	59	169	1.68	125	71	35	24
	D4	Male	40	82	188	2.08	116	60	47	40

Table 3. Demographic and clinical data of four healthy controls, four stable patients and four dilating patients.

Summarized demographic and clinical data								
	Age [years]	Weight [kg]	Height [cm]	BSA [m2]	SBP [mmHg]	DBP [mmHg]	Diameter root [mm]	Diameter AAo [mm]
Control	32.5 ± 1.9	65.0 ± 2.7	176 ± 2	1.78 ± 0.03	119 ± 3	66 ± 6	29.8 ± 1.4	25.5 ± 1.5
Stable	21.5 ± 1.5	86.0 ± 5.9	185 ± 9	2.10 ± 0.13	136 ± 6	70 ± 4	38.4 ± 2.2	28.0 ± 1.7
Dilating	35.0 ± 4.5	70.0 ± 7.3	179 ± 4	1.88 ± 0.10	125 ± 9	68 ± 5	40.8 ± 2.7	36.8 ± 5.8
p values								
Control vs Stable	0,019	0,029	0,306	0,083	0,083	0,773	0,020	0,144
Control vs Dilating	0,384	0,773	0,372	0,773	0,773	0,772	0,020	0,108
Stable vs Dilating	0,081	0,083	0,767	0,110	0,386	0,767	0,564	0,146

Table 4. Average demographic and clinical history of healthy controls, stable and dilating Marfan patients.

Overall, 6 (50%) were men and 6 (50%) were women, with a mean age of 32.5±3.8 years in healthy controls, and 21.5±3.0 and 35.0±9.0 years in stable and dilating MFS patients, respectively. Age, weight, height, BSA, SBP and DBP parameters were significantly different ($p<0.05$) comparing controls versus dilating patients and between stable and dilating patients. However, age and weight were not statistically different in our small cohort comparing control versus stable patients. Remarkably, diameter at the aortic root was significantly different between control and both type of patients while it was not significantly different between stable and dilating patients. Diameter at the ascending aorta was significantly different in all cases.

3.3. Simulation analysis

This section presents the simulation process of each healthy control and Marfan patient analyzed. Main steps of the pre-process, calculus and visualization of the results are shown. Regarding the pre-process, geometry extraction from MRI images, generation of the CAD file, meshing, 4D-flow data and their treatment are presented for each case. Regarding the calculations, the convergence of each case is analyzed. Finally, regarding the post-process, velocity, pressure, shear stress, vorticity and displacement fields are shown.

Control 1

Control 1 is a 38 years old female. This healthy control is the one tested during the simulation model (3.1). Figure 58 shows the vessel geometry in an MRI image. Table 5 presents the values extracted and used in the Solidworks macro to reconstruct the vessel.

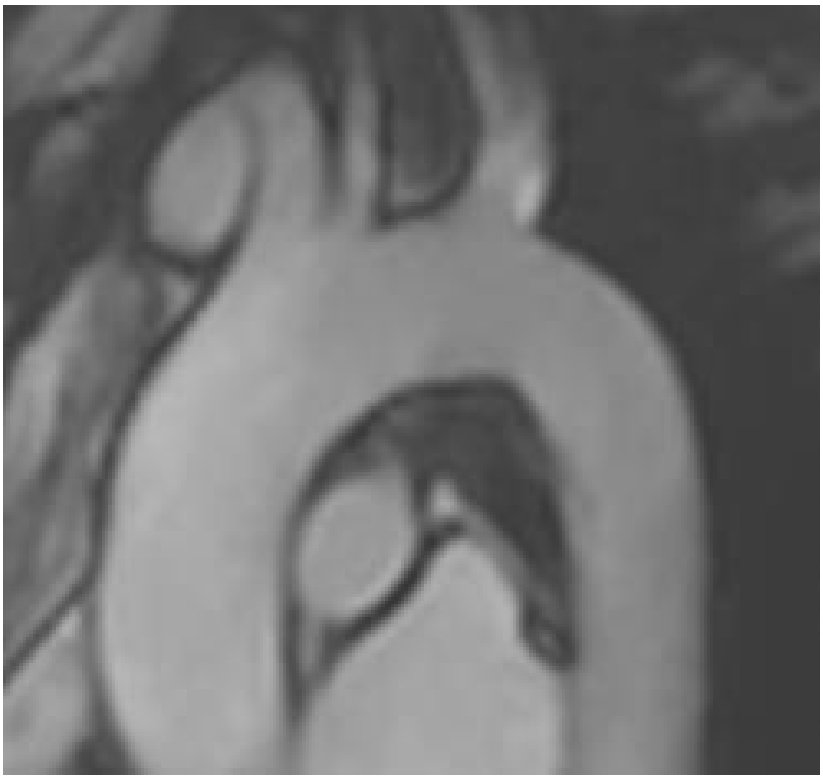

Figure 58. Visualization of C1 aorta with MRI using Mass.

	Nº Plane	X (mm)	Y (mm)	Z (mm)	R (mm)	δ (mm)
ASCENDING AORTA	1	0,0	0,0	0,0	11,6	1,5
	2	-1,2	0,0	10,0	12,3	1,5
	3	-1,6	1,0	20,0	12,5	1,5
	4	1,2	1,0	30,0	12,7	1,5
	5	3,0	0,5	35,0	13,9	1,5
AORTIC ARCH	1	21,5	4,0	52,4	11,9	1,0
	2	26,5	5,6	54,4	11,0	1,0
	3	31,5	7,0	55,4	10,4	1,0
	4	36,5	8,5	55,5	10,3	1,0
	5	41,5	10,0	54,0	10,0	1,0
DESCENDING AORTA	1	55,4	15,0	35,0	9,5	1,0
	2	56,1	15,3	30,0	9,5	1,0
	3	56,9	15,9	20,0	9,0	1,0
	4	57,3	16,5	10,0	8,5	1,0
	5	56,9	16,8	0,0	8,3	1,0

Table 5. Geometry data extracted from MRI images to reconstruct C1 aorta in SolidWorks.

Figure 59A shows the reconstruction of the vessel in green and the wall in white. Figure 59B shows the mesh of the fluid domain and Figure 59C the mesh of the solid domain.

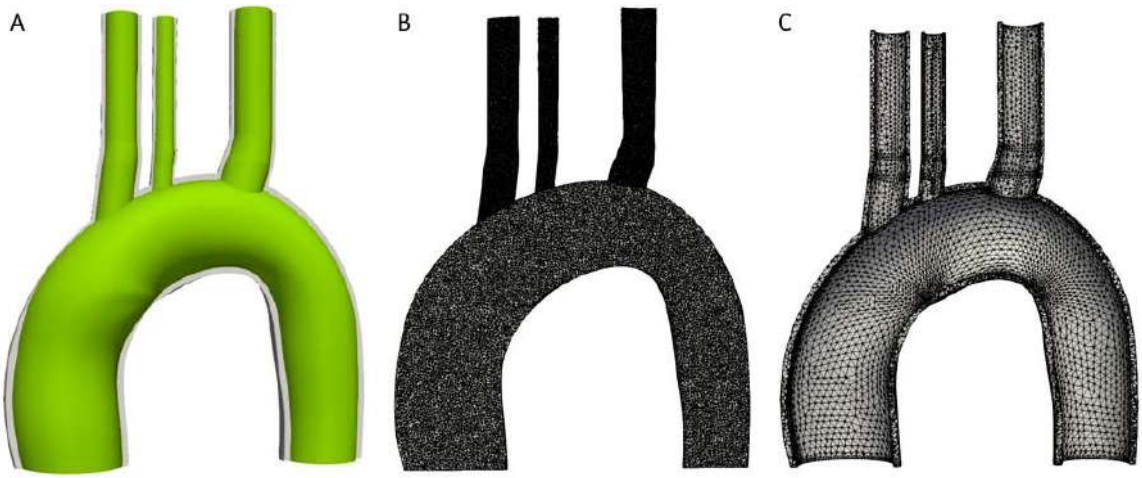

Figure 59. (A) Reconstruction of the aorta vessel and the wall, (B) meshing of the fluid and (C) meshing of the wall.

Minimum Jacobian criterion does not present negative values in the fluid mesh and neither in the solid mesh. The fluid mesh contains $1{,}94 \cdot 10^6$ elements and the solid mesh $4{,}38 \cdot 10^5$.

Figure 60 shows the flow curve at the sinotubular junction and at the descending aorta extracted from MRI images.

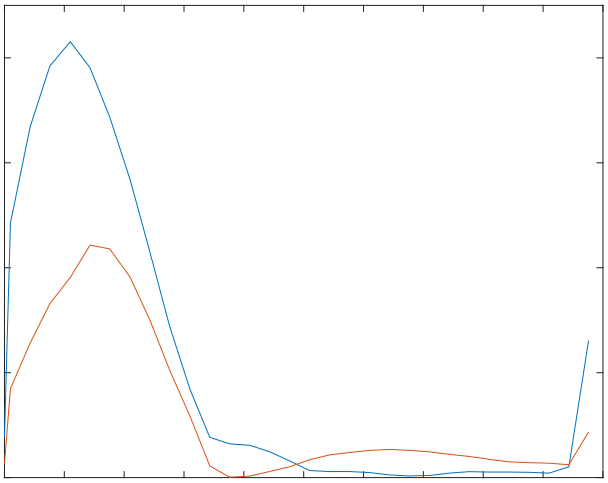

Figure 60. Flows at sinotubular junction and descending aorta of C1 from MRI images.

Figure 61 shows the flow profile extracted from 4D-MRI images and treated spatiotemporally in Matlab. The result flow curve is the inlet condition for the CFD and FSI simulations.

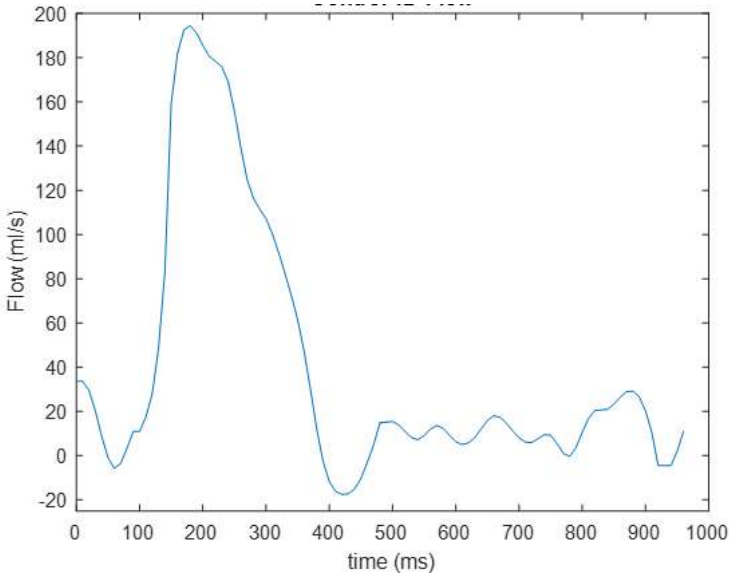

Figure 61. Sinotubular junction blood flow profile after interpolation of C1.

The convergence of this control is already shown and explained in simulation model (3.1). To sum up, CFD and FSI simulation does not diverge at any point, maximum velocity curve (Figure 45A) does not present any abnormal value and the coupling part needs between 4 to 6 coupling iterations (Figure 49C).

With both simulations converged, flow ratio between ascending and descending aorta were compared to match the simulations with clinical data. PWV cannot be compared to clinical data in C1 because no data is available, so no iterations were performed. The Young's modulus value used in C1 FSI simulation was 1E+6 $kg \cdot s^{-2} \cdot m^{-1}$. This value would have been used if the PWV value from clinical data would have been 6,5 m/s, an average value for healthy aortas[85,86].

The flow ratio between sinotubular junction and descending aorta is iterated to match the calculated MRI flow ratio with the Windkessel. First simulation (R=0 $mmHg \cdot s/cm^3$) calculated a flow in descending aorta of 127 ml/s, which results in a flow ratio of 8,6%, higher from the 57,2% expected. As flow in the descending aorta was higher, Windkessels were applied at the descending aorta surface. The flow in descending aorta decreased until an error of 5,0% and 3,9% in CFD and FSI simulations respectively. Clinical and final simulation values of flow are presented in Table 6.

CONTROL 1	Flow Sinotubular Junction (ml/s)	Flow Descending (ml/s)	Flow (%)	Error (%)
MRI	208	119	57,2%	-
CFD	193	120	62,2%	5,0%
FSI	193	118	61,1%	3,9%

Table 6. Final flows at descending aorta and flow ratio of C1.

The results of healthy control C1 were analyzed after flow ratio was matched with the clinical data. Figure 62 presents the velocity field, vorticity, wall axial and circumferential shear stresses, displacement of the wall and shear stress ratio at systolic peak (step 18).

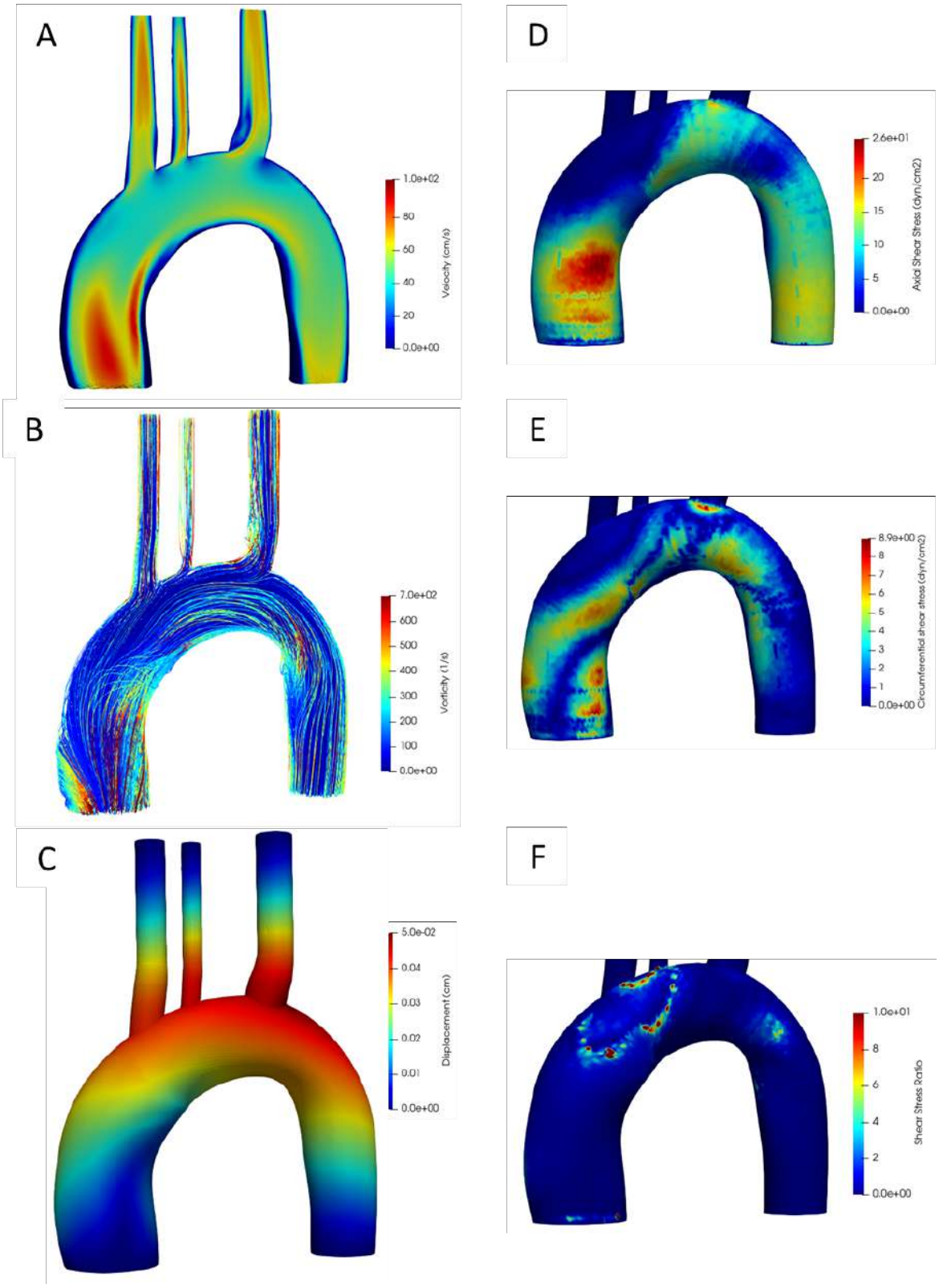

Figure 62. Fluid dynamic results of healthy control 1; (A) velocity, (B) vorticity, (C) displacement, (D) axial shear stress, (E) circumferential shear stress and (F) shear stress ratio.

Maximum velocities observed inside the aorta are 100 cm/s at systolic peak. The maximum velocity is located at the sinotubular junction, just after the valve. At the ascending aorta, the jet velocity is orientated from the center of the vessel to the exterior part of the artery. It can also be observed that no areas of low velocities (<20 cm/s) exist, except for the edges at the three upper arteries.

Vorticity streamlines are presented in Figure 62B. It can be observed that maximum vorticity values are at the initial part of the ascending aorta reaching 600 s^{-1}. The aortic arch and the descending aorta present values between 100 and 300 s^{-1} in most streamlines. At the interior part of the beginning of descending aorta, there is a small zone where vorticity reach 600 s^{-1}.

Maximum displacement is observed in the aortic arch and at the beginning of the three upper arteries with a value of 0.5 mm. It can be observed that the restriction of no displacement imposed at inlet and outlets surfaces affects impacts the displacement distribution. One would expect, when observing CINE 3D MRI sequences, that the maximum displacement happens at the sinotubular junction. This finding has been observed in all cases analyzed and is not discussed further.

Figure 62D and Figure 62E show the axial and circumferential shear stress respectively. Highest axial shear stress is observed at the anterior ascending aorta, with values of 26 dyn/cm^2. The rest of the ascending aorta present values much lower, from 0 to 5 dyn/cm^2. Circumferential shear stress also presents its highest value of 9 dyn/cm^2 at ascending aorta but not exactly at the same zone as axial shear stress. The zone of high circumferential shear stress follows the path of vorticity streamlines. Axial shear stress in the aortic arch presents a large area with values of 10-15 dyn/cm^2. The circumferential shear stress in the aortic arch is also presenting a large zone with values of 3-6 dyn/cm^2. At the descending aorta, axial shear stress presents a homogenous large area in the range of 15 dyn/cm^2. Oppositely, circumferential shear stress is close to 0 dyn/cm^2 at the descending aorta, except for interior part where values of 3 dyn/cm^2 can be observed.

Finally, the shear stress ratio presents a null value along the vessel except for two zones, the end of the ascending aorta and the initial part of the descending aorta (4 dyn/cm^2).

Control 2

Control 2 is a 30 years old male. Figure 63 shows the vessel geometry from an MRI image. Table 7 presents the values extracted and used in the SolidWorks macro to reconstruct the vessel.

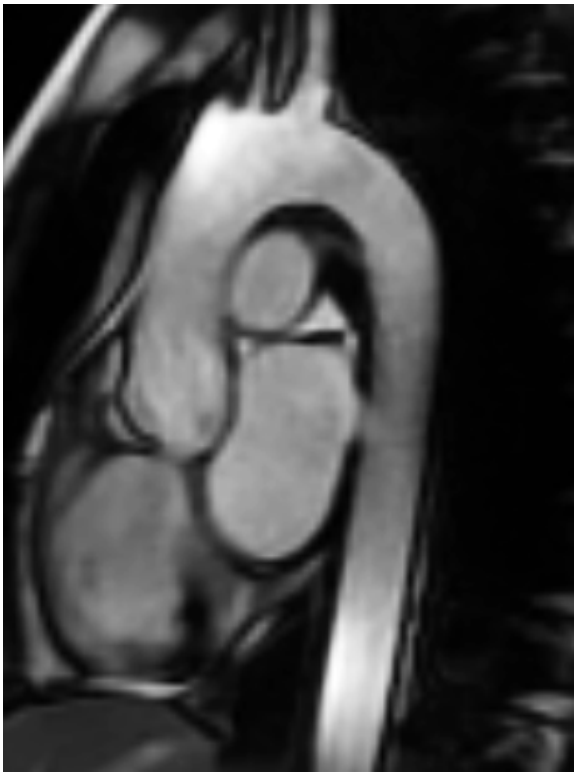

Figure 63. Visualization of C2 aorta with MRI using Mass.

	Nº Plane	X (mm)	Y (mm)	Z (mm)	R (mm)	δ (mm)
ASCENDING AORTA	1	0,0	0,0	0,0	13,5	1,5
	2	0,0	0,0	10,0	13,5	1,5
	3	2,0	2,0	20,0	13,8	1,5
	4	7,0	3,0	30,0	14,2	1,5
AORTIC ARCH	1	25,0	7,0	45,0	12,2	1,0
	2	30,0	9,4	46,6	11,7	1,0
	3	35,0	12,0	47,8	11,6	1,0
	4	40,0	14,5	48,5	11,6	1,0
	5	45,0	17,0	48,2	11,3	1,0
DESCENDING AORTA	1	61,0	23,0	35,0	11,0	1,0
	2	62,0	24,0	30,0	11,0	1,0
	3	64,0	24,0	20,0	10,5	1,0
	4	65,0	24,0	10,0	10,5	1,0
	5	63,0	24,0	0,0	10,0	1,0

Table 7. Geometry data extracted from MRI images to reconstruct C2 aorta in SolidWorks.

Figure 64A shows the reconstruction of the vessel in green and the wall in white. Figure 64B and Figure 64C show the meshes of the fluid and solid domains respectively.

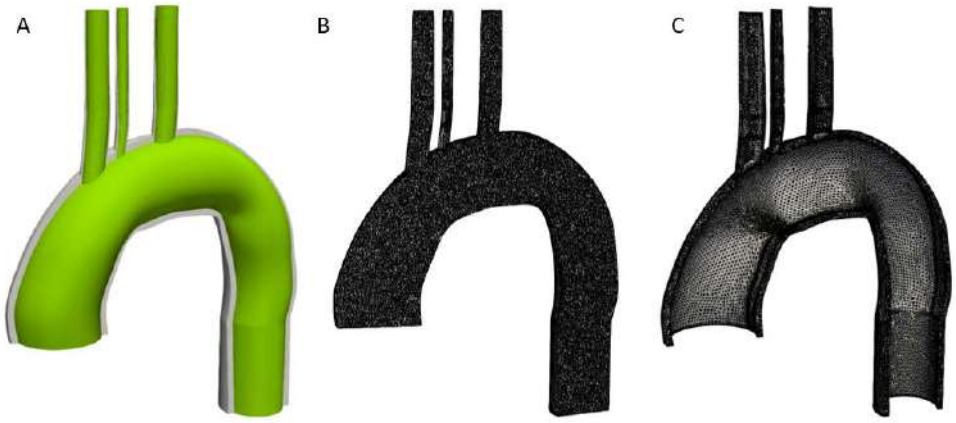

Figure 64. Reconstruction of the aorta vessel and the wall (A), meshing of the fluid (B) and the wall (C).

Minimum Jacobian criterion does not present negative values in the fluid mesh and neither in the solid mesh. The fluid mesh contains $1{,}16 \cdot 10^6$ elements and the solid mesh $4{,}51 \cdot 10^5$. Figure 65 shows the flow curve at the sinotubular junction and at the descending aorta extracted from MRI images.

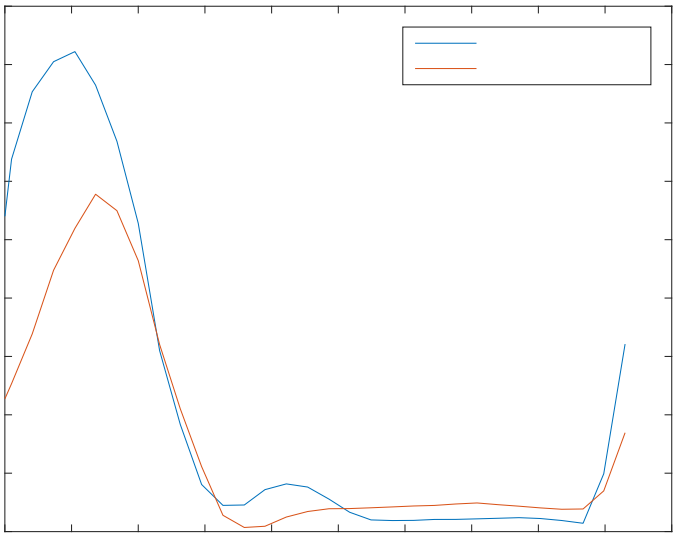

Figure 65. Flows at sinotubular junction and descending aorta of C2 with MRI technique.

Figure 66 shows the flow profile extracted from 4D-MRI images and treated spatiotemporally in Matlab. The result flow curve is the inlet condition for the CFD and FSI simulations of control 2.

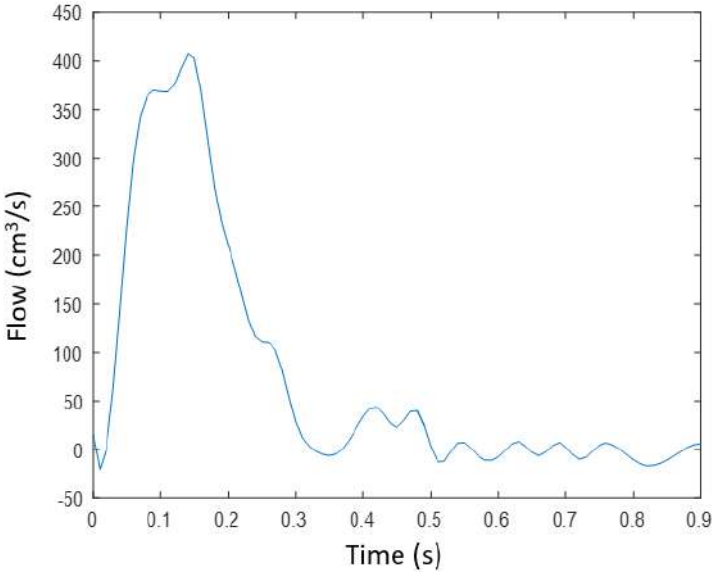

Figure 66. Flow curve of C2 at sinotubular junction after B-spline interpolation.

Smoothness in the curves are different between Figure 65 and Figure 66 flow curves, with peaks and valleys more prominent in 4D-MRI than MRI. However, the most relevant data, maximum velocity at the systolic peak and duration of systole and diastole is the same for data extracted from both types of image.

After meshing the geometry and imposing all the boundary conditions, CFD and FSI simulations are performed. FSI convergence is the one showed due to CFD convergence is similar FSI. The biggest difference is the number of iterations needed to perform all the steps, which in CFD is 800 iterations, but the velocity curve is equal, and residuals are achieved in all time steps in both simulations.

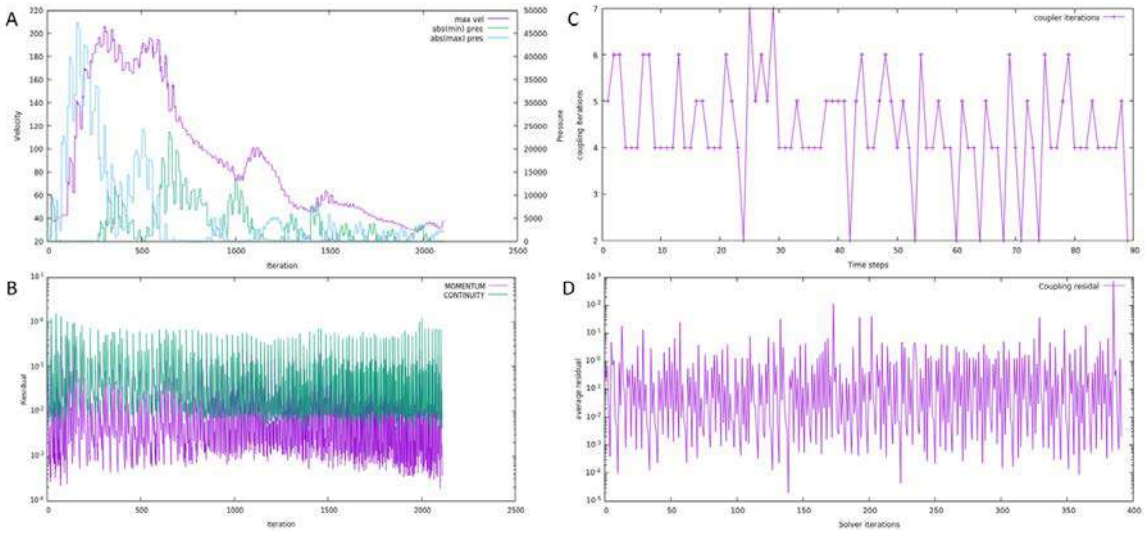

Figure 67. C2 FSI convergence of (A, B) the fluid, (C, D) the coupling.

Figure 67A shows that FSI simulation does not diverge at any point due to coherent values of maximum velocity. Figure 67B shows that all time steps reach the residual value desired and that the number of iterations per timestep is approximately 25 for systole and 10 for diastole so the continuity solver iterations are significantly affected by the cardiac cycle. For the coupling, Figure 67C and Figure 67D, it can be observed that most steps needed between 4 to 6 coupling iterations to converge and that residual is achieved in all time steps. With both simulations converged, flow ratio and PWV were compared to clinical data.

The ratio between flow at the sinotubular junction and at the descending aorta is iterated to match the flow ratio calculated from MRI data. The first simulation (R=0 mmHg·s/cm^3) calculated a flow in descending aorta of 324 ml/s, which results in a flow ratio of 75,2%, higher from the 70,3% expected. As flow in the descending aorta was higher, Windkessel boundary conditions were applied at the descending aorta surface. With a resistance of 800 mmHg·s/cm^3, flow at the descending aorta decreased until an error of 2,4% and 0,4% in CFD and FSI simulations respectively. Clinical and final simulation values for flow are presented in Table 8.

CONTROL 2	Flow Sinotubular Junction (ml/s)	Flow Descending Aorta (ml/s)	Flow ratio (%)	Error (%)
MRI	411	289	70,3%	-
CFD	407	296	72,7%	2,4%
FSI	407	288	70,8%	0,4%

Table 8. Final flows at descending aorta and flow ratio of C2.

The PWV calculated using 4D-MRI is 10,3 m/s. As seen in Table 9, three iterations were required to reduce the error below 5%.

CONTROL 2	E_0 (kg·s^{-2}·m^{-1})	PWV (m·s^{-1})	Error (%)
Clinical	-	10,3	-
Simulation 1	3,80	12,4	16,9
Simulation 2	3,16	11,6	6,9
Simulation 3	2,80	11,1	4,5

Table 9. Young's modulus iterations to match clinical PWV of C2.

Young's modulus for the first FSI simulation was estimated at 3,80 MPa after measuring 10,3 m/s as PWV from 4D-MRI date. After three iterations, a PWV value of 11,1 m/s was determined and the Young's modulus imposed was 2,80 MPa. The PWV calculated from

4D-MRI is high compared to that expected in a healthy control according to the literature. Controls generally present values of 4-6 m/s for their PWV and/or Young's moduli of 0.3-0.7 MPa[86,87].

The results of healthy control C2 were analyzed after PWV and flow ratio were matched with the clinical data. Figure 68 presents the velocity field, vorticity, wall axial and circumferential shear stresses, displacement of the wall and shear stress ratio at systolic peak (step 16). Maximum velocities observed inside the aorta are 150 cm/s at the systolic peak. The maximum velocity is located at the beginning of the brachiocephalic artery and at the exterior part of the descending aorta. At the ascending aorta, the jet velocity is 80 cm/s and is orientated from the center of the vessel to the exterior part of the artery. The increase in velocity is due to the narrowing of the artery. It can also be observed that two areas of low velocities (<30 cm/s) exist, both located at the interior parts of the ascending and descending aorta. This seems logic as the jet is oriented towards the external part.

Vorticity streamlines are presented in Figure 68B. It can be observed that maximum vorticity values are at the exterior part of the descending aorta with values reaching 1000 s^{-1}. The ascending aorta presents values between 200 and 400 s^{-1} in most streamlines. At the beginning of interior descending aorta, there are no streamlines because velocity is zero in that area. Maximum displacement is observed in the aortic arch with a value of 1.5 mm. This value represents a 7% of the radius.

Figure 68D and Figure 68E show the axial and circumferential shear stress respectively. Axial shear stress is low at most of the ascending aorta, below 10 dyn/cm^2, except for the zone where the jet impacts, where values reach 30 dyn/cm^2. Circumferential shear stress peaks at the ascending aorta is in the same region that axial shear stress, up to 12 dyn/cm^2 where the jet impacts. The rest of the ascending aorta present values between 4 and 8 dyn/cm^2, higher than axial shear stress. Axial shear stress in the aortic arch presents a large area of 20-25 dyn/cm^2 while circumferential shear stress in the aortic arch is close to 0, with an average value below 4 dyn/cm^2. At the descending aorta, axial shear stress presents a very large area in the range of 20 dyn/cm^2. Oppositely, the highest circumferential shear stress is observed at the beginning of the descending aorta (15 dyn/cm^2) and almost null elsewhere.

Finally, the shear stress ratio at ascending aorta presents a value of 4 at the initial part and a small zone with a value of 10. At the aortic arch and at the descending aorta, the shear stress ratio is 0 except for the initial part of the descending aorta where circumferential shear stress presented its higher value.

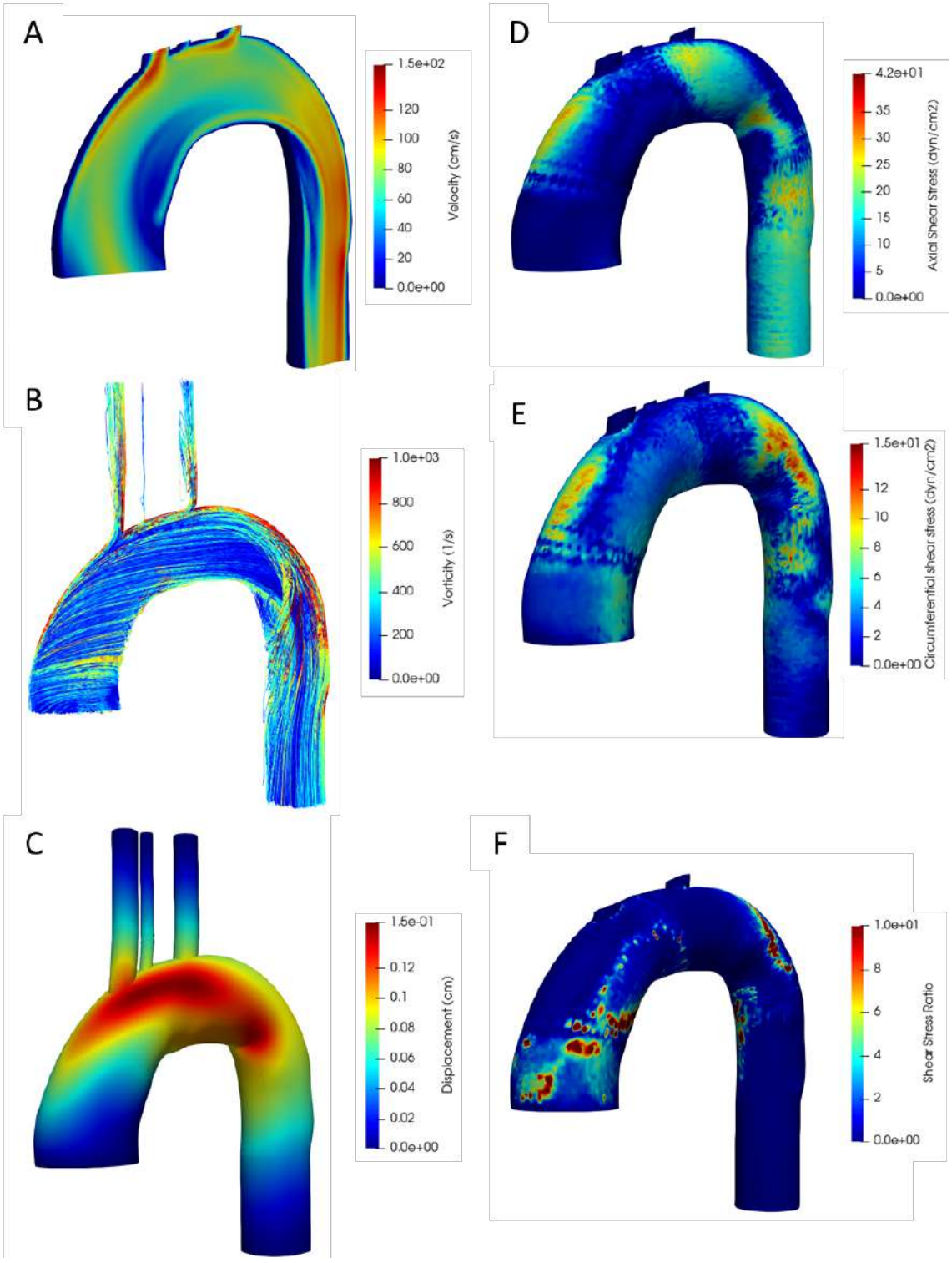

Figure 68. Fluid dynamic results of healthy control 2; (A) velocity, (B) vorticity, (C) displacement, (D) axial shear stress, (E) circumferential shear stress and (F) shear stress ratio.

Control 3

Control 3 is a 32 years old female. Figure 69 shows the vessel geometry from an MRI image. Table 10 presents the values extracted and used in the Solidworks macro to reconstruct the vessel.

Figure 69. Visualization of C3 aorta with MRI using Mass.

	Nº Plane	X (mm)	Y (mm)	Z (mm)	r (mm)	δ (mm)
ASCENDING AORTA	1	0	0	0	12,5	1,5
	2	-0,5	-2,0	10,0	13,0	1,5
	3	-0,5	-4,0	20,0	13,0	1,5
	4	0,0	-5,0	30,0	13,0	1,5
	5	2,0	-5,0	35,0	13,3	1,5
AORTIC ARCH	1	15,0	-1,6	47,7	13,0	1,0
	2	20,0	1,3	50,7	11,9	1,0
	3	25,0	4,5	51,6	11,6	1,0
	4	30,0	7,1	51,9	11,6	1,0
	5	35,0	9,4	51,9	11,4	1,0
DESCENDING AORTA	1	52,7	15,5	35,0	10,0	1,0
	2	53,0	16,0	30,0	10,0	1,0
	3	52,0	17,0	20,0	9,8	1,0
	4	51,0	18,0	10,0	9,5	1,0
	5	50,0	19,0	0,0	9,5	1,0

Table 10. Geometry data extracted from MRI images to reconstruct C3 aorta in SolidWorks.

Figure 70A shows the reconstruction of the vessel in green and the wall in white. Figure 70B shows the mesh of the fluid domain and Figure 70C the mesh of the solid domain.

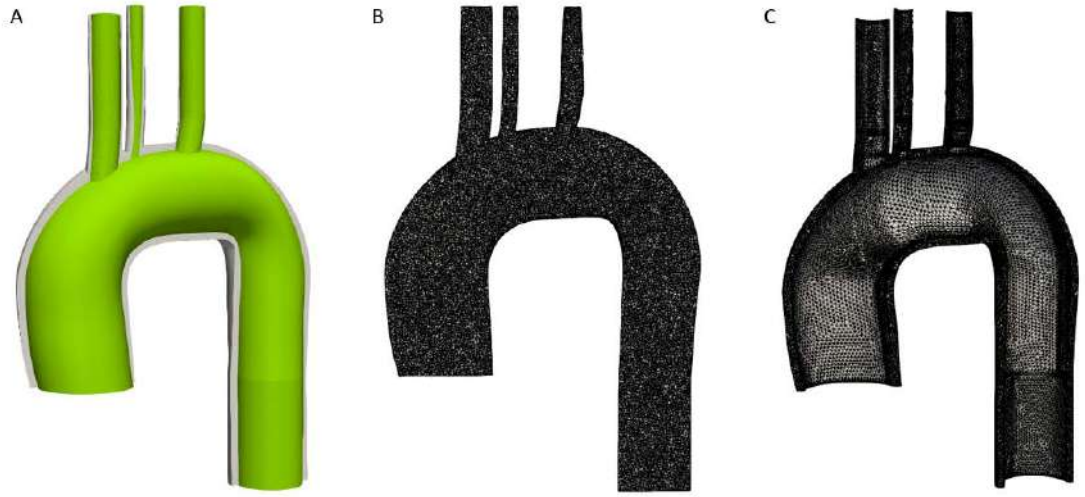

Figure 70. (A) Reconstruction of the aorta vessel and the wall, (B) meshing of the fluid and (C) meshing of the wall.

Minimum Jacobian criterion does not present negative values in the fluid mesh and neither in the solid mesh. The fluid mesh contains $1{,}12 \cdot 10^6$ elements and the solid mesh $4{,}46 \cdot 10^5$.

Figure 71 shows the flow curve at the sinotubular junction and at the descending aorta extracted from MRI.

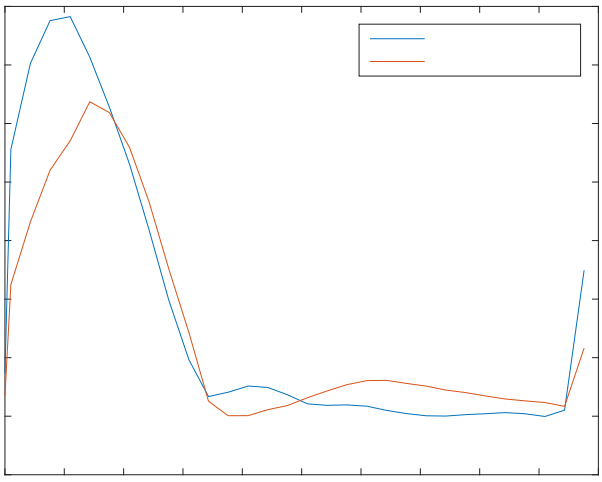

Figure 71. Flows at sinotubular junction and descending aorta of C3 with MRI technique.

Figure 72 shows the flow profile extracted from 4D-MRI images at the sinotubular junction and treated spatiotemporally in Matlab. The result flow curve is the inlet condition for the CFD and FSI simulations of healthy control 3.

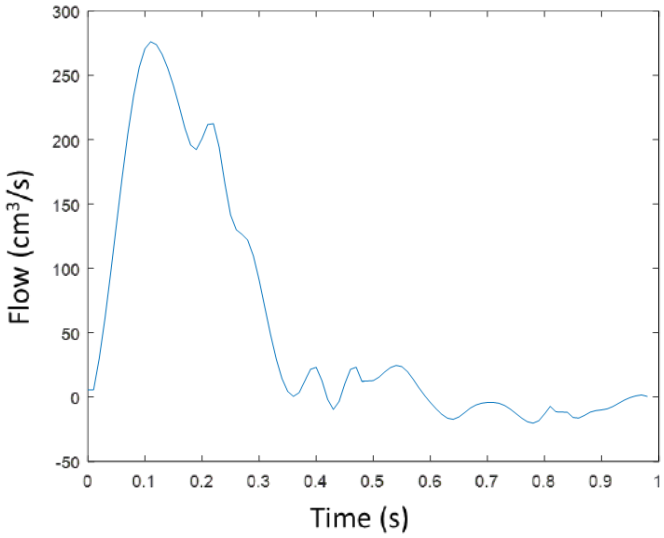

Figure 72. Flow curve of C3 at sinotubular junction after B-spline interpolation.

The difference between MRI and 4D-MRI flow profiles stand out when comparing Figure 71 and Figure 72. 4D-MRI flow profile is more sharpened and contains continuative ups and downs along the cardiac cycle, even in the systolic peak, while MRI flow profile is smoother. The duration of systolic and diastolic phases is the same in both techniques; from MRI images is 341 ml/s and from 4D-MRI is 286 ml/s.

After imposing all the boundary conditions and meshing the geometries, CFD and FSI simulations are performed. Figure 73 shows the convergence of the FSI simulation.

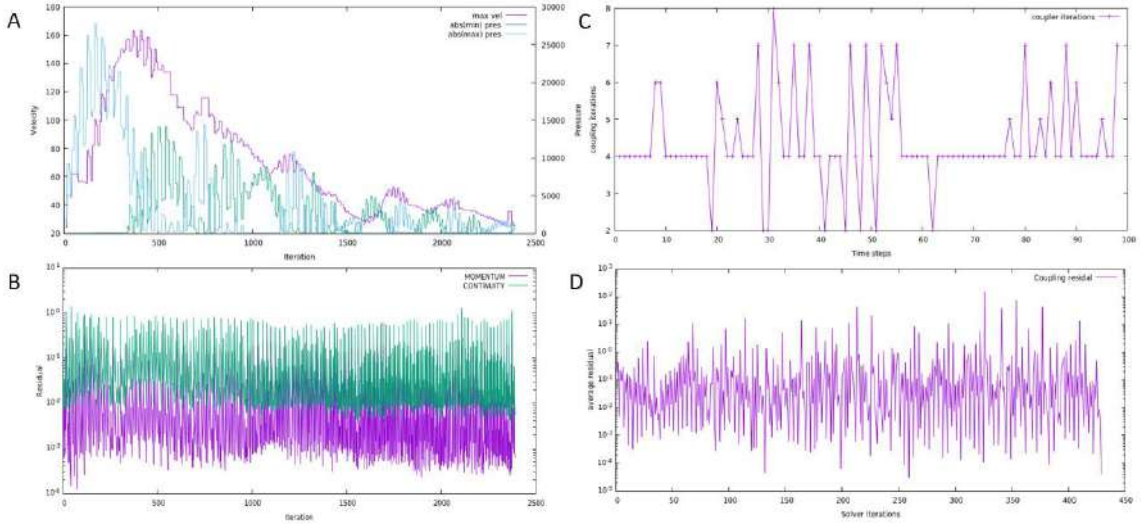

Figure 73. C3 FSI convergence of (A, B) the fluid, (C, D) the coupling.

Figure 73A shows that FSI simulation does not diverge at any point due to normal velocities along the cardiac cycle. It can also be observed that all the steps reached the residual value set and that the number of iterations per timestep was 30 for the systolic

phase and 15 for the diastolic phase (Figure 73B). Convergence of CFD simulation has the same patterns of FSI simulation, the main difference is the reduction of 2400 iterations in FSI to 700 iterations in CFD. The convergence of the coupling shows that all time steps achieved the residual value with no more than 8 coupling iterations. The mean value for coupling iterations is 4.

With both simulations converged, values from flow ratio between the ascending and the descending aorta and PWV were compared to clinical data in order to match them with the ones in the simulation. The flow ratio between sinotubular junction and descending aorta is iterated to match the calculated MRI flow ratio with the Windkessel. First simulation (R=0 mmHg·s/cm^3) calculated a flow in descending aorta of 200 ml/s, which results in a flow ratio of 72%, lower from the 79% expected. As flow in the descending aorta was lower, Windkessel was applied at the three upper arteries. The flow in descending aorta increased until an error of 2.9% and 1.7% in CFD and FSI simulations respectively. Clinical and final simulation values of flow are presented in Table 11.

Control 3	Flow Sinotubular Junction (ml/s)	Flow Descending (ml/s)	Flow ratio (%)	Error (%)
MRI	341	268	78,6%	-
CFD	276	203	73,6%	5,0%
FSI	276	206	74,6%	4,0%

Table 11. Final flows at descending aorta and flow ratio of C3.

The PWV calculated using 4D-MRI is 6.3 m/s. Two iterations were required to reduce the error value below 5%. The values of the iterations can be seen in Table 12.

Control 3	E_0 (MPa)	PWV (m·s^{-1})	Error (%)
Clinical	-	6,3	-
Simulation 1	0,90	6,8	7,9%
Simulation 2	0,97	6,6	4,8%

Table 12. Young's modulus iterations to match clinical PWV of C3.

Young modulus for the first FSI simulation was estimated at 0,90 MPa after measuring 6,3 m/s as PWV from 4D-MRI data. After two iterations, the PWV value of 6,6 m/s was accepted and the Young's modulus of 0,97 MPa. The results of healthy control 3 were analyzed after PWV and flow ratio were matched with the clinical data. Figure 74

presents the velocity field, vorticity, wall axial and circumferential shear stresses, displacement of the wall and shear stress ratio at systolic peak (step 13).

Maximum velocities observed inside the aorta are 100 cm/s at systolic peak. The maximum velocity is located at the exterior parts of the ascending and the descending aorta. At the ascending aorta, the jet velocity is 70 cm/s and is orientated from the center of the vessel to the exterior part of the artery. It can also be observed that two areas of low velocities (<20 cm/s) exist, both located at the interior parts of the ascending and descending aorta. This seems logic as the jet is oriented towards the external part.

Vorticity streamlines are presented in Figure 74B. It can be observed that maximum vorticity values are at the exterior part of the ascending aorta with values reaching 900 s^{-1}. However, most of the ascending aorta presents values much lower, between 200 and 400 s^{-1}. Along the descending aorta values of vorticity increase until 600 s^{-1}.

Maximum displacement is observed in the aortic arch and at the beginning of descending aorta with a value of 1 mm. This value represents a 5% of the diameter.

Figure 74D and Figure 74E show the axial and circumferential shear stress respectively. Axial shear stress is low at most of the ascending aorta, values less than 5 dyn/cm^2, except for the zone where the jet impacts, where values reach 23 dyn/cm^2. Circumferential shear stress at the whole ascending aorta is below 4 dyn/cm^2. Axial and circumferential shear stress in the aortic arch presents a small area of 18-22 dyn/cm^2 and 6-8 dyn/cm^2 respectively. At the descending aorta, axial shear stress presents a very large area in the range of 15 dyn/cm^2. Oppositely, the circumferential shear stress is almost null in the whole descending aorta.

Finally, the shear stress ratio presents null values in most of the domain. This seems logic due to circumferential shear stress presents low values along the entire aorta. There are just two small areas located at the beginning and at the final parts of the aortic arch where shear stress ratio presents values from 8 to 10.

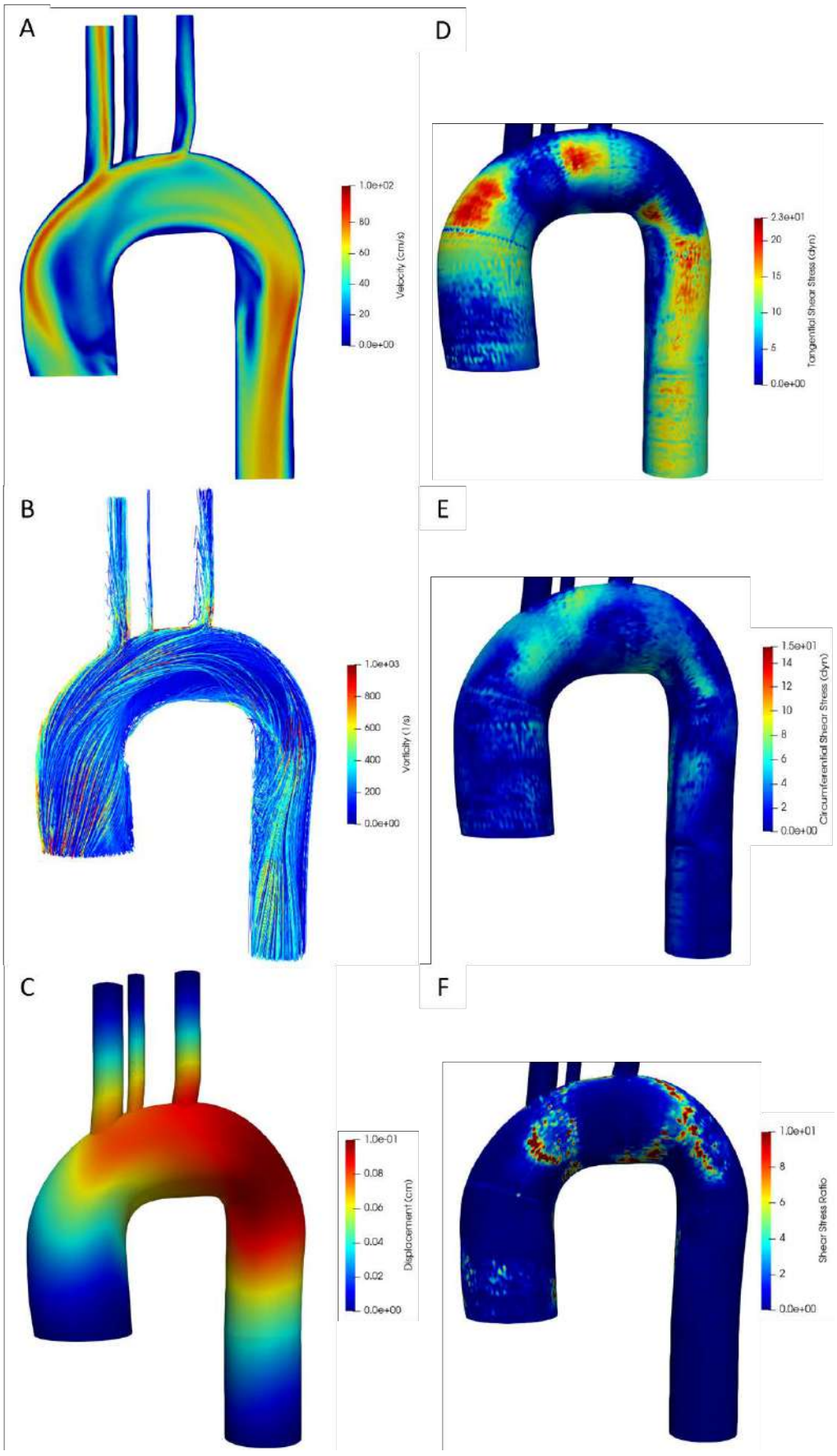

Figure 74. Fluid dynamic results of healthy control 3; (A) velocity, (B) vorticity, (C) displacement, (D) axial shear stress, (E) circumferential shear stress and (F) shear stress ratio.

Control 4

Control 4 is a 30 years old female. Figure 75 shows the vessel geometry from an MRI image. Table 13 presents the values extracted and used in the Solidworks macro to reconstruct the vessel.

Figure 75. Visualization of C4 aorta with MRI using Mass.

	Nº Plane	X (mm)	Y (mm)	Z (mm)	r (mm)	δ (mm)
ASCENDING AORTA	1	0,0	0,0	0,0	12,5	1,5
	2	0,0	0,0	10,0	12,5	1,5
	3	1,5	2,0	20,0	12,8	1,5
	4	3,0	4,0	30,0	12,8	1,5
	5	4,6	4,9	35,0	12,6	1,5
AORTIC ARCH	1	19,0	9,1	45,9	11,8	1,0
	2	24,0	13,0	49,4	11,5	1,0
	3	30,0	15,5	50,0	11,2	1,0
	4	35,0	18,4	49,4	11,0	1,0
DESCENDING AORTA	1	49,0	17,2	35,0	10,8	1,0
	2	49,0	16,0	30,0	10,5	1,0
	3	49,0	15,0	20,0	10,5	1,0
	4	48,5	14,0	10,0	10,5	1,0
	5	48,0	13,0	0,0	10,2	1,0

Table 13. Geometry data extracted from MRI images to reconstruct C4 aorta in SolidWorks.

Figure 76A shows the reconstruction of the vessel in green and the wall in white. Figure 76B shows the mesh of the fluid domain and Figure 76C the mesh of the solid domain.

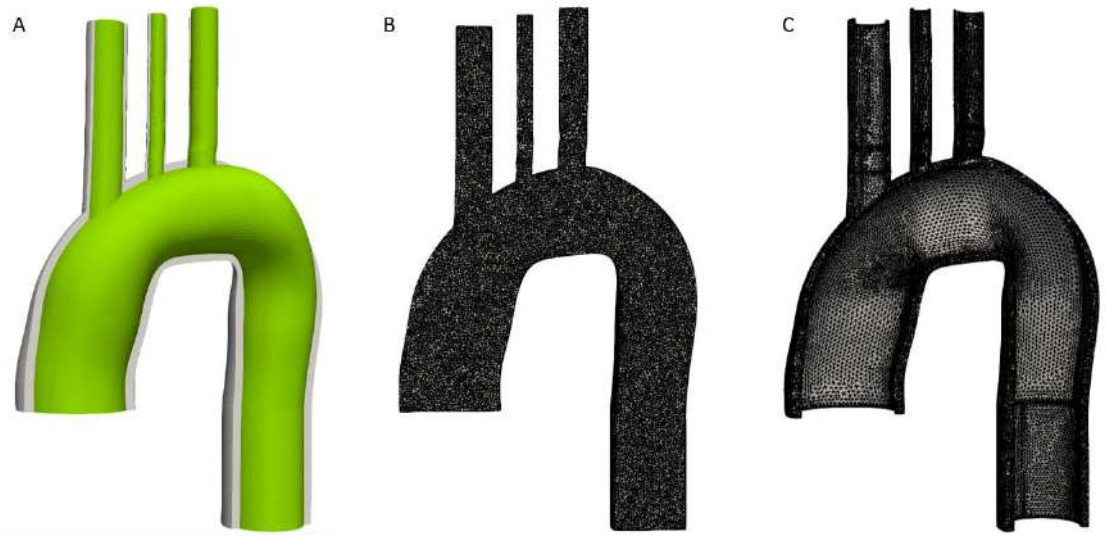

Figure 76. (A) Reconstruction of the aorta vessel and the wall, (B) meshing of the fluid and (C) meshing of the wall.

Minimum Jacobian criterion does not present negative values in the fluid mesh and neither in the solid mesh. The fluid mesh contains $1{,}02 \cdot 10^6$ elements and the solid mesh $4{,}17 \cdot 10^5$.

Figure 77 shows the flow curve at the sinotubular junction and descending aorta extracted from the MRI images.

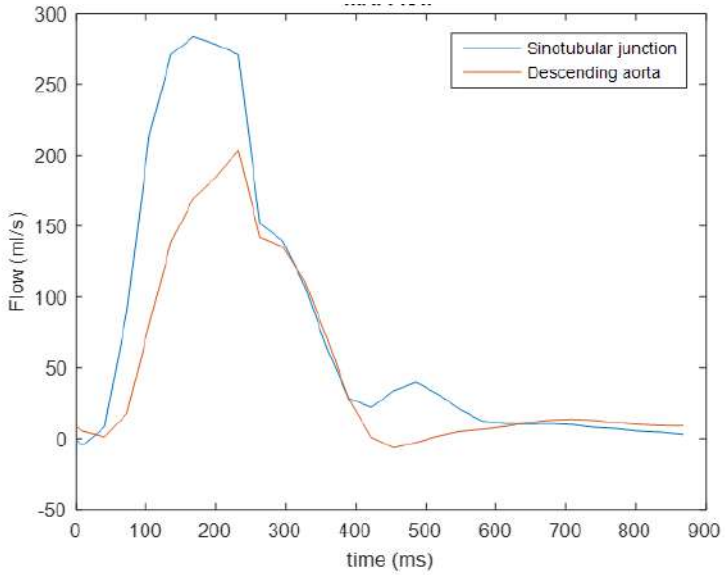

Figure 77. Flows at sinotubular junction and descending aorta with MRI technique of C4.

Figure 78 shows the flow profile extracted from 4D-MRI images at sinotubular junction and treated spatiotemporally in Matlab. The result flow curve is the inlet condition for the CFD and FSI simulations of healthy control 4.

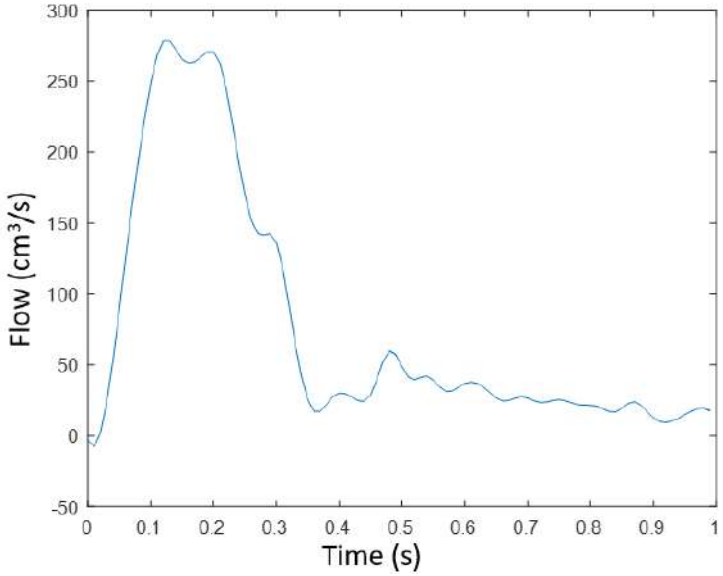

Figure 78. Flow curve of C4 at sinotubular junction after B-spline interpolation.

The flow profiles between MRI and 4D-MRI are similar when comparing Figure 77 and Figure 78. The duration of systolic phase is the same in both techniques, but diastolic phase is 100 ms longer in 4D-MRI. Maximum flow observed with both techniques is 284 ml/s from MRI and 270 ml/s from 4D-MRI.

After imposing all the boundary conditions and meshing the geometries, CFD and FSI simulations are performed. Figure 79 shows the convergence of the FSI simulation.

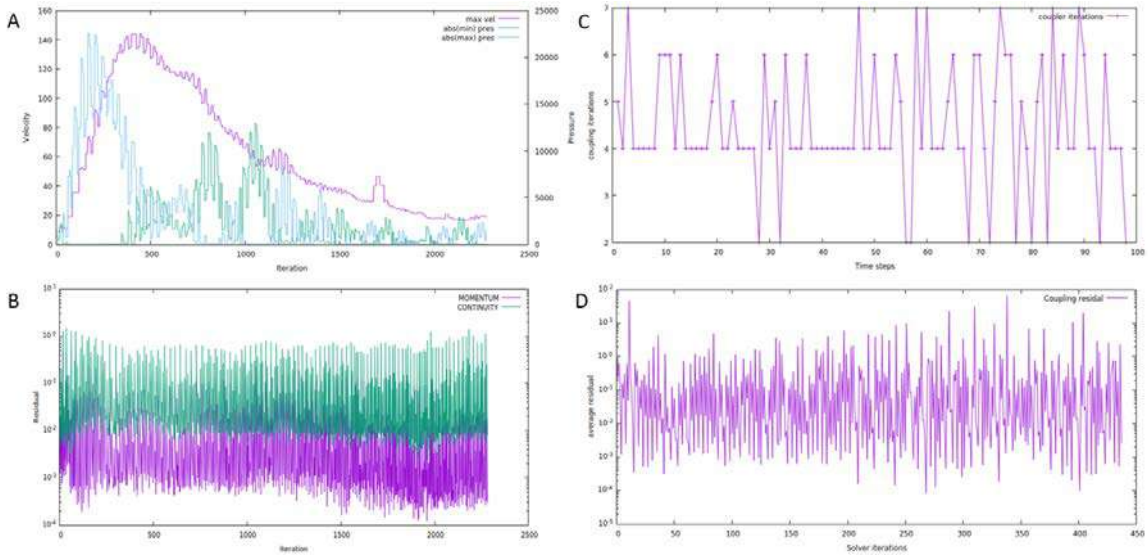

Figure 79. C4 FSI convergence of (A, B) the fluid, (C, D) the coupling.

Figure 79A shows that FSI simulation does not diverge at any point due to coherent values of maximum velocity. Figure 79B shows that all time steps reach the residual value desired and that the number of iterations per timestep is approximately 35 for systole and 15 for diastole. For the coupling, Figure 79C and Figure 79D, it can be observed that most steps needed between 4 to 6 coupling iterations to converge and that residual is achieved in all time steps. With both simulations converged, flow ratio and PWV were compared to clinical data.

The first FSI simulation (R=0 mmHg·s/cm^3) calculated a flow in descending aorta of 198 ml/s, which results in a flow ratio of 73,3%, close to the 72,2% expected. As the error is below 5% without Windkessel, this boundary condition has not been applied in healthy control C4. Flow at the descending aorta in CFD without Windkessel is 203 ml/s which results in a flow ratio of 75,2%. The error in CFD is 3%, also below 5%. Clinical and final simulation values for flow are presented in Table 8. Although differences exist between flow at the sinotubular junction measured with MRI versus simulations, the final flow ratio error was below 1% error.

Control 4	Flow Sinotubular Junction (ml/s)	Flow Descending (ml/s)	Flow ratio (%)	Error (%)
MRI	284	205	72,2%	-
CFD	270	203	75,2%	3,0%
FSI	270	198	73,3%	1,2%

Table 14. Final flows at descending aorta and flow ratio of C4.

The PWV calculated using 4D-MRI is 5,8 m/s. Three iterations were required to reduce the error value below 5%. The values of the iterations can be seen in Table 15.

CONTROL 4	E_0 (MPa)	PWV (m·s^{-1})	Error (%)
Clinical	-	5,8	-
Simulation 1	0,65	6,4	10,30%
Simulation 2	0,60	6,1	5,20%
Simulation 3	0,58	6	3,40%

Table 15. Young's modulus iterations to match clinical PWV of C4.

Young modulus for the first FSI simulation was estimated at 0,65 MPa after measuring 5,8 m/s as PWV from 4D-MRI data. After three iterations, the PWV value of 6,0 m/s was accepted and the Young's modulus of 0,58 MPa.

The results of healthy control 4 were analyzed after PWV and flow ratio were matched with the clinical data. Figure 80 presents the velocity field, vorticity, wall axial and circumferential shear stresses, displacement of the wall and shear stress ratio at systolic peak (step 12).

Maximum velocities observed inside the aorta are 110 cm/s at systolic peak. The maximum velocity is located at the brachiocephalic artery and at the exterior parts of the ascending and the descending aorta. At the ascending aorta, the jet velocity is 80 cm/s and is orientated from the center of the vessel to the exterior part of the artery. Three areas of low velocities (<20 cm/s) can be observed at the interior part of ascending aorta, aortic arch and descending aorta, logic as the jet is oriented towards the external part.

Vorticity streamlines are presented in Figure 80B. It can be observed that maximum vorticity values are at the exterior part of the aortic arch with values reaching 1000 s^{-1}. However, most of the ascending aorta presents values much lower, between 300 and 400 s^{-1}. The descending aorta presents a vorticity of 400 to 800 s^{-1}. Maximum displacement is observed at the initial part of descending aorta reaching values of 2 mm.

Figure 80D and Figure 80E show the axial and circumferential shear stress respectively. Axial shear stress presents values of 10-15 dyn/cm^2 at the external part of ascending aorta, where velocity is higher. Circumferential shear stress at the whole ascending aorta is below 4 dyn/cm^2 expect for a small zone of 6 dyn/cm^2. At aortic arch, axial shear stress presents a large area of 15 dyn/cm^2 while circumferential shear stress presents values below 2 dyn/cm^2. At the descending aorta, axial shear stress presents a very large area between 15 and 20 dyn/cm^2. Oppositely, the circumferential shear stress is almost null in the whole descending aorta expect for the initial part with an area of 6 dyn/cm^2.

The shear stress ratio is presented in Figure 80F. Null values are observed in most of the domain. This seems logic due to circumferential shear stress presents low values along the entire aorta. There are just two small areas located at the external part of aortic arch and at the interior part of descending aorta that present values above 2.

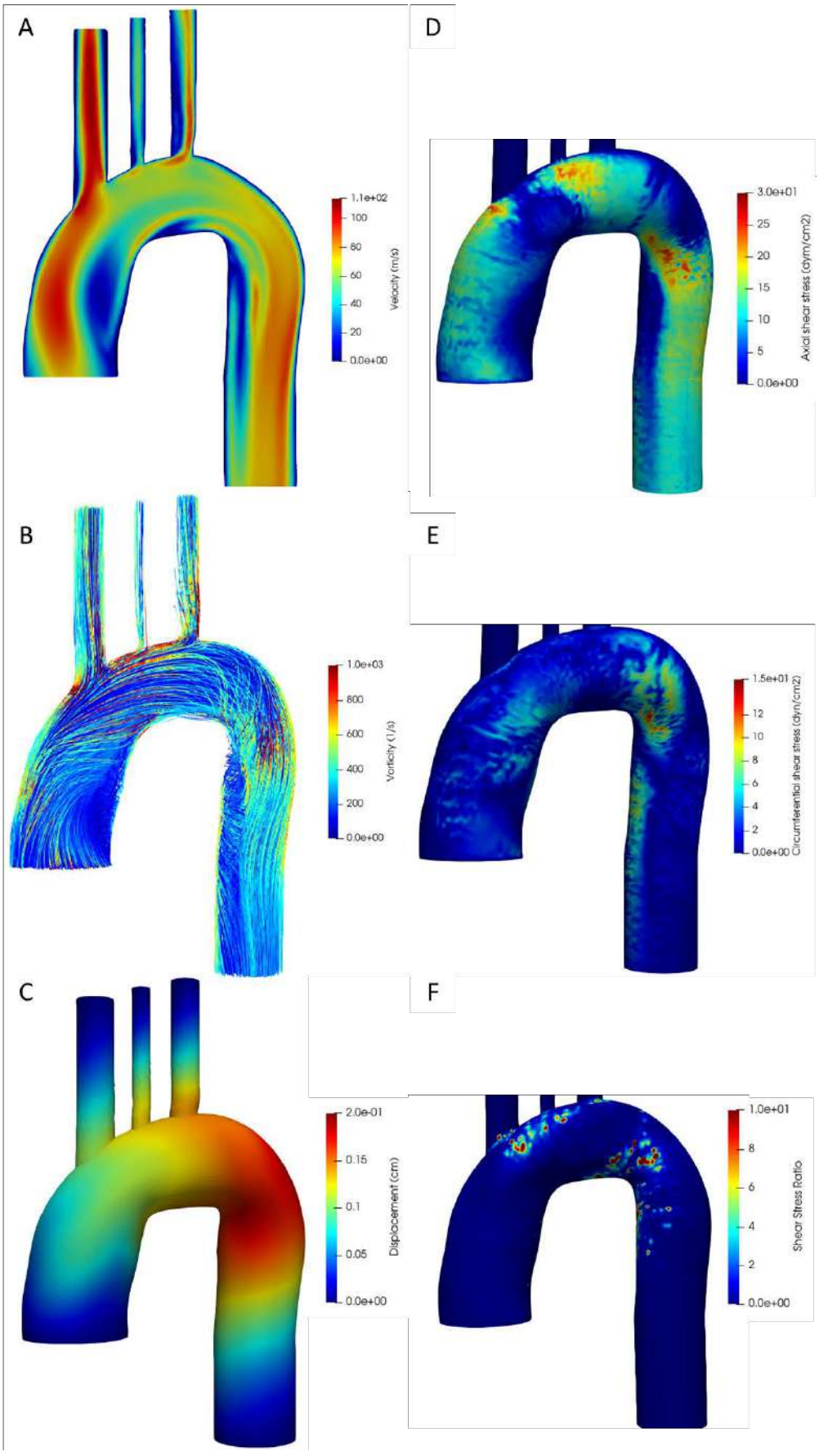

Figure 80. Fluid dynamic results of healthy control 4; (A) velocity, (B) vorticity, (C) displacement, (D) axial shear stress, (E) circumferential shear stress and (F) shear stress ratio.

Stable 1

Stable 1 is a 25 years old male. Figure 81 shows the vessel geometry from an MRI image. Table 16 presents the values extracted and used in the Solidworks macro to reconstruct the vessel.

Figure 81. Visualization of S1 aorta with MRI using Mass.

	Nº Plane	X (mm)	Y (mm)	Z (mm)	r (mm)	δ (mm)
ASCENDING AORTA	1	0,0	0,0	0,0	15,2	1,5
	2	-4,0	0,0	10,0	14,8	1,5
	3	-6,0	0,0	20,0	14,8	1,5
	4	-5,5	0,0	30,0	14,8	1,5
	5	-2,5	0,0	40,0	14,6	1,5
AORTIC ARCH	1	20,0	8,0	69,7	12,1	1,5
	2	25,0	12,5	72,5	12,1	1,5
	3	30,0	14,8	75,0	12,1	1,5
	4	35,0	16,7	75,0	12,1	1,5
	5	40,0	19,0	75,6	12,1	1,5
DESCENDING AORTA	1	67,8	30,1	40,0	12,1	1,5
	2	66,2	32,5	30,0	12,0	1,5
	3	65,5	33,5	20,0	11,6	1,5
	4	64,9	34,0	10,0	11,0	1,5
	5	65,0	34,0	0,0	11,0	1,5

Table 16. Geometry data extracted from MRI images to reconstruct S1 aorta in SolidWorks.

Figure 82A shows the reconstruction of the vessel in green and the wall in white. Figure 82B shows the mesh of the fluid domain and Figure 82C the mesh of the solid domain.

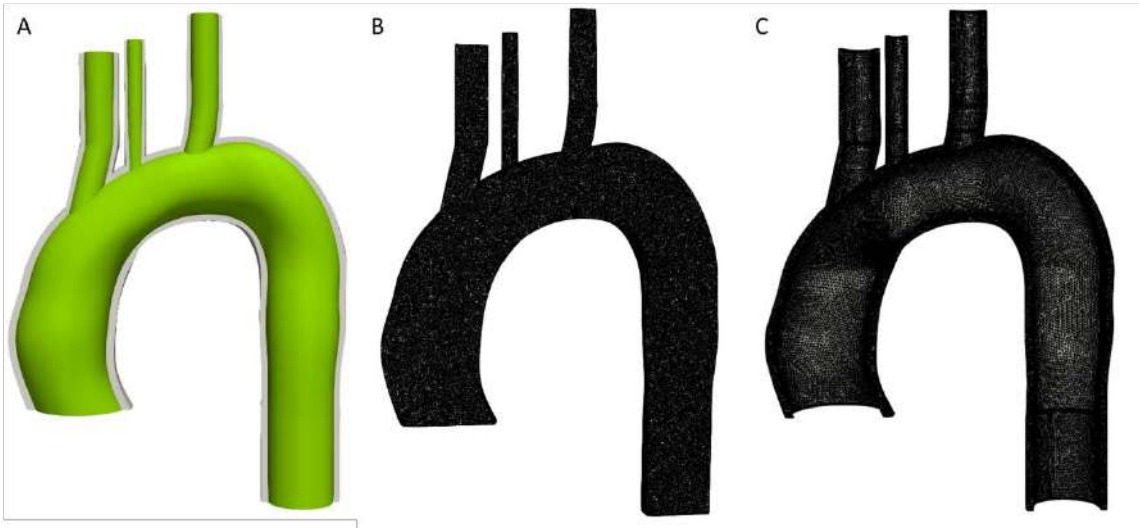

Figure 82. (A) Reconstruction of the aorta vessel and the wall, (B) meshing of the fluid and (C) meshing of the wall.

Minimum Jacobian criterion does not present negative values in the fluid mesh and neither in the solid mesh. The fluid mesh contains $1{,}16 \cdot 10^6$ elements and the solid mesh $4{,}34 \cdot 10^5$.

Figure 83 shows the flow curve at sinotubular junction and descending aorta extracted from MRI images.

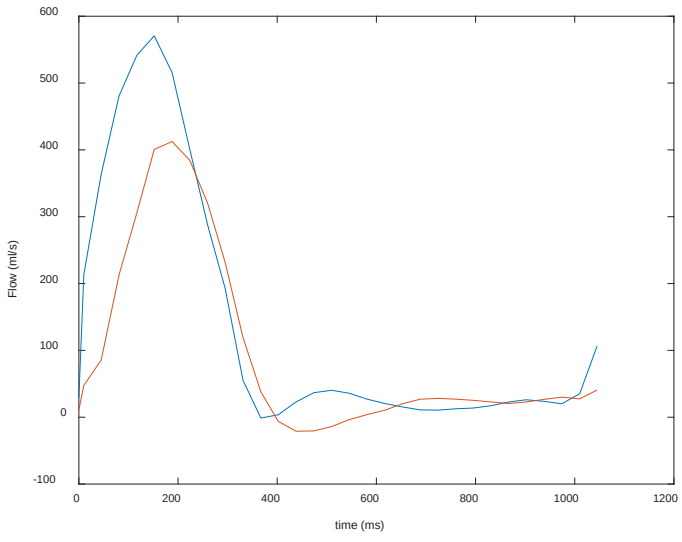

Figure 83. Flows at sinotubular junction and descending aorta of S1 with MRI technique.

Figure 84 shows the flow profile extracted from 4D-MRI images at sinotubular junction and treated spatiotemporally in Matlab. The result flow curve is the inlet condition for the CFD and FSI simulations of stable patient 1.

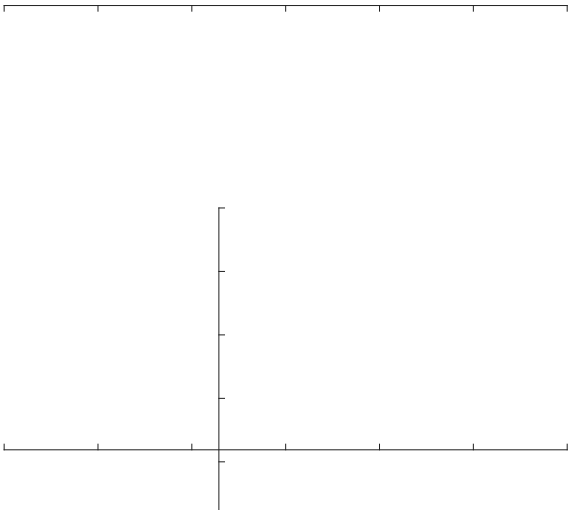

Figure 84. Flow curve of S1 at sinotubular junction after B-spline interpolation.

The flow profiles between MRI and 4D-MRI are different when comparing Figure 83 and Figure 84. The duration of systolic phase is the same in both techniques, but diastolic phase is 50 to 100 ms longer in 4D-MRI. Maximum flow observed with both techniques differs 40 ml/s and the negative diastolic peak just appears in 4D-MRI.

After imposing all the boundary conditions and meshing the geometries, CFD and FSI simulations are performed. Figure 85 shows the convergence of the FSI simulation.

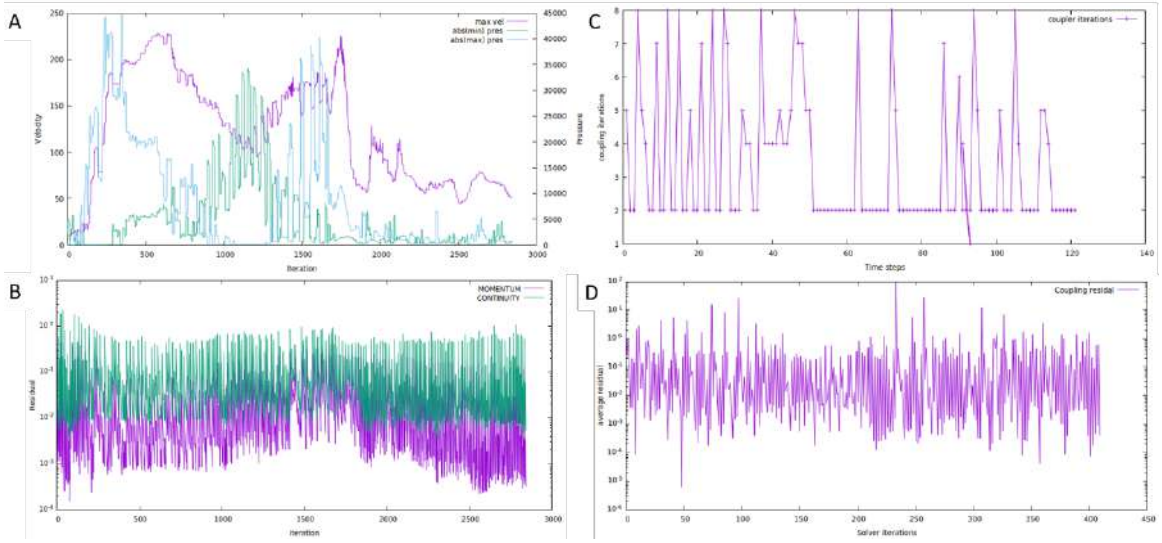

Figure 85. S1 FSI convergence of (A, B) the fluid, (C, D) the coupling.

Figure 85A shows that FSI simulation does not diverge at any point due to coherent values of maximum velocity. However, from iteration 1300 to 1800, the system struggles to converge the first diastolic steps because of high negative inflow. Figure 85B shows that all time steps reach the residual value desired. For the coupling, Figure 85C and Figure 85D, it can be observed that most steps needed between 2 to 8 coupling iterations to converge and that residual is achieved in all time steps. With both simulations converged, flow ratio and PWV were compared to clinical data.

The flow ratio between the sinotubular junction and the descending aorta is iterated to match the flow ratio calculated from MRI data. The first FSI simulation (R=0 mmHg·s/cm^3) calculated a flow in descending aorta of 377 ml/s, which results in a flow ratio of 71,0%, close to the 72,3% expected. As the error is below 5% without Windkessel, this boundary condition has not been applied in stable patient 1. Flow at the descending aorta in CFD without Windkessel is 373 ml/s which results in a flow ratio of 70,2%. The error in CFD is also below 5%. Clinical and final simulation values for flow are presented in Table 17.

Stable 1	Flow Sinotubular Junction (ml/s)	Flow Descending (ml/s)	Flow ratio (%)	Error (%)
MRI	570	412	72,3%	-
CFD	531	373	70,2%	2,0%
FSI	531	377	71,0%	1,3%

Table 17. Final flows at descending aorta and flow ratio of S1.

The PWV calculated using 4D-MRI is 11,0 m/s. Two iterations were required to reduce the error value below 5%. The values of the iterations can be seen in Table 18.

Stable 1	E_0 (MPa)	PWV (m·s^{-1})	Error (%)
Clinical	-	11,0	-
Simulation 1	4,22	12,3	11,8
Simulation 2	3,86	11,6	5,2

Table 18. Young's modulus iterations to match clinical PWV of S1.

Young's modulus for the first FSI simulation was estimated at 4,2 MPa after measuring 11,0 m/s as PWV from 4D-MRI data. After two iterations, the PWV value of 11,6 m/s was accepted and the Young's modulus of 3,8 MPa.

The results of stable patient 1 were analyzed after PWV and flow ratio were matched with the clinical data. Figure 86 presents the velocity field, vorticity, wall axial and circumferential shear stresses, displacement of the wall and shear stress ratio at systolic peak (step 20).

Maximum velocity observed inside the aorta is 220 cm/s at systolic peak and is located at the brachiocephalic artery. At the ascending aorta, the jet velocity is 120 cm/s and is centered. Two areas of low velocities (<30 cm/s) can be observed at the interior part of ascending aorta and descending aorta.

Vorticity streamlines are presented in Figure 86B. It can be observed that maximum vorticity values are at the aortic arch and its bifurcations with values reaching 1000 s^{-1}. The ascending aorta presents values much lower, between 100 and 200 s^{-1}. The zone of low velocity at the beginning of descending aorta presents high vorticity with values of 600 and 800 s^{-1}.

Maximum displacement is observed at the initial part of the aortic arch reaching values of 1,2 mm. It can be observed that the restriction of no displacement imposed at inlet and outlets surfaces is affecting the whole aorta with less realistic results.

Figure 86D and Figure 86E show the axial and circumferential shear stress respectively. Axial shear stress present values of 20 dyn/cm^2 at the external part of ascending aorta, where velocity is higher. Circumferential shear stress is also presenting high values of 10 dyn/cm^2 at external part. At aortic arch, axial shear stress presents a large area of 35 dyn/cm^2 while circumferential shear stress presents a small zone of 17 dyn/cm^2. At the descending aorta, axial shear stress presents a very large area between 15 and 25 dyn/cm^2. Oppositely, the circumferential shear stress is almost null in the whole descending aorta.

The shear stress ratio is presented in Figure 86F. Null values are observed in most of the domain. This seems logic due to circumferential shear stress presents low values along the entire aorta. There are just small areas located at the initial part of the aortic arch and at the beginning part of descending aorta that present values above 4.

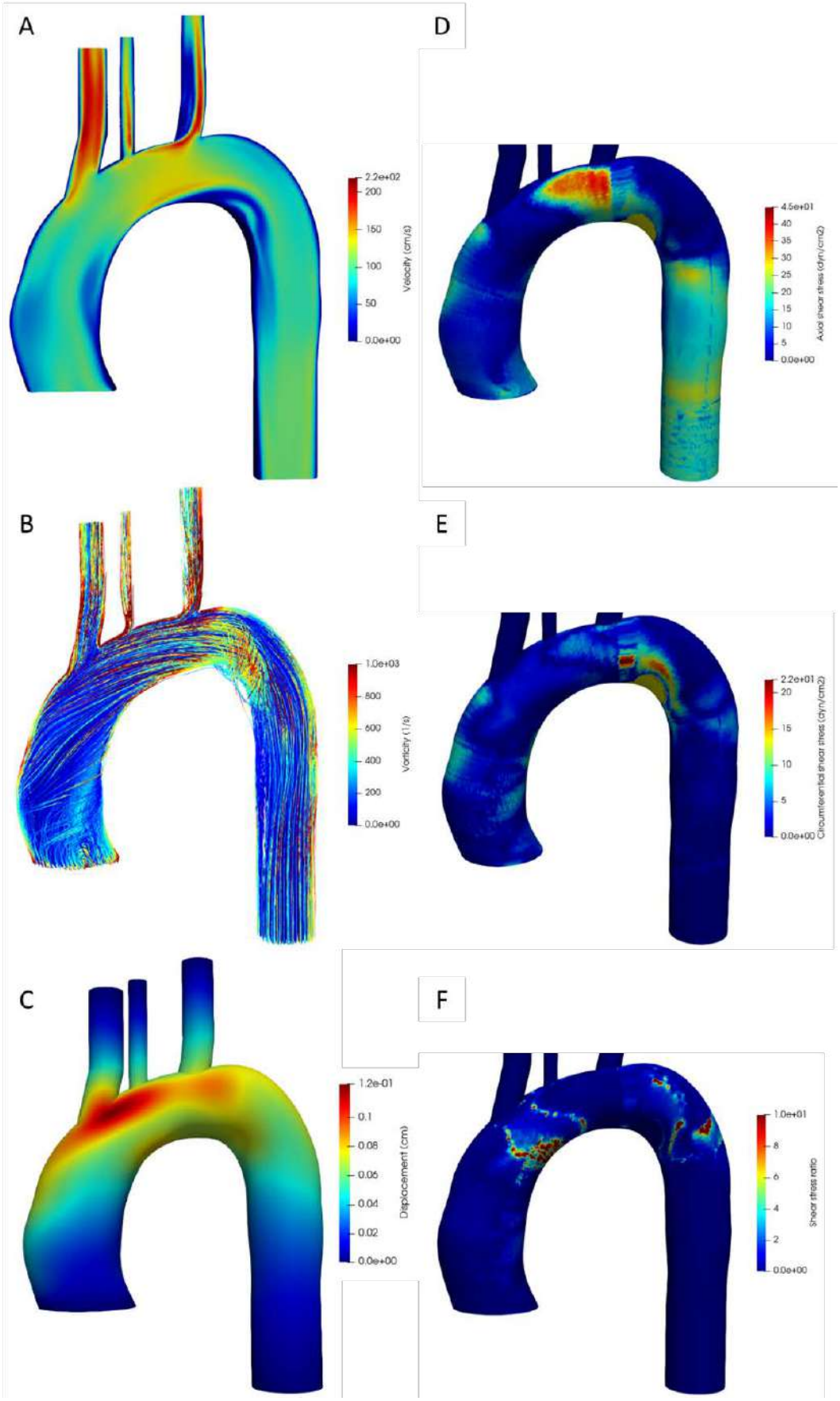

Figure 86. Fluid dynamic results of stable patient 1; (A) velocity, (B) vorticity, (C) displacement, (D) axial shear stress, (E) circumferential shear stress and (F) shear stress ratio.

Stable 2

Stable 2 is a 19 years old female. Figure 87 shows the vessel geometry from two MRI images, the final part of aortic arch and descending aorta in the first image was not visible due to the plane location. Table 19 presents the values extracted and used in the Solidworks macro to reconstruct the vessel.

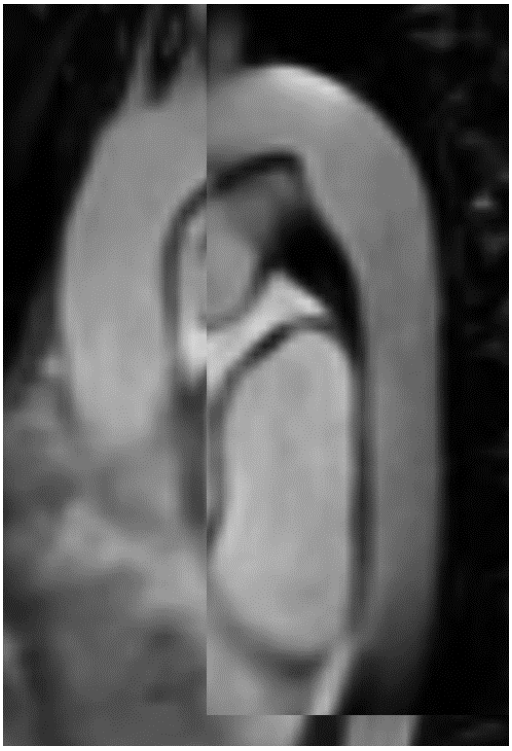

Figure 87. Visualization of S2 aorta with MRI using Mass.

	Nº Plane	X (mm)	Y (mm)	Z (mm)	r (mm)	δ (mm)
ASCENDING AORTA	1	0,0	0,0	0,0	14,0	1,5
	2	-2,5	-2,0	10,0	13,4	1,5
	3	-5,0	-3,0	20,0	13,0	1,5
	4	-5,0	-3,0	30,0	13,0	1,5
	5	-3,0	-1,5	40,0	13,0	1,5
AORTIC ARCH	1	15,0	3,0	53,4	11,5	1,5
	2	20,0	5,0	54,9	11,3	1,5
	3	25,0	7,5	55,9	11,0	1,5
	4	30,0	10,0	56,0	11,0	1,5
	5	35,0	12,6	55,8	11,0	1,5
DESCENDING AORTA	1	49,6	16,8	40,0	10,8	1,0
	2	51,9	18,0	30,0	10,5	1,0
	3	53,0	19,0	20,0	10,0	1,0
	4	53,0	19,0	10,0	10,0	1,0
	5	53,0	19,0	0,0	10,0	1,0

Table 19. Geometry data extracted from MRI images to reconstruct S2 aorta in SolidWorks.

Figure 88A shows the reconstruction of the vessel in green and the wall in white. Figure 88B shows the mesh of the fluid domain and Figure 88C the mesh of the solid domain.

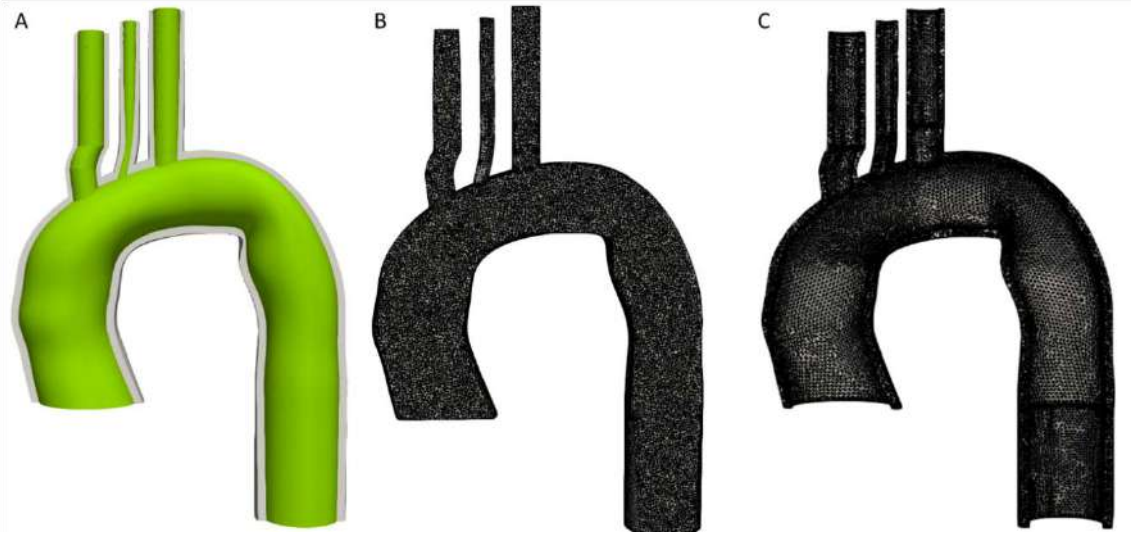

Figure 88. (A) Reconstruction of the aorta vessel and the wall, (B) meshing of the fluid and (C) meshing of the wall.

Minimum Jacobian criterion does not present negative values in the fluid mesh and neither in the solid mesh. The fluid mesh contains $8{,}94 \cdot 10^5$ elements and the solid mesh $4{,}68 \cdot 10^5$.

Figure 89 shows the flow curve at the sinotubular junction and descending aorta extracted from MRI images.

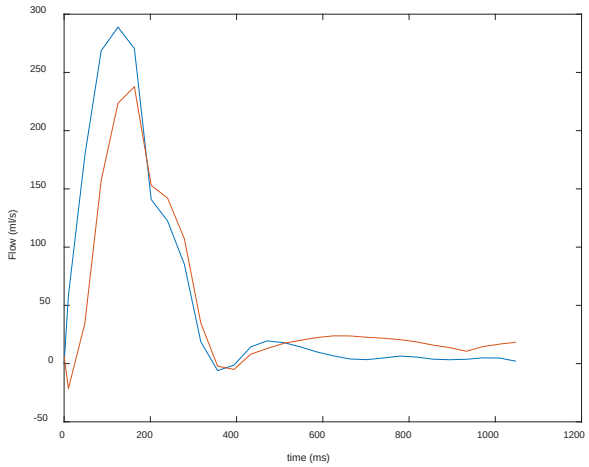

Figure 89. Flows at sinotubular junction and descending aorta with MRI technique of S2.

Figure 90 shows the flow profile extracted from 4D-MRI images at the sinotubular junction and treated spatiotemporally in Matlab. The result flow curve is the inlet condition for the CFD and FSI simulations of stable patient 2.

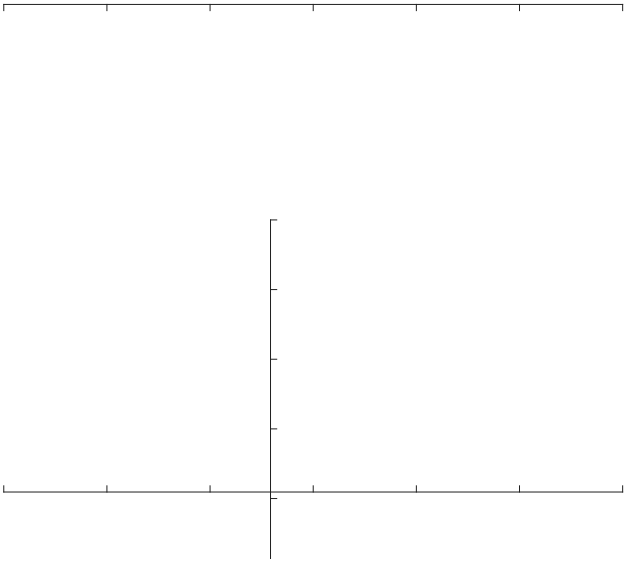

Figure 90. Flow curve of S2 at sinotubular junction after B-spline interpolation.

The flow profiles between MRI and 4D-MRI are different when comparing Figure 89 and Figure 90. The duration of systolic phase is 100 ms longer in 4D-MRI and the shape strongly differs but maximum flow observed at systolic peak is similar, just 9 ml/s above in MRI.

After imposing all the boundary conditions and meshing the geometries, CFD and FSI simulations are performed. Figure 91 shows the convergence of the FSI simulation.

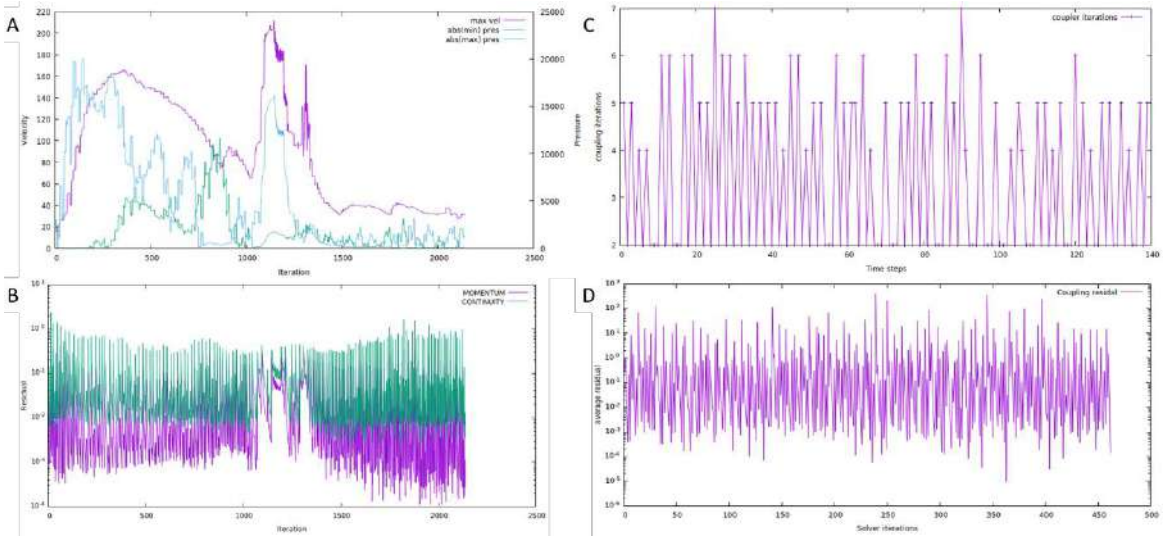

Figure 91. S2 FSI convergence of (A, B) the fluid, (C, D) the coupling.

Figure 91A shows that FSI simulation converges all time steps of the cardiac cycle. From iteration 1000 to 1300, an abnormal high peak of velocity can be observed, and residuals are not achieved in all the iterations. These steps are in diastolic phase, between 0.4 and

0.6 s. Even though these iterations do not achieve the residual, they do not make diverge the problem and all the cardiac cycle is simulated. At the coupling part, Figure 91C and Figure 91D, it can be observed that most steps needed between 2 to 5 coupling iterations to converge and that residual is achieved in all time steps. So, the non-convergence of the fluid is not affecting the convergence of the coupling part. With FSI and CFD simulations performed, flow ratio and PWV were compared to clinical data.

The flow ratio between the sinotubular junction and the descending aorta is iterated to match the flow ratio calculated from MRI data. The first FSI simulation (R=0 mmHg·s/cm^3) calculated a flow in descending aorta of 218 ml/s, which results in a flow ratio of 79,6%, close to the 80,7% expected. As the error is below 5% without Windkessel, this boundary condition has not been applied in stable patient 2. Flow at the descending aorta in CFD without Windkessel is 212 ml/s which results in a flow ratio of 77,4%. The error in CFD is 3%, also below 5%. Clinical and final simulation values for flow are presented in Table 20.

Stable 2	Flow Sinotubular Junction (ml/s)	Flow Descending (ml/s)	Flow ratio (%)	Error (%)
MRI	285	230	80,7%	-
CFD	274	212	77,4%	3,3%
FSI	274	218	79,6%	1,1%

Table 20. Final flows at descending aorta and flow ratio of S2.

The PWV calculated using 4D-MRI is 5,4 m/s. Three iterations were required to reduce the error value to 5%. The values of the iterations can be seen in Figure 19.

Stable 2	E_0 (MPa)	PWV (m·s^{-1})	Error (%)
Clinical	-	5,4	-
Simulation 1	1,06	6,5	16,9
Simulation 2	0,88	6,0	10,0
Simulation 3	0,79	5,7	5,3

Table 21. Young's modulus iterations to match clinical PWV of S2.

Young modulus for the first FSI simulation was estimated at 1,06 MPa after measuring 5,4 m/s as PWV from 4D-MRI data. After three iterations, the PWV value of 5,7 m/s was accepted and the Young's modulus of 0,79 MPa.

The results of stable patient 2 were analyzed after PWV and flow ratio were matched with the clinical data. Figure 92 presents the velocity field, vorticity, wall axial and

circumferential shear stresses, displacement of the wall and shear stress ratio at systolic peak (step 21).

Maximum velocity observed inside the aorta is 160 cm/s at systolic peak. The maximum velocity is located at the interior part of ascending aorta because jet is orientated to that part. A large area of low velocities (<20 cm/s) can be observed at the interior part of the descending aorta.

Vorticity streamlines are presented in Figure 92B. It can be observed that maximum vorticity values are at the interior part of the ascending aorta with values reaching 1000 s-1. The whole aorta presents high values, between 400 and 600 s-1 expect for the final part of the descending. The zone of low velocity at the beginning of descending aorta presents no streamlines. Maximum displacement is observed at the aortic arch reaching values of 1,5 mm.

Figure 92D and Figure 92E show the axial and circumferential shear stress respectively. Axial shear stress present values of 20-30 dyn/cm2 at the interior part of ascending aorta, where velocity is higher. Circumferential shear stress presents values from 5-10 dyn/cm2 at the whole ascending aorta. At aortic arch, axial shear stress presents a large area of 35 dyn/cm2 while circumferential shear stress presents a zone of 10 dyn/cm2. At the descending aorta, axial shear stress presents a very large area between 15 and 25 dyn/cm2. Oppositely, the circumferential shear stress is almost null in the whole descending aorta except for the initial part where a small area of 15 can be observed.

The shear stress ratio is presented in Figure 92F. Values below 2 are observed in most of the domain. There are two areas where it can be observed high shear stress ratio; the initial part of the aortic arch and at the beginning part of descending aorta.

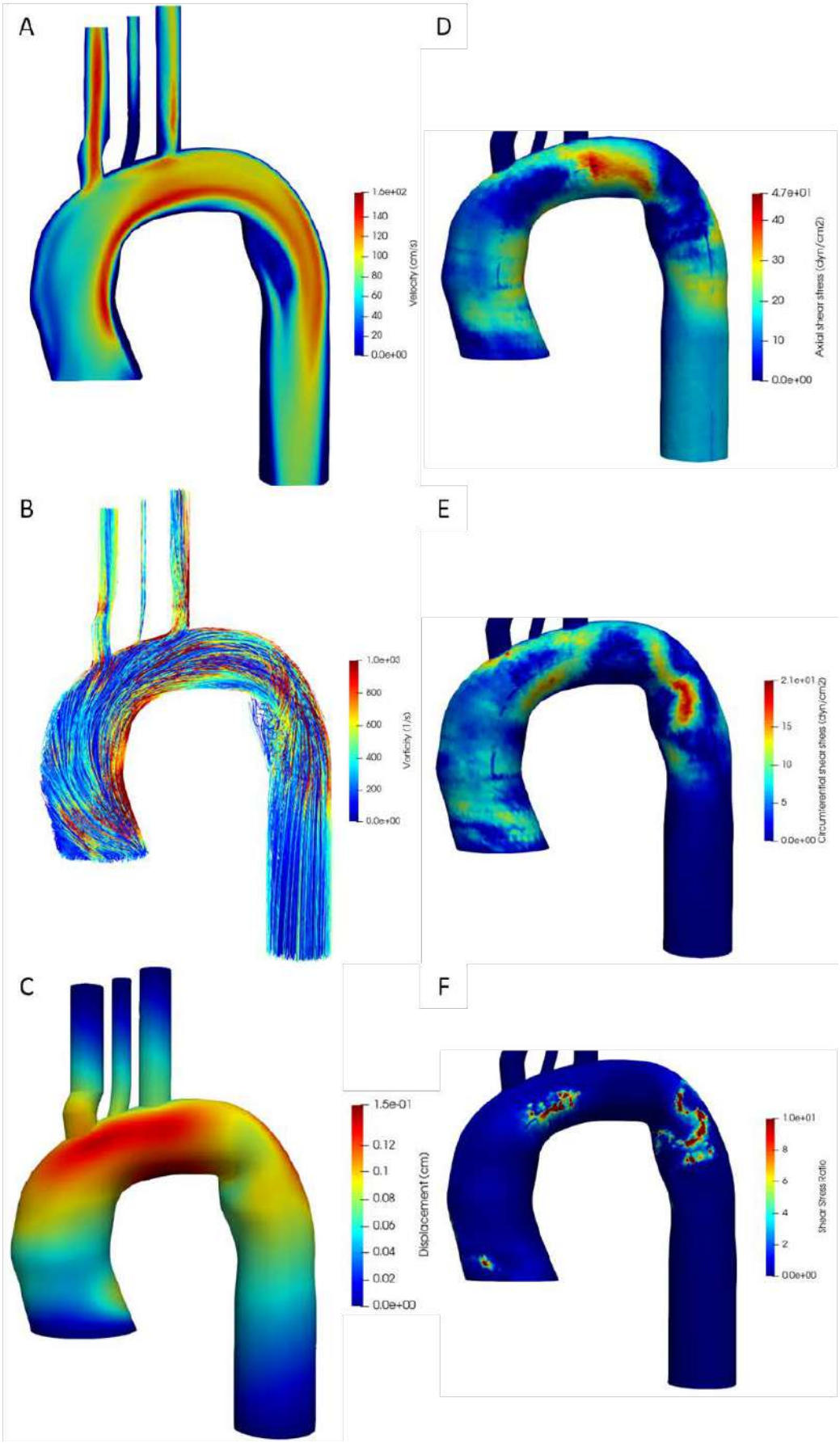

Figure 92**.** Fluid dynamic results of stable patient 2; (A) velocity, (B) vorticity, (C) displacement, (D) axial shear stress, (E) circumferential shear stress and (F) shear stress ratio.

Stable 3

Stable 3 is a 23 years old male. Figure 93 shows the vessel geometry from an MRI image. Table 22 presents the values extracted and used in the Solidworks macro to reconstruct the vessel.

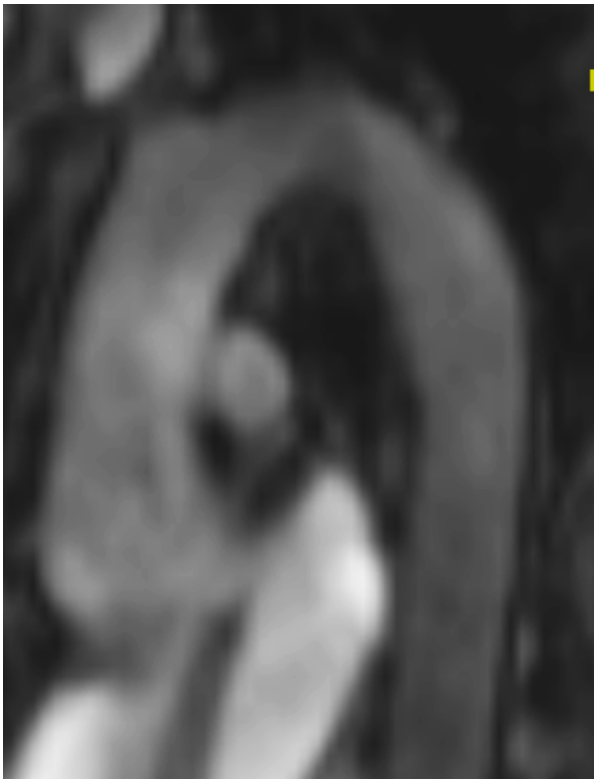

Figure 93. Visualization of S3 aorta with MRI using Mass.

	Nº Plane	X (mm)	Y (mm)	Z (mm)	r (mm)	δ (mm)
ASCENDING AORTA	1	0,0	0,0	0,0	14,3	1,5
	2	0,0	0,0	10,0	14,0	1,5
	3	-1,0	-0,5	20,0	13,2	1,5
	4	0,0	0,0	30,0	13,0	1,5
	5	3,0	0,5	40,0	12,6	1,5
AORTIC ARCH	1	20,0	3,3	56,0	12,5	1,5
	2	25,0	5,9	58,5	12,3	1,5
	3	30,0	8,4	60,7	11,5	1,5
	4	35,0	11,0	62,0	10,9	1,5
	5	40,0	13,6	61,7	10,5	1,5
ºDESCENDING AORTA	1	57,0	17,5	40,0	10,0	1,0
	2	56,5	17,5	30,0	9,5	1,0
	3	56,0	17,5	20,0	9,5	1,0
	4	55,5	17,5	10,0	9,5	1,0
	5	55,0	17,5	0,0	9,5	1,0

Table 22. Geometry data extracted from MRI images to reconstruct S3 aorta in SolidWorks.

Figure 94A shows the reconstruction of the vessel in green and the wall in white. Figure 94B shows the mesh of the fluid domain and Figure 94C the mesh of the solid domain.

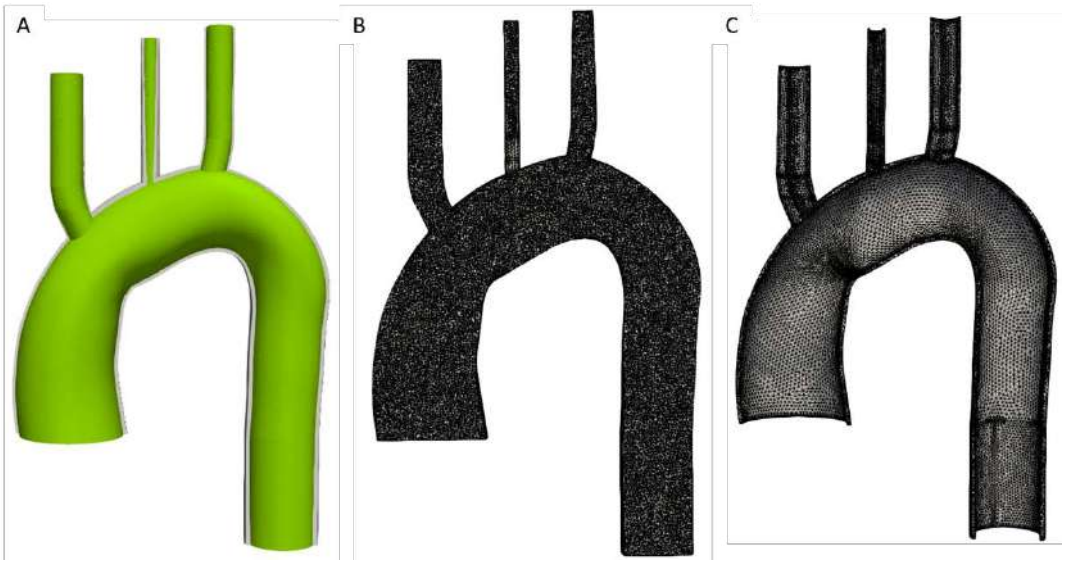

Figure 94. (A) Reconstruction of the aorta vessel and the wall, (B) meshing of the fluid and (C) meshing of the wall.

Minimum Jacobian criterion does not present negative values in the fluid mesh and neither in the solid mesh. The fluid mesh contains $1{,}33 \cdot 10^6$ elements and the solid mesh $6{,}12 \cdot 10^5$.

Figure 95 shows the flow curve at the sinotubular junction and descending aorta extracted with the contour creation from MRI images.

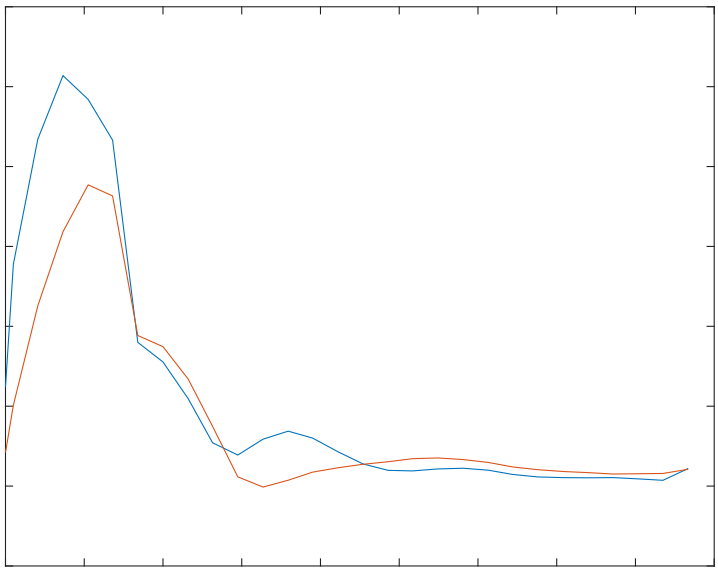

Figure 95. Flows at sinotubular junction and descending aorta with MRI technique of S3.

Figure 96 shows the flow profile extracted from 4D-MRI images at sinotubular junction and treated spatiotemporally in Matlab. The result flow curve is the inlet condition for the CFD and FSI simulations of stable patient 3.

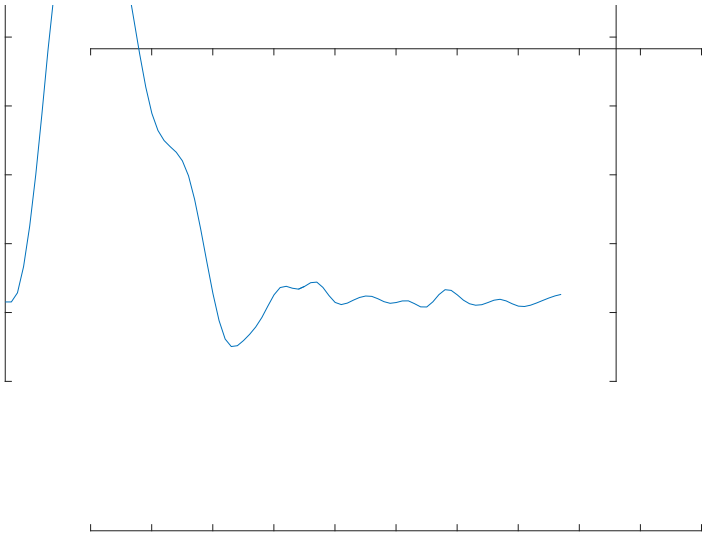

Figure 96. Flow curve of S3 at sinotubular junction after B-spline interpolation.

The flow profiles between MRI and 4D-MRI are different when comparing Figure 95 and Figure 96. The duration of systolic phase is longer in 4D-MRI by 50 ms, the maximum velocity at systolic peak differs from 77 ml/s and 4D-MRI presents negative flow at the beginning of the diastole.

After imposing all the boundary conditions and meshing the geometries, CFD and FSI simulations are performed. Figure 97 shows the convergence of the FSI simulation.

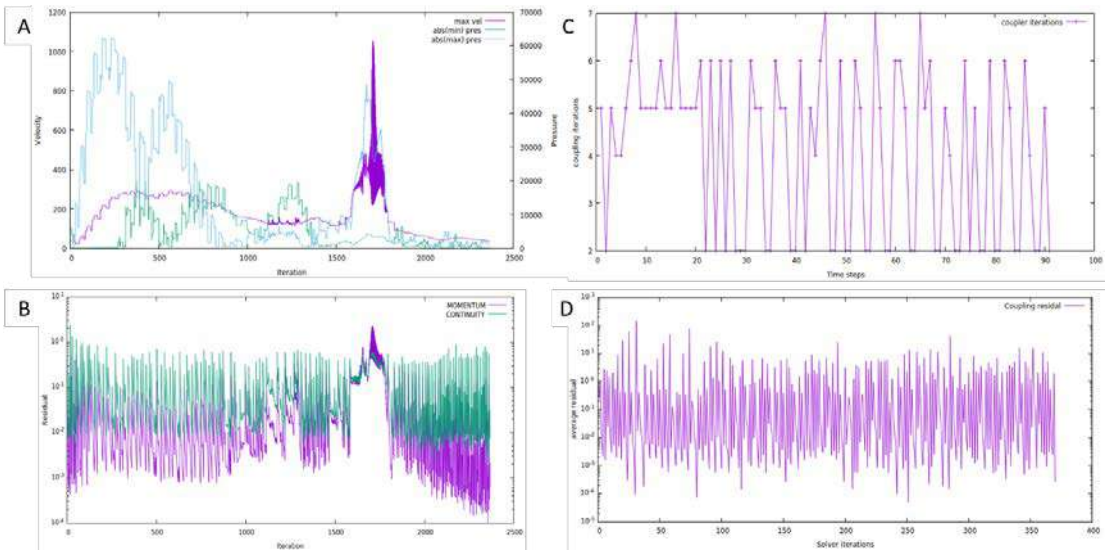

Figure 97. S3 FSI convergence of (A, B) the fluid, (C, D) the coupling.

Figure 97A shows that FSI simulation does not converge all time steps of the cardiac cycle. From iteration 1600 to 1800, an abnormal high peak of velocity can be observed, and residuals are not achieved. These steps are in diastolic phase, between 0.4 and 0.5 s. Even though these steps do not converge, they do not make diverge the problem and all the cardiac cycle is simulated. At the coupling part, Figure 91C and Figure 91D, it can be observed that most steps needed between 2 to 6 coupling iterations to converge and that residual is achieved in all time steps. So, the non-convergence of the fluid is not affecting the convergence of the coupling part. With FSI and CFD simulations performed, flow ratio and PWV were compared to clinical data.

The flow ratio between the sinotubular junction and the descending aorta is iterated to match the flow ratio calculated from MRI data. The first FSI simulation (R=0 mmHg·s/cm^3) calculated a flow in descending aorta of 440 ml/s, which results in a flow ratio of 74,5%, close to the 73,3% expected. As the error is below 5% without Windkessel, it has not been applied in stable patient 3. Flow at the descending aorta in CFD without Windkessel is 446 ml/s which results in a flow ratio of 75,5%. The error in CFD is also below 5%. Clinical and final simulation values for flow are presented in Table 23.

Stable 3	Flow Sinotubular Junction (ml/s)	Flow Descending (ml/s)	Flow ratio (%)	Error (%)
MRI	514	377	73,3%	-
CFD	591	446	75,5%	2,1%
FSI	591	440	74,5%	1,1%

Table 23. Final flows at descending aorta and flow ratio of S3.

The PWV calculated using 4D-MRI is 13,5 m/s. Two iterations were required to reduce the error value to 5%. The values of the iterations can be seen in Table 24.

Stable 2	E_0 (MPa)	PWV (m·s^{-1})	Error (%)
Clinical	-	13,5	-
Simulation 1	3,42	12,6	7,1
Simulation 2	3,61	12,9	4,7

Table 24. Young's modulus iterations to match clinical PWV of S3.

Young modulus for the first FSI simulation was estimated at 3,4 MPa after measuring 13,5 m/s as PWV from 4D-MRI data. After two iterations, the PWV value of 12,9 m/s was accepted and the Young's modulus of 3,6 MPa.

The results of stable patient 3 were analyzed after PWV and flow ratio were matched with the clinical data. Figure 98 presents the velocity field, vorticity, wall axial and circumferential shear stresses, displacement of the wall and shear stress ratio at systolic peak (step 17).

Maximum velocities observed inside the aorta are 260 cm/s at systolic peak. The maximum velocity is located at the brachiocephalic artery and at the exterior part of the descending aorta. At the ascending aorta, the jet velocity is 150 cm/s and is orientated from the center of the vessel to the interior part of the artery. Three areas of low velocities (<30 cm/s) can be observed at the exterior part of ascending aorta and at the interior part of aortic arch and descending aorta.

Vorticity streamlines are presented in Figure 98B. It can be observed that maximum vorticity values are at the exterior part of the descending aorta with values reaching 1500 s^{-1}. The ascending aorta presents values much lower, between 200 and 400 s^{-1}, at the external part than at the interior part, between 600 and 1000 s^{-1}. Maximum displacement is observed at the aortic arch and at the initial part of the descending aorta reaching values of 2 mm.

Figure 98D and Figure 98E show the axial and circumferential shear stress respectively. Axial shear stress present values of 30 dyn/cm^2 at the anterior part of the ascending aorta. Circumferential shear stress also presents values of 8 dyn/cm^2 in the same area. At aortic arch, axial shear stress presents a small area of 25 dyn/cm^2 while circumferential shear stress presents a large area of 15 dyn/cm^2. At the descending aorta, axial shear stress presents a very large area between 40 and 60 dyn/cm^2. Oppositely, the circumferential shear stress is almost null in the whole descending aorta expect for two zones of 10 dyn/cm^2.

The shear stress ratio is presented in Figure 98F. Null values are observed in most of the domain. There is just one area located at the interior part of the aortic arch which presents values above 8.

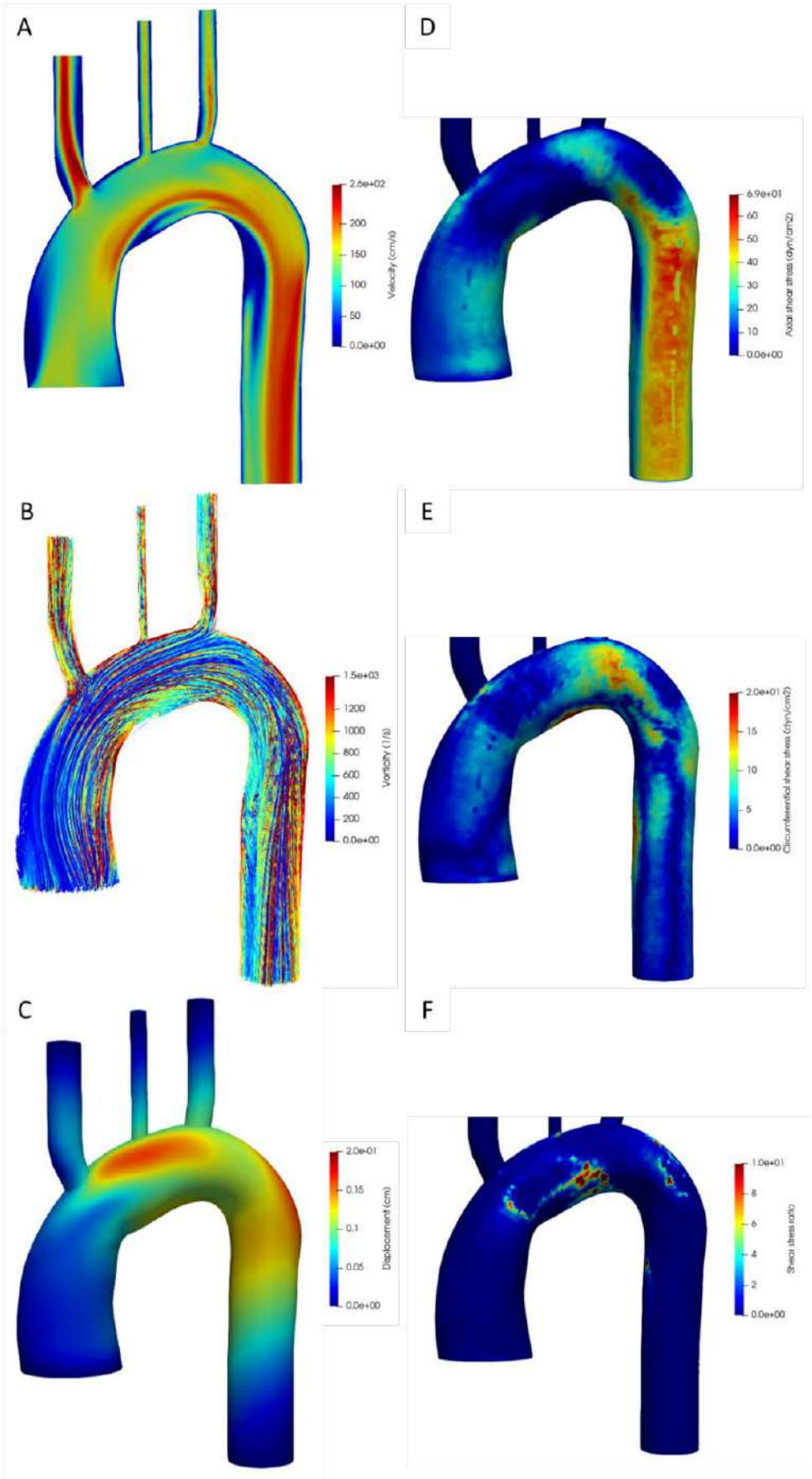

Figure 98. Fluid dynamic results of stable patient 3; (A) velocity, (B) vorticity, (C) displacement, (D) axial shear stress, (E) circumferential shear stress and (F) shear stress ratio.

Stable 4

Stable patient 4 is a 19 years old male. Figure 99 shows the vessel geometry from MRI. Table 25 presents the values extracted and used in the Solidworks macro to reconstruct the vessel.

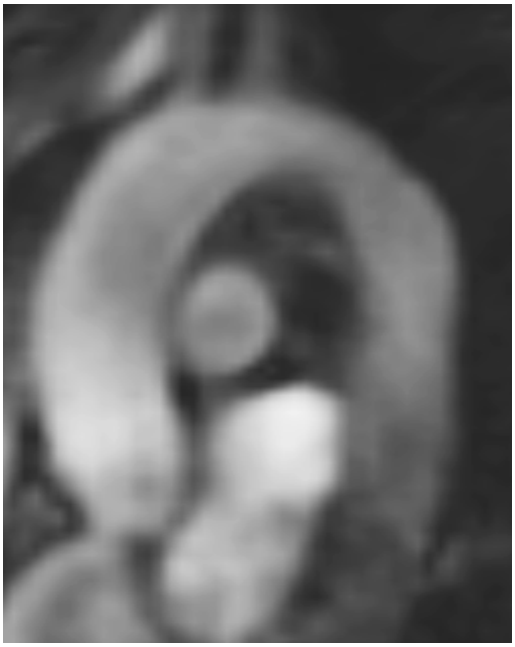

Figure 99. Visualization of S4 aorta with MRI using Mass.

	Nº Plane	X (mm)	Y (mm)	Z (mm)	r (mm)	δ (mm)
ASCENDING AORTA	1	0,0	0,0	0,0	14,0	1,5
	2	-1,5	2,5	10,0	14,0	1,5
	3	-1,5	5,5	20,0	14,0	1,5
	4	0,0	9,0	30,0	13,3	1,5
	5	2,0	11,5	35,0	13,0	1,5
AORTIC ARCH	1	17,5	24,3	48,0	11,4	1,0
	2	22,5	26,5	49,0	10,5	1,0
	3	27,5	28,4	50,0	10,0	1,0
	4	32,5	30,7	49,8	9,8	1,0
	5	37,5	33,4	49,7	9,5	1,0
DESCENDING AORTA	1	53,3	32,4	35,0	9,5	1,0
	2	55,0	31,0	30,0	9,5	1,0
	3	54,3	28,5	20,0	9,0	1,0
	4	53,7	26,4	10,0	9,0	1,0
	5	53,0	26,0	0,0	9,0	1,0

Table 25. Geometry data extracted from MRI images to reconstruct S4 aorta in SolidWorks.

Figure 100A shows the reconstruction of the vessel in green and the wall in white. Figure 100B shows the mesh of the fluid domain and Figure 100C the mesh of the solid domain.

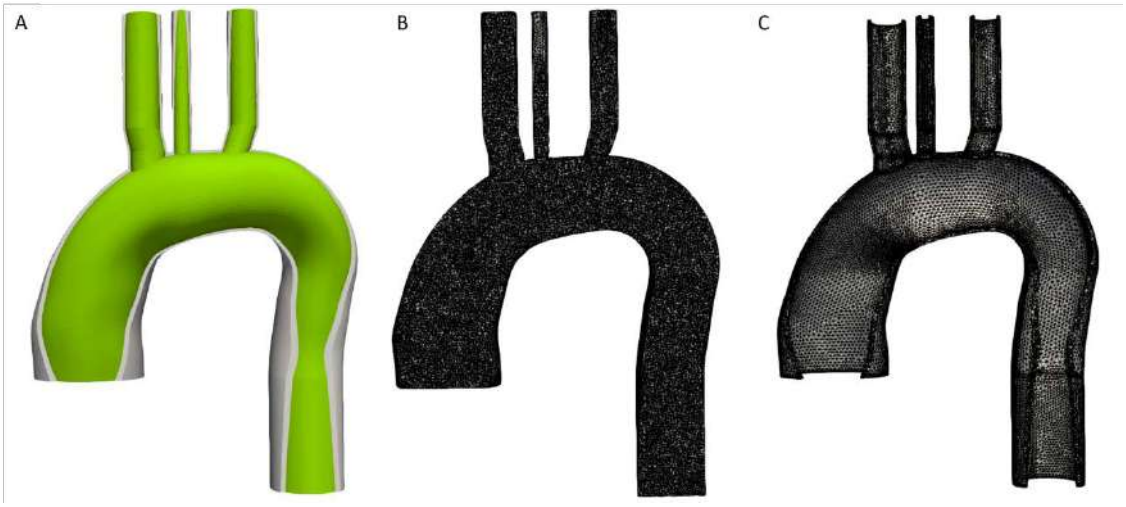

Figure 100. (A) Reconstruction of the aorta vessel and the wall, (B) meshing of the fluid and (C) meshing of the wall.

Minimum Jacobian criterion does not present negative values in the fluid mesh and neither in the solid mesh. The fluid mesh contains $8{,}87 \cdot 10^5$ elements and the solid mesh $4{,}48 \cdot 10^5$.

Figure 101 shows the flow curve at the sinotubular junction and descending aorta extracted from MRI images.

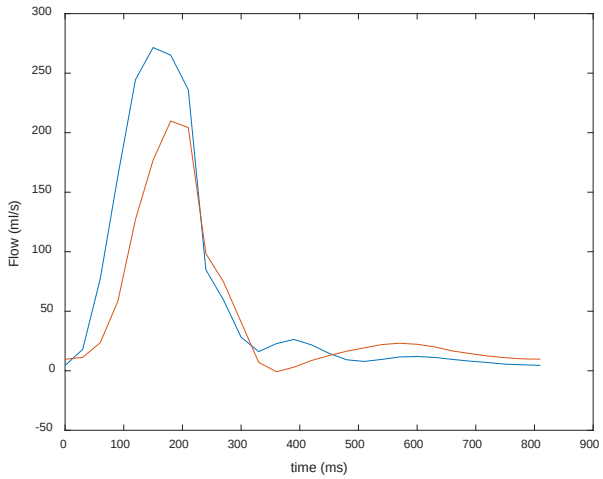

Figure 101. Flows at sinotubular junction and descending aorta of S4 with MRI technique.

Figure 102 shows the flow profile extracted from 4D-MRI images at sinotubular junction and treated spatiotemporally in Matlab. The result flow curve is the inlet condition for the CFD and FSI simulations of stable patient 4.

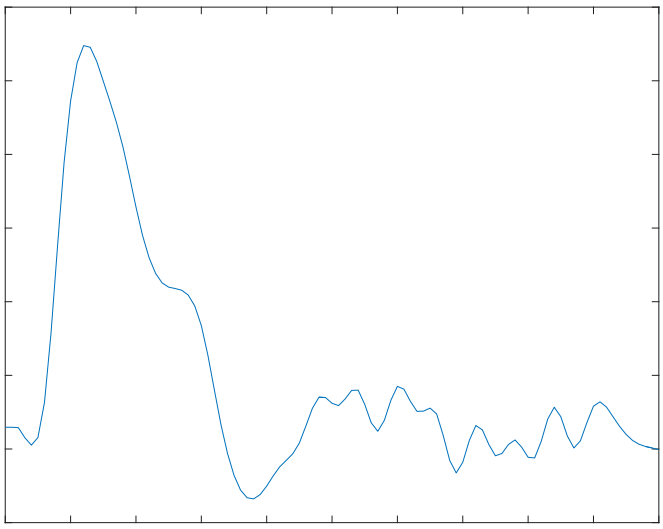

Figure 102. Flow curve of S4 at sinotubular junction after B-spline interpolation.

The flow profiles between MRI and 4D-MRI are similar when comparing Figure 101 and Figure 102. The duration of systolic phase is the same in both techniques and maximum flow just differs for 2 ml/s. After imposing all the boundary conditions and meshing the geometries, CFD and FSI simulations are performed. Figure 103 shows the convergence of the FSI simulation.

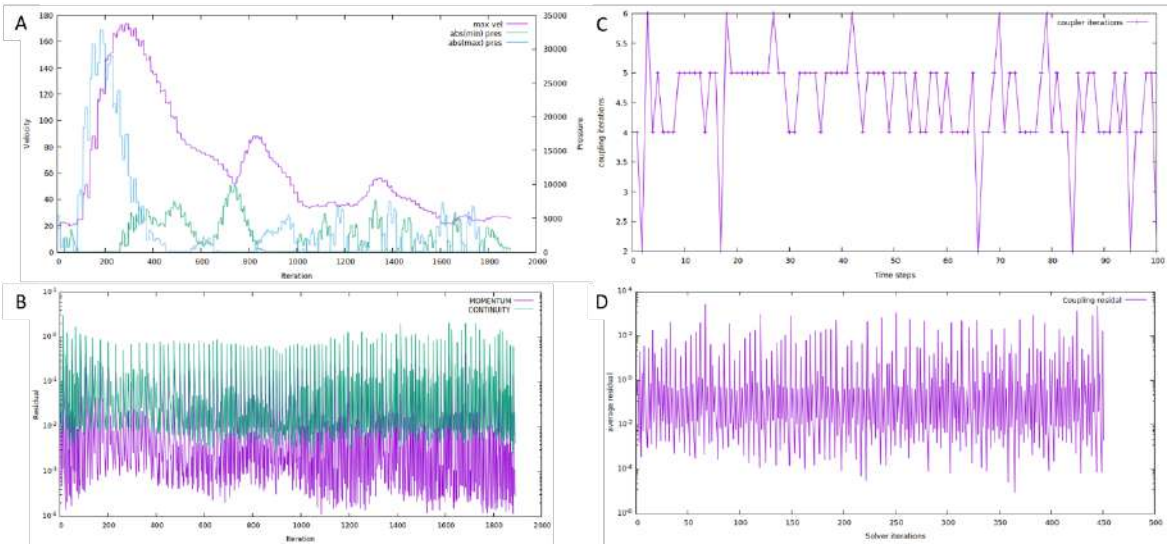

Figure 103. S4 FSI convergence of (A, B) the fluid, (C, D) the coupling.

Figure 103A shows that FSI simulation does not diverge at any point due to coherent values of maximum velocity. Figure 103B shows that all time steps reach the residual value desired and that the number of iterations per timestep is approximately 25 for systole and 10 for diastole. At the coupling part, Figure 103C and Figure 103D, it can be

observed that most steps needed between 4 to 6 coupling iterations to converge and that residual is achieved in all time steps. With FSI and CFD simulations are performed, flow ratio and PWV were compared to clinical data.

The flow ratio between the sinotubular junction and the descending aorta is iterated to match the flow ratio calculated from MRI data. The first FSI simulation (R=0 mmHg·s/cm^3) calculated a flow in descending aorta of 210 ml/s, the same as from MRI. Without Windkessel the error of both simulations is below 5%. Clinical and final simulation values for flow are presented in Table 26.

Stable 4	Flow Sinotubular Junction (ml/s)	Flow Descending (ml/s)	Flow ratio (%)	Error (%)
MRI	272	210	77,2%	-
CFD	274	213	77,7%	0,5%
FSI	274	210	76,6%	0,6%

Table 26. Final flows at descending aorta and flow ratio of S4.

The PWV calculated using 4D-MRI is 5,9 m/s. Two iterations were required to reduce the error value to 5%. The values of the iterations can be seen in Table 27.

Stable 4	E_0 (MPa)	PWV (m·s^{-1})	Error (%)
Clinical	-	5,9	-
Simulation 1	0,9	6,5	9,2
Simulation 2	0,8	6,1	3,3

Table 27. Young's modulus iterations to match clinical PWV of S4.

Young modulus for the first FSI simulation was estimated at 0,9 MPa after measuring 5,9 m/s as PWV from 4D-MRI data. After two iterations, the PWV value of 6,1 m/s was accepted and the Young's modulus of 0,8 MPa.

The results of stable patient 2 were analyzed after PWV and flow ratio were matched with the clinical data. Figure 104 presents the velocity field, vorticity, wall axial and circumferential shear stresses, displacement of the wall and shear stress ratio at systolic peak (step 14).

Maximum velocities observed inside the aorta are 160 cm/s at systolic peak. The maximum velocity is located at the brachiocephalic artery. At the ascending aorta, the jet velocity is 90 cm/s and is orientated from the center of the vessel to the interior part of the artery. Two areas of low velocities (<20 cm/s) can be observed at the interior part of the aortic arch and descending aorta.

Vorticity streamlines are presented in Figure 104B. It can be observed that maximum vorticity values are at the anterior part of the descending aorta with values reaching 800 s^{-1}. The whole ascending aorta presents low values below 200 s^{-1}.

Maximum displacement is observed at the aortic arch and at the initial part of the descending aorta reaching values of 0,8 mm. The movement is lower than other cases due to high Young's modulus. It can be observed that the restriction of no displacement imposed at inlet and outlets surfaces is affecting the whole aorta with less realistic results.

Figure 104D and Figure 104E show the axial and circumferential shear stress respectively. Axial shear stress presents a large area of 15 dyn/cm^2 at the final part of the ascending aorta. Circumferential shear stress presents values below 3 dyn/cm^2 at the ascending aorta. At aortic arch, axial shear stress presents an area of 20 dyn/cm^2 at its final part and circumferential shear stress presents a small area of 6 dyn/cm^2 at the interior part. At the descending aorta, axial shear stress presents a very large area between 15 and 35 dyn/cm^2. Oppositely, the circumferential shear stress is almost null in the whole descending aorta expect for a small area at the beginning of 8 dyn/cm^2.

The shear stress ratio is presented in Figure 104F. Null values are observed in most of the domain. Two areas of high shear stress ratio are observed at the initial part of the ascending and the descending aorta.

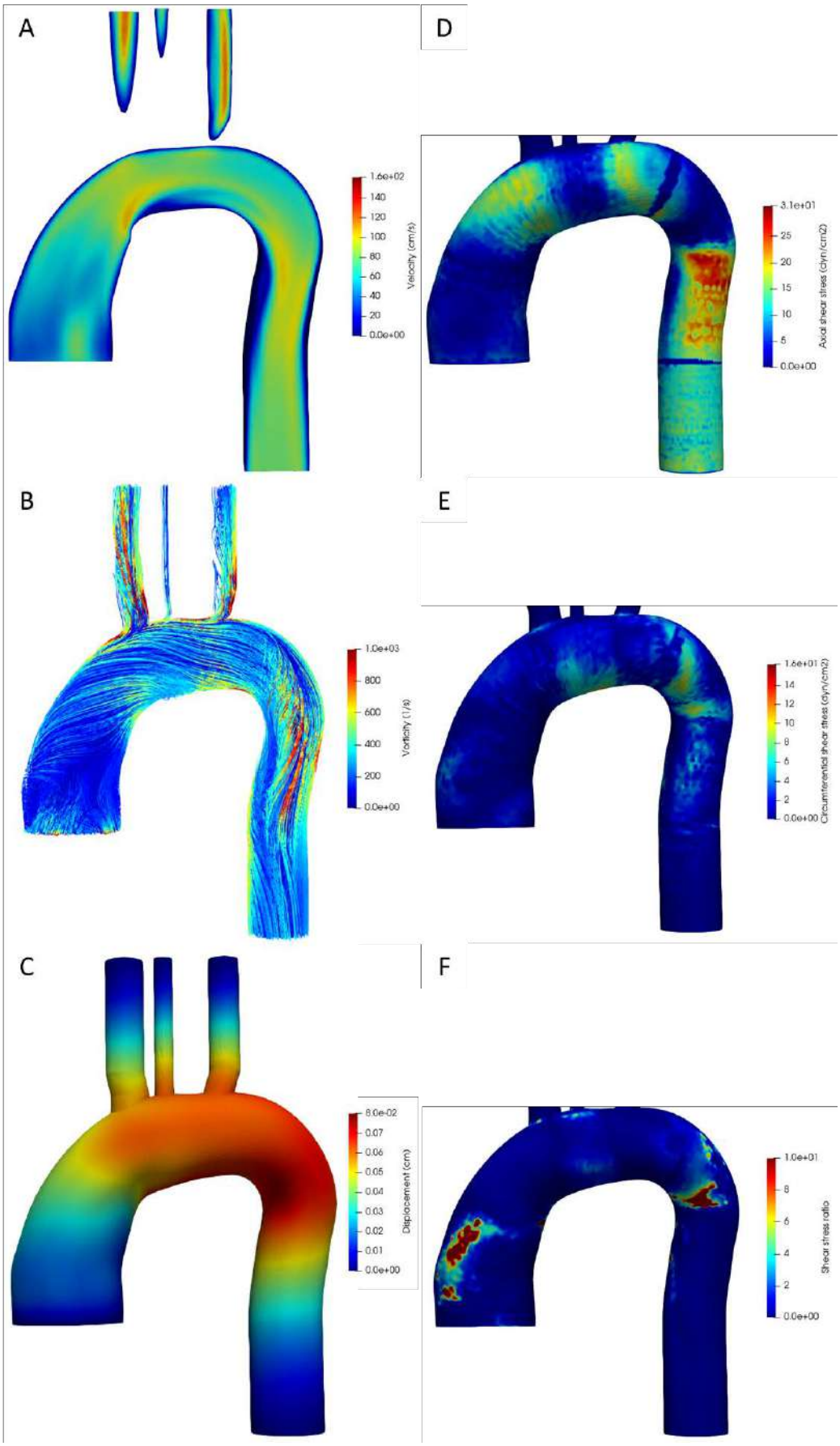

Figure 104. Fluid dynamic results of stable patient 4; (A) velocity, (B) vorticity, (C) displacement, (D) axial shear stress, (E) circumferential shear stress and (F) shear stress ratio.

Dilating 1

Dilating patient 1 is a 32 years old female. Figure 105 shows the vessel geometry from MRI. Table 28 presents the values extracted and used in the Solidworks macro to reconstruct the vessel.

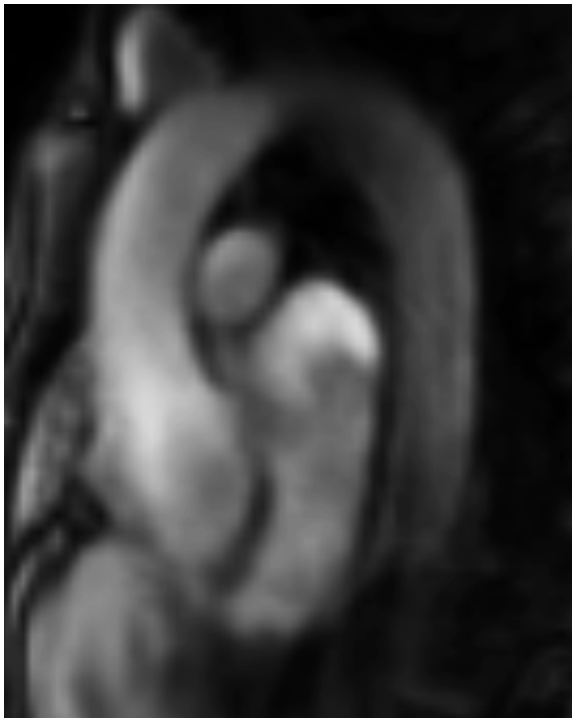

Figure 105. Visualization of patient D1 aorta with MRI using Mass.

	Nº Plane	X (mm)	Y (mm)	Z (mm)	r (mm)	δ (mm)
ASCENDING AORTA	1	0,0	0,0	0,0	12,8	2,0
	2	-2,0	0,0	10,0	15,3	2,0
	3	-4,0	0,0	20,0	20,4	2,0
	4	-3,0	2,0	30,0	21,7	2,0
	5	0,0	5,0	40,0	16,7	2,0
AORTIC ARCH	1	15,0	16,4	54,0	12,6	1,5
	2	20,0	18,0	56,9	11,7	1,5
	3	25,0	19,6	59,3	11,4	1,5
	4	30,0	21,5	61,0	10,8	1,5
	5	35,0	22,8	61,7	10,5	1,5
DESCENDING AORTA	1	54,0	23,3	40,0	10,2	1,5
	2	55,0	25,0	30,0	9,0	1,5
	3	56,0	25,0	20,0	8,5	1,5
	4	57,0	25,0	10,0	8,5	1,5
	5	57,0	25,0	0,0	8,5	1,5

Table 28. Geometry data extracted from MRI images to reconstruct D1 aorta in SolidWorks.

Figure 106A shows the reconstruction of the vessel in green and the wall in white. Figure 106B shows the mesh of the fluid domain and Figure 106C the mesh of the solid domain.

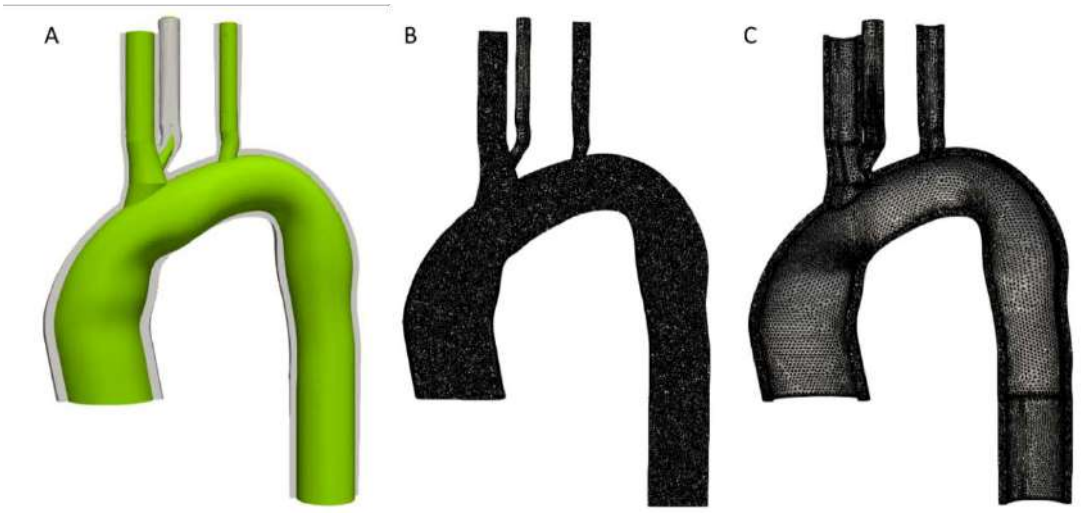

Figure 106. (A) Reconstruction of the D1 aorta vessel and the wall, meshing (B) of the fluid and (C) of the wall.

Minimum Jacobian criterion does not present negative values in the fluid mesh and neither in the solid mesh. The fluid mesh contains $1{,}33 \cdot 10^6$ elements and the solid mesh $6{,}12 \cdot 10^5$.

Figure 107 shows the flow curve at the sinotubular junction and descending aorta extracted from MRI images.

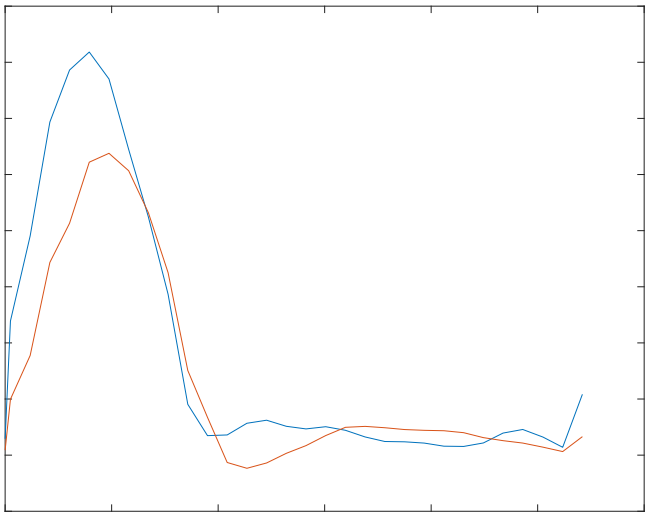

Figure 107. Flows at sinotubular junction and descending aorta of D1 with MRI technique.

Figure 108 shows the flow profile extracted from 4D-MRI images at sinotubular junction and treated spatiotemporally in Matlab. The result flow curve is the inlet condition for the CFD and FSI simulations of dilating patient 1.

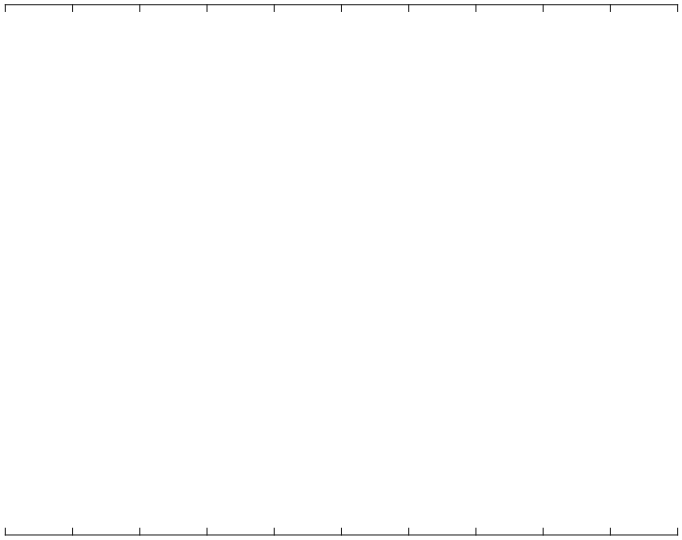

Figure 108**.** Flow curve of D1 at sinotubular junction after B-spline interpolation.

The flow profiles between MRI and 4D-MRI differ in the duration of systolic phase by 80 ms and 20 ml/s in the maximum flow. Both techniques have not detected negative flow at the diastolic phase.

After imposing all the boundary conditions and meshing the geometries, CFD and FSI simulations are performed. Figure 109 shows the convergence of the FSI simulation.

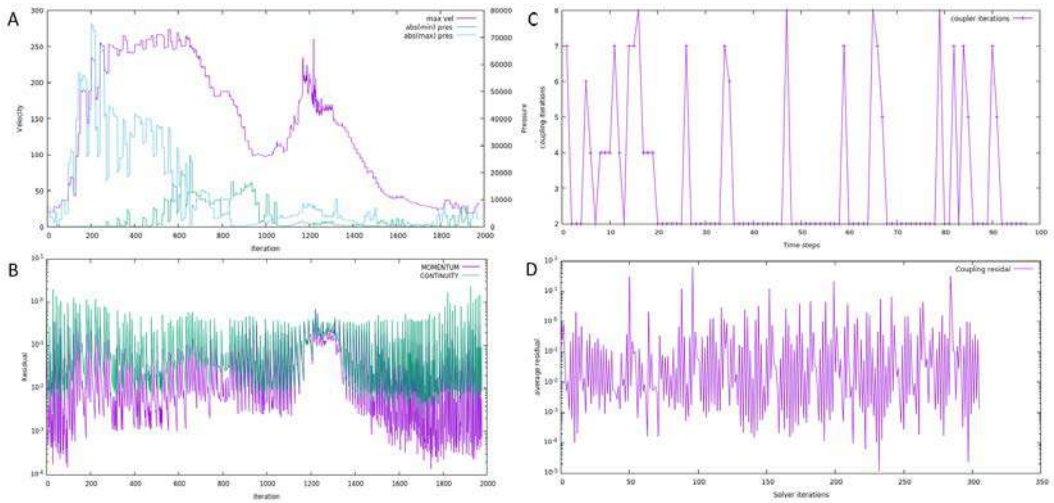

Figure 109. D1 FSI convergence of (A, B) the fluid, (C, D) the coupling.

Figure 109A shows that FSI simulation does not diverge at any point, but some difficulties are observed between iterations 1200 and 1300. Figure 109B shows that all time steps reach the residual value desired expect for the first steps of diastolic phase. For the coupling, Figure 109C and Figure 109D, it can be observed that most steps needed 2 coupling iterations to converge and that residual is achieved in all time steps. With both simulations converged, flow ratio and PWV were compared to clinical data.

The flow ratio between the sinotubular junction and the descending aorta is iterated to match the flow ratio calculated from MRI data. The first FSI simulation (R=0 mmHg·s/cm^3) calculated a flow in descending aorta of 283 ml/s, which results in a flow ratio of 75,1%, close to the 74,9% expected. As the error is below 5% without Windkessel, boundary condition has not been applied in dilating patient 1. Flow at the descending aorta in CFD without Windkessel is 280 ml/s which results in a flow ratio of 74,3%, also below 5%. Clinical and final simulation values for flow are presented in Table 29.

Dilating 1	Flow Sinotubular Junction (ml/s)	Flow Descending (ml/s)	Flow ratio (%)	Error (%)
MRI	359	269	74,9%	-
CFD	377	280	74,3%	0,7%
FSI	377	283	75,1%	0,1%

Table 29. Final flows at descending aorta and flow ratio of D1.

The PWV calculated using 4D-MRI is 5,5 m/s. Three iterations were required to reduce the error value below 5%. The values of the iterations can be seen in Table 30.

Dilating 1	E_0 (kg·s^{-2}·m^{-1})	PWV (m·s^{-1})	Error (%)
Clinical	-	5,5	-
Simulation 1	1,1	6,8	19,1
Simulation 2	0,86	6,2	11,3
Simulation 3	0,76	5,8	5,2

Table 30. Young's modulus iterations to match clinical PWV of D1.

Young modulus for the first FSI simulation was estimated at 1,1 MPa after measuring 5,5 m/s as PWV from 4D-MRI data. After three iterations, the PWV value of 5,8 m/s was accepted and the Young's modulus of 0,76 MPa.

The results of dilating patient 1 were analyzed after PWV and flow ratio were matched with the clinical data. Figure 110 presents the velocity field, vorticity, wall axial and

circumferential shear stresses, displacement of the wall and shear stress ratio at systolic peak (step 19).

Maximum velocities observed inside the aorta are 280 cm/s at systolic peak. The maximum velocity is located at the brachiocephalic artery and at the external descending aorta. At the ascending aorta, the jet velocity is 140 cm/s and is orientated from the center of the vessel to the interior part of the artery. Two large areas of low velocities (<30 cm/s) can be observed at the exterior part of the ascending aorta and at the interior part of the descending aorta.

Vorticity streamlines are presented in Figure 110B. It can be observed that maximum vorticity values are at the aortic arch with values reaching 1500 s^{-1}. The whole ascending aorta presents low values below 400 s^{-1}. Maximum displacement is observed at the beginning of descending aorta reaching values of 4 mm.

Figure 110D and Figure 110E show the axial and circumferential shear stress respectively. Axial shear stress presents values below 10 dyn/cm^2 at the ascending aorta. Circumferential shear stress presents values below 5 dyn/cm^2 at the ascending aorta and the aortic arch. At aortic arch, axial shear stress presents two areas of 30 to 40 dyn/cm^2 and circumferential shear stress presents values below 5 dyn/cm^2 as the ascending aorta. At the descending aorta, axial shear stress presents a very large area between 30 and 50 dyn/cm^2. Oppositely, the circumferential shear stress is almost null in the whole descending aorta expect for a small area at the beginning of 15 dyn/cm^2.

The shear stress ratio is presented in Figure 110F. Highest values between 1 and 3 are observed at the exterior part of the ascending aorta. Another large area of high shear stress ratio is observed at the initial part of the descending aorta.

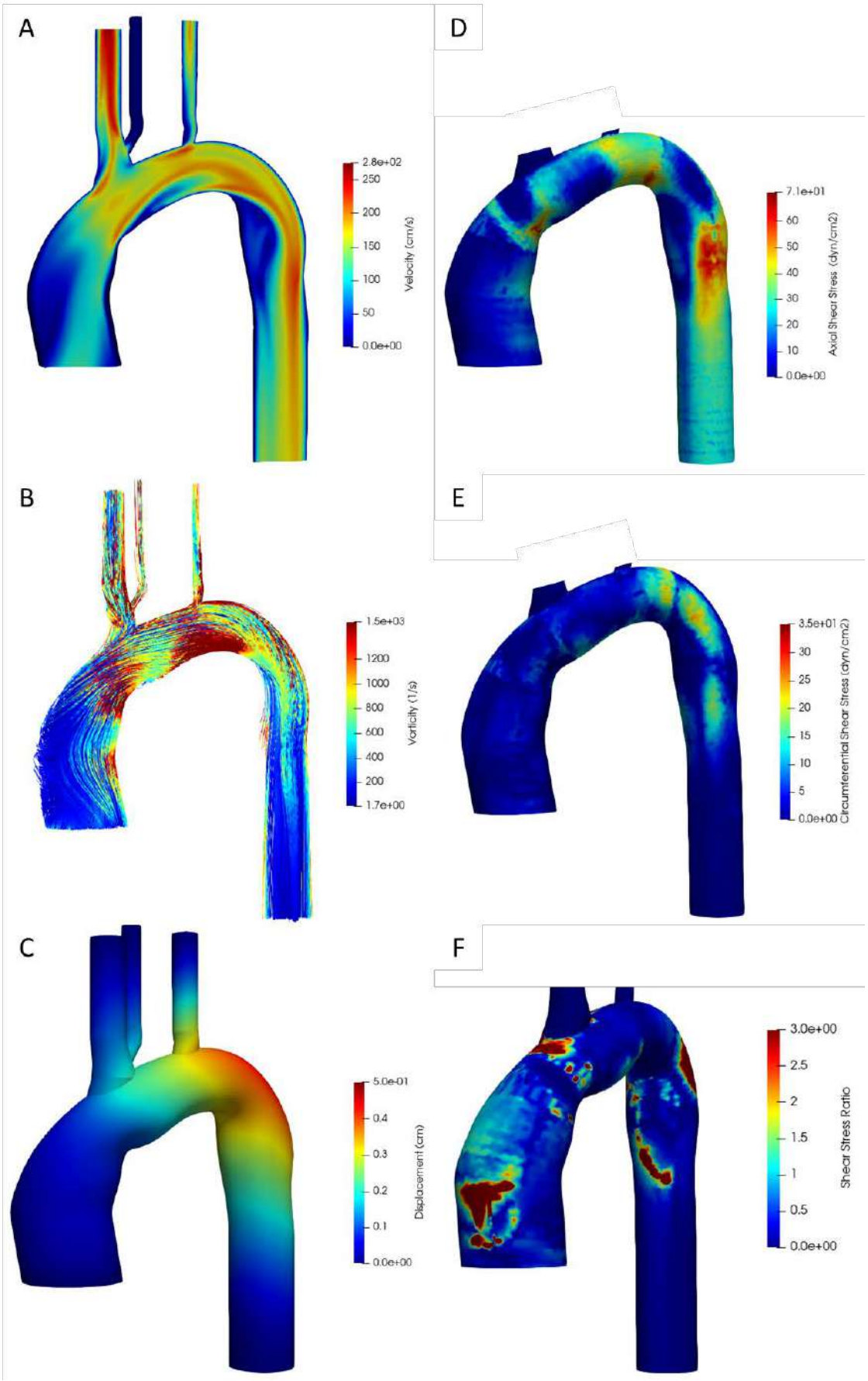

Figure 110. Fluid dynamic results of dilating patient 1; (A) velocity, (B) vorticity, (C) displacement, (D) axial shear stress, (E) circumferential shear stress and (F) shear stress ratio.

Dilating 2

Patient dilating 2 is a 36 years old male. Figure 111 shows the vessel geometry from MRI. Table 31 presents the values extracted and used in the Solidworks macro to reconstruct the vessel.

Figure 111. Visualization of D2 aorta with MRI using Mass.

	Nº Plane	X (mm)	Y (mm)	Z (mm)	r (mm)	δ (mm)
ASCENDING AORTA	1	0,0	0,0	0,0	17,0	2,0
	2	0,0	0,0	10,0	16,5	2,0
	3	1,0	-1,0	20,0	16,0	2,0
	4	2,0	0,0	30,0	16,0	2,0
	5	3,8	0,5	35,0	16,0	2,0
AORTIC ARCH	1	20,0	6,4	49,7	14,3	1,5
	2	27,5	11,2	53,6	13,4	1,5
	3	35,0	17,0	54,9	12,9	1,5
	4	42,5	22,6	54,8	12,4	1,5
	5	50,0	28,2	51,8	12,4	1,5
DESCENDING AORTA	1	62,5	35,2	35,0	11,5	1,5
	2	63,5	35,5	30,0	11,0	1,5
	3	65,0	36,5	20,0	11,0	1,5
	4	65,0	37,5	10,0	11,0	1,5
	5	65,0	37,5	0,0	11,0	1,5

Table 31. Geometry data extracted from MRI images to reconstruct D2 aorta in SolidWorks.

Figure 112A shows the reconstruction of the vessel in green and the wall in white. Figure 112B shows the mesh of the fluid domain and Figure 112C the mesh of the solid domain.

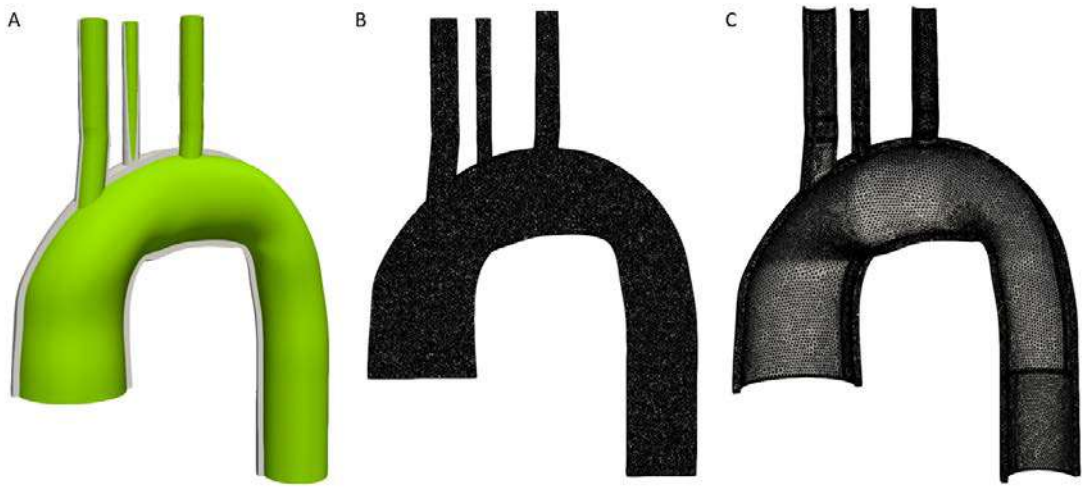

Figure 112. (A) Reconstruction of the aorta vessel and the wall, (B) meshing of the fluid and (C) meshing of the wall.

Minimum Jacobian criterion does not present negative values in the fluid mesh and neither in the solid mesh. The fluid mesh contains $1{,}91 \cdot 10^6$ elements and the solid mesh $6{,}60 \cdot 10^5$.

Figure 77 shows the flow curve at sinotubular junction and descending aorta extracted from MRI images.

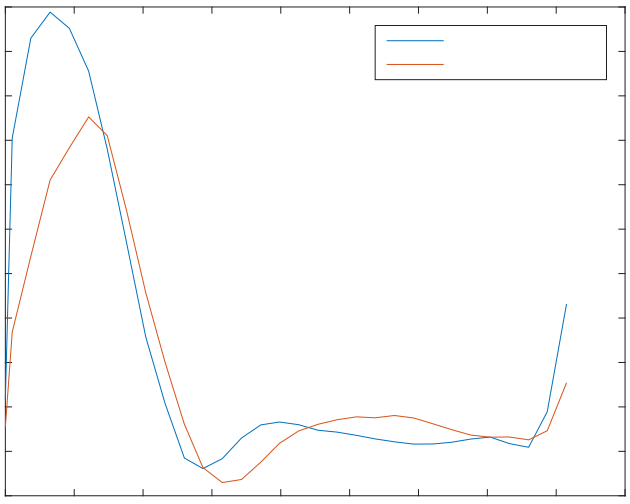

Figure 113. Flows at sinotubular junction and descending aorta with MRI technique of D2.

Figure 78 shows the flow profile extracted from 4D-MRI images at sinotubular junction and treated spatiotemporally in Matlab. The result flow curve is the inlet condition for the CFD and FSI simulations of dilating patient 2.

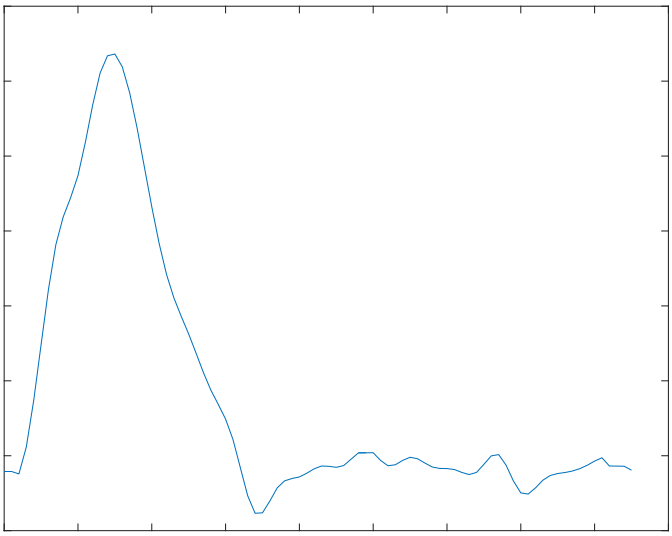

Figure 114. Flow curve of D2 at sinotubular junction after B-spline interpolation.

The flow profiles between MRI and 4D-MRI are similar when comparing Figure 113 and Figure 114. The duration of systolic and diastolic phases is the same in both techniques and maximum flow peak from MRI images is 494 ml/s and from 4D-MRI is 536 ml/s.

After imposing all the boundary conditions and meshing the geometries, CFD and FSI simulations are performed. Figure 79 shows the convergence of the FSI simulation.

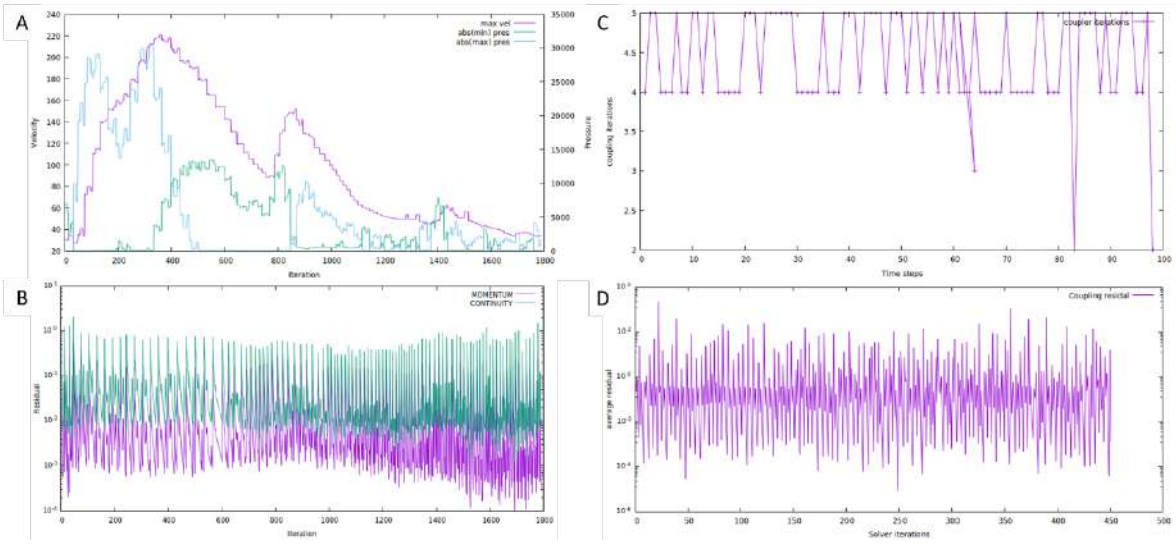

Figure 115. D2 FSI convergence of (A, B) the fluid, (C, D) the coupling.

Figure 115A shows that FSI simulation does not diverge at any point due to coherent values of maximum velocity. Figure 115B shows that all time steps reach the residual value desired and that the number of iterations per timestep is approximately 30 for systole and less than 10 for diastole. For the coupling, Figure 115C and Figure 115D, it

can be observed that most steps needed between 4 to 5 coupling iterations to converge and that residual is achieved in all time steps. With both simulations converged, flow ratio and PWV were compared to clinical data.

The flow ratio between the sinotubular junction and the descending aorta is iterated to match the flow ratio calculated from MRI data. The first FSI simulation (R=0 mmHg·s/cm^3) calculated a flow in descending aorta of 419 ml/s, which results in a flow ratio of 78,2%, close to the 76,1% expected. As the error is below 5% without the Windkessel, it has not been applied in dilating patient 2. Flow at the descending aorta in CFD without Windkessel is 421 ml/s, which results in a flow ratio of 78,5%, also below the 5% error. Clinical and final simulation values for flow are presented in Table 32.

Dilating 2	Flow Sinotubular Junction (ml/s)	Flow Descending (ml/s)	Flow ratio	Error (%)
MRI	494	376	76,1%	-
CFD	536	421	78,5%	2,4%
FSI	536	419	78,2%	2,1%

Table 32. Final flows at descending aorta and flow ratio of D2.

The PWV calculated using 4D-MRI is 21,8 m/s. Two iterations were required to reduce the error value below 5%. The values of the iterations can be seen in Table 33.

Dilating 2	E_0 (MPa)	PWV (m·s^{-1})	Error (%)
Clinical	-	21,8	-
Simulation 1	13,0	20,1	7,8
Simulation 2	14,1	20,8	4,6

Table 33. Young's modulus iterations to match clinical PWV of D2.

Young modulus for the first FSI simulation was estimated at 13,0 MPa after measuring 21,8 m/s as PWV from 4D-MRI data. After two iterations, the PWV value of 20,8 m/s was accepted and the Young's modulus of 14,1 MPa. PWV value of dilating patient 3 is the highest from the twelve cases analyzed, being close to double the second highest value (13,5 m/s). This high value makes perform FSI simulation as a CFD simulation due to low elasticity of the wall, no movement. This is not a normal value in young people (36 years old)[86].

The results of dilating patient 2 were analyzed after PWV and flow ratio were matched with the clinical data. Figure 116 presents the velocity field, vorticity, wall axial and

circumferential shear stresses, displacement of the wall and shear stress ratio at systolic peak (step 19).

Maximum velocities observed inside the aorta are 180 cm/s at systolic peak. The maximum velocity is located at the exterior part of the descending aorta. At the ascending aorta, the jet velocity is 110 cm/s and is orientated from the center of the vessel to the exterior part of the artery. Two areas of low velocities (<20 cm/s) can be observed at the interior part of the ascending and the descending aorta.

Vorticity streamlines are presented in Figure 116B. It can be observed that maximum vorticity values are at the initial part of the descending aorta with values reaching 1000 s^{-1}. The whole ascending aorta presents low values below 300 s^{-1} expect for the exterior part where there is an area of 600 s^{-1}.

Maximum displacement is observed at the aortic arch reaching values of 0,8 mm. It can be observed that the restriction of no displacement imposed at inlet and outlets surfaces is affecting the whole aorta with less realistic results.

Figure 116D and Figure 116E show the axial and circumferential shear stress respectively. Axial shear stress presents a large area of 20 dyn/cm^2 at the exterior part of the ascending aorta. Circumferential shear stress presents values below 5 dyn/cm^2 in most of the ascending aorta. At aortic arch, axial shear stress presents a large area of 20 to 40 dyn/cm^2 and circumferential shear stress presents a similar area with lower shears, 8 to 12 dyn/cm^2 at the interior part. At the descending aorta, axial shear stress presents a very large area between 15 and 35 dyn/cm^2. Oppositely, the circumferential shear stress is almost null in the whole descending aorta expect for a small area at the beginning of 10 dyn/cm^2.

The shear stress ratio is presented in Figure 116F. Values below 2 are observed in most of the domain. Two areas of high shear stress ratio are observed at the final part of the ascending aorta and of the aortic arch.

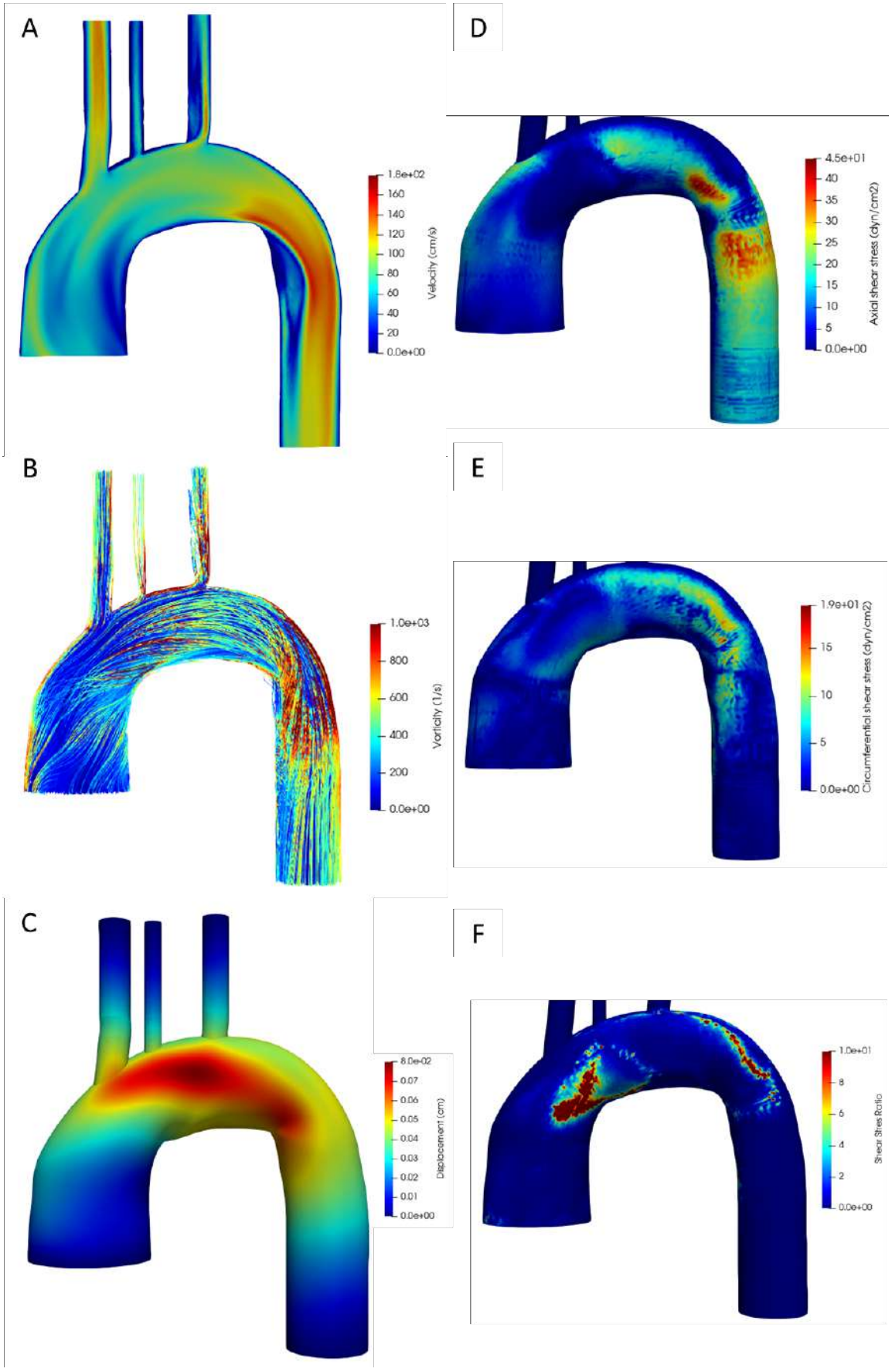

Figure 116. Fluid dynamic results of healthy control 4; (A) velocity, (B) vorticity, (C) displacement, (D) axial shear stress, (E) circumferential shear stress and (F) shear stress ratio.

Dilating 3

Patient dilating 3 is a 42 years old female. Figure 117 shows the vessel geometry from two MRI image, the final part of the aortic arch in the first image was not visible due to the high tortuosity of the vessel. Table 31 presents the values extracted and used in the Solidworks macro to reconstruct the vessel.

Figure 117. Visualization of D3 aorta with MRI using Mass.

	Nº Plane	X (mm)	Y (mm)	Z (mm)	r (mm)	δ (mm)
ASCENDING AORTA	1	0,0	0,0	0,0	15.5	2,0
	2	-1,0	1,0	10,0	15,5	2,0
	3	-2,0	2,0	20,0	15,8	2,0
	4	-1,0	4,0	30,0	16,0	2,0
	5	2,5	8,2	40,0	15,7	2,0
AORTIC ARCH	1	20,0	16,1	55,2	13,5	1,5
	2	25,0	21,7	58,7	13,0	1,5
	3	30,0	26,4	61,4	12,5	1,5
	4	35,0	30,0	64,0	12,3	1,5
	5	40,0	33,8	67,5	12,0	1,5
DESCENDING AORTA	1	57,6	34,2	40,0	11,2	1,5
	2	58,2	33,7	30,0	11,0	1,5
	3	58,0	33,0	20,0	11,0	1,5
	4	57,0	32,0	10,0	11,0	1,5
	5	56,0	31,0	0,0	11,0	1,5

Table 34. Geometry data extracted from MRI images to reconstruct D3 aorta in SolidWorks.

Figure 118A shows the reconstruction of the vessel in green and the wall in white. Figure 118B shows the mesh of the fluid domain and Figure 118C the mesh of the solid domain.

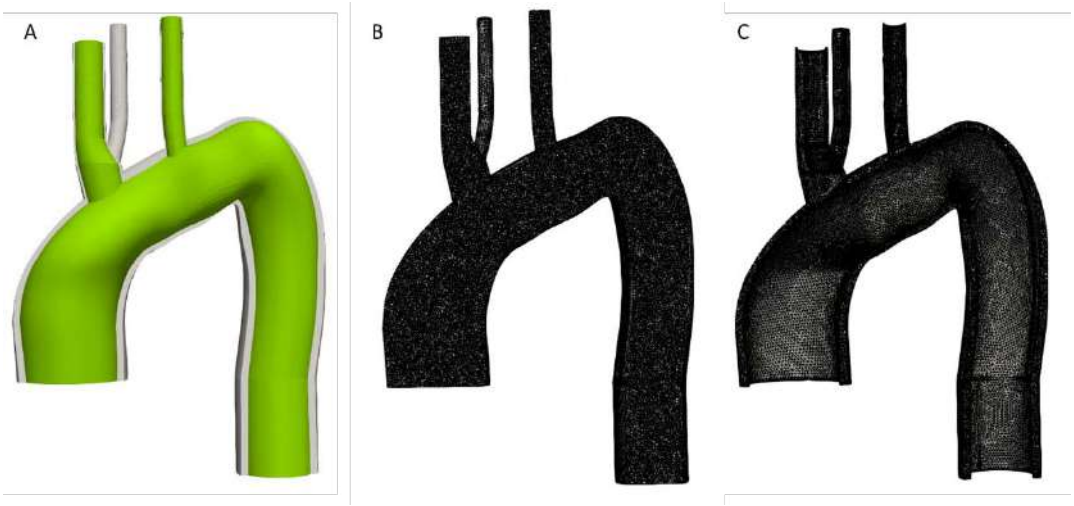

Figure 118. (A) Reconstruction of the aorta vessel and the wall, (B) meshing of the fluid and (C) meshing of the wall.

Minimum Jacobian criterion does not present negative values in the fluid mesh and neither in the solid mesh. The fluid mesh contains $1{,}40 \cdot 10^6$ elements and the solid mesh $4{,}96 \cdot 10^5$.

Figure 119 shows the flow curve at sinotubular junction and descending aorta extracted from MRI images.

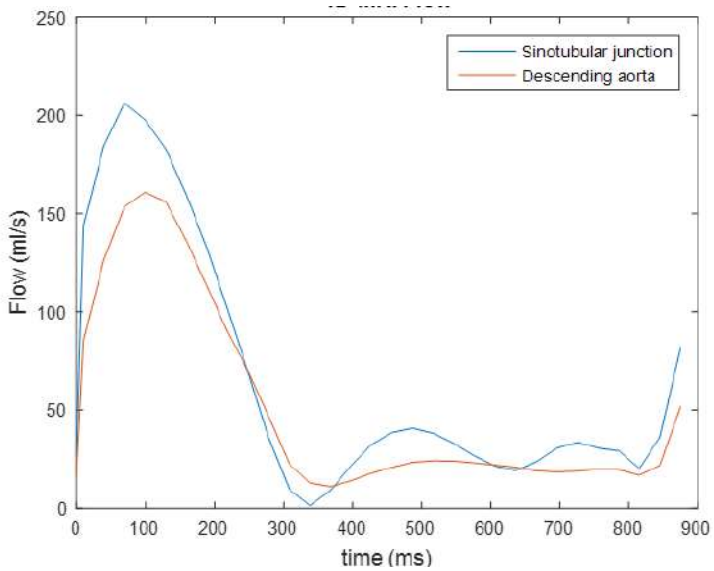

Figure 119. Flows at sinotubular junction and descending aorta with MRI technique of D3.

Figure 120 shows the flow profile extracted from 4D-MRI images at sinotubular junction and treated spatiotemporally in Matlab. The result flow curve is the inlet condition for the CFD and FSI simulations of dilating patient 3.

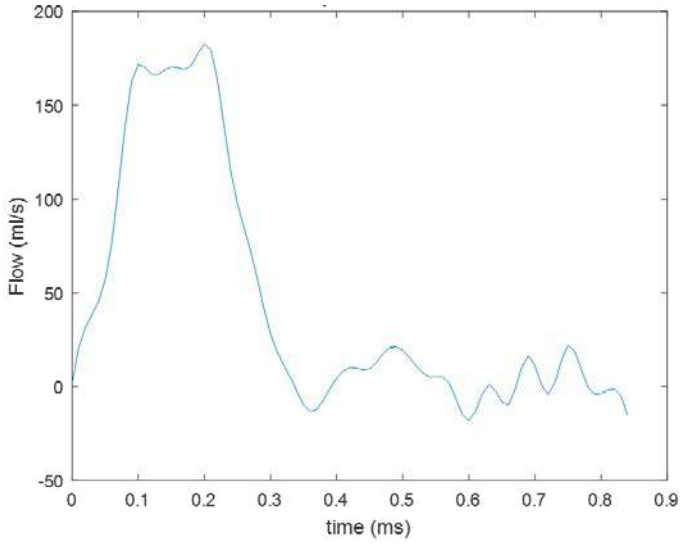

Figure 120. Flow curve of D3 at sinotubular junction after B-spline interpolation.

The flow profiles between MRI and 4D-MRI are different when comparing Figure 119 and Figure 120. The duration of systolic and diastolic phases is the same in both techniques, but at the systolic peak of 4D-MRI the maximum flow is maintained during 100 ms while MRI presents the typical peak. Moreover, there is a difference of 30 ml/s between both peaks.

After imposing all the boundary conditions and meshing the geometries, CFD and FSI simulations are performed. Figure 121 shows the convergence of the FSI simulation.

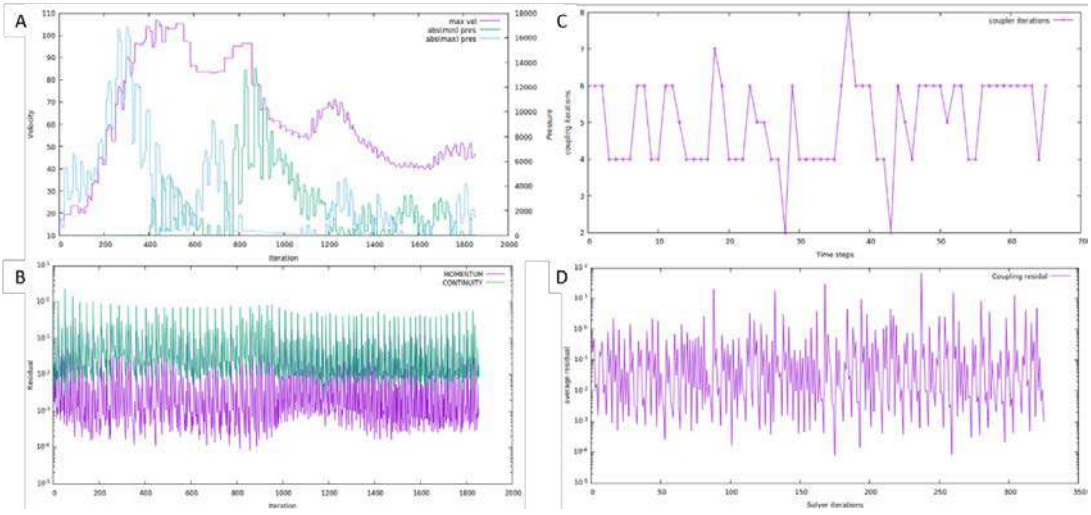

Figure 121. D3 FSI convergence of (A, B) the fluid, (C, D) the coupling.

Figure 121A shows that FSI simulation does not diverge at any point due to coherent values of maximum velocity. Figure 121B shows that all time steps reach the residual value desired and that the number of iterations per timestep is approximately 40 for

systole and 10 for diastole. For the coupling, Figure 121C and Figure 121D, it can be observed that most steps needed between 4 to 6 coupling iterations to converge and that residual is achieved in all time steps.

With both simulations converged, flow ratio and PWV were compared to clinical data. The flow ratio between the sinotubular junction and the descending aorta is iterated to match the flow ratio calculated from MRI data. The first FSI simulation (R=0 mmHg·s/cm^3) calculated a flow in descending aorta of 136 ml/s, which results in a flow ratio of 72%, close to the 78% expected. After applying a Windkessel of R=1500, flow at the descending aorta in CFD and FSI is 139 ml/s and 142 ml/s which results in a flow ratio of 73,5% and 75,1% respectively. Both errors are below 5%. Clinical and final simulation values for flow are presented in Table 35.

Dilating 3	Flow Sinotubular Junction (ml/s)	Flow Descending (ml/s)	Flow (%)	Error (%)
MRI	206	161	78,2%	-
CFD	189	139	73,5%	4,6%
FSI	189	142	75,1%	3,0%

Table 35. Final flows at descending aorta and flow ratio of D3.

The PWV calculated using 4D-MRI is 8,2 m/s. Two iterations were required to reduce the error value below 5%. The values of the iterations can be seen in Table 36.

Dilating 3	E_0 (kg·s^{-2}·m^{-1})	PWV (m·s^{-1})	Error (%)
Clinical	-	8,2	-
Simulation 1	2,16	7,2	12,2
Simulation 2	2,46	7,8	4,9

Table 36. Young's modulus iterations to match clinical PWV of C4.

Young modulus for the first FSI simulation was estimated at 2,16 MPa after measuring 5,8 m/s as PWV from 4D-MRI data. After two iterations, the PWV value of 7,8 m/s was accepted with the Young's modulus of 2,46 MPa.

The results of dilating patient 3 were analyzed after PWV and flow ratio were matched with the clinical data. Figure 122 presents the velocity field, vorticity, wall axial and circumferential shear stresses, displacement of the wall and shear stress ratio at systolic peak (step 20).

Maximum velocities observed inside the aorta are 90 cm/s at systolic peak. The maximum velocity is located at the brachiocephalic artery. At the ascending aorta, the jet velocity is 75 cm/s and is orientated from the center of the vessel to the exterior part of the artery. Four areas of low velocities (<20 cm/s) can be observed. The largest one is located at the interior part of the ascending aorta.

Vorticity streamlines are presented in Figure 122B. The whole aorta presents a vorticity below 200 s^{-1}, lower than other cases. Few streamlines present values of 500 s^{-1}, especially in the aortic arch.

Maximum displacement is observed at the final part of the aortic arch and at the initial part of the descending aorta reaching values of 2 mm. It can be observed that the restriction of no displacement imposed at inlet and outlets surfaces is affecting the whole aorta with less realistic results.

Figure 122D and Figure 122E show the axial and circumferential shear stress respectively. Axial shear stress presents a large area of 10 dyn/cm^2 along the exterior part of the ascending aorta. Circumferential shear stress also presents values from 3 to 6 dyn/cm^2 at the same zone. At aortic arch, axial shear stress presents values below 4 dyn/cm^2 expect for a small area of 10 dyn/cm^2. Circumferential shear stress presents a large area of 5 dyn/cm^2 at the interior part. At the descending aorta, axial shear stress presents a very large area between 7 and 15 dyn/cm^2. Oppositely, the circumferential shear stress is almost null in the whole descending aorta expect for an area at the beginning of 7 dyn/cm^2.

The shear stress ratio is presented in Figure 122F. Multiple areas of high shear stress ratio are observed along the aorta. The largest one is located at the initial part of the ascending aorta and the second one is also located at the ascending aorta but closer to the aortic arch.

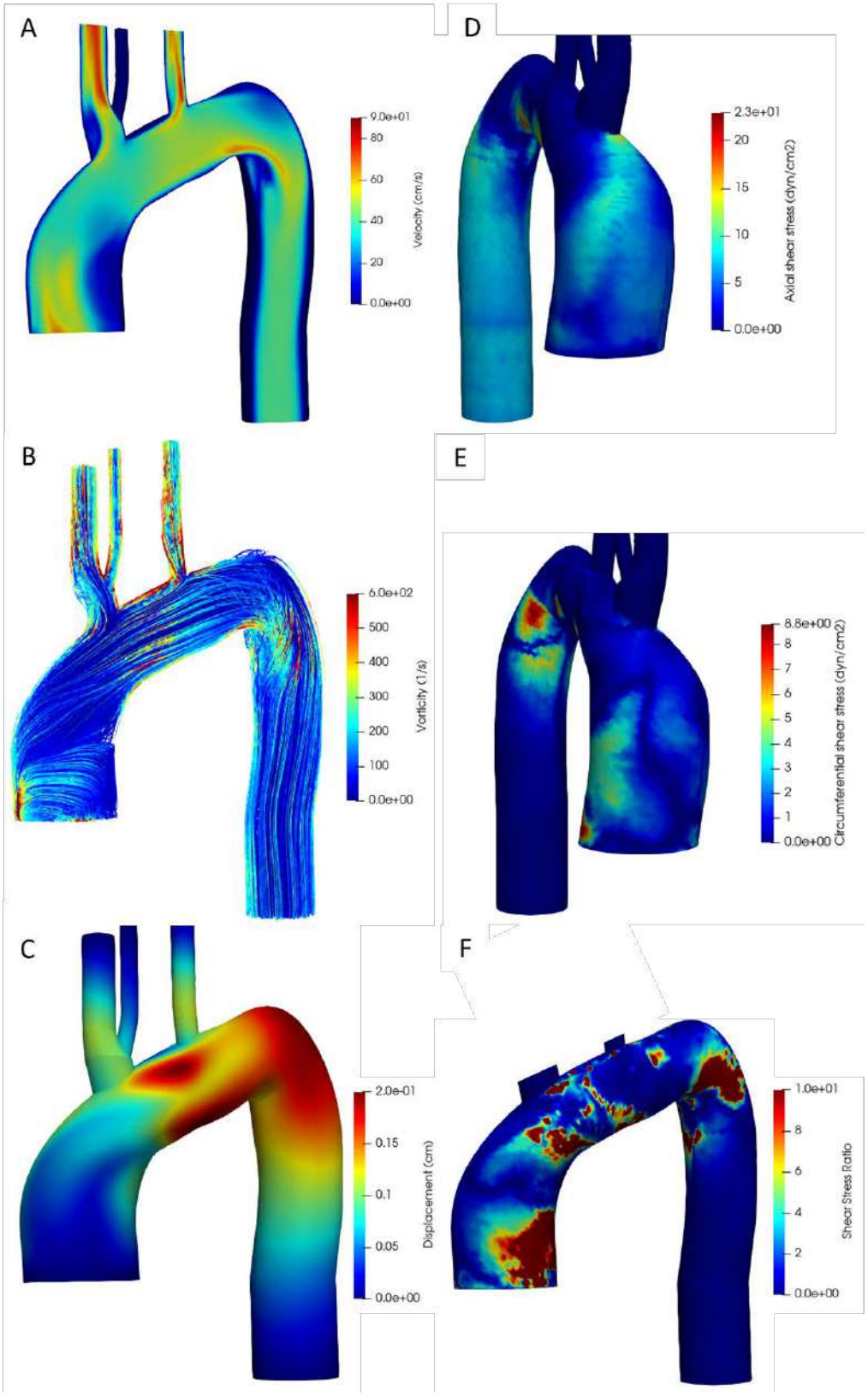

Figure 122**.** Fluid dynamic results of dilating patient 3; (A) velocity, (B) vorticity, (C) displacement, (D) axial shear stress, (E) circumferential shear stress and (F) shear stress ratio.

Dilating 4

Patient dilating 3 is a 40 years old male. Figure 123 shows the vessel geometry from two MRI images, the aortic arch in the first image was not visible due to the high tortuosity of the vessel. Table 37 presents the values extracted and used in the Solidworks macro to reconstruct the vessel.

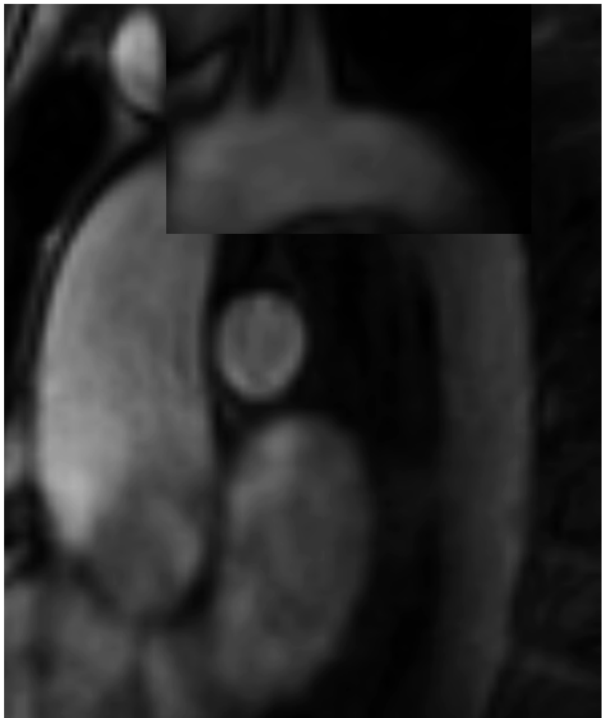

Figure 123. Visualization of D4 aorta with MRI using Mass.

	Nº Plane	X (mm)	Y (mm)	Z (mm)	r (mm)	δ (mm)
ASCENDING AORTA	1	0,0	0,0	0,0	19,5	2,0
	2	0,0	1,0	10,0	20,0	2,0
	3	1,0	3,0	20,0	19,7	2,0
	4	1,0	6,0	30,0	19,3	2,0
	5	1,5	11,3	40,0	18,8	2,0
AORTIC ARCH	1	22,5	30,3	58,8	14,2	1,5
	2	28,0	32,7	60,0	13,4	1,5
	3	33,5	34,0	61,0	13,0	1,5
	4	39,0	34,7	61,4	13,0	1,5
	5	45,0	36,6	60,4	13,0	1,5
DESCENDING AORTA	1	64,0	34,0	40,0	13,0	1,5
	2	67,0	32,0	30,0	13,0	1,5
	3	69,0	32,0	20,0	13,0	1,5
	4	71,0	33,0	10,0	13,0	1,5
	5	73,0	33,0	0,0	13,0	1,5

Table 37. Geometry data extracted from MRI images to reconstruct D4 aorta in SolidWorks.

Figure 124A shows the reconstruction of the vessel in green and the wall in white. Figure 124B shows the mesh of the fluid domain and Figure 124C the mesh of the solid domain.

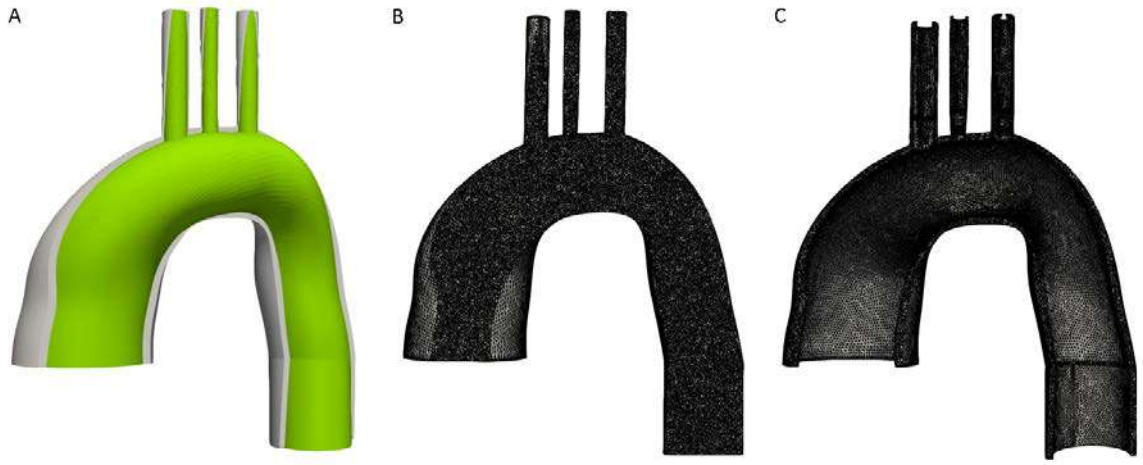

Figure 124. (A) Reconstruction of the aorta vessel and the wall, (B) meshing of the fluid and (C) meshing of the wall.

Minimum Jacobian criterion does not present negative values in the fluid mesh and neither in the solid mesh. The fluid mesh contains $1{,}91 \cdot 10^6$ elements and the solid mesh $5{,}67 \cdot 10^5$.

Figure 125 shows the flow curve at sinotubular junction and descending aorta extracted from MRI images.

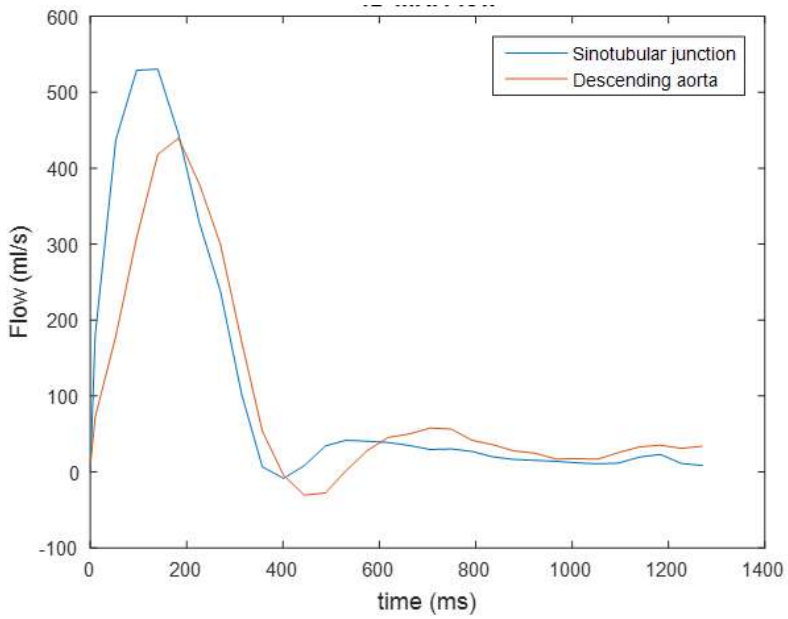

Figure 125. Flows at sinotubular junction and descending aorta with MRI technique of D4.

Figure 126 shows the flow profile extracted from 4D-MRI images at sinotubular junction and treated spatiotemporally in Matlab. The result flow curve is the inlet condition for the CFD and FSI simulations of dilating patient 4.

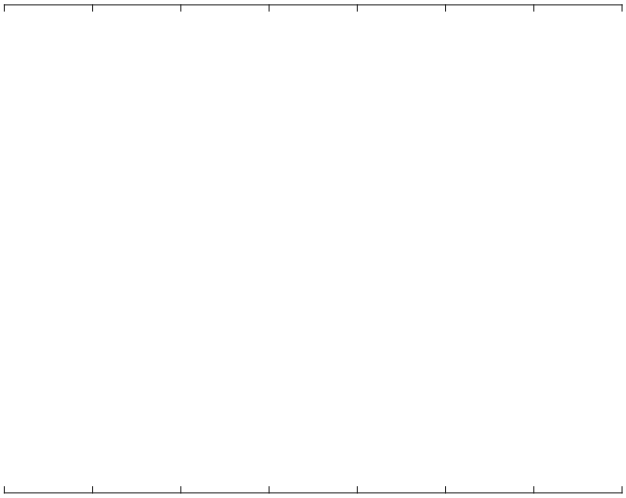

Figure 126. Flow curve of D4 at sinotubular junction after B-spline interpolation.

The flow profiles between MRI and 4D-MRI are different when comparing Figure 125 and Figure 126. The duration of systolic and diastolic phases is the same in both techniques, but the systolic peak differs in 30 ml/s and at the beginning of diastole the negative peak of 4D-MRI is higher than the peak observed in MRI, 75 ml/s and 9 ml/s respectively. Moreover, most of the diastolic phase presents negative flows from 4D-MRI data while flow is always close to 0 in MRI.

After imposing all the boundary conditions and meshing the geometries, CFD and FSI simulations are performed. Figure 127 shows the convergence of the FSI simulation.

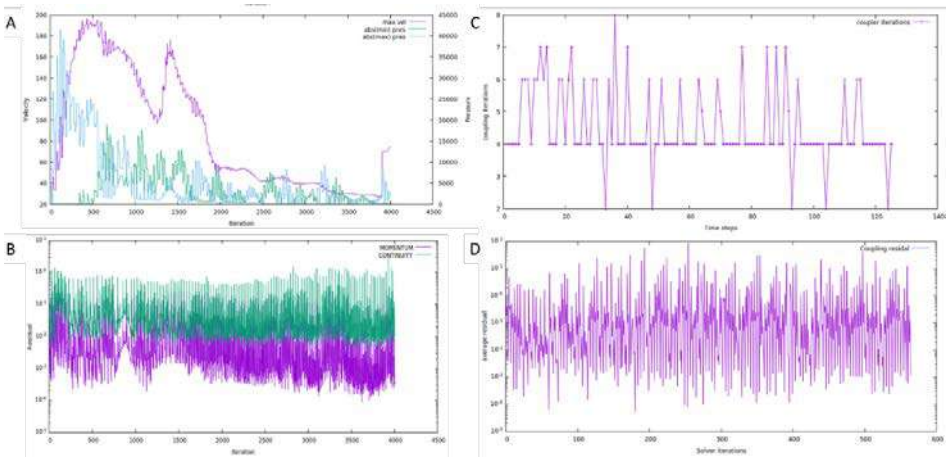

Figure 127. D4 FSI convergence of (A, B) the fluid, (C, D) the coupling.

Figure 127A shows that FSI simulation does not diverge at any point due to coherent values of maximum velocity. Figure 127B shows that most of the time steps reach the residual value desired, except for 7 steps between iteration 750-1000, and that the number of iterations per timestep is approximately 60 for systole and 15 for diastole. For the coupling, Figure 127C and Figure 127D, it can be observed that most steps needed between 4 to 6 coupling iterations to converge and that residual is achieved in all time steps.

With both simulations converged, flow ratio and PWV were compared to clinical data. The flow ratio between the sinotubular junction and the descending aorta is iterated to match the flow ratio calculated from MRI data. The first FSI simulation (R=0 mmHg·s/cm^3) calculated a flow in descending aorta of 472 ml/s, which results in a flow ratio of 84%, close to the 83% expected. As results being so close, no Windkessel were applied at dilating patient 4. Clinical and final simulation values for flow are presented in Table 38.

Dilating 4	Flow Sinotubular Junction (ml/s)	Flow Descending (ml/s)	Flow (%)	Error (%)
MRI	530	439	82,8%	-
CFD	561	476	84,8%	2,0%
FSI	561	472	84,1%	1,3%

Table 38. Final flows at descending aorta and flow ratios of D4.

The PWV calculated using 4D-MRI is 11,5 m/s. Three iterations were required to reduce the error value below 5%. The values of the iterations can be seen in Table 39.

Dilating 4	E_0 (MPa)	PWV (m·s^{-1})	Error (%)
Clinical	-	11,5	-
Simulation 1	3,40	13,4	16,5
Simulation 2	2,92	12,7	10,4
Simulation 3	2,64	12,0	4,2

Table 39. Young's modulus iterations to match clinical PWV of D4.

Young modulus for the first FSI simulation was estimated at 3,4 MPa. After three iterations, the PWV value of 12,0 m/s was accepted with the Young's modulus of 2,64 MPa.

The results of dilating patient 4 were analyzed after PWV and flow ratio were matched with the clinical data. Figure 128 presents the velocity field, vorticity, wall axial and circumferential shear stresses, displacement of the wall and shear stress ratio at systolic peak (step 13).

Maximum velocities observed inside the aorta are 170 cm/s at systolic peak. The maximum velocity is located at the center of the descending aorta. At the ascending aorta, the jet velocity is 80 cm/s and is orientated to the exterior part of the artery. One large area of low velocities (<20 cm/s) can be observed at the interior part of the ascending aorta.

Vorticity streamlines are presented in Figure 128B. It can be observed that maximum vorticity values are at the descending aorta with values reaching 800 s^{-1}. The whole ascending aorta presents low values below 200 s^{-1}. Maximum displacement is observed at the initial part of descending aorta reaching values of 1,5 mm, 5% of the diameter.

Figure 128D and Figure 128E show the axial and circumferential shear stress respectively. Axial and circumferential shear stress present values below 5 dyn/cm^2 at the whole ascending aorta. At aortic arch, axial shear stress presents an area of 15 dyn/cm^2 at the anterior part and circumferential shear stress presents a small area at the interior part of 8 dyn/cm^2 at the interior part. At the descending aorta, axial shear stress presents an area between 20 and 30 dyn/cm^2 but it is not as homogenous as previous cases. Oppositely, the circumferential shear stress which in previous cases was really low, in dilating patient 4 present two areas of 13 dyn/cm^2.

The shear stress ratio is presented in Figure 128F. Distal ascending aorta is presenting a large area above 8. Null values are observed in the aortic arch and two small areas in the descending aorta.

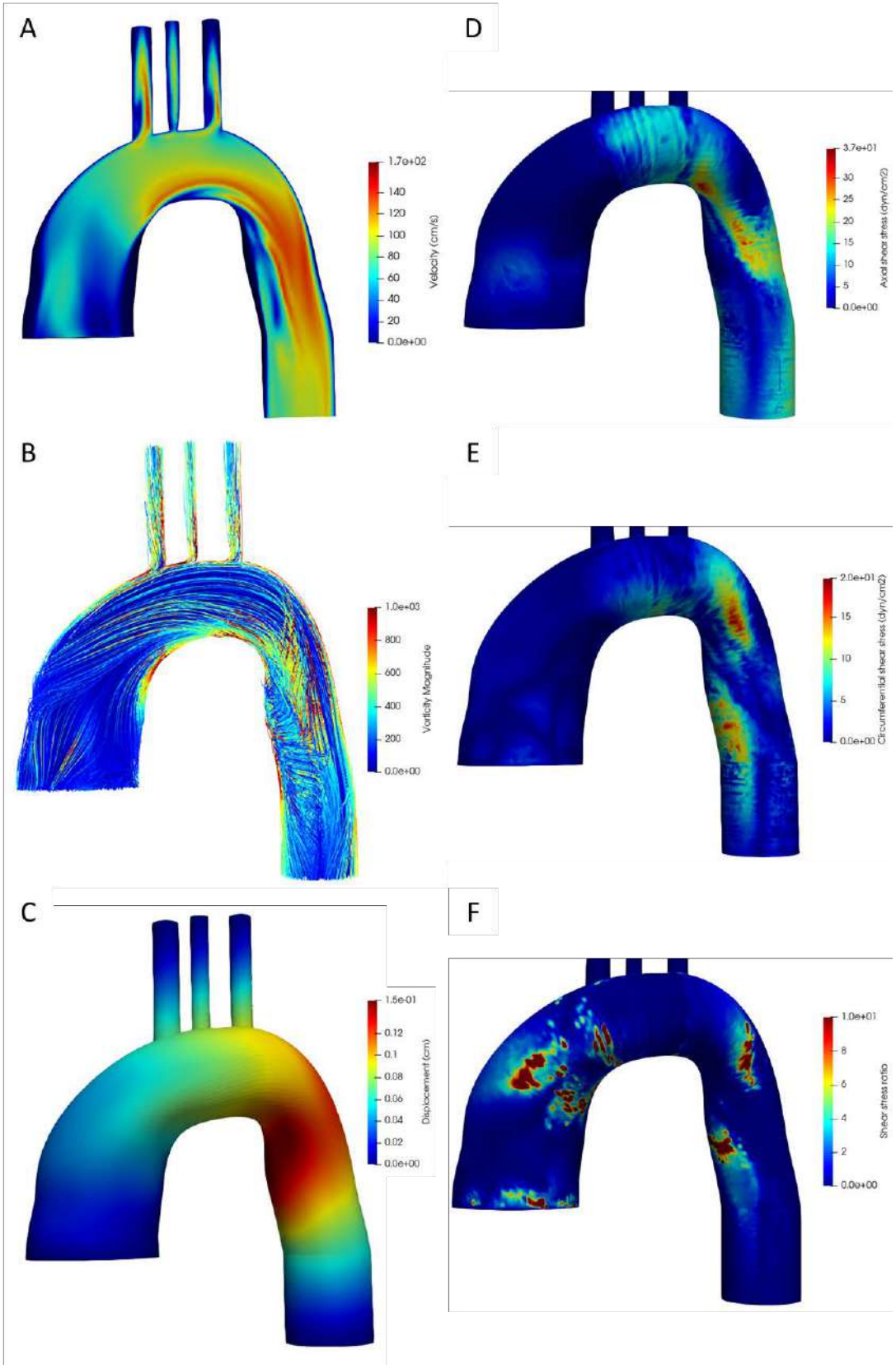

Figure 128. Fluid dynamic results of dilating patient 4; (A) velocity, (B) vorticity, (C) displacement, (D) axial shear stress, (E) circumferential shear stress and (F) shear stress ratio.

3.4. Windkessel Effect

Flow distribution extracted from MRI images was compared to 4D-MRI data to observe the difference between both medical techniques. 4D-MRI data was used to impose the inlet flow at the ascending aorta but was not available at the descending aorta. MRI was available at both ends so, coherently; MRI was the source to analyze flow ratio between both ends of the aorta. However, as it was 4D-MRI that was imposed as boundary condition, it was important to understand its relation to MRI data.

Figure 129 shows the correlation between flow extracted from MRI and 4D-MRI, with a quadratic error of 0,94. The difference observed between both techniques at systolic peak are because contours are created manually and factors such as grey scale and luminosity affect the visualization of the perimeter. Moreover, both techniques do not acquire and process the data in the same way, so error is increased.

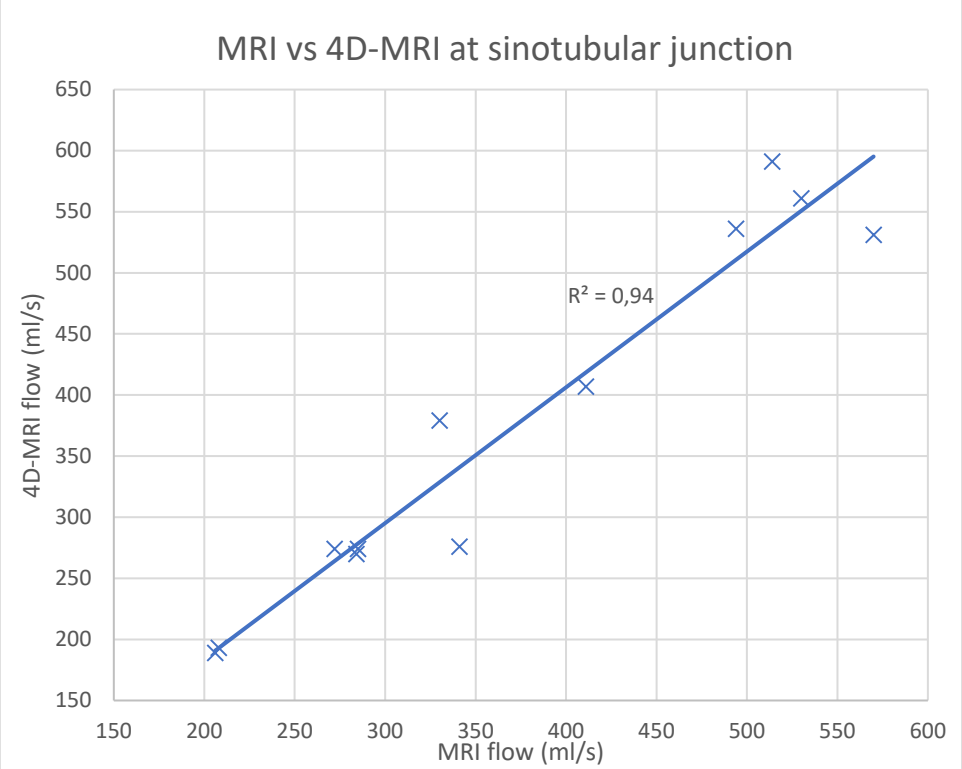

Figure 129. Comparison of flow extracted from MRI images versus 4D-MRI images at systolic peak.

Every flow ratio measured using MRI and those simulated by CFD and FSI are presented individually for each case in section 3.3. The Windkessel effect was applied evenly on the three supra-aortic branches as no clinical data on their respective flow was available. Coherently, blood not flowing through the descending aorta was proportionally distributed across the supra-aortic branches according to their respective diameters.

The flow ratio between descending and ascending aorta is compared in Figure 130. The statistical analysis shows strong correlations for both simulations, FSI with a quadratic error of 0.921 and 0.910 for CFD, supporting the use of Windkessel boundary conditions to match the simulations with the clinical data.

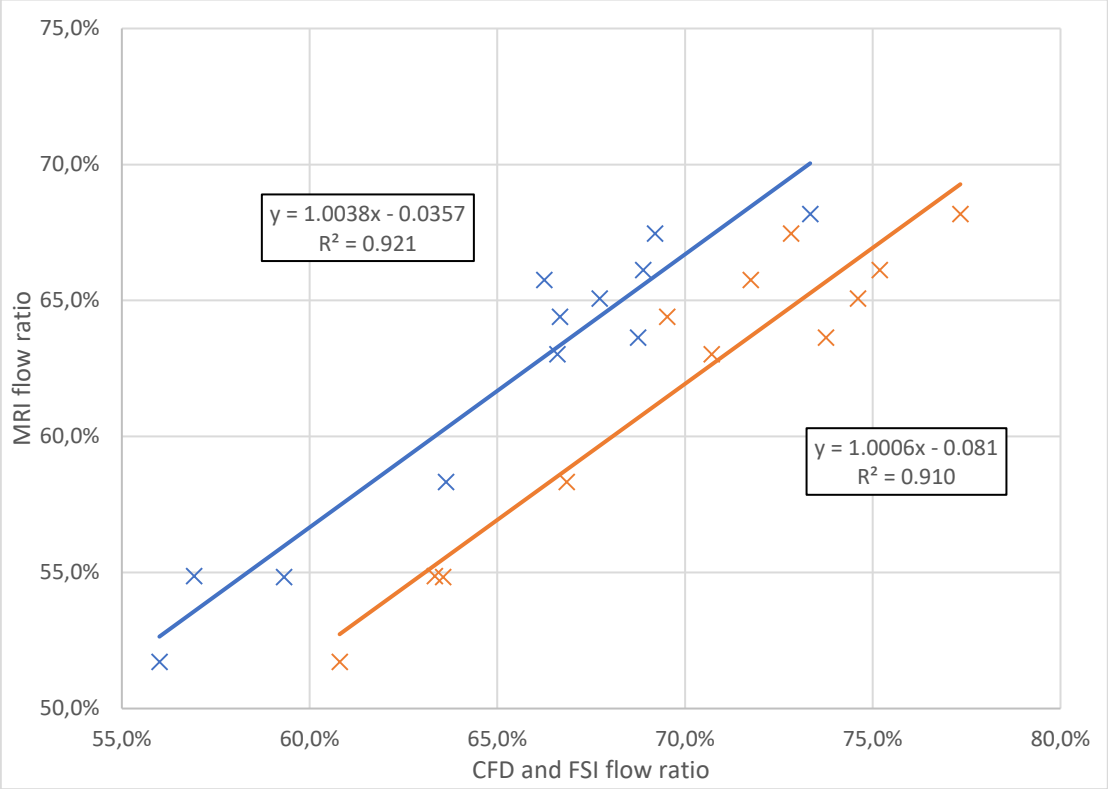

Figure 130. Flow ratio of CFD and FSI simulations versus MRI.

3.5. Pulse Wave Velocity

Elasticity of the aorta is a critical parameter to determine its biomechanical status. 4D-flow derived PWV was the starting point of an iterative process aimed to define the Young's modulus of the aorta and to minimize the difference between FSI and 4D-MRI derived PWV. Every PWV measured using 4D-MRI and that imposed in FSI are presented individually for each case in section 3.3.

As seen, after three iterations or less, the estimated PWV closely matched the PWV measured *in vivo*. Simulated and measured PWV were highly correlated (R^2=0.991) as shown in Figure 131, showing the strength of our method.

The use of anisotropic model instead of hyperelastic model, which may better reproduce the movement of the aorta, is a limitation. However, the extraction of patient-specific hypereleastic model parameters is, to the best of our knowledge, not feasible non-invasively.

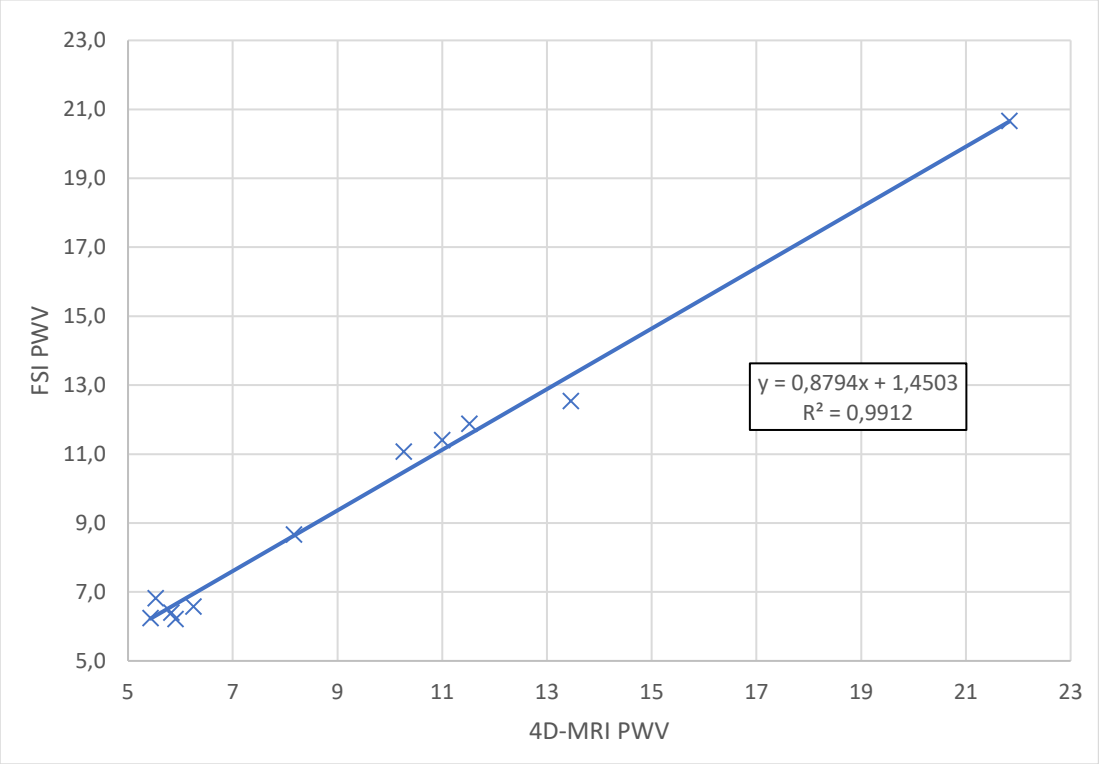

Figure 131. PWV calculated from 4D-MRI versus FSI simulation.

3.6. Primary fluidodynamic parameters

In this section, maximum velocity, jet angle and normalized displacement measured from 4D-MRI images are compared to CFD and FSI simulations. The comparison of these parameters between simulations has helped discerning the importance of adding the wall motion coupling; in the end, deciding how critical using complex FSI simulations versus simpler and more cost-effective CFD simulations. Table 40, Table 41 and Table 42 contain the comparison of normalized displacement, jet angle and maximum velocity calculated from 4D-MRI images versus those simulated with CFD or FSI respectively.

	Normalized Displacement					
	Ascending Plane			Descending Plane		
	4D-MRI	CFD	FSI	4D-MRI	CFD	FSI
C1	-	-	-	-	-	-
C2	0,026	0,017	0,022	0,052	0,045	0,048
C3	0,041	0,034	0,037	0,017	0,019	0,016
C4	0,046	0,037	0,045	0,035	0,031	0,032
S1	0,036	0,044	0,047	0,040	0,036	0,039
S2	0,040	0,046	0,042	0,032	0,035	0,035
S3	0,056	0,062	0,053	0,057	0,062	0,060
S4	0,041	0,037	0,043	0,037	0,033	0,036
D1	0,061	0,054	0,058	0,036	0,031	0,033
D2	0,038	0,045	0,041	0,031	0,028	0,030
D3	0,069	0,057	0,064	0,048	0,043	0,044
D4	0,094	0,068	0,078	0,030	0,023	0,025

Table 40. Normalized displacement calculated from 4D-MRI, CFD and FSI simulations in both planes.

	Jet Angle (º)					
	Ascending Plane			Descending Plane		
	4D-MRI	CFD	FSI	4D-MRI	CFD	FSI
C1	-	-	-	-	-	-
C2	6,4	5,2	5,9	9,2	7,8	8,4
C3	7,2	6,3	6,7	8,5	7,6	8,1
C4	4,3	4,8	4,6	2,9	4,3	3,6
S1	14,7	9,3	9,7	5,3	4,5	5,2
S2	8,8	7,2	7,5	11,6	8,7	9,7
S3	7,3	7,6	7,1	6,9	6,1	6,6
S4	9,8	8,0	8,8	4,7	5,5	5,3
D1	7,7	9,5	8,9	5,8	4,9	5,3
D2	5,0	5,5	5,2	7,5	6,2	6,9
D3	11,2	9,3	10,4	5,9	7,4	6,3
D4	17,6	13,4	14,1	7,9	6,6	7,2

Table 41. Jet angle calculated from 4D-MRI, CFD and FSI simulations in both planes.

	Maximum Velocity (cm/s)					
	Ascending Plane			Descending Plane		
	4D-MRI	CFD	FSI	4D-MRI	CFD	FSI
C1	-	-	-	-	-	-
C2	126	142	136	122	133	128
C3	157	148	154	139	151	146
C4	131	137	135	125	136	129
S1	133	125	121	166	127	131
S2	122	134	128	127	138	133
S3	161	152	157	155	169	162
S4	120	132	125	131	122	125
D1	143	156	151	140	148	143
D2	127	137	132	157	167	161
D3	96	112	106	78	97	94
D4	117	131	128	103	114	109

Table 42. Maximum velocity calculated from 4D-MRI, CFD and FSI simulations in both planes.

With the collected data we were able to calculate the relative errors of both techniques, revealing that, consistently, FSI accomplished a significant error reduction in both planes. All differences were statically significant ($p<0.05$), except for jet angle at ascending plane ($p=0.18$). These results are presented in Table 43 for the ascending aortic plane and Table 44 for the descending aortic plane. Figure 132 presents a bar diagram and their error reduction for ascending and descending plane for each parameter studied. Consequently, in this thesis, all derived fluidodynamic parameters were obtained from FSI simulations. Although it is true that FSI outperforms CFD, CFD is still valid for preliminary studies as their absolute errors are all below 20%. This can be acceptable for initial estimations.

Ascending Aorta Percentage Difference Reduction				
	Average CFD Simulation Error (%)	Average FSI Simulation Error (%)	Error Reduction (%)	p
Normalized Displacement	18.5 ± 2.3	10.0 ± 2.5	46.0	<0.01
Jet Angle	1.8 ± 0.5	1.3 ± 0.5	27.7	0,18
Maximum Velocity	9.1 ± 1.1	5.7 ± 0.9	37.3	0,02

Table 43. Error reduction of FSI versus CFD at the ascending aortic plane.

Descending Aorta Percentage Difference Reduction				
	Average CFD Simulation Error (%)	Average FSI Simulation Error (%)	Error Reduction (%)	P
Normalized Displacement	12.1 ± 1.2	7.1 ± 1.2	40.9	<0.01
Jet Angle	1.3 ± 0.2	0.6 ± 0.1	50.5	<0.01
Maximum Velocity	11.2 ± 2.0	7.3 ± 2.1	34.6	<0.01

Table 44. Error reduction of FSI versus CFD at the descending aortic plane.

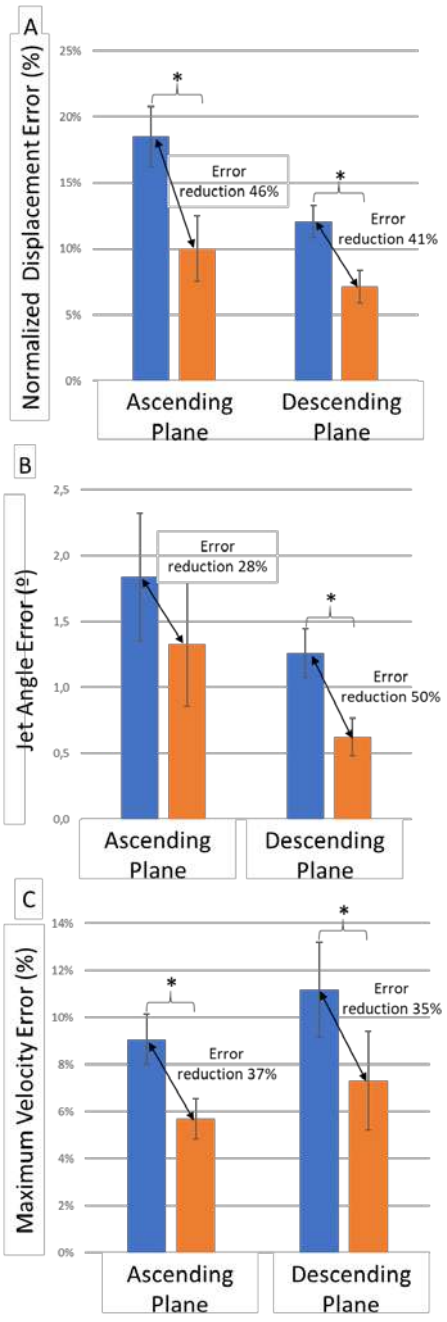

Figure 132. Comparison between 4D-MRI and both simulation of (A) normalized displacement, (B) jet angle and (C) maximum velocity in ascending and descending planes.

3.7. Secondary fluidodynamic parameters

This section analyzes the results of derived fluidodynamic parameters at systolic peak such as axial and circumferential shear stress, vorticity and shear stress ratios, which were hypothesized as candidate predictors of aneurysm progression. It is remarkable that the method to calculate shear stress evolved along this thesis and the results of this evolution are presented. At the end of this evolution, it was decided to present all cases in circumferences with the mean superficial value calculated by dividing the aorta in three parts; ascending aorta, aortic arch and descending aorta, and each part divided again in four quadrants; anterior, posterior, exterior and interior as showed and explained in Methods 2.3.2.

3.7.1 Methodology of shear stress calculation

During the thesis, two methods have been developed to calculate shear stress in the aorta. Although these equations are relatively simple, the development of a method to calculate shear stress from randomly distributed discrete data was challenging.

Both methods use central derivatives to resolve the derivative term of the shear stress equation as explained in Methods 2.3.2. However, the two methods differed in the treatment of the discrete data to apply the derivative. The division of the aorta in a grid of rectangles made the calculation possible, but the first method, which defines the velocity of the rectangle as the average velocity of all the nodes inside the rectangle, presented some difficulties to show smooth and errorless results. Some rectangles presented aberrant results because there were no nodes inside the rectangle, resulting in a NaN value which was visualized as 0 in Paraview.

With a year of experience calculating shear stress with the initial methods, our group thought that the errors were too widespread, and an evolution of the method was deemed. Using a grid data from the discrete data was the basic idea to evolve the method. Grid data would interpolate extra points to ensure that no rectangles presented NaN values and then apply central derivatives without the risk of errors. This strategy created smaller rectangles, improving the smoothness and accuracy of the displayed results.

The following figures present the results of the shear stress calculation in aneurysm affected aorta using the initial and the final code. The results presented correspond to the tangential and the circumferential shear stress at systolic peak. The results of axial and circumferential shear stress with both methods are presented in Figure 133 and Figure 134 respectively.

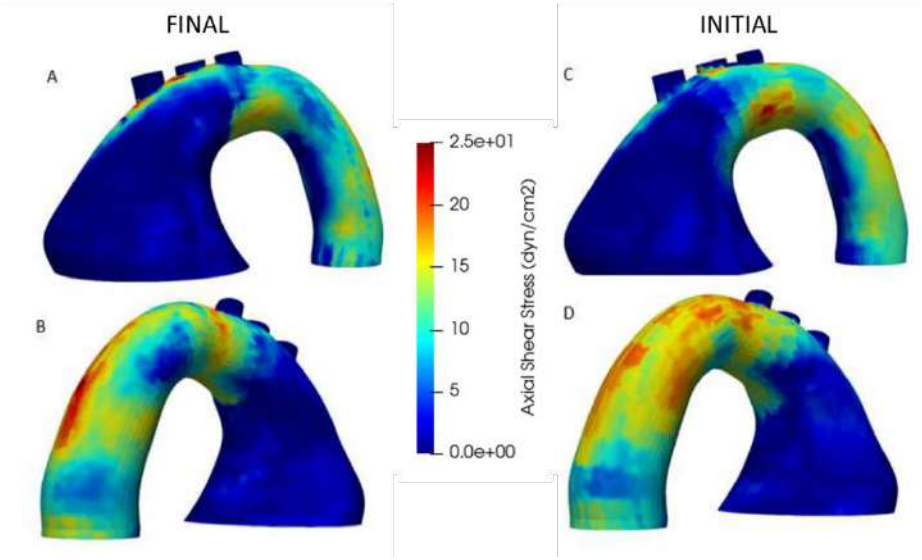

Figure 133. Visualization of axial shear stress with the old and the new method.

In the anterior face of the aorta (Figure 133A and Figure 133C), the zones with high tangential shear stress are located in the same region for both calculations, but the absolute values are lower with the final method. In the posterior face of the aorta, the zones with high shear stress were initially more extended along the aortic wall but got more concentrated with the final method.

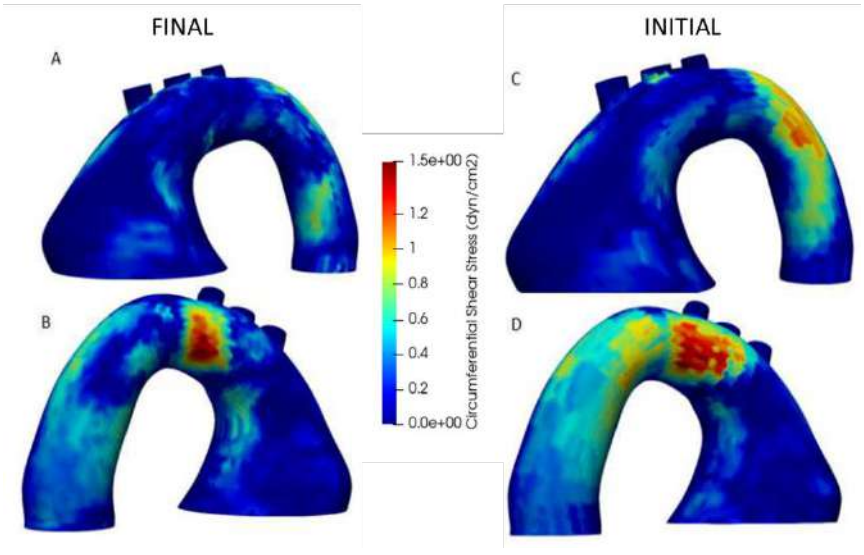

Figure 134. Visualization of circumferential shear stress with the old and the new method.

In the anterior face of the aorta (Figure 134A and Figure 134C), the evolution of the method is quite significant. Initially, we estimated a large zone with a shear stress above 0.9 dyn/cm^2. This zone became smaller, with lower shear stress values and more proximal to the descending aorta. In the posterior face of the aorta, the region with higher shear stress was in similar zones using both methods. However, this zone became smaller after refining the method, while the absolute values did not change appreciably.

In conclusion, the evolved strategy delivered slightly lower shear stress, and the regions of high shear stress became smaller. This is probably due to the improvement of the calculation precision caused by the increase of divisions. The visualization of the results also improved notably, with smoother transitions and the elimination of delimited rectangles visualization.

It is important to discuss that shear stress (and further derived parameters) were not compared to medical data. Despite the availability of medical data extracted from 4D-MRI of axial and circumferential shear stress, the significant differences in resolution and methods impeded an adequate comparison.

3.7.2 Axial and Circumferential Shear Stresses and Vorticity analysis

Axial and circumferential shear stresses and vorticity were derived from the velocity results of FSI simulations. The first parameter studied was wall axial shear stress and Figure 135 presents the mean value of each group of cases. The values are presented in dyn/cm^2.

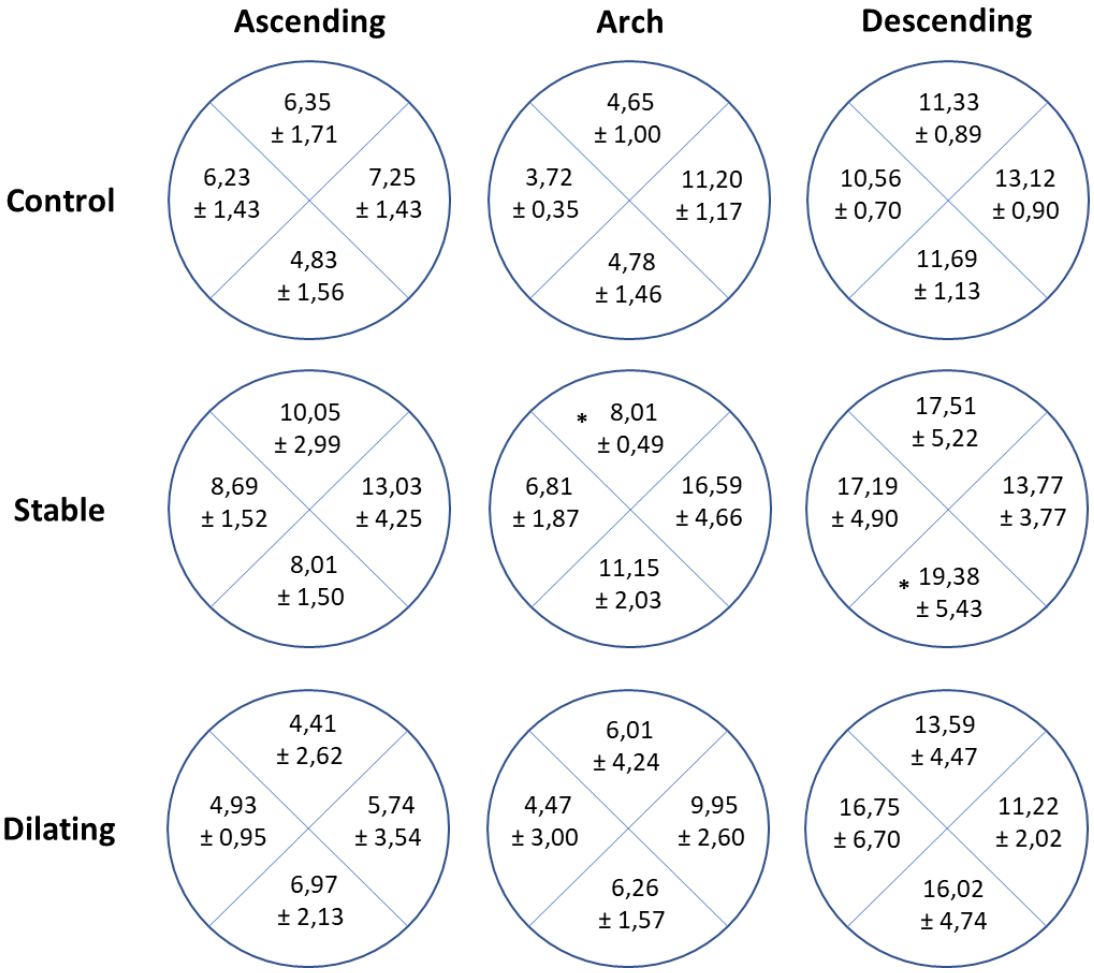

Figure 135. Axial shear stress in healthy controls and stable and dilating patients at the ascending aorta, aortic arch and descending aorta.

At systolic peak, the mean axial shear stress presented clear differences between controls and stable patients but not between controls and dilating patients. At the ascending aorta, maximum volumetric mean value of 7.25±1.43 dyn/cm^2 and 13.03±4.25 dyn/cm^2 of healthy controls and stable patients respectively is presented at the interior quarter while dilating patients presented the maximum value at the anterior quadrant of 6.97±2.13 dyn/cm^2. The stable patients presented higher values in all quadrant respectively controls and dilating patients.

At the aortic arch, maximum values increased in all cases. In healthy controls, the maximum value increased to 11.20±1.17 dyn/cm^2 at interior quarter, even tough, in the remaining three quadrants decreased. In exterior and posterior quarters, the mean values decreased approximately 50% while in anterior quarter the mean value reduced slightly. In stable patients something similar happened, the maximum value continued at interior quarter increasing to 16.59±4.66 dyn/cm^2. The mean values of posterior and exterior quadrants decreased approximately 20%, less in percent than the controls but similar with absolute value. Anterior quadrant is the difference at arch, while in controls the value remained in stable patient the mean value increased 40%. Dilating patients also increased the maximum value at interior quadrant to 9.95±2.60 dyn/cm^2. Exterior and anterior quadrants remain equal and posterior quadrant increased approximately a 20%.

At the descending aorta most values increased from ascending and aortic arch parts. The maximum value is located at interior, anterior and exterior quarters in controls, stable and dilating patients respectively. The mean value of controls in the whole descending aorta was 11.54±0.7 dyn/cm^2, stable patients presented a mean value of 16.94±4.84 dyn/cm^2 and dilating patients a mean value of 14.34±4.50 dyn/cm^2.

Results indicate clear differences between controls and stable patients, increasing the values approximately 50% in ascending aorta and arch. However, dilating patients presented values close to healthy controls which do axial shear stress an inadequate parameter to differentiate aneurysm progression versus non-dilating cases.

The second parameter studied is wall circumferential shear stress and Figure 136 presents the mean values of each group of cases. The values are presented in dyn/cm^2.

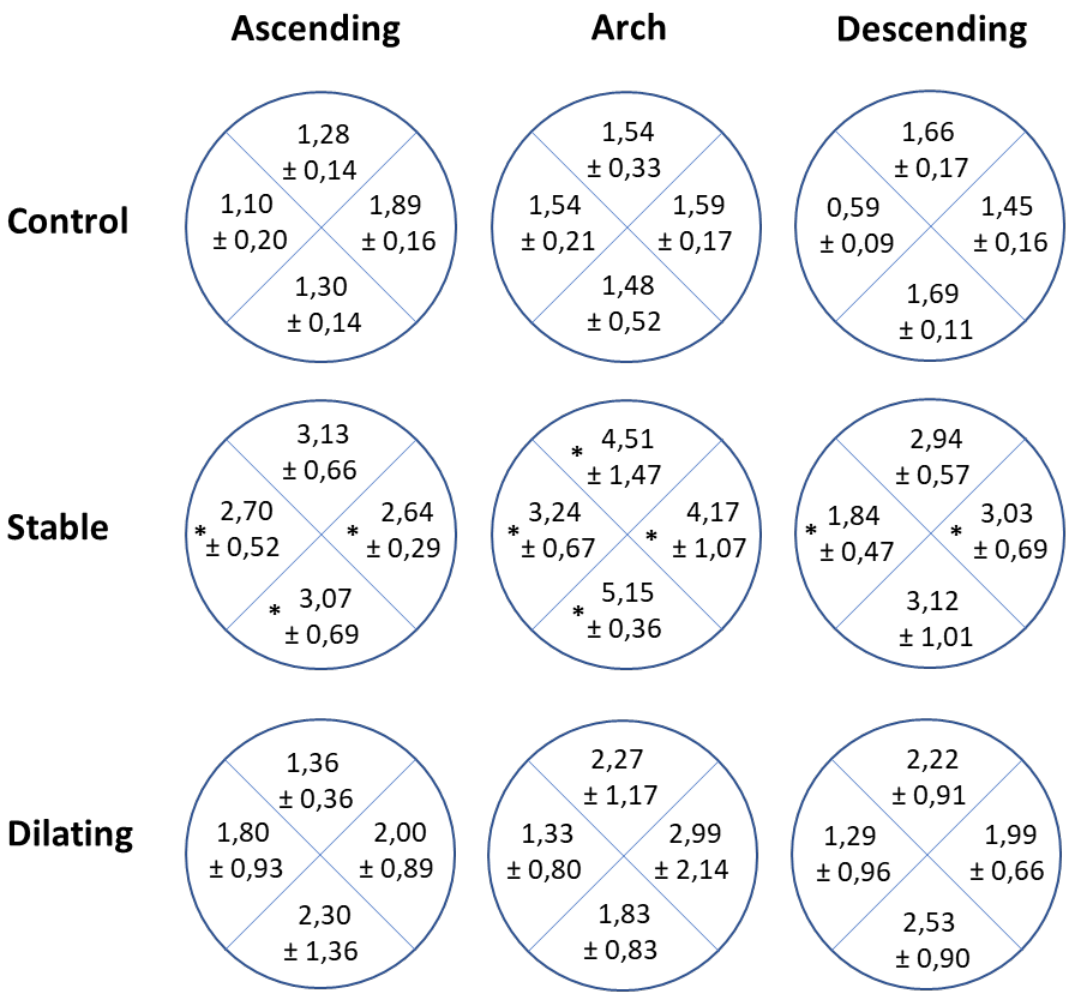

Figure 136. Circumferential shear stress in healthy controls and stable and dilating patients at the ascending aorta, aortic arch and descending aorta.

In general, the values are lower than axial shear stress due to circumferential velocities are not as higher as axial, although in some quarters of stable and dilating patients' values are not that far. Controls presented values much lower than the patients ones.

At the ascending aorta, controls presented a homogenous value in the four quadrants, being the highest value of 1.89±0.16 dyn/cm^2 at the interior quarter as axial shear stress and the lowest of 1.10±0.20 dyn/cm^2 at exterior quarter. Stable patients also presented a homogeneous ascending zone, with its maximum value of 3.07±0.69 dyn/cm^2 at anterior quarter where axial shear stress presented its minimum, stablishing a zone of high stagnation time. The minimum value of 2.64±0.29 dyn/cm^2 was at interior zone, where axial shear stress presented its maximum. Dilating patients presented its maximum as stable patients at anterior zone with a value of 2.30±1.36 dyn/cm^2 and its minimum of 1.36±0.36 dyn/cm^2 at posterior zone. Standard deviation errors are higher

in dilating patients, reaching 50% of the value, which shows that the dilating patients differ a lot between them.

At aortic arch, healthy controls continued with a homogenous value in the four quadrants, the highest value of 1.59±0.17 dyn/cm^2 at interior quadrant and lowest of 1.48±0.52 dyn/cm^2 at anterior quadrant. The values at healthy controls remain lower than patients as at the ascending aorta. Stable patients presented the highest values of all cases, with maximum of 5.15±0.36 dyn/cm^2 at anterior quarter and minimum of 3.24±0.67 dyn/cm^2 at the exterior quarter. Circumferential shear stress at dilating patients arch was unstable, with highest value of 2.99±2.14 dyn/cm^2 at interior quarter and lowest value of 1.33±0.80 dyn/cm^2 at exterior quarter. Standard deviation errors remain higher than healthy controls and stable patients.

At descending aorta, a pattern is observed in all cases. Interior quadrant presented a lower value than anterior, posterior and exterior quadrants, which presented a homogenous value. Healthy controls presented a value of 0.59±0.09 dyn/cm^2 at interior quadrant and a mean value of 1.60±0.13 dyn/cm^2 at the other three. Stable patients presented a value of 1.84±0.47 at interior quadrant dyn/cm^2 and a mean value of 3.03±0.76 dyn/cm^2. Dilating patients presented a value of 1.29±0.96 dyn/cm^2 at interior quadrant and mean value of 2.25±0.82 dyn/cm^2 at the other three.

Overall, healthy controls presented values much lower and stable than patients, with ascending aorta and arch being pretty much the same. The unique point sheared between controls and patients was the pattern in descending aorta, even though values remained lower. The difference between stable and dilating patients was the one observed in tangential shear stress, stable patients presented higher values in all regions of the aorta and most of them were statistically significant compared to controls.

The third parameter studied is vorticity and Figure 137 presents the mean values of each group of cases. The values are presented in s^{-1}.

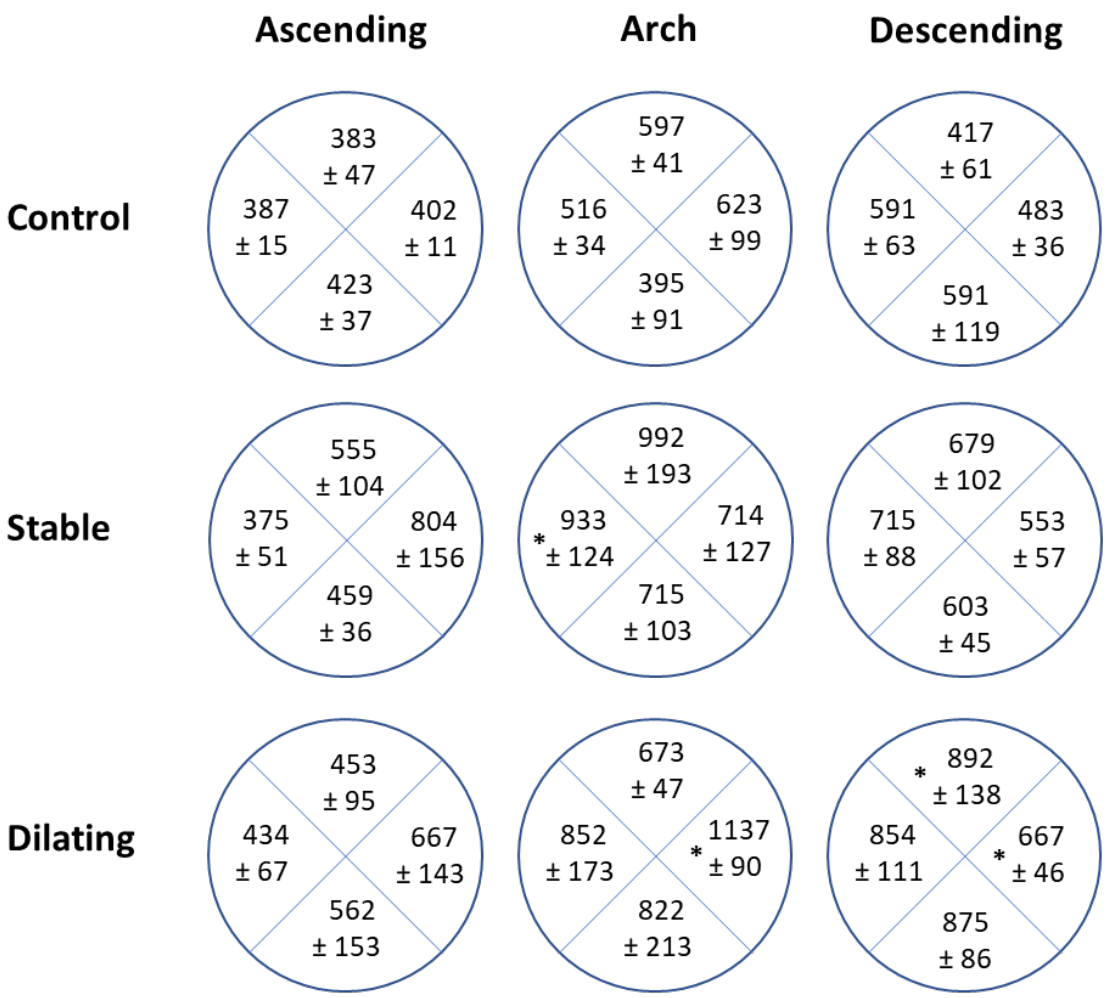

Figure 137. Circumferential shear stress in healthy controls and stable and dilating patients at the ascending aorta, aortic arch and descending aorta.

At the ascending aorta, healthy controls presented a homogenous value in the four quadrants, being the highest value of 423±37 s^{-1} at the anterior quarter and the lowest of 383±47 s^{-1} at the posterior quarter. Stable patients presented the highest value of 804±156 s^{-1} at the interior quarter as the axial shear stress. The minimum value of 375±51 s^{-1} is located at the exterior quarter. Dilating patients present their maximum values of 667±147 s^{-1} and 562±153 s^{-1} at the interior quarter and at the anterior quarter respectively as axial and circumferential shear stress.

At aortic arch, healthy controls continued with a homogenous zone being the highest value of 623±99 s^{-1} at the interior quarter, with the exception at anterior quarter with a value of 395±91 s^{-1}. The values at healthy controls remain lower than patients as at the ascending aorta. Stable patients presented the highest values of all cases, with maximum of 992±193 s^{-1} at the posterior quarter and minimum of 714±127 s^{-1} at the

interior quarter. Vorticity at dilating patients arch was unstable as circumferential shear stress, with highest value of 1137±90 s^{-1} at the interior quarter as axial and circumferential shear stress and lowest value of 673±47 s^{-1} at the posterior quarter.

At descending aorta, a pattern is observed in all cases as happened in both shear stresses. Interior quadrant presents high values of 591±63 s^{-1}, 715±88 s^{-1} and 854±111 s^{-1} in healthy controls, stable and dilating patients respectively, while exterior quarter presents low values of 483±36 s^{-1}, 553±57 s^{-1} and 667±46 s^{-1} in healthy controls, stable and dilating patients respectively. This pattern is like the one observed in axial shear stress and contrary to that observed in circumferential shear stress.

Overall, vorticity values from healthy controls presented values much lower than stable and dilating patients, with the whole aorta being pretty much the same. The values of dilating patients were higher than stable patients except for ascending aorta. Standard deviation errors were higher in dilating patients than healthy controls and stable patients.

Results indicate an obvious correlation between both wall shear stresses and vorticity. The zones with higher vorticity mostly match with zones of high shear stress. The zone with higher vorticity and shear rotates along the aorta as the fluid advances. In most cases, at the ascending aorta, the fluid rotates from posterior to exterior. At the aortic arch, the rotation is identified from exterior to anterior, with higher vorticity, circumferential and especially axial shear stress as the artery narrows down. Finally, in the descending aorta, the anterior sector presents the highest values of stresses.

3.7.3 Shear Stress Ratio Analysis

The analysis of shear stresses and vorticity was inconclusive regarding behavior at specific regions of aneurysms. However, the observation that axial and circumferential shear stress are not always correlated led us to propose a new non-dimensional parameter, defined as shear stress ratio (SSR). The shear stress ratio is the ratio between the in-plane rotation of the fluid (circumferential shear stress) and the through-plane progress of the fluid (axial shear stress). Apart from SSR, Oscillatory Shear Index (OSI) and Time-Averaged Wall Shear Stress (TAWSS) have also been included in the analysis. The three parameters are calculated as explained in 2.3.2.

This analysis has been performed for all nodes in the simulations and studied at the ascending aorta volumetrically and superficially. Volumetrically, the ascending aorta is divided into proximal and distal aorta and, superficially, it is divided as shear stress and vorticity in interior, exterior, anterior and posterior quarters. Average, median value and the 90th percentile of these parameters have been evaluated (Figure 45).

Volumetric analysis		Average			90th percentile		
		Control	Stable	Dilating	Control	Stable	Dilating
OSI	proximal	0,17	0,25*	0,19	0,44	0,43	0,43
	distal	0,15	0,23*	0,19	0,43	0,43	0,43
TAWSS	proximal	1,32	1,16	0,97*	1,82	2,40	1,74
	distal	1,63	1,35	1,00*	2,34	2,97	1,93
SSR	proximal	1,06	1,26	1,90	1,35	1,82	2,71*
	distal	1,12	1,26	3,10	1,55	2,65	4,54*

Table 45. Volumetric analysis of OSI, TAWSS and SSR at distal and proximal aorta from healthy controls and stable and dilating patients.

OSI presents average and median values able to differentiate healthy control of stable and dilating patients, but no difference is observed between stable and dilating patients. The 90th percentile values do not differentiate any case.

TAWSS presents average and median values higher in healthy controls than in patients but no important differences are observed between stable and dilating patients. The 90th percentile present higher values in stable patients, while controls and dilating patients are not statistically different.

SSR presents average and median values higher in dilating patients, while values for healthy controls and stable patients are similar. The 90th percentile values are the lowest

for healthy controls, not statistically different from control patients. Dilating patients, however, present significantly higher shear stress ratio than controls and stable patients.

Overall, OSI and TAWSS could not differentiate between healthy controls and patients or between stable and dilating patients in any of the ways studied. On the other hand, SSR preliminary results seem to group healthy controls and stable patients, even though stable patients present slightly higher results, and differentiate them of dilating patients which present higher values. As observed, SSR holds the potential to stratify aneurysm progression in Marfan patients.

Figure 138A, Figure 139A and Figure 140A present the two volumetric divisions of each case into proximal (red centerline) and distal (yellow centerline). Figure 138B, Figure 139B and Figure 140B and Figure 138C, Figure 139C and Figure 140C present the SSR values of nodes versus the distance to the aortic root in centimeters at proximal and distal ascending aorta respectively.

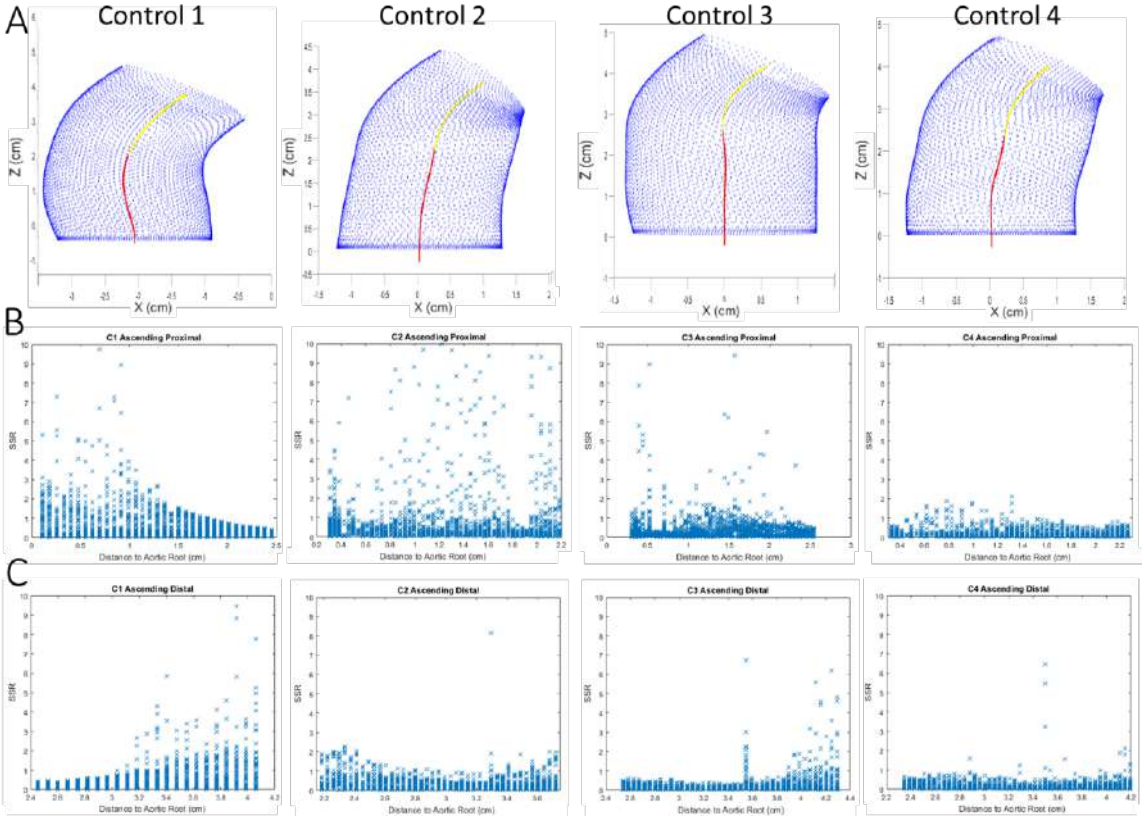

Figure 138. (A) Ascending aorta division into proximal (red) and distal (yellow) and SSR versus the distance to the aortic root at (B) proximal and (C) distal aorta in healthy controls.

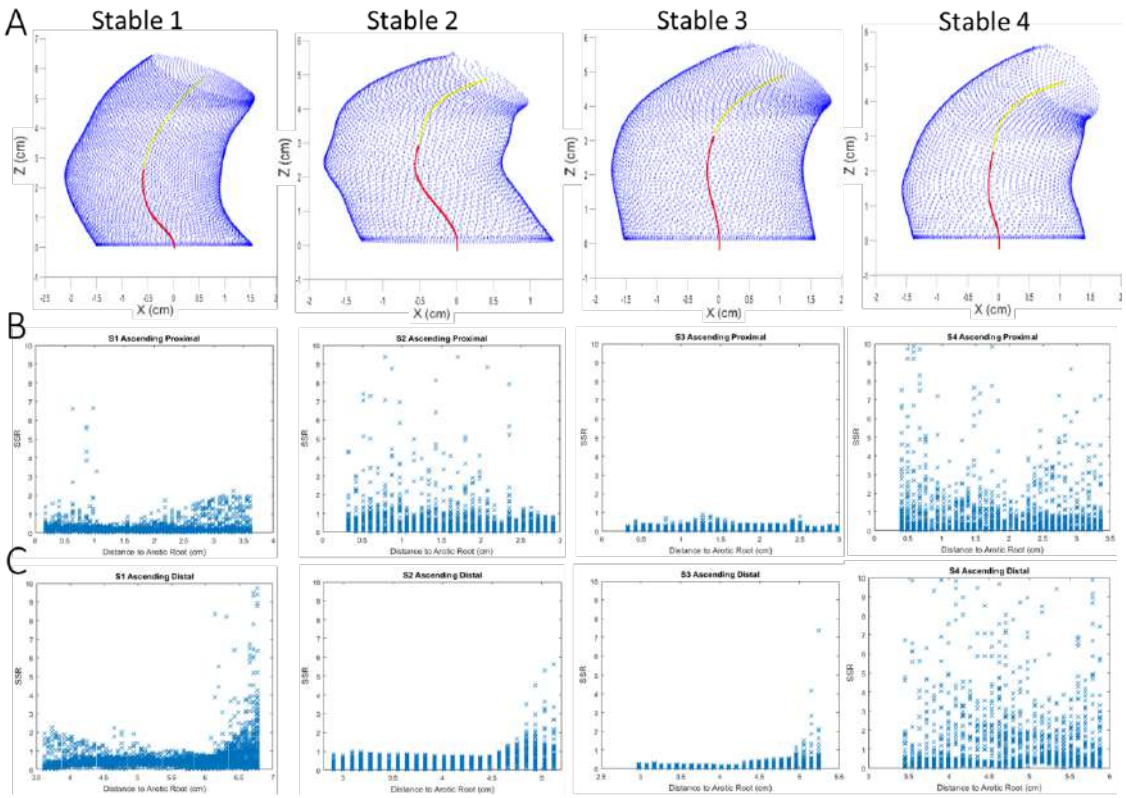

Figure 139. (A) Ascending aorta division into proximal (red) and distal (yellow) and SSR versus the distance to the aortic root at (B) proximal and (C) distal aorta in stable patients.

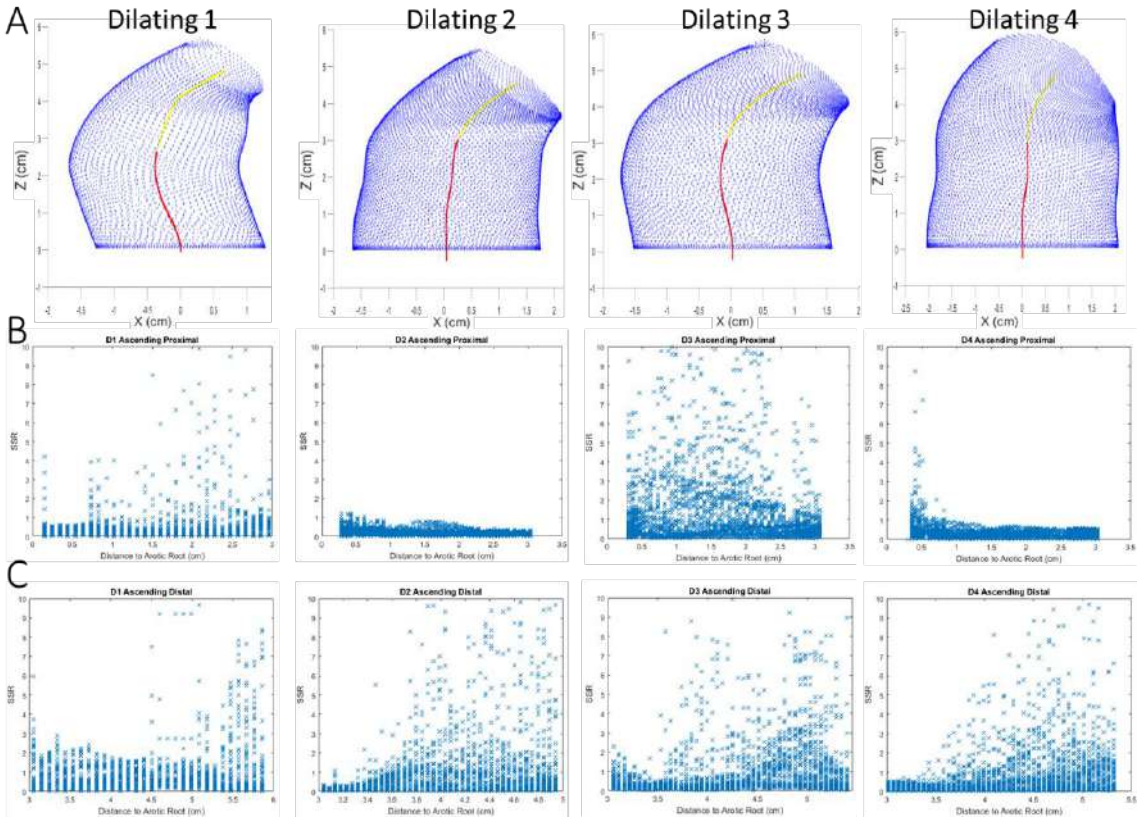

Figure 140. (A) Ascending aorta division into proximal (red) and distal (yellow) and SSR versus the distance to the aortic root at (B) proximal and (C) distal aorta in dilating patients.

In general, the proximal ascending aorta presents higher SSR than the distal aorta. The mathematical constrains imposed to the simulations (no movement at the inlet surface) could affect the results. As seen, dilating patients 2 and 4 have unexpectedly low values of SSR at the proximal aorta, not different from those of healthy controls and stable patients. Once the effect of the constraints is diluted, consistent differences between controls and patients can be observed in the distal ascending aorta. Indeed, stable patients present lower values than dilating patients at distal aorta and not different than those of healthy controls.

As SSR at the distal aorta was the best parameter to stratify aneurysm progression and mechanotransduction behind aneurysm expansion is critical at the aortic wall, we analyzed the wall SSR at the distal ascending aortae of our cases.

Surface Analysis		Average			90^{th} percentile		
		Control	Stable	Dilating	Control	Stable	Dilating
SSR	interior	0,23	0,49*	1,21*	0,34	1,22*	2,23*
	exterior	0,85	0,34	1,11	0,72	0,87	1,97*
	anterior	0,87	0,22	1,18	0,94	1,01	1,50
	posterior	0,66	0,85	5,86*	1,15	1,42	5,83*

Table 46. Shear stress ratio at interior, exterior, anterior and posterior wall surfaces.

Surface analysis (Table 46)showed that dilating patient are statistically different from healthy controls and stable patient at the interior and posterior quarters with average value and at the interior, exterior and posterior quarters with 90^{th} percentile value. Moreover, stable patients are not statistically different from healthy controls posterior quarter with average value and at exterior and posterior quarters with 90^{th} percentile value.

Cumulative frequency was plotted to better visualize the differences between cases (Figure 141). Healthy controls are presented in green lines, stable patient in blue lines and dilating patients in red lines. The mean 90^{th} percentile value of the ascending distal in healthy controls presents an SSR cumulative frequency of 0,80. Moreover, two of the controls present the lowest values of 0,4 of all cases studied. In stable patients (blue), (with one exception), 90% of the wall presented an average SSR cumulative frequency of 0.80. A close look should be taken to the exceptional patient as subsequent follow-ups may change the patient condition from stable to dilating. Dilating patients (red) achieved an average SSR cumulative frequency of 90 % at 2,38. This is coherent with the

plots of Figure 138C, Figure 139C and Figure 140C, where one can observe high SSR at the distal ascending aorta which is not observed in healthy controls and stable patients. These results indicate that cumulative SSR analysis could be a good tool to stratify aneurysm progression in Marfan patients. This gains relevance as this is the first direct evidence of the impact of rigid-wall assumption on the relationship between aneurysm growth and flow characteristics. Figure 142 synthetizes these findings.

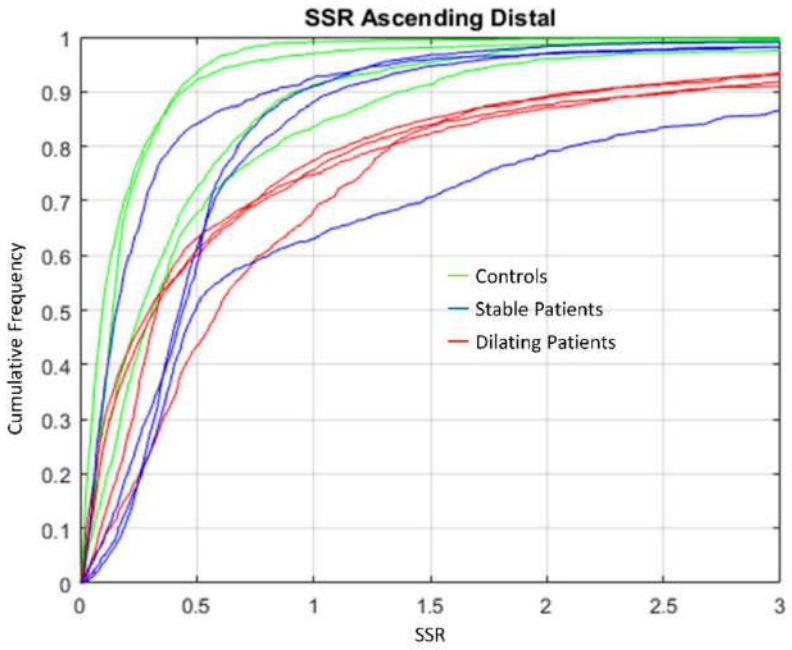

Figure 141. Cumulative frequency of shear stress ratio from all the cases.

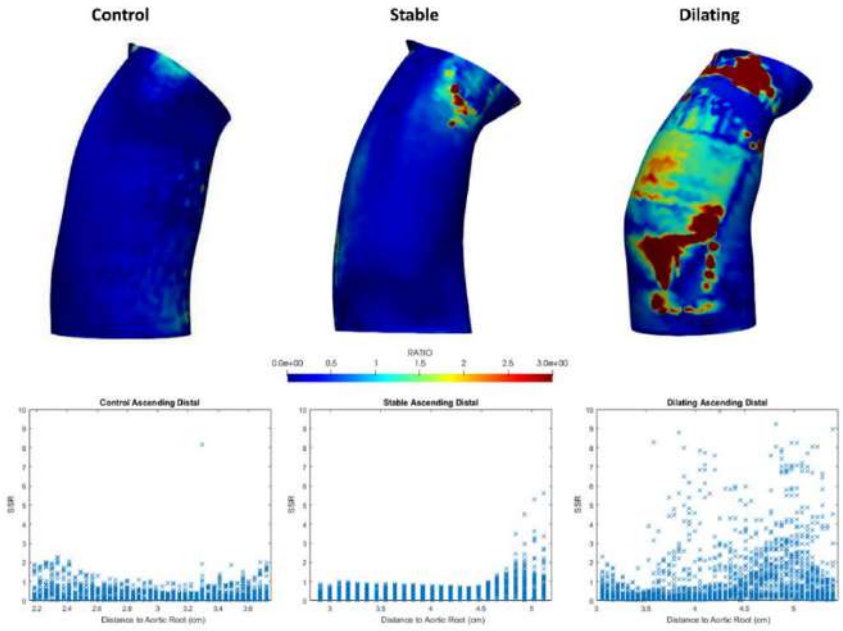

Figure 142. Ascending aorta shear stress ratio from one control, one stable patient and one dilating patient with their respective graphs versus the distance to aortic root.

3.8 Replicating rotating flow in vitro

To support the conclusions from the study of secondary fluidodynamic parameters, an *in vitro* (Figure 143) system was designed to tests such flow in human endothelial cells. The setup consisted of a helix coupled to a straight tube with the aim of imposing rotational flow to mimic aortic flow. Two helixes were designed in SolidWorks with different rotation (Figure 144A and Figure 144C) and printed in 3D (Figure 144B and Figure 144D), and flow through them was simulated to extract wall shear stress maps.

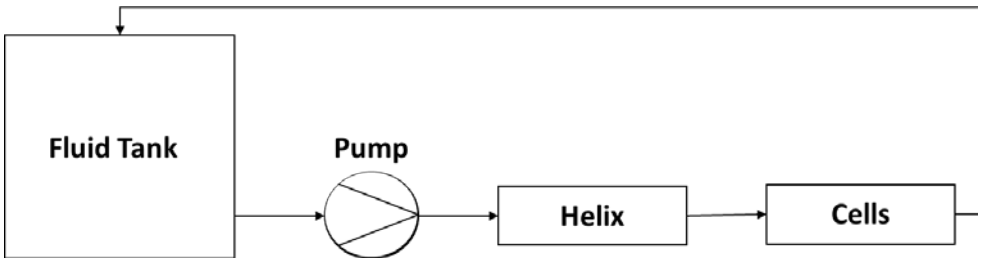

Figure 143. *In vitro* system designed to test endothelial cells.

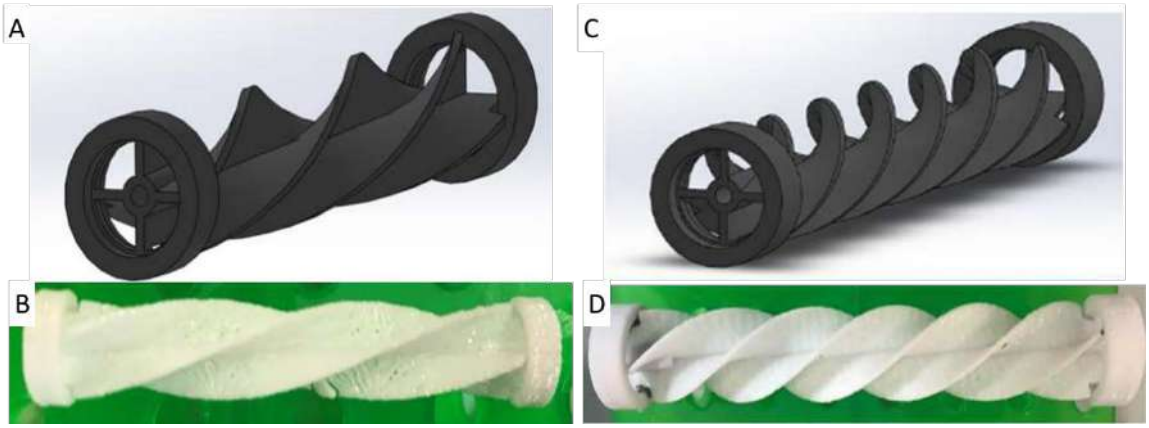

Figure 144. Helixes designed to replicate the rotational flow from simulations (A) 0,75 revolutions and (B) 1,5 revolutions and (B, D) printed in 3D.

The axial velocities used are calculated from the available flow of two pumps; one peristaltic and the other plastic bolted. For each experiment in this section, wall axial and circumferential shear stress values are shown on the Paraview platform and are compared to average values of our aortic simulations; 0.5 to 2.5 Pa wall axial shear stress and 0.05 to 0.15 Pa wall circumferential shear stress during the systole.

3.8.1 Straight tube of 10 mm diameter

In the first simulation performed, the tube had a diameter of 10 mm and the helix presented 0.75 revolutions paddle rotation. The peristaltic pump could reach flow up to 6 ml/s, which represented an axial velocity of 7.7 cm/s. The simulation was performed with a parabolic inlet velocity profile with a maximum value of 14.4 cm/s (double the average velocity). Flow is considered laminar as Reynolds is 227. Figure 145 presents the wall axial and circumferential shear stress results in Paraview.

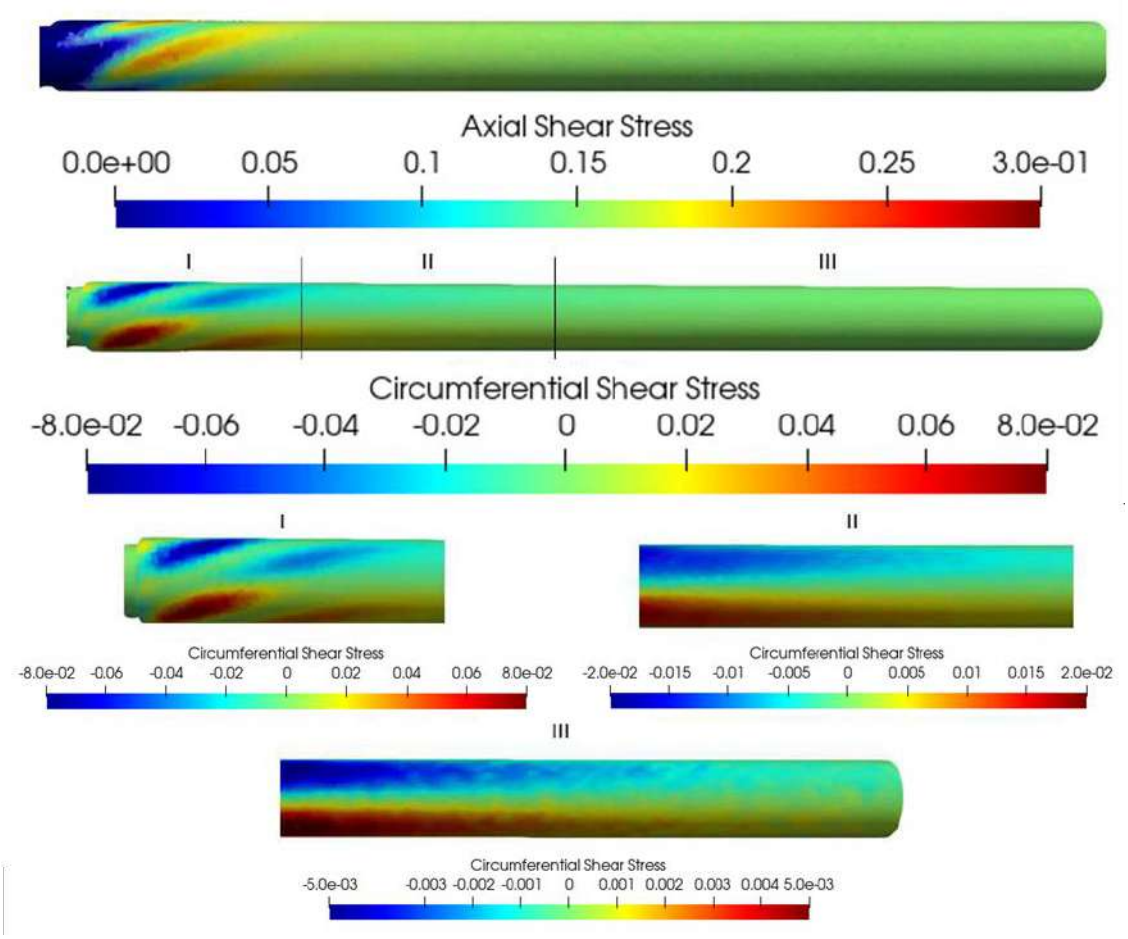

Figure 145. Axial and circumferential shear stress after the helix in the first simulation.

Analyzing the results of the simulation, one can affirm that the first simulation did not reproduce the aorta systole conditions in the tube. The velocity generated by the pump was not enough to reach the aortic shear stress values. The average axial velocity at the aorta is 70-80 cm/s while simulation 1 had 7.7 cm/s average velocity at the inlet.

Consequently, axial shear stress at the simulation is approximately 10 times lower than aortic. The axial shear stress at the simulation reaches 0.3 Pa close to the helix end and it is stabilized at 0.15 Pa 30-40 mm after the helix end.

Nevertheless, circumferential shear stress values are close to aortic, as helicoidal flow presents circumferential shear stress between 0.03 and 0.08 Pa during the first 35 mm. Helicoidal flow is slowly damped and circumferential shear stress decreased below 0.01 Pa 50 mm after the helix.

Therefore, it was necessary to change the conditions to increase axial shear stress 5 to 10-fold and circumferential shear stress 2-fold. Increasing the inlet velocity by using another pump could be a good solution to obtain the desired values. Unfortunately, our group had seen that, in this system, human endothelial cells could not withstand flow and would detach from the tube surface. However, stronger endothelial cells subjection strategies were being developed and, for that reason, a new simulation increasing the inlet velocity was performed.

In the second simulation, the tube diameter and the helix geometry were the same as simulation 1. The inlet velocity was introduced with a parabolic profile with a maximum value of 50 cm/s. Flow continues to be laminar with Reynolds 737. Figure 146 presents wall axial shear stress in Paraview.

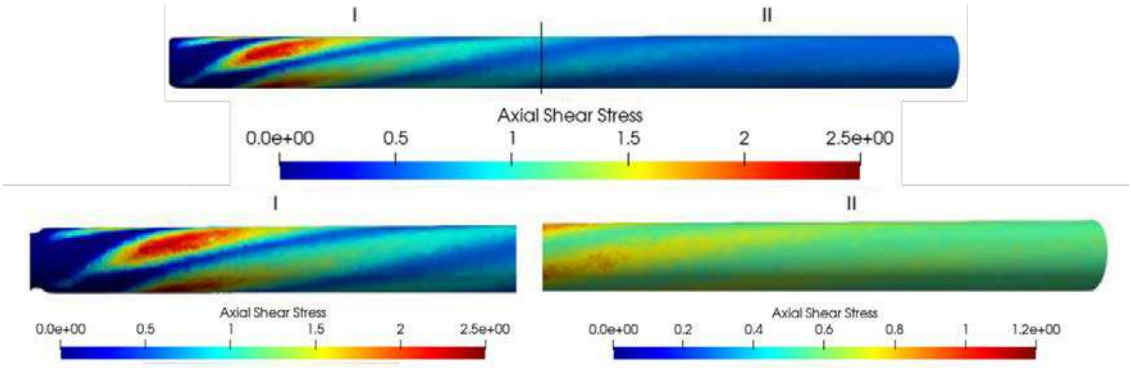

Figure 146. Axial shear stress after the helix in the second simulation.

Axial shear stress generated with the new higher inlet velocity was the one expected, obtaining values between 0.5 and 2.5 Pa. The desired higher axial shear stresses appeared just after the helix following a helicoidal tendency generated by the helix form.

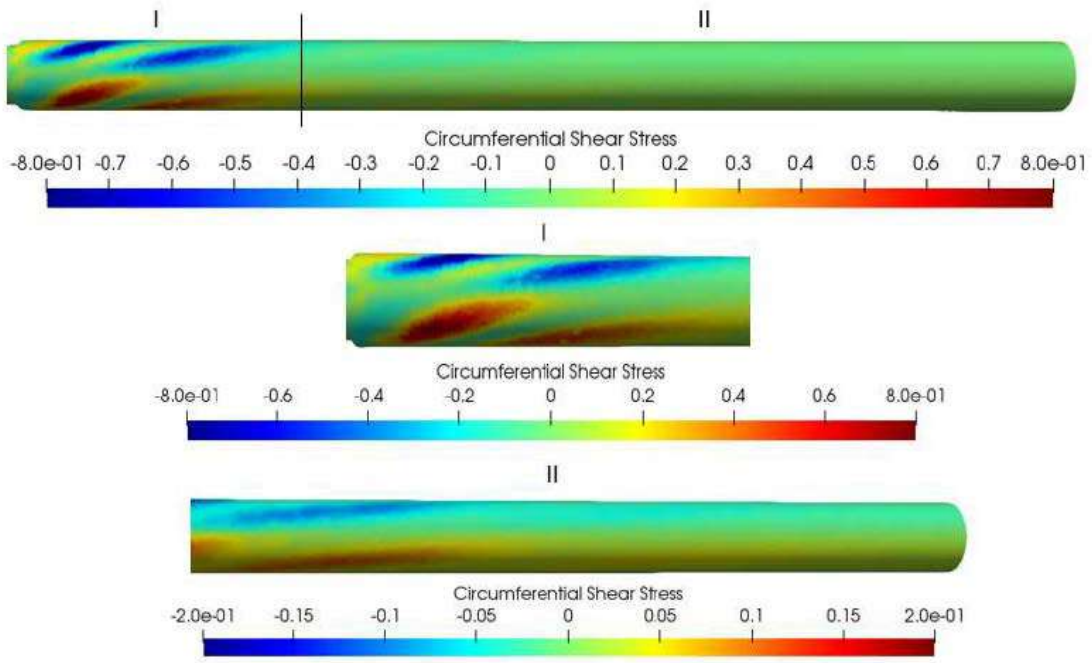

Figure 147. Circumferential shear stress after the helix in the second simulation.

The circumferential shear stress also increased versus simulation 1 but remained below 0.05 Pa for an important part of the tube. Although the first section after the helix end satisfied the desired values, the section would be too short section to culture endothelial cells and the shear stress would present significant variability due to flow rotation induced by the helix.

Consequently, a helix with more rotation per length (1.5 revolutions, Figure 144C) was considered to extend the range of aortic circumferential shear stress. Tube diameter and inlet velocity profile remained unchanged. Figure 148 presents the wall axial shear stress in Paraview.

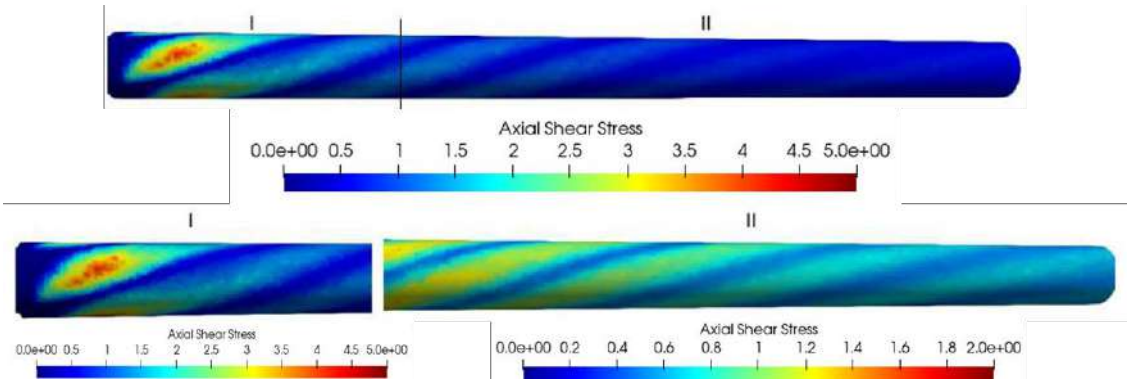

Figure 148. Axial shear stress after the helix in the third simulation.

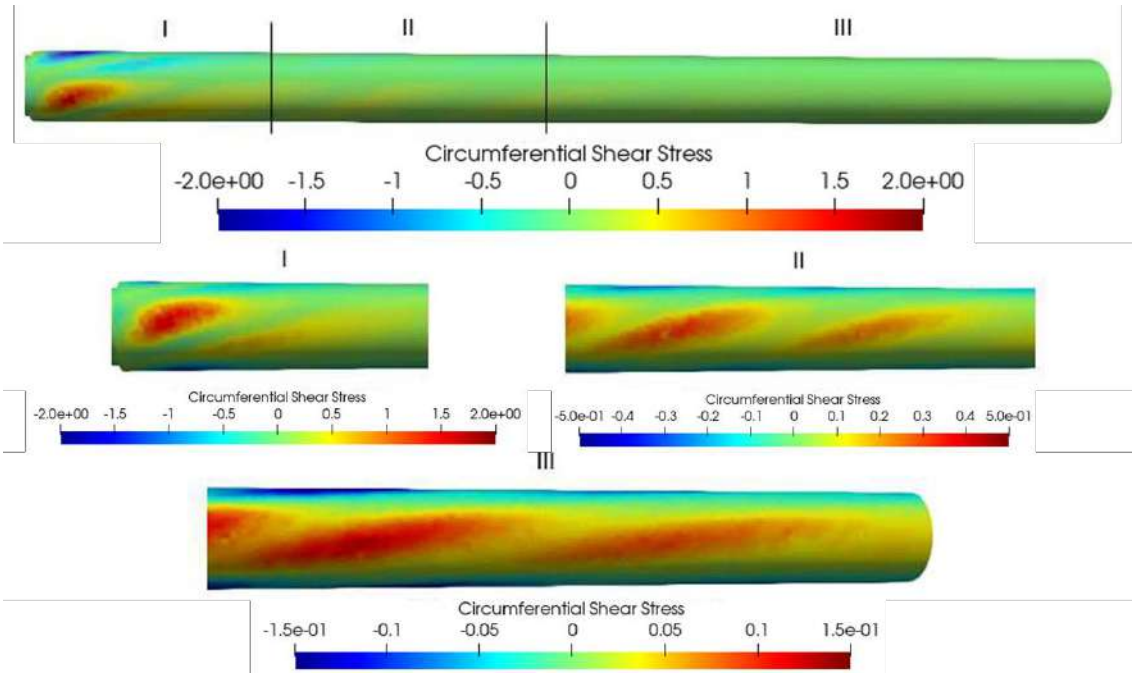

Figure 149. Circumferential shear stress after the helix in the third simulation.

With the new helix design implemented in simulation 3, axial shear stress presented a slight increase, specifically right past the helix. Nevertheless, a large are with acceptable axial shear stress was maintained. Circumferential shear stress increased notably. In section III, the circumferential shear stress oscillates between 0-0.15 Pa. Thus, cells should be cultured in this section III (75-150 mm after the helix).

The inlet velocity required to achieve aortic shear stress levels in the above simulations is 3 times lower than the aorta's axial velocity during systole. It should be examined if the low axial velocities presented in the above simulations have any distortion effect into the analysis of shear stress influence. These velocities differences should not have effect in our study because the endothelial cells are cultured in the wall where the fluid velocity is almost zero. Endothelial cells are more affected by shear stress conditions than velocity ranges.

An initial estimation of SSR from the values calculated of axial and circumferential shear stress is done and SSR would be very low, with values from 0.1 to 0.5. These SSR would be comparable to healthy controls but more circumferential shear stress is needed in order to match aortic SSR of dilating patient. To acquire those values, one possibility could be to rotate the helix with a motor. This rotation, apart from increasing the circumferential shear stress, would achieve more homogenous results after the helix.

Conclusions

A platform to replicate aortic flow in Marfan patients and study their fluid dynamics has been developed in this thesis. Patient-specific boundary conditions have been imposed in all the studied cases. Aortic geometry was reconstructed with an in-house macro for SolidWorks using magnetic resonance imaging. The macro allows creating CAD files that can be later used for CFD and FSI simulations and for polymeric scaffold manufacturing using 3D printers.

Using 4D magnetic resonance imaging, 3D velocity profiles were extracted from each case and spatiotemporally treated in Matlab to set inlet velocities. Windkessel conditions of order 1 were imposed at the outlets to adjust flow ratios. Wall stiffness, one of the most critical parameters in FSI simulations, was estimated and iterated successfully following a strategy that eliminates the need for accurate wall thickness measurement.

These simulations allowed comparing primary fluidodynamic parameters like jet angle, normalized displacement and maximum velocity to medical data. These results revealed that coupling solid to fluid in thoracic aortic simulations reduces the error of classical computational fluid dynamics. Fluid-structure interaction simulations with patient-specific geometry, boundary conditions and aortic wall mechanical properties outperform rigid-wall fluid dynamics simulations in the reproduction of thoracic aorta fluid dynamics at a moderate computational cost.

Axial and circumferential wall shear stress, vorticity, oscillatory shear index and time averaged wall shear stress failed to present differences between stable and dilating Marfan patients. However, the shear stress ratio allows to overcome these limitations and constitutes a potentially interesting predictor of dilatation in Marfan patients.

This study opens the door to further *in vitro* research on the effect of shear stress ratio on the endothelium and clinical investigation using shear stress ratio as a stratification tool.

Publications and Conference communications

The following section includes the publications and conference communications derived from the research conducted by the PhD candidate during his thesis.

- Pons R, Guala A, Rodríguez-Palomares JF, Cajas JC, Dux-Santoy L, Teixidó-Tura G, Molins JJ, Vázquez M, Evangelista A, Martorell J. Fluid-structure interaction simulations outperform computational fluid dynamics and provide prognostic information for aneurysm progression in Marfan patients. *R Soc Open Sci.* 2020 Feb 5;7(2):191752. doi: 10.1098/rsos.191752.
- Cajas J. C, Houzeaux G, Vázquez M, García M, Casoni E, Calmet H, Artigues A, Borrell R, Lehmkuhl O, Pastrana D, Yáñez D. J, Pons R, Martorell J. Fluid-structure interaction based on HPC multicode coupling. *SIAM J. Sci. Comput*. (2018) doi:10.1137/17M1138868.
- Martorell J, Pons R, Dux-Santoy L, Rodríguez-Palomares JF, Molins JJ, Evangelista A. 4D-MRI coupled to fluid dynamics simulations to improve patient management. *Tecnicas endovasculares.*

- Engineered Platform to Predict and Repair Aortic Diseases. Poster at the *Global Medical Engineering & Physics Exchange/Pan American Health Care Exchanges*, 7th April 2016, Madrid, Spain.
- Aortic wall motion increases accuracy and relevance of fluid dynamic simulations of the aortic arch. Poster at the *SITE 2017: International Symposium on Endovascular Therapeutics*, 10th April 2017, Barcelona, Spain.
- Aortic wall motion is critical to accurately simulate fluid dynamics at the aortic arch. Poster and Oral presentation at the *The Joint EuroCMR*/SCMR Meeting (CMR 2018): Improving Clinical Value by Technical Advances,* 2nd February 2018, Barcelona, Spain.
- Should we worry about the hemodynamic effects after TEVAR? Are we missing something? Poster at the *SITE 2019: International Symposium on Endovascular Therapeutics*, 29th March 2019, Barcelona, Spain.

References

1. Hutchison, S. J. *Aortic Disease : Clinical Diagnostic Imaging Atlas*. *Cardiovascular Imaging* (2007). doi:10.1016/B978-1-4160-5009-4.50004-2.
2. Saratzis, A. & Bown, M. J. The genetic basis for aortic aneurysmal disease. *Heart* **100**, 916–22 (2014).
3. Koeppen, B. M. & Stanton, B. A. *Berne & Levy Physiology*. *Mosby Elsevier* (2010). doi:10.1017/CBO9781107415324.004.
4. Boron, W. F. & Boulpaep, E. L. *Medical physiology: a cellular and molecular approach*. *Potentials* (2005).
5. OpenStax College. *Anatomy and Physiology*. (OpenStax CNS, 2013).
6. Testut, L. & Latarjet, A. *Compendio de anatomía descriptiva*. *Elsevier Health Sciences-Masson* (2001).
7. Bonow, R., Mann, D., Zipes, D. & P, L. *Braunwald's heart disease: A textbook of cardiovascular medicine (10th edition)*. *Elsevier/Saunders* (2015).
8. Kimura, N. *et al.* Patient-specific assessment of hemodynamics by computational fluid dynamics in patients with bicuspid aortopathy. in *Journal of Thoracic and Cardiovascular Surgery* (2017). doi:10.1016/j.jtcvs.2016.12.033.
9. Barannyk, O. & Oshkai, P. The Influence of the Aortic Root Geometry on Flow Characteristics of a Prosthetic Heart Valve. *J. Biomech. Eng.* (2015) doi:10.1115/1.4029747.
10. Tennant, M. & McGeachie, J. K. BLOOD VESSEL STRUCTURE AND FUNCTION: A BRIEF UPDATE ON RECENT ADVANCES. *Aust. N. Z. J. Surg.* **60**, 747–753 (1990).
11. Wagenseil, J. E. & Mecham, R. P. Vascular Extracellular Matrix and Arterial Mechanics. *Physiol. Rev.* (2009) doi:10.1152/physrev.00041.2008.
12. Kierszenbaum, A. L. *Histology and Cell Biology: An Introduction to Pathology 4th Edition*. *Journal of Chemical Information and Modeling* (2013). doi:10.1017/CBO9781107415324.004.
13. Erbel, R. *et al.* 2014 ESC guidelines on the diagnosis and treatment of aortic diseases. *Russ. J. Cardiol.* (2015) doi:10.15829/1560-4071-2015-07-7-72.
14. Lavall, D., Schäfers, H.-J., Böhm, M. & Laufs, U. Aneurysms of the Ascending Aorta. *Dtsch. Aerzteblatt Online* (2018) doi:10.3238/arztebl.2012.0227.
15. Evangelista, A. Diseases of the aorta: aneurysm of the ascending aorta. *Heart* **96**, 979–85 (2010).
16. Wu, D., Shen, Y. H., Russell, L., Coselli, J. S. & Lemaire, S. A. Molecular mechanisms of thoracic aortic dissection. *Journal of Surgical Research* (2013)

doi:10.1016/j.jss.2013.06.007.

17. Wu, D., Shen, Y. H., Russell, L., Coselli, J. S. & Lemaire, S. A. Molecular mechanisms of thoracic aortic dissection. *Journal of Surgical Research* (2013) doi:10.1016/j.jss.2013.06.007.
18. Daily, P. O., Trueblood, H. W., Stinson, E. B., Wuerflein, R. D. & Shumway, N. E. Management of Acute Aortic Dissections. *Ann. Thorac. Surg.* (1970) doi:10.1016/S0003-4975(10)65594-4.
19. Clouse, W. D. *et al.* Improved prognosis of thoracic aortic aneurysms: a population-based study. *JAMA* **280**, 1926–1929 (1998).
20. Chau, K. H. & Elefteriades, J. A. Natural history of thoracic aortic aneurysms: Size matters, plus moving beyond size. *Prog. Cardiovasc. Dis.* (2013) doi:10.1016/j.pcad.2013.05.007.
21. Evangelista, A. Aneurysm of the ascending aorta. *Heart* (2010) doi:10.1136/hrt.2008.152751.
22. Xu, J. & Shi, G. P. Vascular wall extracellular matrix proteins and vascular diseases. *Biochimica et Biophysica Acta - Molecular Basis of Disease* (2014) doi:10.1016/j.bbadis.2014.07.008.
23. Watton, P. Computational model can predict aneurysm growth. *SPIE Newsroom* (2008) doi:10.1117/2.1200801.0999.
24. Hoffjan, S. Genetic dissection of Marfan syndrome and related connective tissue disorders: An update 2012. *Mol. Syndromol.* **3**, 47–58 (2012).
25. Tellides, G. Further evidence supporting a protective role of transforming growth factor-β (TGFβ) in aortic aneurysm and dissection. *Arteriosclerosis, Thrombosis, and Vascular Biology* (2017) doi:10.1161/ATVBAHA.117.310031.
26. Hoffjan, S. Genetic dissection of Marfan syndrome and related connective tissue disorders: An update 2012. *Molecular Syndromology* (2012) doi:10.1159/000339441.
27. El-Hamamsy, I. & Yacoub, M. H. Cellular and molecular mechanisms of thoracic aortic aneurysms. *Nature Reviews Cardiology* (2009) doi:10.1038/nrcardio.2009.191.
28. Barbour, J. R., Spinale, F. G. & Ikonomidis, J. S. Proteinase Systems and Thoracic Aortic Aneurysm Progression. *Journal of Surgical Research* (2007) doi:10.1016/j.jss.2006.09.020.
29. Kau, T. *et al.* Aortic development and anomalies. *Seminars in Interventional Radiology* (2007) doi:10.1055/s-2007-980040.
30. Lavall, D., Schäfers, H. J., Böhm, M. & Laufs, U. Aneurysmen der Aorta ascendens. *Deutsches Arzteblatt International* (2012) doi:10.3238/arztebl.2012.0227.

31. Jain, D., Dietz, H. C., Oswald, G. L., Maleszewski, J. J. & Halushka, M. K. Causes and histopathology of ascending aortic disease in children and young adults. *Cardiovasc. Pathol.* **20(1)**, 15–25 (2011).
32. Febina, J., Sikkandar, M. Y. & Sudharsan, N. M. Wall Shear Stress Estimation of Thoracic Aortic Aneurysm Using Computational Fluid Dynamics. *Comput. Math. Methods Med.* **2018**, 12 (2018).
33. McLaughlin, D. P. & Stouffer, G. A. Aortic stenosis. in *Cardiovascular Hemodynamics for the Clinician: Second Edition* (2016). doi:10.1002/9781119066491.ch8.
34. Sibon, I. Carotid stenosis. *Arch. des Mal. du Coeur des Vaiss. - Prat.* (2012) doi:10.1016/S1261-694X(12)70438-8.
35. Jayalath, R. W., Mangan, S. H. & Golledge, J. Aortic calcification. *European Journal of Vascular and Endovascular Surgery* (2005) doi:10.1016/j.ejvs.2005.04.030.
36. Siu, S. C. & Silversides, C. K. Bicuspid Aortic Valve Disease. *Journal of the American College of Cardiology* (2010) doi:10.1016/j.jacc.2009.12.068.
37. Tadros, T. M., Klein, M. D. & Shapira, O. M. Ascending aortic dilatation associated with bicuspid aortic valve. Pathophysiology, molecular biology, and clinical implications. *Circulation* (2009) doi:10.1161/CIRCULATIONAHA.108.795401.
38. Della Corte, A. *et al.* Surgical treatment of bicuspid aortic valve disease: knowledge gaps and research perspectives. *J. Thorac. Cardiovasc. Surg.* **147**, 1749–57, 1757.e1 (2014).
39. Dietz, H. C. *et al.* Marfan syndrome caused by a recurrent de novo missense mutation in the fibrillin gene. *Nature* (1991) doi:10.1038/352337a0.
40. Loeys, B. L. *et al.* The revised Ghent nosology for the Marfan syndrome. *J. Med. Genet.* (2010) doi:10.1136/jmg.2009.072785.
41. Fanelli, F. & Dake, M. D. Standard of practice for the endovascular treatment of thoracic aortic aneurysms and type B dissections. *Cardiovasc. Intervent. Radiol.* **32(5)**, 849–860 (2009).
42. Evangelista, A. *et al.* Echocardiography in aortic diseases: EAE recommendations for clinical practice. *European Journal of Echocardiography* (2010) doi:10.1093/ejechocard/jeq056.
43. Cozijnsen, L. *et al.* What is new in dilatation of the ascending aorta?: Review of current literature and practical advice for the cardiologist. *Circulation* (2011) doi:10.1161/CIRCULATIONAHA.110.949131.
44. Van Puyvelde, J., Verbeken, E., Verbrugghe, P., Herijgers, P. & Meuris, B. Aortic wall thickness in patients with ascending aortic aneurysm versus acute aortic dissection. *Eur. J. Cardio-thoracic Surg.* **49(3)**, 756–762 (2016).

45. Ergin, M. A. *et al.* Surgical treatment of the dilated ascending aorta: When and how? *Ann. Thorac. Surg.* **67(6)**, 1834–1839 (1999).
46. Goodney, P. P. *et al.* Survival after open versus endovascular thoracic aortic aneurysm repair in an observational study of the medicare population. *Circulation* (2011) doi:10.1161/CIRCULATIONAHA.111.033944.
47. Giles, K. A. *et al.* Risk prediction for perioperative mortality of endovascular vs open repair of abdominal aortic aneurysms using the Medicare population. *J. Vasc. Surg.* (2009) doi:10.1016/j.jvs.2009.01.044.
48. Report, C. Experience of non-vascular complications following endovascular aneurysm repair for abdominal aortic aneurysm. 67–70 (2011) doi:10.4174/jkss.2011.80.Suppl.
49. Fillinger, M. F., Marra, S. P., Raghavan, M. L. & Kennedy, F. E. Prediction of rupture risk in abdominal aortic aneurysm during observation: Wall stress versus diameter. *J. Vasc. Surg.* **37(4)**, 724–732 (2003).
50. Rodríguez Palomares, J. *et al.* Aortic flow patterns and wall shear stress maps by 4D-flow cardiovascular magnetic resonance in the assessment of aortic dilatation in bicuspid aortic valve disease. *J Cardiovasc Magn Reson.* **20(1)**, 28 (2018).
51. Bäck, M., Gasser, T. C., Michel, J. B. & Caligiuri, G. Biomechanical factors in the biology of aortic wall and aortic valve diseases. *Cardiovascular Research* (2013) doi:10.1093/cvr/cvt040.
52. Chandra, S. *et al.* Fluid-Structure Interaction Modeling of Abdominal Aortic Aneurysms: The Impact of Patient-Specific Inflow Conditions and Fluid/Solid Coupling. *J. Biomech. Eng.* **135(8)**, 81001 (2013).
53. Shang, E. K. *et al.* Peak wall stress predicts expansion rate in descending thoracic aortic aneurysms. *Ann. Thorac. Surg.* **95(2)**, 593–598 (2013).
54. Speelman, L. *et al.* Patient-Specific AAA Wall Stress Analysis: 99-Percentile Versus Peak Stress. *Eur. J. Vasc. Endovasc. Surg.* **36**, 668–676 (2008).
55. Malkawi, A. H. *et al.* Patient-specific biomechanical profiling in abdominal aortic aneurysm development and rupture. *J. Vasc. Surg.* **52**, 480–488 (2010).
56. Bazilevs, Y., Gohean, J. R., Hughes, T. J. R., Moser, R. D. & Zhang, Y. Patient-specific isogeometric fluid-structure interaction analysis of thoracic aortic blood flow due to implantation of the Jarvik 2000 left ventricular assist device. *Comput. Methods Appl. Mech. Eng.* **198**, 3534–3550 (2009).
57. Westerhof, N., Lankhaar, J. W. & Westerhof, B. E. The arterial windkessel. *Medical and Biological Engineering and Computing* (2009) doi:10.1007/s11517-008-0359-2.
58. Du, T., Hu, D. & Cai, D. Outflow boundary conditions for blood flow in arterial trees.

PLoS One (2015) doi:10.1371/journal.pone.0128597.

59. Villa-Uriol, M. C. *et al.* Toward integrated management of cerebral aneurysms. *Philos. Trans. A. Math. Phys. Eng. Sci.* **368(1921)**, 2961–2982 (2010).
60. Jayendiran, R., Nour, B. & Ruimi, A. Computational fluid–structure interaction analysis of blood flow on patient-specific reconstructed aortic anatomy and aneurysm treatment with Dacron graft. *J. Fluids Struct.* (2018) doi:10.1016/j.jfluidstructs.2018.06.008.
61. Leung, J. H. *et al.* Fluid structure interaction of patient specific abdominal aortic aneurysms: a comparison with solid stress models. *Biomed. Eng. Online* **5**, 33 (2006).
62. Stankovic, Z., Allen, B. D., Garcia, J., Jarvis, K. B. & Markl, M. 4D flow imaging with MRI. *Cardiovasc. Diagn. Ther.* **4**, 1–20 (2014).
63. Nair, S. *Introduction to continuum mechanics*. *Introduction to Continuum Mechanics* (2009). doi:10.1017/CBO9780511841576.
64. Ganghoffer, J. F. Continuum Mechanics. in *Multiscale Biomechanics* (2018). doi:10.1016/B978-1-78548-208-3.50002-2.
65. Merci, B. Introduction to fluid mechanics. in *SFPE Handbook of Fire Protection Engineering, Fifth Edition* (2016). doi:10.1007/978-1-4939-2565-0_1.
66. Rathakrishnan, E. Fundamentals of Fluid Mechanics. in *Instrumentation, Measurements, and Experiments in Fluids* (2013). doi:10.1201/b15874-3.
67. Simao, M., Ferreira, J., Tomás, A. C., Fragata, J. & Ramos, H. M. Aorta Ascending Aneurysm Analysis Using CFD Models towards Possible Anomalies. *Fluids* **31(2)**, 1–15 (2017).
68. Trachet, B. *et al.* An Animal-Specific FSI Model of the Abdominal Aorta in Anesthetized Mice. *Ann. Biomed. Eng.* **43(6)**, 1298–1309 (2015).
69. Valencia, A. *et al.* Fluid Structural Analysis of Human Cerebral Aneurysm Using Their Own Wall Mechanical Properties. *Comput. Math. Methods Med.* **2013**, 18 (2013).
70. Suito, H., Takizawa, K., Sze, D. Y. & Ueda, T. FSI analysis of the blood flow and geometrical characteristics in the thoracic aorta. *Comput. Mech.* **54(4)**, 1035–1045 (2014).
71. Lin, S., Han, X., Bi, Y., Ju, S. & Gu, L. Fluid-Structure Interaction in Abdominal Aortic Aneurysm : Effect of Modeling Techniques. **2017**, (2017).
72. Johnson, K. M. *et al.* Improved 3D phase contrast MRI with off-resonance corrected dual echo VIPR. *Magn Reson Med.* **60(6)**, 1329–1336 (2008).
73. Marco Paluszny, Hartmut Prautzsch, W. B. *Métodos de Bézier y B-Splines*. (2002).
74. Westerhof, N., Lankhaar, J. W. & Westerhof, B. E. The arterial windkessel. *Med. Biol.*

Eng. Comput. **47(2)**, 131–141 (2009).

75. Guala, A. *et al.* Influence of Aortic Dilation on the Regional Aortic Stiffness of Bicuspid Aortic Valve Assessed by 4-Dimensional Flow Cardiac Magnetic Resonance. *JACC Cardiovasc. Imaging* 2604 (2018) doi:10.1016/j.jcmg.2018.03.017.
76. Dogui, A. *et al.* Consistency of aortic distensibility and pulse wave velocity estimates with respect to the Bramwell-Hill theoretical model: A cardiovascular magnetic resonance study. *J. Cardiovasc. Magn. Reson.* **13**, 11 (2011).
77. Houzeaux, G. *et al.* Domain Decomposition Methods for Domain Composition Purpose: Chimera, Overset, Gluing and Sliding Mesh Methods. *Arch. Comput. Methods Eng.* (2017) doi:10.1007/s11831-016-9198-8.
78. Dettmer, W. & Perić, D. A computational framework for fluid-structure interaction: Finite element formulation and applications. *Comput. Methods Appl. Mech. Eng.* **195(41–43)**, 5754–5779 (2006).
79. Minotauro La Super computadora Europea. 5199 (2015).
80. Soulis, J. V., Lampri, O. P., Fytanidis, D. K. & Giannoglou, G. D. Relative residence time and oscillatory shear index of non-Newtonian flow models in aorta. *10th Int. Work. Biomed. Eng. BioEng 2011* 0–3 (2011) doi:10.1109/IWBE.2011.6079011.
81. Soulis, J., Fytanidis, D., Papaioannou, V. & Giannoglou, G. *Oscillating shear index, wall shear stress and low density lipoprotein accumulation in human RCAs*. (2011).
82. Cajas, J. C. *et al.* Fluid-structure interaction based on HPC multicode coupling. *SIAM J. Sci. Comput.* (2018) doi:10.1137/17M1138868.
83. Pons, R. *et al.* Fluid–structure interaction simulations outperform computational fluid dynamics in the description of thoracic aorta haemodynamics and in the differentiation of progressive dilation in Marfan syndrome patients. *R. Soc. Open Sci.* (2020) doi:10.1098/rsos.191752.
84. Mitchell, G. F. *et al.* Aortic diameter, wall stiffness, and wave reflection in systolic hypertension. *Hypertension* (2008) doi:10.1161/HYPERTENSIONAHA.107.099721.
85. Reusz, G. S. *et al.* Reference values of pulse wave velocity in healthy children and teenagers. *Hypertension* (2010) doi:10.1161/HYPERTENSIONAHA.110.152686.
86. Díaz, A., Galli, C., Tringler, M., Ramírez, A. & Cabrera Fischer, E. I. Reference Values of Pulse Wave Velocity in Healthy People from an Urban and Rural Argentinean Population. *Int. J. Hypertens.* (2014) doi:10.1155/2014/653239.
87. Salvi, P. *et al.* Aortic dilatation in Marfan syndrome: Role of arterial stiffness and fibrillin-1 variants. *J. Hypertens.* (2018) doi:10.1097/HJH.0000000000001512.

Annex

A repository is attached to this thesis, that can be found on the link (https://iqsmail-my.sharepoint.com/:f:/g/personal/ramonponsc_iqs_edu/Eu6w1cHkvahKjy3bGgUbfJMBVCwsECcCbRG7_s9xtwcRig?e=oouwox) containing the codes for:

1. Macro of the Solidworks to reconstruct the aortic lumen and wall
2. Script for the shear stress calculation
3. CFD simulation case
4. FSI simulation case

Moreover, in the link below, an example of complete FSI simulation (stable patient 3) can be found: https://doi.org/10.5061/dryad.zcrjdfn6j

All raw data are available on demand by e-mail to jordi.martorell@iqs.edu